Improving the Image Quality of Synthetic Transmit Aperture Ultrasound Images - Achieving Real-Time In-Vivo Imaging

Gammelmark, Kim

Publication date:
2004

Document Version
Publisher's PDF, also known as Version of record

Improving the Image Quality of Synthetic Transmit Aperture Ultrasound Images

Achieving Real-Time In-Vivo Imaging

Kim Løkke Gammelmark

September 9, 2004

Center for Fast Ultrasound Imaging
Ørsted·DTU
Technical University of Denmark
2800 Kgs. Lyngby
Denmark

SUBMITTED IN PARTIAL FULFILLMENT OF THE
REQUIREMENTS FOR THE DEGREE OF
DOCTOR OF PHILOSOPHY
AT
THE TECHNICAL UNIVERSITY OF DENMARK
SEPTEMBER 2004

Signature of Author

Contents

Preface

A long journey has come to an end. A journey, which actually began in the autumn of 1997, when I as a bachelor student back then became familiar with the existence of medical ultrasound scanners, during an internship at B-K Medical A/S. And today, seven years later, this thesis marks the completion of my PhD study on synthetic aperture ultrasound imaging.

This PhD study was carried out at the Center for Fast Ultrasound Imaging (CFU) located in the Ørsted department at the Technical University of Denmark with Professor Jørgen Arendt Jensen as director, who was also my head adviser on the project. The project was initiated on September 1st, 2001, approximately 3 years ago.

The title of the present thesis is *Improving the Image Quality of Synthetic Transmit Aperture Images* with subtitle *Achieving Real-Time In-Vivo Imaging*. The goal of the PhD study has been to show, that real-time applications of synthetic transmit aperture (STA) imaging is feasible with an image quality, that is competitive with the traditional scanning techniques. The foundation of the PhD was established during my Master of Science project, completed at CFU in August 2001 prior to the engagement in the PhD programme, which investigated a new method for increasing the signal-to-noise ratio in STA imaging. The results obtained in this project were very promising, and thus the work was continued in the PhD. This effort proved to be very valuable, which hopefully will be apparent by the time the end of this thesis is reached.

I hope you will enjoy reading this thesis.

Kim L. Gammelmark
Ørsted·DTU
September 2004

Acknowledgments

During my time at the Center for Fast Ultrasound Imaging (CFU), I have had the pleasure of working with several extraordinary people, whom I would like thank.

First of all I would like to say exceptionally thank you to professor, Dr. Techn. **Jørgen Arendt Jensen**, Head of CFU and my adviser, for basically everything. For introducing me to the world of synthetic aperture ultrasound imaging, and for making this PhD study possible. I am deeply thankful for the opportunities you have given me, the learning environment you have provided, and the continuous trust and confidence you have shown in my work. You have been a true inspiration through the years, and I admire and highly respect your capabilities as researcher.

My co-advisor and associate professor **Jørgen Dall** for his invaluable help in making me understand the basics of synthetic aperture radar theory.

A special thank you to all my colleagues at CFU:

- Dr. Med., PhD **Morten Høgholm Pedersen** for being a superb colleague and for his invaluable help in performing the clinical measurements, which have played a very important role of this PhD study.
- Assistant professors **Svetoslav Ivanov Nikolov** and **Borislav Tomov** for their exquisite work on making our experimental ultrasound scanner RASMUS become the only research scanner in the world capable of performing real-time synthetic aperture data acquisition.
- Assistant professor **Malene Schlaikjer** and PhD students **Jesper Udesen**, **Frederik Gran**, and **Louise Kold Taylor** for creating a pleasant working atmosphere at CFU, and for the many laughs and insightful discussions on various aspects of ultrasound and life in general.

Thank you to former colleague at CFU, PhD **Peter Munk**, for his extensive knowledge in ultrasound imaging, the often stressful struggle on making the analog front-end in RASMUS do its job correctly, and for being a great friend.

To PhD **Thanassis Misaridis**, also a former colleague at CFU, for his profound work on coded excitation signals, which has become an integral part of this PhD study.

Thank you to **Henrik Laursen** for his continuous effort to make out large computer cluster network run as smooth as possible, and for his help addressing and solving various software related problems encountered during the daily routines.

A sincere thanks to **Keld Martinsen** for manufacturing phantoms and various holders for our transducers, which have made the execution and accuracy of the experiments significantly better.

My parents, sister, and brother for being the wonderful family they are, for their faith in me, and for always being there for me.

Finally, the deepest thank you to my beloved girlfriend **Karina** for her love and magnificent support, and for bearing with me during this, on many occasions, stressful and demanding period.

And to the ones that I may have forgotten - accept my deepest apology.

This work was supported by grants 9700883 and 9700563 from the Danish Science Foundation, by Ph.D. grant 11-3160-55173 from the Technical University of Denmark, and by B-K Medical A/S, Herlev, Denmark.

Abstract

Synthetic transmit aperture (STA) imaging has the potential to increase the image quality of medical ultrasound images beyond the levels obtained by conventional imaging techniques (linear, phased, and convex array imaging). Currently, however, in-vivo applications of STA imaging is limited by a low signal-to-noise ratio (SNR), due to the application of a single transducer element at each emission, and higher susceptibility to tissue motion, produced by the summation of sequentially acquired low resolution images. In order to make real-time STA imaging feasible for in-vivo applications, these issues need to solved.

The goal of this PhD study has been to find methods that can be used to overcome the above mentioned limitations, and hereby improve the image quality of STA imaging to a clinically desirable level, enabling real-time in-vivo STA imaging.

The thesis investigates a new method to increase the SNR, which employs multi-element subapertures and linearly frequency modulated (FM) signals at each emission. The subaperture is applied to emulate a high power spherical wave transmitted by a virtual point source positioned behind the subaperture, and the linear FM signal replaces the conventional short excitation signal to increase the transmitted temporal energy. This approach, named Temporally encoded Multi-element Synthetic transmit aperture (TMS) imaging, is evaluated in detail for linear array and convex array imaging applications using simulations, and phantom and in-vivo experiments.

The thesis contains summaries of four journal articles and four corresponding conference publications, which comprise the primary contributions of the PhD. The first two papers give elaborated evaluations of TMS imaging for linear array and convex array imaging, respectively. The results, including initial in-vivo experiments, showed, that TMS imaging can increase the SNR by as much as 17 dB compared to the traditional imaging techniques, which improves the in-vivo image quality to a highly competitive level.

An in-vivo evaluation of convex array TMS imaging for abdominal imaging applications is presented in the third paper, based on a clinical trial with 7 healthy male volunteers. Real-time movie sequences of 3 seconds duration were acquired and analyzed by experienced medical doctors using blinded clinical evaluation. The results showed a statistically significant improvement in image quality of convex array TMS imaging compared to conventional convex array imaging. Only minor motion artifacts causing subtle image brightness fluctuations were reported in TMS imaging, which did not depreciate the diagnostic value of the images.

The influence of tissue motion and a method for two-dimensional motion compensation is investigated in the fourth and final paper. The method estimates the tissue velocity and motion

direction at each image point by correlating image lines beamformed along a set of motion directions and selects the direction and velocity corresponding to the highest correlation. Using these estimates, motion compensation is obtained by tracking the location of each pixel, when reconstructing the low resolution images. The presented phantom and in-vivo results showed, that severe tissue motion has a negative influence on the image quality of STA imaging as expected, but, most importantly, that the proposed method successfully compensates for the motion, thus, retaining the image quality of TMS imaging, when scanning moving tissue.

In conclusion, the results of the research presented in this thesis have demonstrated, that TMS imaging is feasible for real-time in-vivo imaging, and that the obtained image quality is highly competitive with the techniques applied in current medical ultrasound scanners. Hereby, the goals of the PhD have been successfully achieved.

Resumé (Danish)

Syntetisk transmit apertur (STA) billeddannelse kan potentielt forbedre billedkvaliteten af medicinske ultralydsbilleder til et niveau, der overstiger det, som opnås med de traditionelle billeddannelsesmetoder. På nuværende tidspunkt er anvendelsen af STA metoden til klinisk skanning dog begrænset af et lavt signal-støj forhold, forårsaget af anvendelsen af et enkelt transducer element ved hver udsendelse, og en større følsomhed overfor vævsbevægelse, som fremkommer ved summeringen af de sekventielt optagne lavopløsningsbilleder. For at gøre STA metoden anvendelig til klinisk skanning i realtid er det derfor nødvendigt at finde løsninger på disse problemer.

Målet med dette PhD studie har været at finde metoder til at overvinde de ovenfor nævnte begrænsninger og derved forbedre billedkvaliteten af STA metoden til et klinisk ønskeligt niveau, for herved at tilvejebringe anvendelsen af STA metoden til klinisk skanning i realtid.

Afhandlingen udforsker en ny metode til forøgelse signal-støj forholdet, som anvender et subapertur bestående af multiple elementer og et lineært frekvensmoduleret (FM) signal ved hver udsendelse. Subaperturet anvendes til at efterligne en sfærisk bølge med høj energi udsendt af en virtuel punkt kilde placeret bagved subaperturet, og det lineære FM signal erstatter den konventionelle korte eksitationspuls for at øge den udsendte energi yderligere. Denne metode, kaldet Temporalt kodet Multi-element Syntetisk transmit apertur (TMS) billeddannelse, bliver undersøgt i detaljer med primær henblik på lineær array og konveks array transducer applikationer gennem simuleringstudier, samt fantom og in-vivo eksperimenter.

Afhandlingen indeholder sammendrag af fire tidsskriftartikler og fire tilhørende konference publikationer, som udgør de primære forskningsmæssige bidrag fra PhD'et. De to første artikler giver en udførlig evaluering af TMS billeddannelsesmetoden ved anvendelse af henholdsvis lineær array transducere og konveks array transducere. Resultaterne, som omfatter indledende in-vivo forsøg, viste, at TMS metoden kan øge signal-støj forholdet med op til 17 dB sammenlignet med de konventionelle skanneteknikker, hvilket forbedrede billedkvaliteten in-vivo til et konkurrencedygtigt niveau.

En klinisk evaluering af konveks array TMS billeddannelse til abdominal skanning præsenteres i den tredje artikel, baseret på kliniske afprøvninger på 7 frivillige raske mænd. Videosekvenser med en varighed op ca. 3 sekunder blev optaget i realtid og analyseret af efarne læger med ekspertise indenfor ultralydskanning. Resultaterne viste, at konveks array TMS billeddannelse frembringer en statistisk signifikant forbedring af billedkvaliteten i sammenligning med konventionel konveks array billeddannelse. Kun minimale bevægelsesforstyrrelser blev observeret, som forårsagede diskrete fluktationer i billedernes intensitetsniveau, men disse påvirkede ikke den diagnostiske værdi af billederne negativt.

Påvirkningen af vævsbevægelse og en metode til to-dimensional bevægelseskompensation bliver undersøgt i den fjerde og sidste artikel. Metoden estimerer hastigheden og retningen, hvormed vævet har bevæget sig, ved at korrelere signaler rekonstrueret langs et udvalg af forskellige bevægelsesretninger ved hvert punkt i billedet, for herefter at vælge den retning og hastighed, som har den største korrelationsværdi. Disse estimater anvendes til kompensation for bevægelsen, hvilket opnås ved kontinuert at forfølge den spatiale placering af hver pixel i de rekonstruerede lavopløsningsbilleder. De præsenterede fantom og in-vivo resultater viste, at voldsom vævsbevægelse har en ødelæggende virkning på billedkvaliteten i STA billeddannelse som forventet, men vigtigst, at den udviklede metode kompenserer for bevægelsen med stor succes, hvilket derfor bevirker, at billedkvaliteten bliver opretholdt ved TMS billeddannelse, når bevægeligt væv skannes.

Forskningsresultaterne, som er blevet præsenteret i denne afhandling, viser, at TMS billeddannelse er anvendelig til klinisk skanning i realtid, og at den opnåede billedkvalitet er konkurrencedygtig med de nuværende skanneteknikker. De fremsatte mål med dette PhD studie er derfor blevet opnået.

List of Abbreviations

ADC	Analog to digital converter
B-mode	Brightness mode
CR	Contrast Resolution
CT	Computerized tomography
E-mode	Estimation mode (used for tissue motion compensation)
F-number	Ratio between the distance to focus and width of aperture - the focal number
FDA	Food and Drug Administration (USA)
FM	Frequency modulation
MRI	Magnetic resonance imaging
NDT	Nondestructive testing
PSF	Point spread function
RF	Radio frequency
SA	Synthetic Aperture (imaging)
SAR	Synthetic aperture radar
SD	Standard deviation
SNR	Signal to noise ratio
STA	Synthetic Transmit Aperture (imaging)
TGC	Time gain compensation curve
3D	Three dimensional
TMS	Temporally encoded Multi-element Synthetic transmit aperture (imaging)
2D	Two dimensional

CHAPTER

ONE

Introduction

Medical ultrasound imaging systems are used by medical doctors every day for diagnosis, inspection, and guidance during surgery in a variety of application areas such as fetal imaging, cardiac imaging, blood flow imaging, abdominal imaging, etc. The ultrasound scanner is used intensively, because it provides realtime imaging with high quality of soft tissue by non-invasive means[1], and, at the same time, it is mobile, inexpensive, and safe for the patient. This is compared to other medical imaging modalities, such as computerized tomography (CT) and (nuclear) magnetic resonance imaging (MRI), both of which comprise large expensive systems that cannot easily be transported to the patient.

Research within ultrasound imaging is progressing continuously. New imaging methods are constantly being exploited, aiming to extend the application of ultrasound imaging into new areas, and to improve the quality of the ultrasound images and, thus, their diagnostic value. Acoustic radiation force imaging [1] and tissue harmonic imaging [2] are examples of recently developed methods, which utilize the properties of ultrasound imaging to make new types of ultrasound images. Another method, which has been investigated for almost a decade in ultrasound imaging, is synthetic transmit aperture (STA) imaging [3, 4]. This method is based on principles, originally adapted from synthetic aperture radar (SAR) systems [5, 6, 7], which are quite different from the imaging methods applied in the traditional ultrasound systems used today.

In modern medical ultrasound scanners, linear and phased array techniques are used to generate the displayed images. These techniques build up the images over a number of transmit events by transmitting focused beams in distinctive directions in the medium. After each transmission, all or a portion of the transducer elements are used to record the echo signals scattered by the tissue. For each direction, the received echoes are focused dynamically along the same direction, and the produced scan lines are stacked together to create the displayed image. This produces the best possible receive beam pattern in terms spatial resolution, and very often dynamic amplitude weighting (apodization) of the receive elements is also applied to control the beam width and sidelobe levels. The overall spatial resolution is compromised by the single transmit focal point. Thus, the spatial resolution is only optimal at the transmit focal point. To minimize this effect, compound imaging is often applied, which composes each line from several transmissions, each having a different transmit focus location [8].

In contrast to the narrow spatial extend of the ultrasound field transmitted by the traditional methods, the basic principle in STA imaging is to transmit a spherical wave using a single transducer element, which propagates in all directions in the medium simultaneously. The

[1] This excludes intravascular ultrasound imaging, which is a relatively new application area of ultrasound imaging, that performs ultrasound imaging inside blood vessels by utilizing a small catheter based transducer.

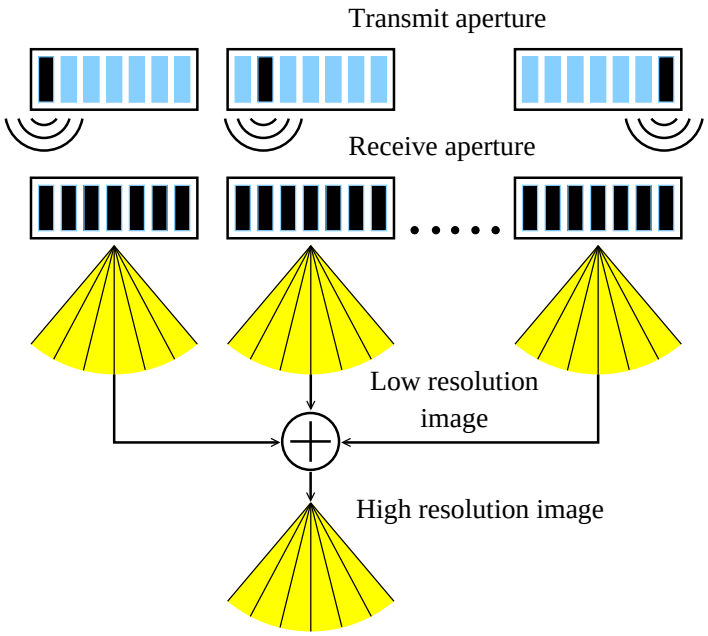

Figure 1.1: Illustration of the STA imaging principle. At each transmit event a single element is used to generate a spherical wave. The ultrasound pulse propagates in all directions in the medium simultaneously, and, thus, the recorded echoes contain information about every scatterer within the interrogated region. By steering and focusing these signals at every image point, a complete image is reconstructed after one emission. This procedure is repeated for all aperture element, and the resulting images are finally summed to produce the displayed ultrasound image.

echoes recorded by the transducer elements used for reception contain information about every scatterer in the illuminated region. Thus, the received signals can be steered and focused at all image points to form a complete image after one emission. This process is repeated by exciting all transducer elements one by one, and the reconstructed images are finally summed to produce the displayed image. Figure 1.1 illustrates this approach.

Conceptually, the reconstruction of each point or pixel in the displayed STA image is performed by coherently summing for all transmissions the echoes received from a point target located at the center of each pixel. This is possible, because the origin and shape of the transmitted wave is known. The origin is determined by the location of the transmitting element, and the wavefront is spherical due to the small aperture elements. Assuming the speed of sound in the medium is known, the arrival time of the echo from a given point target for a specific transmit and receive element pair can be calculated exactly using the geometric relations illustrated in Fig. 1.2. By performing this calculation for all transmit-receive element pairs, picking out the corresponding samples of the recorded echoes, and finally summing these samples, both the transmit and the receive apertures are focused at the point target location, producing the best possible focusing. This process is repeated for all points or pixels in the ultrasound image. Mathematically, this is written as

$$S(\vec{r}_p) = \sum_{m=1}^{M} \sum_{n=1}^{N} w_m(\vec{r}_p) w_n(\vec{r}_p) g_{n,m} \left(\frac{\left|\vec{r}_n - \vec{r}_p\right| + \left|\vec{r}_p - \vec{r}_m\right|}{c} \right) \tag{1.1}$$

where $S(\vec{r}_p)$ is the reconstructed image, $w_m(\vec{r}_p)$ is the apodization for transmit element m, $w_n(\vec{r}_p)$ is the apodization for receive element n, $g_{n,m}(t)$ is the recorded echo data, and M and

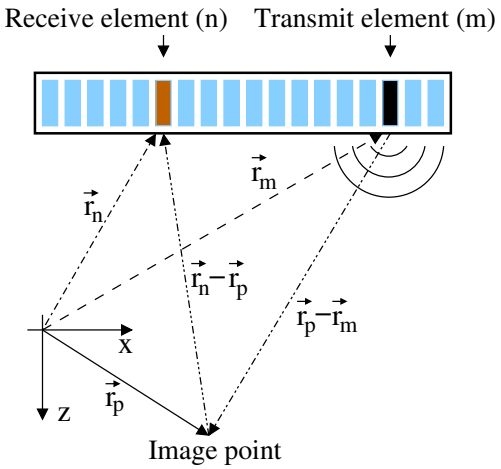

Figure 1.2: Geometrical illustration of the reconstruction of STA images. The core principle is the known origin and shape (spherical) of the emitted wave. Based on this and the knowledge of the speed of sound, the arrival time of the echo from a given point target can be calculated exactly. The vectors $\vec{r}_p$, $\vec{r}_n$, and $\vec{r}_m$ denote the location of the image point, the receive element n, and the transmit element m, respectively.

N are the number of transmit and receive elements, respectively. The vector $\vec{r}_p$ denotes the image point being reconstructed, while $\vec{r}_n$ and $\vec{r}_m$ point to the location of receive element n and transmit element m, respectively.

In practice, the image reconstruction process is performed sequentially as illustrated initially in Fig. 1.1. The image produced after each emission is generally called a low (lateral) resolution image, because it is created using a single transmit element. The process of summing the low resolution images synthesizes the transmit aperture over several transmissions. Hence the name *synthetic transmit aperture imaging*.

1.1 Synthetic Transmit Aperture Imaging - Why?

STA imaging has some clear advantages compared to the traditional techniques:

1. Full control of both the transmit and receive fields.
2. Data from the entire image area are available continuously.
3. Very high frame rates are feasible.

As indicated by Eqn. 1.1, the weighting coefficients applied to the transmit and receive elements can be chosen arbitrarily. Furthermore, both the transmit and receive apertures are focused at every image point by compensating for the total distance travelled by the emitted pulse for every transmit-receive element pair. This enables the application of dynamic transmit and receive apodization as well as dynamic transmit and receive focusing, thus, giving full flexibility in controlling the image quality. Conceptually, this corresponds to a traditional ultrasound scanner, which transmits a focused beam for every image point. Thus, if the image contains 100 lines each with 512 image points, the number of transmissions used by the conventional system

becomes 51200, while, for STA imaging, only 128 emissions are used, if the transmit aperture has 128 elements. Thus, STA imaging is capable of improving both spatial resolution and contrast resolution compared to conventional imaging.

The application of a spherical wave in STA imaging results in a complete low resolution image produced after every emission as explained above. Hereby, data within the entire image plane are available continuously, and frame rates as high as the pulse repetition frequency (f_{prf}) are therefore feasible. For an imaging depth of 15 cm and a speed of sound of 1500 m/s, the maximum f_{prf} is $\frac{1500}{2 \cdot 0.15} = 5$ kHz, resulting in potentially 5000 frames/sec. This opportunity was noticed by Nikolov and colleagues in [9], who developed a high frame rate STA imaging approach called *recursive ultrasound imaging*. In this approach, the displayed STA image is updated after every emission by adding the new low resolution image to the STA image and simultaneously subtracting the old low resolution image corresponding to the same emission. Hereby, a new image is displayed after every emission. Sparse STA imaging [10, 11] is another approach to high frame rate imaging. Here, STA images are generated using a few transmissions, i.e. a few low resolution images, spaced over the entire transmit aperture to maintain spatial resolution. To compensate for the larger spacing between the transmit positions, which in general results in the appearance of grating lobes [12], the apodization functions applied to the transmit and receive apertures are adjusted using the effective aperture approach to minimize their effect [10, 13]. A clear target in obtaining high frame rates is three-dimensional (3D) volumetric imaging, which is in high demand due to its high clinical value. For this application, STA imaging is very feasible.

Therefore, STA imaging holds a great potential of improving the quality of ultrasound images beyond that produced by the traditional methods.

1.1.1 Limited In-Vivo Application

Unfortunately, there are some problems associated with STA imaging in its current form. Basically, there are two issues, which limits the in-vivo application of STA imaging:

1. Low signal-to-noise ratio (SNR)
2. Susceptibility to tissue motion

What limits the penetration depth in ultrasound imaging is the frequency & depth dependent attenuation, which is present in soft human tissue. This attenuation decreases the energy in the transmitted acoustic pulse as it propagates into the tissue, and the attenuation also increases with frequency, such that higher frequency systems obtain smaller penetration depth. Due to the application of a single element at each emission in STA imaging, the emitted acoustic energy is significantly lower than in conventional imaging. Limitations in the front-end electronics of the scanner and transducer cooling issues typically prohibit an increase of the excitation voltage, and the receiver can only perform limited amplification of the received echoes. Thus, the energy in the acoustic field is rapidly attenuated below the noise threshold of the ultrasound system, resulting in a poor SNR and low penetration depth. This limits the in-vivo application of STA imaging significantly.

Because the displayed STA image is produced by adding low resolution images obtained over several emissions, the method inherently relies on that this summation is coherent, i.e. the low resolution images are phase aligned when summed. If the low resolution images are summed

incoherently, the displayed image will become unfocused with a smeared appearance, resulting in loss in image quality. One factor causing phased misalignment is tissue motion, which is primarily produced by the beating heart, blood pulsation, respiration, and transducer motion. The latter is produced by the medical doctor while scanning. The degree of loss in image quality will depend on how severe the motion is, and therefore it will depend on the anatomical location being scanned. Compared to the traditional ultrasound scanners, where motion artifacts occur as distortions of the tissue structures rather than as loss in spatial and contrast resolutions, STA imaging is clearly more susceptible to motion. In general, it may therefore be necessary to compensate for tissue motion to fully retain the advantages of STA imaging.

1.2 State of The Art

Synthetic aperture imaging has been investigated for ultrasound imaging since the late 1960 and early 1970 [14, 15]. In the 1970s and 1980s, it was primarily explored for nondestructive testing (NDT) using a more or less direct implementation of the SAR principle, known today as monostatic synthetic aperture imaging [16]. With the introduction of transducer arrays in the 1970s, focus was gradually directed towards this application area to pursue real time implementations [17, 18, 19].

Until the beginning of 1990, the idea of applying the synthetic aperture imaging approach for medical ultrasound imaging had only been considered occasionally [15, 20]. In 1992, O'Donnell and Thomas published a method intended for intravascular imaging based on synthetic aperture imaging utilizing a circular aperture [21]. To overcome the problem with low SNR and impedance matching between the transducer and receiver circuit, the single element transmission was replaced by simultaneous excitation of a multi-element subaperture. Due to the circular surface of the transducer, the subaperture generated a spherical wave with limited angular extend at each emission, thus, permitting synthetic aperture focusing to be applied. This was the first direct attempt to apply synthetic aperture imaging for medical ultrasound imaging. Since then, the application of multi-element subapertures to increase the SNR of synthetic aperture imaging has been investigated using phased array transducers by Karaman and colleagues for small scale systems [3, 22], by Lockwood and colleagues for sparse synthetic aperture systems with primary focus on 3D imaging applications [10, 11], and by Nikolov and colleagues for recursive ultrasound imaging [9]. In all cases, the multi-element subaperture was used to emulate the radiation pattern of the single element transmission by applying defocusing delays in such a way, that a spherical wave with limited angular extend was produced. The definition of synthetic transmit aperture (STA) imaging was introduced by Chiao and colleagues in [4]. This paper also considered the feasibility of applying spatial encoding to enable transmission on several elements simultaneously, while separating the individual transmissions in the receiver using addition and subtraction of the received signals. A third approach, which utilizes orthogonal Golay codes to increase the SNR, while transmitting simultaneously on several elements, was also considered by Chiao and Thomas in [23].

The influence of motion in STA imaging and methods for compensation have been investigated in several publications [24, 25, 26, 27, 28]. Commonly it is reported, that axial motion is the dominant factor causing image quality degradation due to the significantly higher spatial frequency in this dimension. The presented motion estimation methods are generally based on time-domain cross-correlation of reference signals to find the shift in position in the axial dimension. Since tissue motion is inherently three dimensional, it is however likely, that to

retain the advantages of STA imaging, at least two dimensional (2D) motion correction to compensate successfully for scan plane tissue motion is required. Furthermore, none of the methods have been evaluated using in-vivo experiments.

To this point, it has therefore not been shown, if in-vivo STA imaging is feasible.

1.3 Scope and Aim of Study

Inspired by the great potential of STA imaging and the previously published research, the goal of this PhD study is to show, that real-time in-vivo STA imaging is feasible, and not least demonstrate, that the image quality can be improved to a clinically desirable level, which is competitive with the current techniques.

The primary target will be B-mode imaging, and since full attention is given to improving the image quality, sparse implementations for B-mode imaging will not be considered explicitly.

Much effort has been put on the application of phased array transducers in previous research, but linear and convex array geometries have not been explored directly. To show that STA imaging is not limited to any specific aperture geometry, these imaging geometries will be the main target.

The basis for the PhD study was established during the Master of Science project conducted by the author in [29]. This project investigated a new method for increasing the SNR in STA imaging based on the application of multi-element subapertures and linearly frequency modulated (FM) signals or chirps. In particular, each single element transmission was replaced by a subaperture defocused to emulate a high power virtual point source located behind the subaperture, and the conventional short excitation pulse used to obtain good axial resolution was replaced by a linear FM signal. The results obtained were very promising, and, thus, the work was continued in the PhD study.

1.4 Contributions

On the path of achieving these goals a number of journal as well as conference papers have been written.

Journal Articles

1. **Kim L. Gammelmark** and Jørgen A. Jensen, ”Multielement Synthetic Transmit Aperture Imaging using Temporal Encoding,” published in *IEEE Transactions on Medical Imaging*, vol. 22, no. 4, pp. 552-563, 2003.

2. **Kim L. Gammelmark** and Jørgen A. Jensen, ”Synthetic Transmit Aperture Imaging using Convex Transducer Arrays,” submitted to *IEEE Transactions on Ultrasonics, Ferroelectrics, and Frequency Control* in April 2004.

3. Morten H. Pedersen, **Kim L. Gammelmark**, and Jørgen A. Jensen, ”In-Vivo Evaluation of Convex Array Synthetic Aperture Imaging,” submitted to *Ultrasound in Medicine and Biology* in July 2004.

4. **Kim L. Gammelmark** and Jørgen A. Jensen, ”2D Tissue Motion Compensation of Synthetic Transmit Aperture Images,” submitted to *IEEE Transactions on Medical Imaging* in August 2004.

Conference Papers

1. **Kim L. Gammelmark** and Jørgen A. Jensen, ”Multi-Element Synthetic Transmit Aperture Imaging using Temporal Encoding,” presented at *SPIE - Progress in biomedical optics and imaging* in San Diego, California, February 2002, pp. 25-36.

2. **Kim L. Gammelmark** and Jørgen A. Jensen, ”Experimental Study of Convex Coded Synthetic Transmit Aperture Imaging,” presented at the *IEEE International Ultrasonics Symposium* in Münich, Germany, October 2002, pp. 1573-1576.

3. **Kim L. Gammelmark** and Jørgen A. Jensen, ”Duplex Synthetic Aperture Imaging with Tissue Motion Compensation,” presented at the *IEEE International Ultrasonics Symposium* in Honolulu, Hawaii, October 2003, pp. 552-563.

4. Morten H. Pedersen, **Kim L. Gammelmark**, and Jørgen A. Jensen, ”Preliminary In-Vivo Evaluation of Convex Array Synthetic Aperture Imaging,” presented at *SPIE - Progress in biomedical optics and imaging* in San Diego, California, February 2004, pp. 33-43.

All conference papers have been published in the corresponding conference proceedings on the pages listed above.

Besides the publications listed above, which comprise the primary results from the Ph.D., contributions have been aided to other publications listed below.

Additional Publications

1. J. A. Jensen, O. Holm, L. J. Jensen, H. Bendsen, S. I. Nikolov, B. G. Tomov, P. Munk, M. Hansen, K. Salomonsen, J. Hansen, K. Gormsen, H. M. Pedersen, and **K. L. Gammelmark**, ”Ultrasound Research Scanner for Real-time Synthetic Aperture Image Acquisition”, submitted to *IEEE Transactions on Ultrasonics, Ferroelectrics, and Frequency Control* in 2003.

2. Anna T. Fernandez, **Kim L. Gammelmark**, Jeremy J. Dahl, Constance G. Keen, Roderick C. Gauss, and Gregg E. Trahey, ”Synthetic Receive Beamforming and Image Acquisition Capabilities Using an 8x128 1.75D Array”, published in *IEEE Transactions on Ultrasonics, Ferroelectrics, and Frequency Control*, vol. 50, no. 1, pp. 40-57, 2003.

3. Jørgen A. Jensen, Svetoslav I. Nikolov, Thanassis Misaridis, and **Kim L. Gammelmark**, ”Equipment and methods for synthetic aperture anatomic and flow imaging”, invited presentation at the *IEEE International Ultrasonics Symposium* in Münich, Germany, October 2002, pp. 1518-1527.

1.5 The Thesis

The thesis consists of four main chapters, one for each journal and conference article pair, a conclusion with future remarks, and an appendix including all papers. The four chapters are written as summaries of the respective papers. Therefore, all papers in Appendix A and B are integral parts of each chapter, and they should be read as well to acquire all details. The additional publications listed above are placed in Appendix C. When appropriate, references will be given to these, but they are not directly integrated into the thesis.

Chapter 2 introduces the new method for increasing the SNR in STA imaging mentioned above in the context of linear array imaging, and its performance is investigated using simulations, phantom, and in-vivo experiments. The papers summarized in this chapter are placed in Appendix A.1 and B.1.

Chapter 3 describes the implementation of the method with convex array transducers. New design considerations related to the more complex geometry are discussed, and the performance is evaluated using phantom and in-vivo measurements. The papers summarized in this chapter are placed in Appendix A.2 and B.2.

Chapter 4 presents an in-vivo evaluation of the approach using the convex array implementation described in Chapter 3 in comparison to conventional convex array imaging. The evaluation is performed by medical doctors with substantial experience in ultrasound imaging based on acquired real-time abdominal imaging sequences. The papers summarized in this chapter are placed in Appendix A.3 and B.4.

Chapter 5 evaluates a new method for two-dimensional tissue motion compensation using both linear array and convex array transducers. The method is described in detail, and its performance is investigated through simulations, phantom, and in-vivo measurements. The papers summarized in this chapter are placed in Appendix A.4 and B.3.

Finally, the thesis is concluded in Chapter 6, which also considers future directions.

CHAPTER

TWO

Multi-Element Synthetic Transmit Aperture Imaging using Temporal Encoding

This chapter contains a summary of the journal article

- **Kim L. Gammelmark** and Jørgen A. Jensen, "Multielement Synthetic Transmit Aperture Imaging using Temporal Encoding," published in *IEEE Transactions on Medical Imaging*, vol. 22, no. 4, pp. 552-563, 2003,

and the conference article

- **Kim L. Gammelmark** and Jørgen A. Jensen, "Multi-Element Synthetic Transmit Aperture Imaging using Temporal Encoding," presented at *SPIE - Progress in biomedical optics and imaging* in San Diego, California, February 2002, pp. 25-36,

which are found in full length in Appendix A.1 and B.1, respectively. The journal paper is an extended and elaborated version of the conference paper, and, thus, primary focus will be put on the content of the journal paper (hereinafter referred to as the paper).

2.1 Objective of Study

During the Master of Science project presented in [29], a new approach to increase the SNR of STA imaging was developed and investigated. The method utilized a multi-element subaperture at each emission to emulate a spherical wave with limited angular extend, and the conventional excitation signal was replaced by a linear FM signals. The paper contains an elaborated evaluation of this approach, which is called *Temporally encoded Multi-element Synthetic transmit Aperture* (TMS) imaging. The investigations are performed using a linear array transducer, and the results are compared to conventional linear array imaging.

2.2 Summary of Papers

The application of multi-element subaperture emissions and linear FM signals in STA imaging introduces changes to both the imaging setup and to the image reconstruction, referred to as

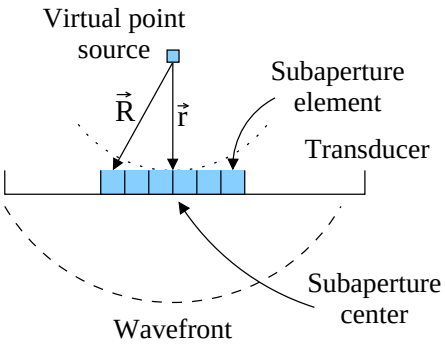

Figure 2.1: Illustration of the setup used when calculating the transmit delays for emulating a spherical wave emitted from a virtual high power point source positioned behind the subaperture. This is a replica of Fig. 3 in [30].

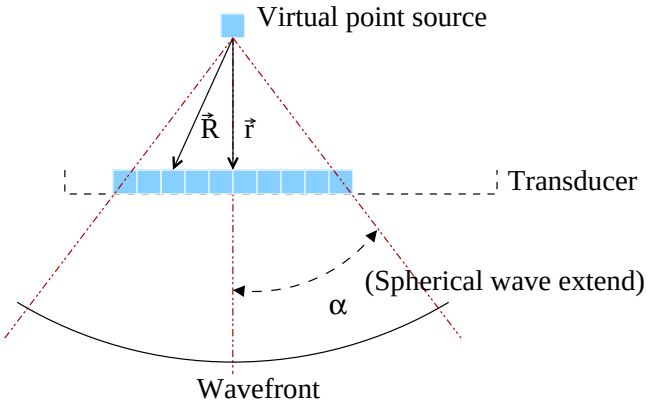

Figure 2.2: Illustration of the relationship between the virtual point source location and the angular extend of the emulated spherical wave transmitted by the subaperture.

STA beamforming in the paper. To emulate the spherical wave emanating from the single element applied conventionally, a virtual point source is positioned behind the center of the subaperture, as illustrated in Fig. 2.1. Based on the location of the virtual point source and the subaperture element coordinates, the defocusing delays $\tau(n)$ are calculated by[1]

$$\tau(n) = \frac{|\vec{R}(n)| - |\vec{r}|}{c}, \tag{2.1}$$

where $\vec{R}(n)$ is the vector from the virtual point source to element n, $\vec{r}$ is the vector from the virtual point source to the subaperture center, and c is the speed of sound. Conceptually, these delays are equal to the difference in arrival time of a spherical wave emitted by the virtual point source relative to the subaperture center. The position of the virtual point source determines the angular extend, over which the transmitted wavefront is spherical, as shown in Fig. 2.2. This relationship is not clearly described in the paper, and, thus, it is included here for clarity. Based on Fig. 2.2, the angular extend of the spherical wavefront α is

$$\alpha = \arctan\left(\frac{D}{2|\vec{r}|}\right), \tag{2.2}$$

[1] Eqn. 2.1 is a slightly modified version of Eqn. 4 in the paper.

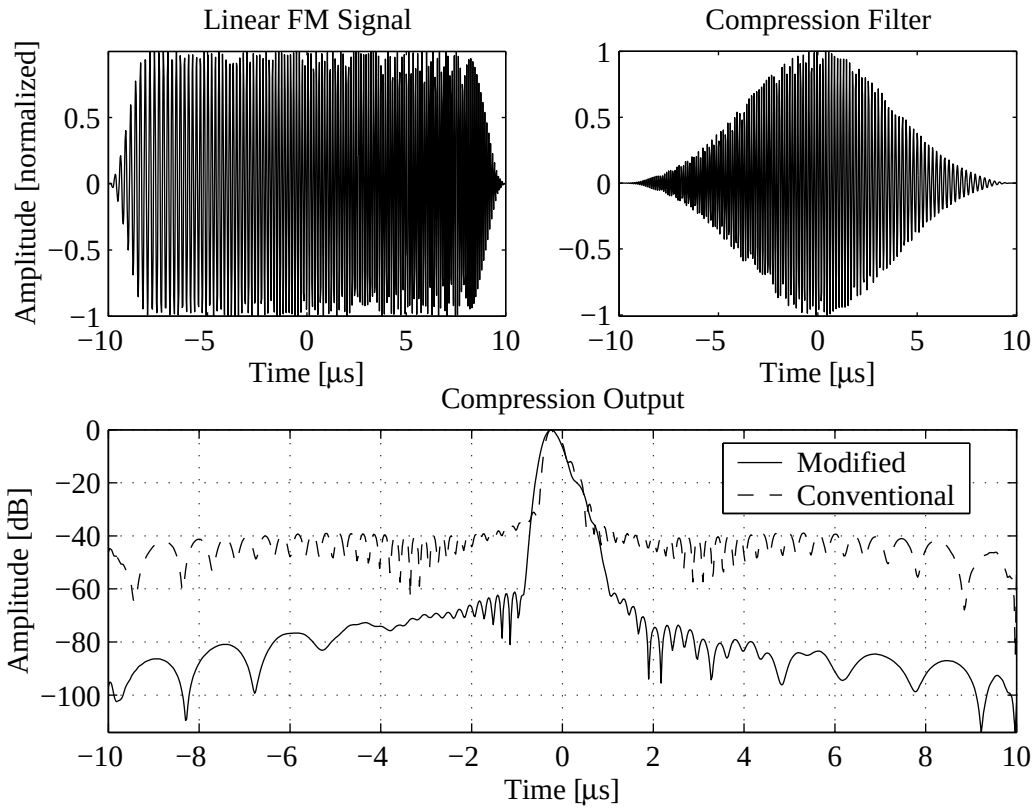

Figure 2.3: Top left: Modified linear FM signal with a 7 MHz center frequency and 7 MHz bandwidth. A Tukey window with a duration of 10% has been applied. Top right: Modified compression filter using a Chebychev window with 70 dB relative sidelobe attenuation. Bottom: Compression output for the conventional FM signal (dashed) and the modified FM signal (solid). The effect of a linear array transducer has been introduced in the compression outputs. This is a replica of Fig. 4 in [30].

where D is the size of the subaperture. The limited angular extend determines the minimum the transmit F-number, that can be applied when using dynamic apodization. The benefit of applying the multi-element emissions is an increase in transmitted energy proportional to the number of subaperture elements.

The linear FM signal was introduced to obtain a further increase in transmitted energy. As mentioned in the paper, these waveforms have been investigated intensively for decades in radar imaging, and for ultrasound imaging since 1979. The implementation was therefore relatively straight forward. One particular challenge in obtaining a successful application of linear FM signals in ultrasound imaging is, however, the reduction of the temporal sidelobes, which are produced by the matched filtering used to compress the linear FM signal. In ultrasound imaging, the dynamic range in the images is typically on the order of 60 dB, and the temporal sidelobe levels therefore need to be below this limit to prevent image artifacts such as ghost objects. This optimization problem has been investigated heavily by Misaridis and colleagues in a series of publications [31, 32, 33, 34]. The sidelobes can be reduced by applying amplitude weighting on the linear FM signal and the corresponding compression filter. In particular, as described in [31], the ripples in the Fourier spectrum of the linear FM signal, which give rise to distant temporal sidelobes, are reduced by attenuating the edges of the linear FM signal. The sidelobes close to the compression peak are reduced by applying weighting on the compression

filter. The weighting scheme applied in this paper, as well as in all other publications presented in this thesis, is identical to the one proposed by Misaridis in [31]. The applied linear FM signal, corresponding compression filter, and the compression output is shown in Fig. 2.3. As seen the weighting scheme has reduced the temporal sidelobes below -60 dB, which is acceptable for in-vivo imaging.

The combination of multi-element STA imaging with linear FM signals produces TMS imaging. In the paper, its performance is compared to conventional linear array imaging in terms of image quality, comprising spatial resolution, contrast resolution, and SNR. A simplified model for the improvement in SNR was developed, which gives an intuitive understanding of the parameters affecting the performance. This model indicates, that a significant increase in SNR and thus penetration depth can be expected in TMS imaging. Further details are found in the paper.

Experiments were performed with an 8.5 MHz linear array transducer with 128 elements. TMS imaging was implemented using a 33 element subaperture and the 20 μs linear FM signal shown in Fig. 2.3. The virtual source was positioned behind the center of the subaperture at a distance equal to the size of the subaperture. With reference to Eqn. 2.2, this corresponds to an angular extend of approximately 30°. 96 emissions were used for each B-mode image, and 128 elements were applied on receive. Linear array imaging used for comparison was setup using 64 transmit elements, 128 receive elements, and a 2 cycle sinusoidal pulse. The number of lines per B-mode image varied from 132 to 165 depending on the applied transmit focus location. For TMS imaging, dynamic transmit and receive focusing was used as well as dynamic transmit and receive apodization utilizing a modified Hamming window and F-number=2. The linear array imaging data were beamformed using dynamic receive focusing and apodization identical to that applied for TMS imaging. Please consult the paper for further details.

The simulations using Field II [35, 36] and measurements with the RASMUS system [37](see appendix C.1) are described in detail in the paper. A few key findings are though included here. The overall performance of TMS imaging in relation to linear array imaging can basically be evaluated from Fig. 2.4, which shows the B-mode images of a tissue mimicking wire phantom. The dynamic range is 50 dB. An increase in penetration depth of approximately 3 cm is obtained, and it is noticed, that the spatial resolution is comparable until 50 mm due to the application of dynamic apodization with F-number=2.

The spatial resolution performance is evaluated in Fig. 2.5. The simulation data are obtained from a wire phantom with axial spacing of 5 mm between the wires, while the measurement data are obtained from the wires in Fig. 2.4. The latter explains the shortened curve for linear array imaging due to lack of data. The improvement in lateral resolution due to the much better control of the transmit field in TMS imaging is clearly noticed, especially for the simulation data, since more data are available here. The axial resolutions have equal performance. Comparing the simulation and measurement results, the lateral resolution is approximately equal, but the measured axial resolution is approximately twice that obtained in the simulations. Two reasons for this difference may be a lower transducer bandwidth than assumed and/or the wire thickness is not small enough compared to the wavelength.

The SNR improvement in TMS imaging is plottet in Fig. 2.6. The dashed line is the SNR in water, and the solid line is the speckle SNR obtained from the tissue mimicking phantom in Fig. 2.4. The SNR is higher in TMS imaging for all depth, and it increases approximately linearly from 4 dB and 15 dB after the linear array focus due to the application of dynamic transmit focusing.

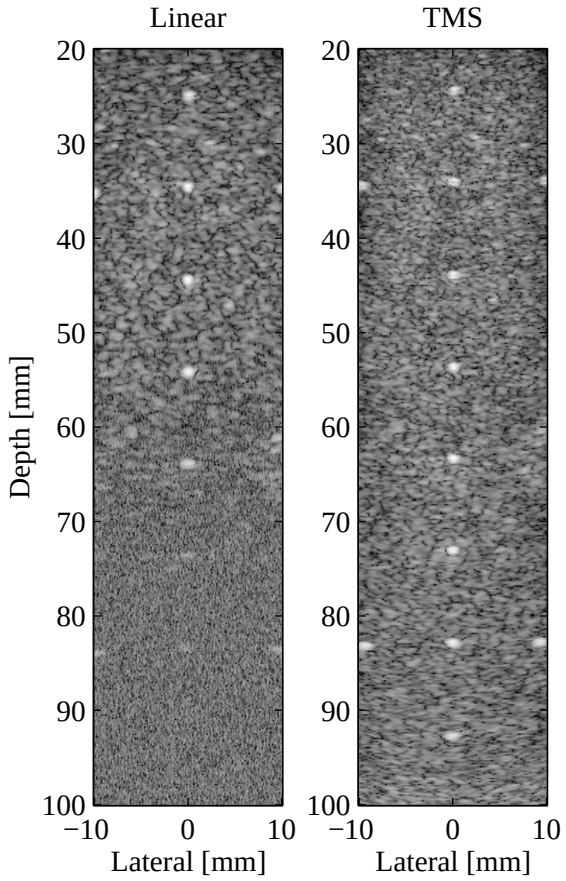

Figure 2.4: Measured linear array image (left) and TMS image (right) on a multi-target phantom with 0.5 dB/[cm MHz] attenuation. The scanned section contains twisted nylon wires spaced axially by 1 cm throughout the imaged region. The dynamic range in the images is 50 dB. This is Fig. 11 in [30].

2.3 Influence of Virtual Source Location

In Chapter 3, results of applying TMS imaging using convex transducer arrays are presented. During this study, it was observed, that the images obtained in both simulations and measurements had a smeared, unfocused appearance. This effect became worse as the subaperture size increased, and to find a solution, wavefront simulations conducted in [29] were reevaluated. It was discovered, that the spherical wave produced by the subaperture had its origin at the location of the virtual point source, and not at the zero phase center of the subaperture as originally assumed. Thus, when performing the image reconstruction described in Chapter 1 and in the paper, this means that the vector $\vec{r}_m$ must point to the virtual source location and not to the center of the subaperture. Furthermore, the time zero reference point needs to be adjusted to the virtual source location for each emission. This is obtained by adding the temporal distance between the virtual point source and the subaperture center to the start time of the recorded echo data. With reference to Fig. 2.1, the new start time of the RF data is

$$T_{s,new} = T_s + \frac{|\vec{r}|}{c}, \tag{2.3}$$

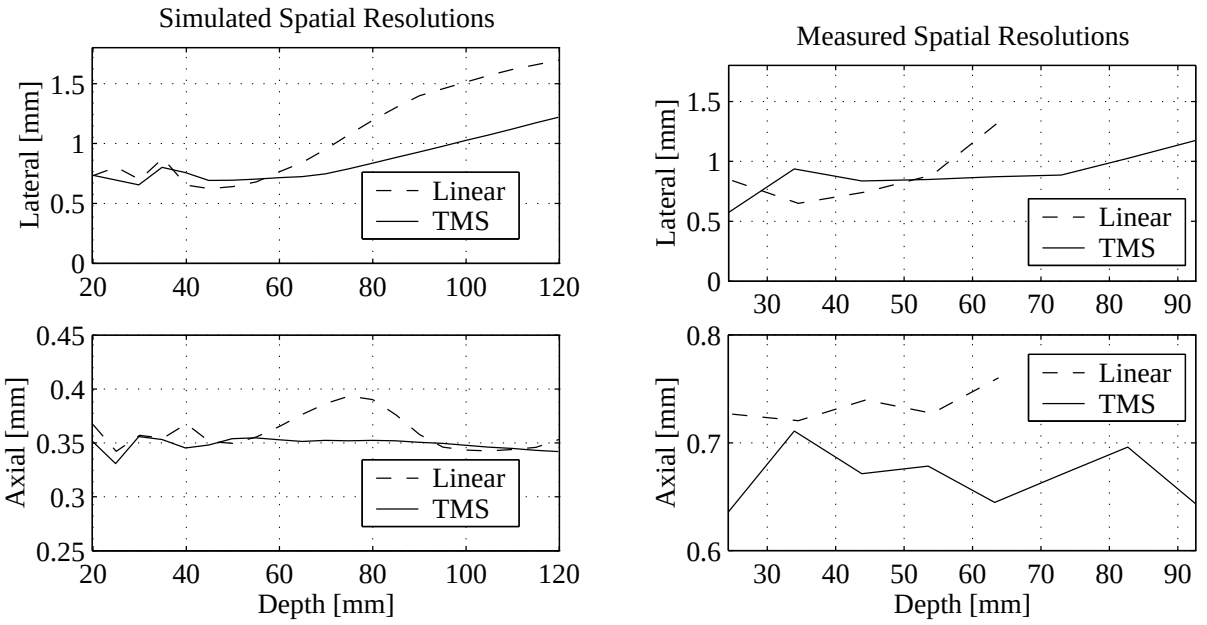

Figure 2.5: Simulated and measured -6 dB lateral (top) and axial (bottom) resolution for linear array imaging (dashed) and TMS imaging (solid), respectively. These are Figs. 7 and 12 in [30].

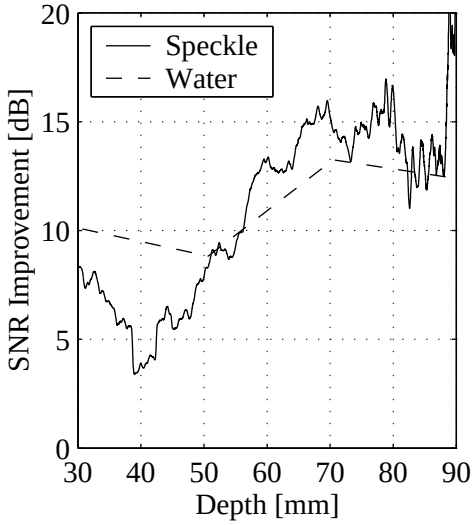

Figure 2.6: Calculated SNR improvement obtained by TMS imaging in water (dashed) and in the tissue mimicking phantom (solid). This is Fig. 13 in [30].

where T_s is the original start time in seconds, and $T_{s,new}$ is the adjusted start time. In general, each emission can have different virtual source locations, and the start time must therefore be adjusted for each emission individually.

Since the spherical wave has its origin at the virtual source location, an error in the arrival time calculation used in Eqn. 1.1 is introduced. This error is significant close to the transducer due to the large curvature of the wavefront, but it reduces with depth as the curvature becomes increasingly flat and the difference between the assumed and true wavefronts decreases.

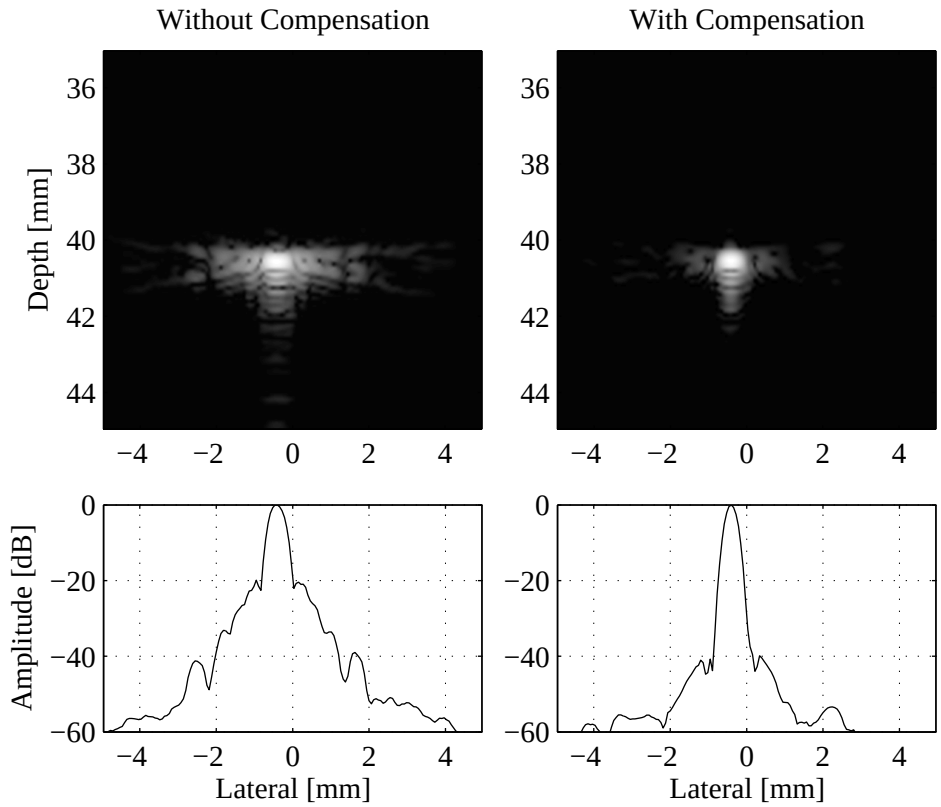

Figure 2.7: Results of a point spread function (PSF) measurements showing the effect of taking into account the location of the virtual point source. The left image shows the PSF with no compensation, and the image to the right shows the PSF with compensation. The dynamic range in both images is 60 dB. Clearly, the compensation has a pronounced effect on the sidelobe levels, which are significantly reduced after compensation.

The result of a point spread function (PSF) measurement with and without compensation for the virtual source location is shown in Fig. 2.7. The PSF without compensation is shown to the left, and the PSF with compensation is shown to the right. The dynamic range in the images is 60 dB. As seen, the sidelobe levels have been reduced significantly, which improves the contrast resolution, but there is no significant difference in spatial resolution between the two PSFs. At ranges closer to the transducer, improvements in lateral resolution are expected though. These results explain why, the influence of the virtual source was not observed earlier. Although the sidelobes are higher in the uncompensated case, the PSF still has an harmonious appearance. In convex array imaging, the effects are, however, much more pronounced due to the more complex geometry, which will be shown in Chapter 3.

The effects are further illustrated in Fig. 2.8, which shows B-mode images of the Carotid artery without (left) and with (right) virtual source compensation. The dynamic range in the image is 40 dB. A significant improvement in contrast resolution is observed, and the boarders of the structures are better defined, indicating improved spatial resolution.

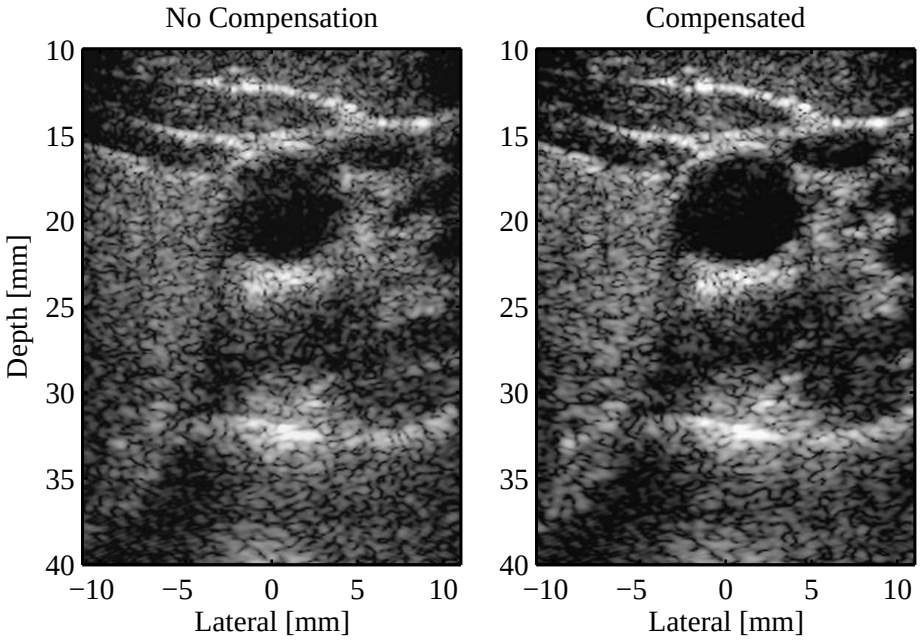

Figure 2.8: B-mode images of the Carotid artery using TMS imaging without (left) and with (right) virtual source compensation. The dynamic range is 40 dB. A significant improvement in image contrast is seen, and the better defined structures indicate an enhanced spatial resolution.

2.4 Updated Results

The influence of the virtual source location was discovered after the publication of the journal article (and the conference paper) summarized in this chapter. Therefore, this section presents updated results from the paper using the virtual source location in the image reconstruction. Only a selection of the measurement results are included, since these are the most interesting to observe, but also to limit the extend. All figures contain results of TMS imaging only, unless noted otherwise.

Figures 2.7 and 2.8 showed, that compensation for the virtual source location produced a significant reduction in sidelobe levels. This effect is also observed in Fig. 2.9, which shows the results for the wire phantom containing water. The B-mode image and axial projection shown in the left part of the figure is the original result without virtual source compensation, while the right part shows the results after compensation. The dynamic range in the B-mode images is 60 dB. The axial projections show no appreciable change in temporal sidelobe levels, but the lateral resolution and sidelobes have been improved, especially in the near field as expected. The improvement in sidelobe levels is further elaborated in Fig. 2.10, which shows the lateral projections of the PSFs at 30 mm and 70 mm in Fig. 2.9.

The results from the tissue mimicking wire phantom are shown in Fig. 2.11 with the uncompensated B-mode image to the left and the corrected image to the right. The dynamic range is both images is 50 dB. The enhanced lateral resolution is clearly observed. The spatial resolution is evaluated further in Fig. 2.12, which shows the -6 dB lateral (top) and axial (bottom) resolutions calculated from the wires in the tissue mimicking phantom. This figure is an updated version of the right part in Fig. 2.5.

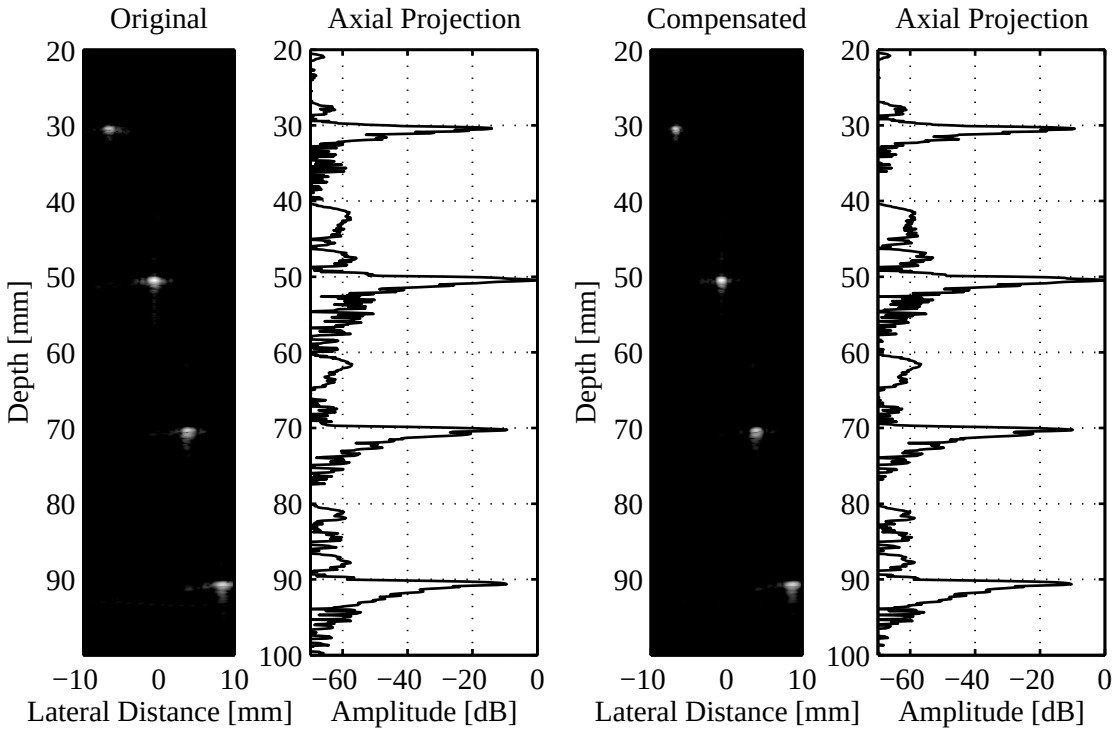

Figure 2.9: Updated results for the wire phantom containing water shown in Fig. 9 in [30]. The B-mode image and axial projection shown in the left part of the figure is the original result without virtual source compensation, while the right part shows the results after compensation. Improvements in near field resolution as well as lower sidelobe levels throughout the image are clearly observed. The dynamic range in the B-mode images is 60 dB.

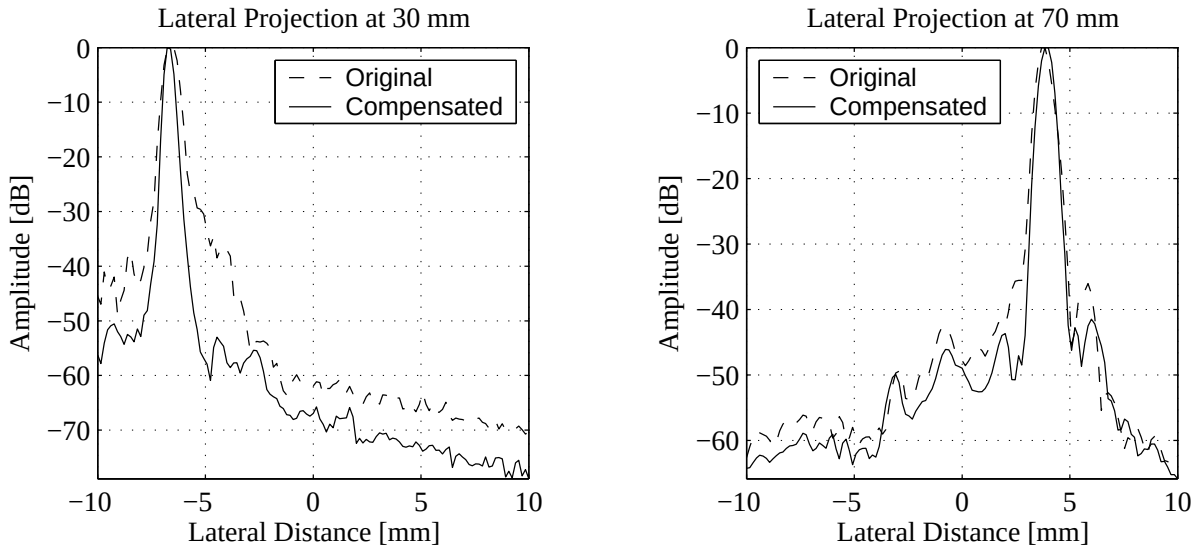

Figure 2.10: Lateral projections of the PSFs at 30 mm and 70 mm in Fig. 2.9 using TMS imaging. The dashed curve is the original result with no compensation, and the solid curve is the result with virtual source compensation. As expected, the improvement in sidelobe levels as well as lateral resolution is most significant at 30 mm.

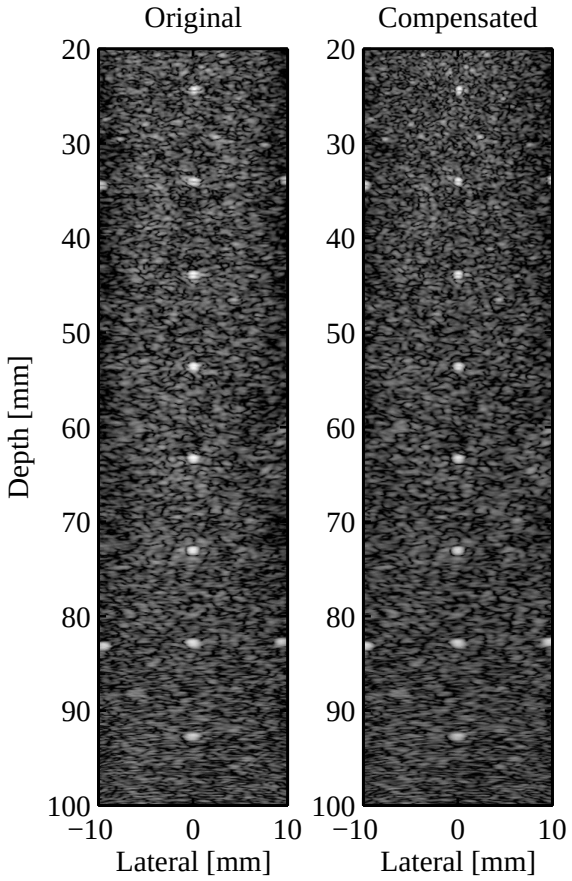

Figure 2.11: Updated results from the tissue mimicking wire phantom shown in Fig. 11 in [30]. The B-mode image shown to the left is the original image without compensation for the virtual point source location, while the image shown to the right is the result after compensation. The improvement in spatial resolution after compensation is easily observed in the upper part of the image. The dynamic range is 50 dB.

The effect of the virtual source compensation on the SNR is plotted in Fig. 2.13. The curves show the improvement in speckle (solid) and water (dashed) SNR after compensation relative to TMS imaging without compensation. Up to 6 dB higher SNR is obtained after correction, and it is noticed, that the improvement decreases with depth. This decrease is due to the gradually smaller phase error introduced in the beamformer by assuming the origin of the spherical wave is at the center of the subaperture.

In conclusion, the results obtained in this study have shown, that the TMS imaging approach produces a significant improvement in the image quality of STA imaging, which makes TMS imaging competitive with conventional linear array imaging. Furthermore, it was shown, that applying the virtual source location in the image reconstruction has a significant influence on the obtained image quality.

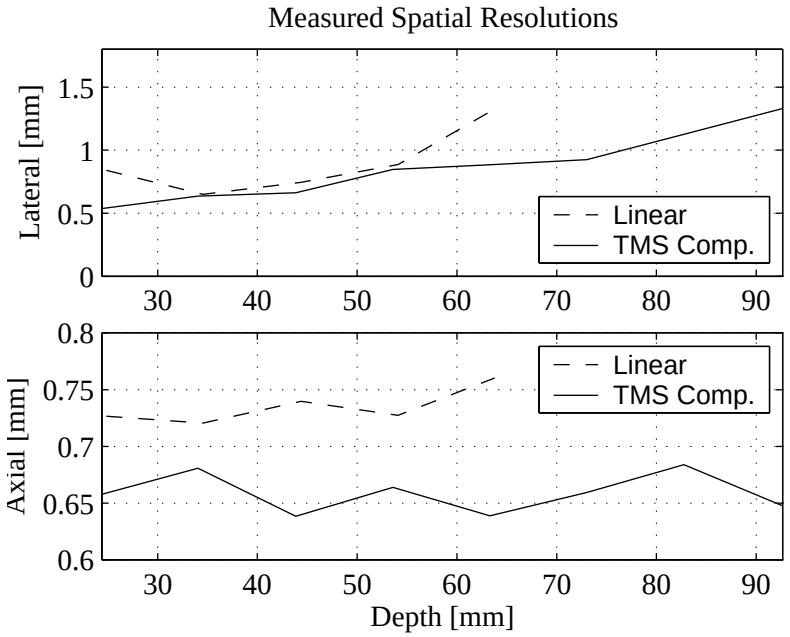

Figure 2.12: Updated version of Fig. 12 in [30] showing lateral (top) and axial (bottom) resolutions for linear array imaging (dashed) and compensated TMS imaging (solid) based on the tissue mimicking wire phantom. For TMS imaging, the results are calculated from the right image in Fig. 2.11, while the results for linear array imaging are takes directly from [30]. As expected, the performance of TMS imaging has been improved in the near field.

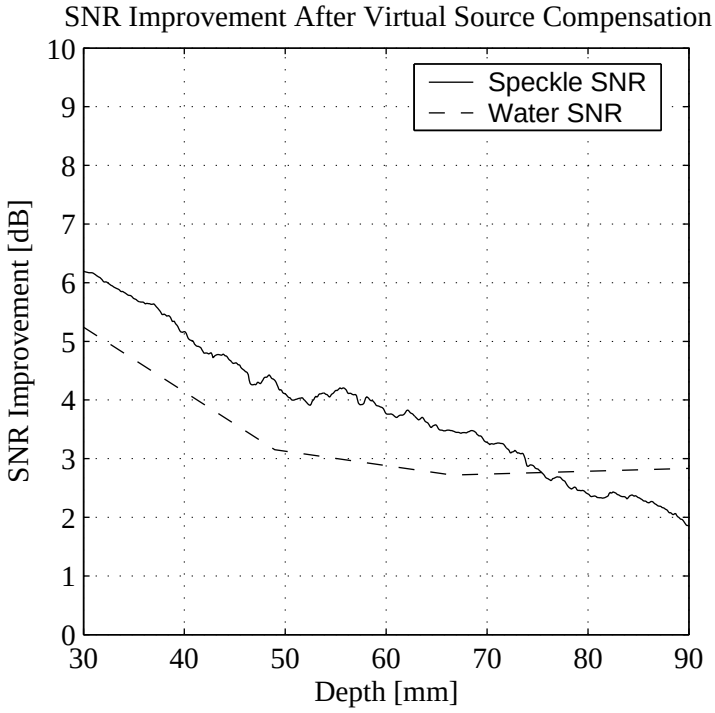

Figure 2.13: Curves showing the improvement in SNR of TMS imaging obtained after compensation relative to the uncompensated result. The dashed curve shows the improvement for the water phantom, and the solid curve is the result for the tissue mimicking phantom. Notice, that the improvement decreases with depth, which is in accordance with relative size of the error between the assumed and true wavefronts as explained earlier.

CHAPTER

THREE

Synthetic Transmit Aperture Imaging using Convex Transducer Arrays

This chapter contains a summary of the journal article

- **Kim L. Gammelmark** and Jørgen A. Jensen, "Synthetic Transmit Aperture Imaging using Convex Transducer Arrays," submitted to *IEEE Transactions on Ultrasonics, Ferroelectrics, and Frequency Control* in April 2004

and the conference article

- **Kim L. Gammelmark** and Jørgen A. Jensen, "Experimental Study of Convex Coded Synthetic Transmit Aperture Imaging," presented at the *IEEE International Ultrasonics Symposium* in Münich, Germany, October 2002, pp. 1573-1576,

which are found in full length in Appendix A.2 and B.2, respectively. The journal paper contains improved and elaborated results compared to the conference paper, and, thus, primary focus will be put on the content of the journal paper (hereinafter referred to as the paper).

3.1 Objective of Study

In Chapter 2, results of performing TMS imaging with linear array transducer geometries were presented. Linear arrays typically have high center frequencies, which makes them highly suitable for short depth applications, such as breast imaging and scanning of the carotid artery, due to the limited penetration depth and, especially, the field of view. Although the penetration depth was increased using TMS imaging, linear arrays are not particularly suitable for abdominal imaging, since beam steering with these arrays will produce unwanted grating lobes in the image. For this reason, the application of TMS imaging with convex array transducers was investigated, and the results of this study are summarized below.

3.2 Summary of Papers

Convex array transducers are highly suitable for abdominal imaging due to their large field of view and often low frequency range, which enables large penetration depths. This is essential, if

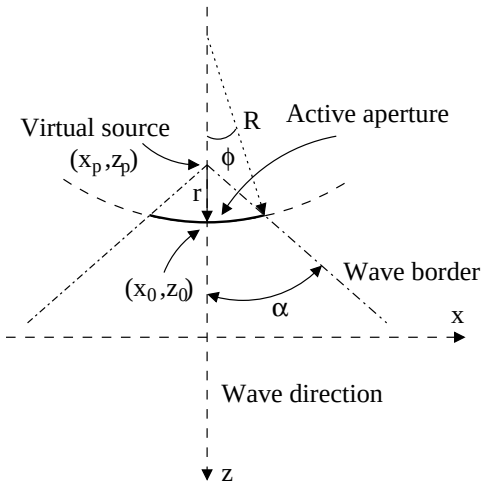

(a) Conventional application where the virtual point source is placed behind the center of the subaperture to produce a symmetric spherical wave.

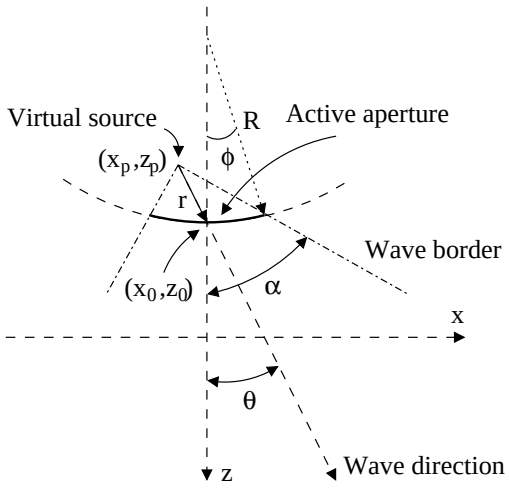

(b) Angled transmission where the virtual point source is placed such that the spherical wave propagates at an angle θ.

Figure 3.1: Illustration of two methods for applying multi-element STA imaging to convex arrays. This is Fig. 3 in [38].

useful abdominal imaging is to be obtained, because the anatomical structures, e.g. the kidneys, the liver, and portal vein branches, have large dimensions.

The paper contains a thorough introduction to TMS imaging, which is similar to that given in Chapter 2, but in the context of convex array transducers. Application of TMS imaging with convex arrays is not straight forward due to the more complex aperture geometry compared to linear arrays. New design considerations regarding both the transmission scheme and image reconstruction algorithm are therefore required.

The conventional implementation of multi-element defocused transmissions is illustrated in Fig. 3.1(a) for a convex aperture geometry. When transmitting from the outer parts of the convex array, the conventional implementation will cause a significant part of the wave to propagate away from the image region, which hereby is unutilized. Therefore, it is advantageous to change the propagation direction of the wavefront towards the region, where the image is reconstructed. Angled transmissions are obtained by moving the virtual point source to the side as illustrated in Fig. 3.1(b). The maximum propagation angle, that can be obtained, is influenced by the directivity of the subaperture elements, and any propagation angle can therefore not be selected. Further details about this topic are found in the paper.

In Section 2.3, the impact of the virtual source location was described. Here, it was explained, that the spherical wave produced by the subaperture at each emission originates from the virtual point source location and not at the zero phase center of the subaperture. The penalty of neglecting this, when reconstructing the B-mode images, is errors in the arrival time calculation, resulting in unfocused images with significantly higher sidelobe levels. As mentioned, this phenomena was discovered during the implementation of TMS imaging with convex array, due to the more complex geometry. An example of not taking into account the true origin of the emitted spherical wave is shown in Fig. 3.2, where the B-mode image without correction is displayed to the left and the B-mode image with correction is shown to the right. The image quality is highly affected by the phase errors introduced by assuming the origin to be at the center of each subaperture. The effect, being an unfocused, smeared appearance, is most pro-

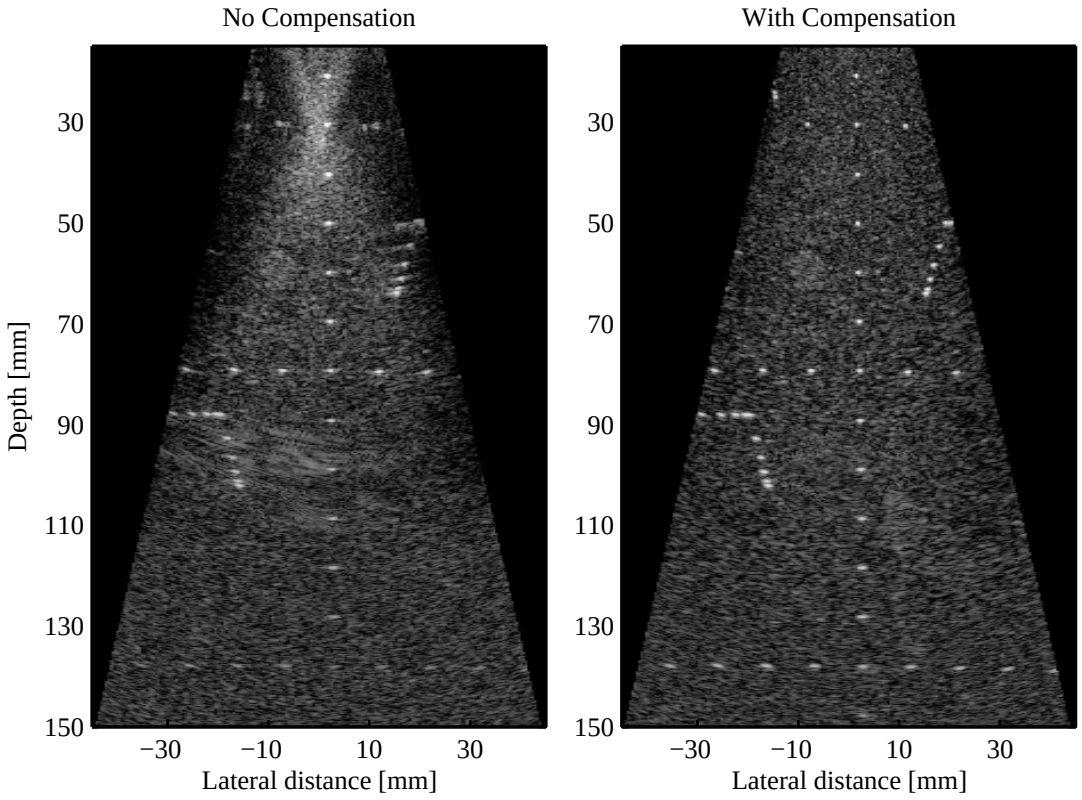

Figure 3.2: B-mode images showing the effect of compensation for the virtual source location. The dynamic range is 45 dB. This is a full view of Fig. 4 in [38].

nounced at low depths due to the larger impact of the phase errors at low ranges. Furthermore, it is noticed, that the image quality degrades with larger image angles, which is caused by the geometry. In the corrected image, the image quality has been fully reestablished, including an increase in penetration depth due to better focusing.

The performance of convex array TMS imaging is evaluated through measurements using the RASMUS research scanner [37](see appendix C.1), and the results are compared to conventional convex array imaging applied in current scanners. A selection of these results are presented below, and a detailed evaluation is found in the paper.

The convex array transducer applied for the measurements was a commercial 5.5 MHz transducer with 192 elements of which only the central 128 elements were accessible by the RASMUS system. TMS imaging was implemented using 33 subaperture elements and a 20 μs linear FM signal with amplitude weighting to reduce the temporal sidelobes. For each emissions, the transmitted wavefront was angled to propagate downwards parallel to the z-axis as explained above. The weighting scheme applied on the linear FM signal was the same as that applied for linear array TMS imaging. The number of emissions was 96, and 128 receive elements were applied. The B-mode images were processed using mismatched filtering to compress the linear FM signal, dynamic focusing, and dynamic apodization keeping the F-number=2. Conventional convex array imaging was performed using a 64 element transmit aperture and 128 receive element, and a 1.5 cycle sinusoid weighted with a Hanning window was applied as excitation signal. The transmit focal range was set to 70 mm, and the number of scanned lines was 142. The recorded echo data for each line were processed using matched filtering to

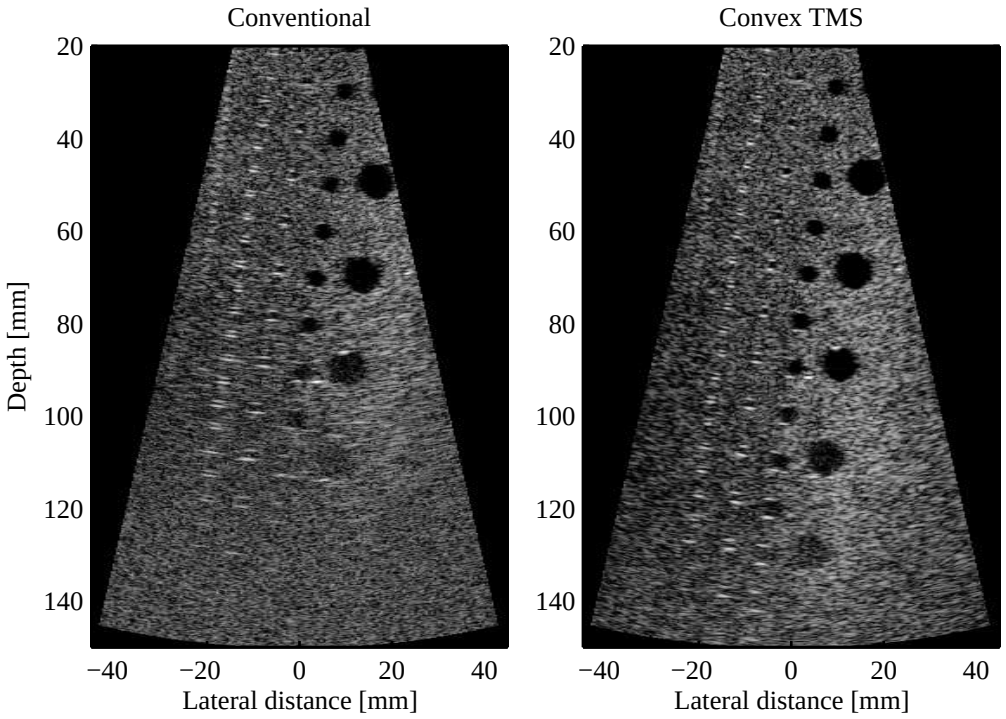

Figure 3.3: B-mode images of a tissue mimicking phantom containing anechoic cylinders placed in angled columns with diameters of $0.5, 1, 2, 4, 8$ mm from left to right. The dynamic range is 35 dB due to a relatively low scattering strength in the phantom. This is Fig. 7 in [38].

increase the SNR, dynamic receive focusing, and dynamic apodization with the F-number=2.

The contrast resolution was evaluated by scanning a tissue mimicking phantom containing anechoic cysts of various sizes. Figure 3.3 shows the results. The conventional B-mode image is shown left, and the TMS image is displayed to the right. The dynamic range is only 35 dB due to a relatively low scattering strength of the material used in the phantom, but this does not directly affect the validity of the results. The penetration depth has been increased by approximately 2 cm, and the contrast resolution has been improved, which is especially noticed at depths beyond 100 mm.

The SNR was evaluated by scanning a tissue mimicking phantom containing only random scattering. The result is plottet in Fig. 3.4 showing the improvement in SNR of TMS imaging relative to convex array imaging as a function of depth. The SNR performance is approximately equal until 60 mm, which is the location of the acoustic focal point of conventinal imaging. This is most likely due to the application of dynamic apodization in transmit and on receive for TMS imaging. After 60 mm, the performance of TMS imaging increases rapidly, and at a depth of 120 mm the SNR has been improved by 14 dB.

Phantom measurements are important when evaluating a new imaging approach, because phantoms provide a controllable environment in which common errors can be corrected, and the method can be optimized. The real challenge is, however, in-vivo application, because this environment cannot in general be controlled. Furthermore, in-vivo imaging is the targeted application area, and, thus, it is natural to perform in-vivo experiments. The results of an in-vivo scanning performed by an experienced medical doctor are shown in Fig. 3.5. The B-mode

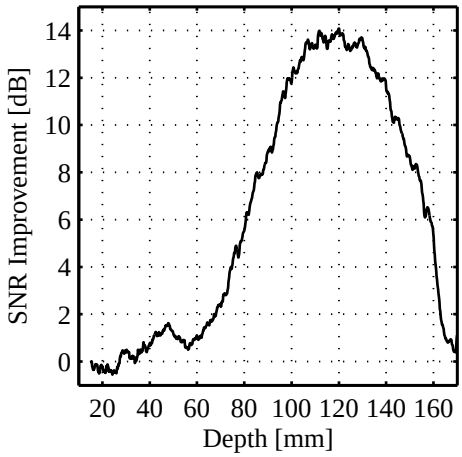

Figure 3.4: The calculated improvement in speckle SNR from a homogeneous phantom containing only randomly distributed scatterers. The SNR of TMS imaging relative to conventional convex array imaging improves rapidly after 60 mm and peaks at 120 mm with a 14 dB increase in SNR. The attenuation was 0.5 dB/[MHz,cm]. This is Fig. 9 in [38].

images show transverse sections of the right liver lobe containing hepatic vein branches, cross sections of portal vein branches, and the diaphragm in the lower part of the images. The dy-

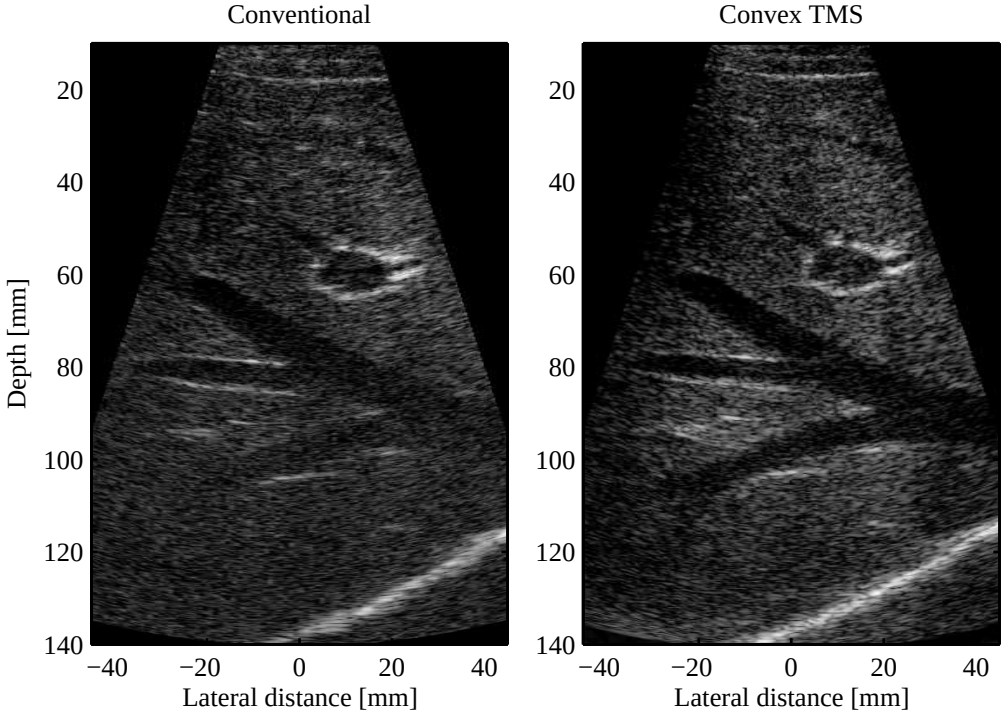

Figure 3.5: The images show transverse sections of the right liver lobe containing hepatic vein branches, cross sections of portal vein branches, and the diaphragm in the lower part of the images. This is Fig. 10 in [38].

namic range is 50 dB. The images are obtained from the exact same anatomical location using the real-time capability of the RASMUS scanner, thus, enabling direct comparison. The improvement in lateral resolution is clearly noticed throughout the image. The large hepatic vein branch in the center of the image is better defined in the TMS image, which indicates improvements in both contrast resolution and penetration depth. In general, the TMS image has a sharper appearance with better defined structures, which also indicates improved image quality.

In conclusion, this study has shown, that TMS imaging can be successfully implemented with convex array transducers, and the obtained image quality is highly competitive with traditional convex array imaging on all parameters.

CHAPTER

FOUR

In-Vivo Evaluation of Synthetic Transmit Aperture Imaging

This chapter contains a summary of the journal article

- Morten H. Pedersen, **Kim L. Gammelmark**, and Jørgen A. Jensen, ”In-Vivo Evaluation of Convex Array Synthetic Aperture Imaging,” submitted to *Ultrasound in Medicine and Biology* in July 2004

and the conference article

- Morten H. Pedersen, **Kim L. Gammelmark**, and Jørgen A. Jensen, ”Preliminary In-Vivo Evaluation of Convex Array Synthetic Aperture Imaging,” presented at *SPIE - Progress in biomedical optics and imaging* in San Diego, California, February 2004, pp. 33-43,

which are found in full length in Appendix A.3 and B.4, respectively. These papers comprise the same material, and thus focus will be put on the content of both papers.

4.1 Objective of Study

STA imaging has been investigated extensively using simulation studies and phantom experiments, but an evaluation of its clinical potential has previously not been conducted. The purpose of this study is therefore to evaluate the viability of convex array TMS imaging for real-time in-vivo imaging. Traditional convex array imaging is used for comparison, and the evaluation is performed by medical doctors specialized in ultrasound imaging.

4.2 Summary of Papers

This study investigates the in-vivo performance of TMS imaging by conducting a clinical trial on healthy volunteers and letting experienced medical doctors evaluate the results. The paper compares convex array TMS imaging with conventional convex array imaging. Seven healthy male volunteers were scanned at two abdominal locations each, yielding 14 independent acquisitions. For each acquisition, a real-time movie sequence with a duration of approximately 3 seconds was recorded using the RASMUS system [37](see appendix C.1). The two imaging

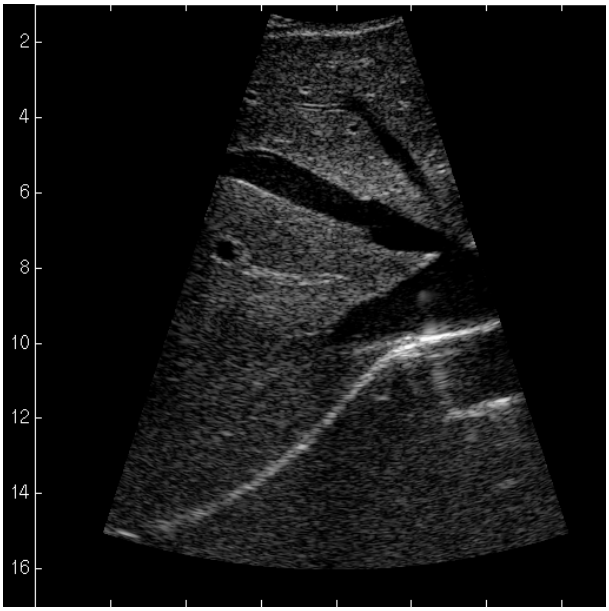

Figure 4.1: Snapshot of a TMS movie sequence used for penetration depth estimation. The image shows a transverse section of the right liver lobe containing hepatic vein branches, cross sections of portal vein branches, and the diaphragm in the lower part of the image. This is Fig. 4(a) in [39].

techniques, conventional and TMS imaging, were interleaved frame-by-frame during the acquisition, such that images of the exact same anatomical location were obtained simultaneously to enable direct comparison. The acquisition setup and processing strategies applied were identical to those used in previous investigations of convex array TMS imaging presented in Chapter 3 and [38]. These are therefore not repeated here.

The in-vivo movies were evaluated by medical doctors with significant experience in ultrasound imaging, but with no prior knowledge of TMS imaging or STA imaging in general. Two hypotheses were tested:

1. TMS imaging has no effect on penetration depth.
2. TMS imaging has no effect on image quality (spatial resolution and image contrast).

To evaluate the penetration depth, the movies were presented one-by-one with no indication of imaging method (blinded), and the doctor was asked to indicate the penetration depth, at which the image quality was degraded significantly. A snapshot of such a movie is shown in Fig. 4.1 for TMS imaging. The differences between the selected depths for paired movie sequences (conventional and TMS imaging of the same view) were calculated for each examiner, and the resulting values were analyzed statistically using paired t-test (Student's one sample t-test). It was found, that TMS imaging provided a small but statistically significant increase in penetration depth of approximately 0.5 cm.

The image quality was evaluated by presenting each examiner with paired movie sequences (conventional and TMS imaging of the same view) displayed side-by-side in random order, but with no indication of imaging methods. The same movie sequence was presented twice, but with opposite left-right placement to remove any preferences of the examiners. For each movie, the examiner was asked to compare the image quality of the two sequences in terms of

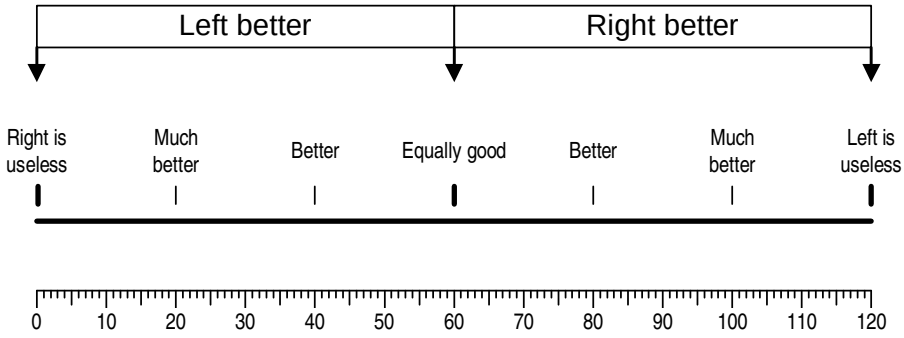

Figure 4.2: Explanation of VAS shown to medical doctors before scoring images. The lower scale was used to read scored values. This is Fig. 5(b) in [39].

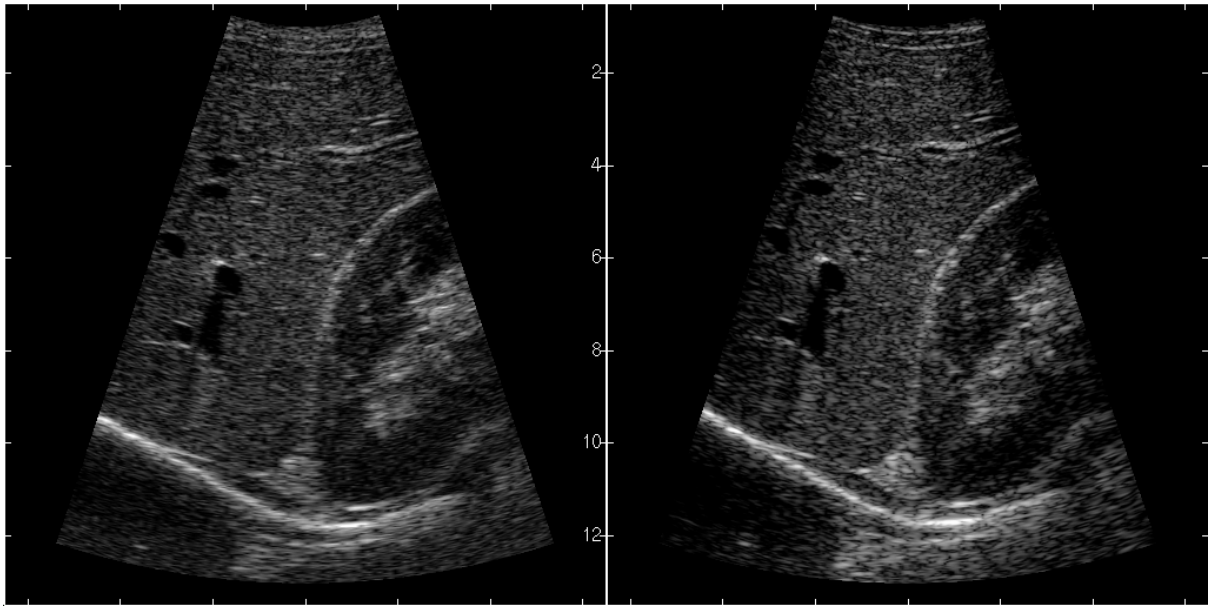

Figure 4.3: Longitudinal section of right liver lobe showing cross sections of hepatic vein branches, longitudinal section of a portal a vein branch (upper left part), the kidney, and diaphragm at the bottom. This is Fig. 8(a) in [39].

spatial resolution and image contrast, and rate his or her preference on a visual analog scale shown in Fig. 4.2. The scores were analyzed using Wilcoxon signed rank test, and the result showed a statistically highly significant preference for TMS imaging, which indicates a significantly better image quality in TMS imaging compared to conventional convex array imaging. A snapshot from a paired movie sequence, as it was presented to the examiners is shown in Fig. 4.3. Conventional imaging is shown to the left in this case and TMS imaging to the right. The improvement in lateral resolution is clearly noticed, and the TMS image generally has a sharper appearance with better defined structures. This is especially observed at the kidney boarder and its interior.

During playback of the movies it was observed, that tissue motion appeared differently in TMS imaging. The individual structures seemed to be moving more independently from the surrounding tissue, thus, representing more closely natural anatomical motion. Some flashing artifacts were observed, when significant tissue motion was present, but these were subtle and reported not to have a visual influence on the image quality.

In conclusion, this study has first of all shown, that tissue motion is not a major problem in STA imaging. It produces some weak fluctuations in the image intensity, but these do not depreciate the image quality. Secondly, the study showed, that TMS imaging is feasible for real-time in-vivo imaging applications with image quality better than conventional imaging.

CHAPTER

FIVE

Tissue Motion Compensation of Synthetic Aperture Images

This chapter contains a summary of the journal article

- **Kim L. Gammelmark** and Jørgen A. Jensen, "2D Tissue Motion Compensation of Synthetic Transmit Aperture Images," submitted to *IEEE Transactions on Medical Imaging* in August 2004

and the conference article

- **Kim L. Gammelmark** and Jørgen A. Jensen, "Duplex Synthetic Aperture Imaging with Tissue Motion Compensation," presented at the *IEEE International Ultrasonics Symposium* in Honolulu, Hawaii, October 2003, pp. 552-563,

which are found in full length in Appendix A.4 and B.3, respectively. Both papers investigate the same method for 2D tissue motion compensation, but for linear array TMS imaging in the conference paper and for convex array TMS imaging in the journal paper. Results from both papers will be presented, but primary focus will be put on the journal paper, because it contains a more elaborated evaluation. Unless otherwise noted, the figures displayed in this chapter are therefore taken from the journal paper.

5.1 Objective of Study

STA imaging is by nature more sensitive to motion during data acquisition, because the displayed image is created by summing low resolution images obtained from several consecutive transmit events. If the scatterers or transducer have moved during the acquisition interval, the low resolution images will not be phased aligned, resulting in incoherently summation. This produces unfocused images with a smeared appearance and thus loss in image quality, if the motion is severe.

The in-vivo evaluation of convex array TMS imaging presented in Chapter 4 showed no particular susceptibility to tissue motion. Subtle image brightness fluctuations (flashing) were reported, but these artifacts did not depreciate the image quality considerably. The abdominal measurements performed in this study only included natural tissue motion produced by the patient due to the beating heart. Transducer motion produced by the sonographer under normal clinical conditions was excluded, and severe tissue motion was therefore not present in these

measurements. The study presented in this chapter investigates the influence of tissue motion on TMS imaging in more detail by evaluating a new method for 2D motion compensation. The results of this study are summarized below.

5.2 Summary of Papers

In traditional imaging, tissue motion produces distortions in the anatomical structures rather than direct loss in image quality. This makes these techniques less susceptible to motion compared to STA imaging. Previously investigated methods for tissue motion estimation in STA imaging have focused on compensation for axial tissue motion due to the significantly higher spatial frequency in this dimension [24, 25, 26, 27, 28, 40]. Compensating for the axial motion component is however not sufficient, if 2D motion is present, because the lateral resolution and image contrast will be degraded in the resulting image. Since tissue motion is inherently three dimensional, axial motion will only in rare cases be present alone in-vivo. Successful compensation for scan plane motion therefore requires at least 2D motion correction to retain the advantages of TMS imaging or STA imaging in general.

The motion compensation method investigated in this study is a 2D model based on a synthetic aperture flow method presented previously by Jensen and Nikolov in [41, 42]. The tissue velocity and motion direction is estimated at selected locations within the image area, and then applies these estimates to track the position of the scatterers, when reconstructing the individual low resolution images. The method is therefore composed by two parts; an algorithm for estimating the tissue motion, and the compensation scheme used in the image reconstruction.

The estimation method utilizes the high correlation that exists between high resolution images acquired using the same emission sequence and receive aperture setup [41]. The motion is found at a given image point by estimating the tissue velocity for a set of motion directions (angles), and then selecting the direction and velocity corresponding to the angle, where the normalized correlation is highest. For the sake of simplicity, the method is illustrated in Fig. 5.1 using high resolution images with two emissions. For a given estimation point, the recorded echo signals from each emission are processed to obtain a set of directional lines along selected angles. The lines corresponding to the same angle are summed for consecutive emissions, here $[m, m+1]$, $[m+1, m+2]$, $[m+2, m+3]$,..., to form high resolution directional lines $g_m(n,l)$, $g_{m+1}(n,l)$, $g_{m+2}(n,l)$,..., where n is the sample number, and l is the line number. The directional lines $g_m(n,l)$ and $g_{m+2}(n,l)$ are obtained using the exact same emission sequence. As explained by Jensen and Nikolov in [41], the distortion will therefore be the same in these signals, if the tissue velocity was constant during the acquisition. By correlating the corresponding signals in $g_m(n,l)$ and $g_{m+2}(n,l)$, the tissue velocity is found for all angles, and the direction of the motion and its velocity is then selected for the angle, at which the normalized correlation is highest. The same is true for $g_{m+1}(n,l)$ and $g_{m+3}(n,l)$, and for $g_{m+2}(n,l)$ and $g_{m+4}(n,l)$, etc. Thus, the estimation procedure is repeated continuously. Under the assumption that the tissue velocity and direction is constant during the acquisition, the correlation functions are averaged prior to the velocity estimation to improve the velocity estimates [43].

Instead of using two emissions per high resolution image, M emissions, denoted E-mode emissions, are generally applied, and the sequence is repeated N_{seq} times. This produces $MN_{seq} - (2M-1)$ correlations, which are averaged to improve the velocity estimate. Motion estimation is only required at discrete tissue locations, due to the elasticity property of soft tissue, which tend to make the tissue move with the same velocity in approximately the same

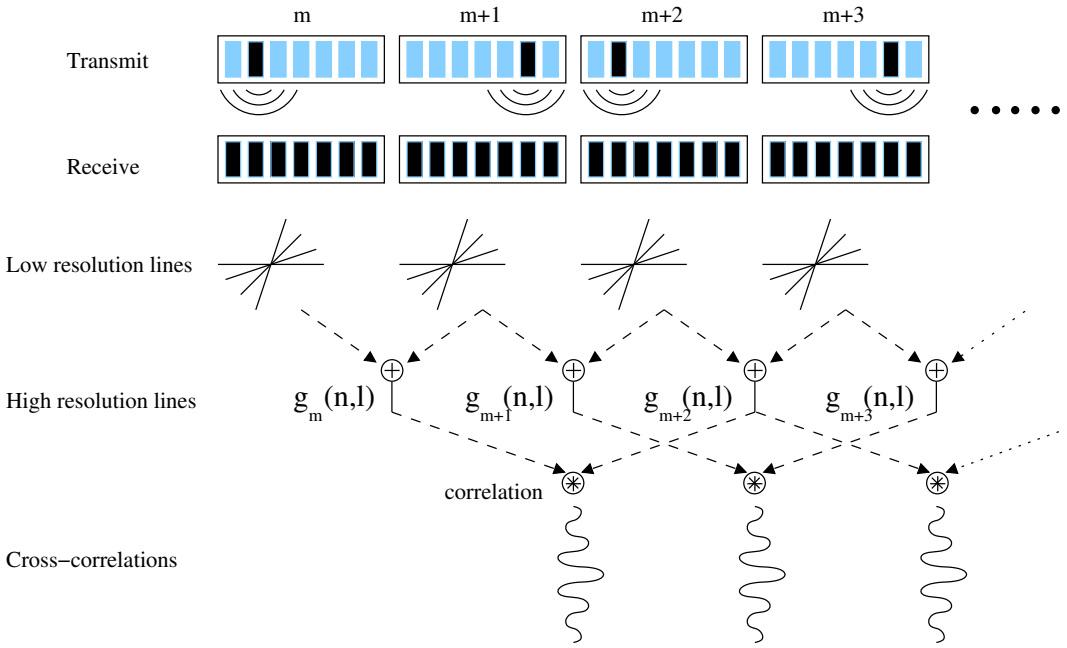

Figure 5.1: Illustration of the tissue velocity estimation approach using two repeating emissions. For each emission and each estimation point a set of low resolution lines are beamformed for selected angles. These lines are summed angle by angle for consecutive emissions, $[m, m+1]$, $[m+1, m+2]$, $[m+2, m+3]$,..., to form high resolution lines $g_m(n,l)$, $g_{m+1}(n,l)$, $g_{m+2}(n,l)$,.... The lines from identical emissions sets are then correlated to find the direction of the motion and the velocity.

direction within a certain region. The density of the estimation points will therefore depend on the anatomical location being scanned. To remove false estimates and to smooth the estimates according to this elasticity property, the estimates were filtered using a 2D vector based median filter, which adjusts the estimated velocity and direction at each point by calculating the median velocity and angle using the neighboring estimates.

Motion compensation is obtained by interleaving the estimation sequence with the normal B-mode emissions in TMS imaging in a 1-to-1 ratio, enabling continuous B-mode imaging and motion estimation. The velocity and direction estimates are used to compensate the low resolution B-mode images by recalculating the location of the image points to be reconstructed as illustrated in Fig. 5.2. Besides this pixel tracking, reconstruction of the B-mode images is performed using the usual strategies described in the previous chapters.

The performance of the method was evaluated by simulations using Field II [35, 36] and measurements with the RASMUS system [37](see appendix C.1). In the journal paper, convex array TMS imaging is investigated, and the conference paper investigates linear array TMS imaging. The acquisition setup and general processing strategies applied in both cases were the same as those described previously in Chapters 3 and 2, respectively.

In a simulation of convex array TMS imaging, tissue motion with a velocity of 15 cm/s and a 45 degree angle was applied to a tissue mimicking target with anechoic cysts. The estimation sequence was implemented with 8 E-mode emissions repeated 12 times, resulting in 96 emissions in total. These emissions were interleaved with the 96 B-mode emissions as explained above. The motion was estimated at 2 mm range intervals along image lines separated by 1

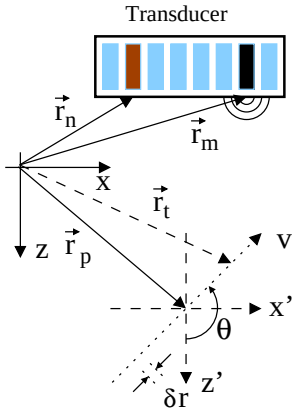

Figure 5.2: Illustration of the tracking principle used to compensate the low resolution B-mode images. The vectors $\vec{r}_m$, $\vec{r}_n$, and $\vec{r}_t(m)$ denote the locations of transmit element m, receive element n, and the tracked pixel for emission m, respectively.

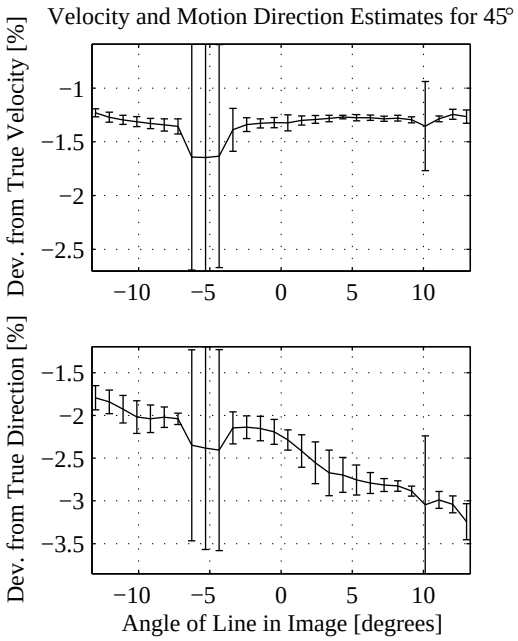

Figure 5.3: Results of the velocity and direction estimation in the simulation. The top figure shows the relative bias $\pm$ 1 SD of the velocity estimates in percent deviation from the true velocity, and the bottom figure shows the relative bias $\pm$ 1 SD of the motion direction estimates ($\hat{\theta}_{l_{int}}$) in percent deviation from the true motion angle. The figures are obtained by calculating the bias and SD for each image line, and the x-axis is therefore image angle.

degree in angle. For each of these lines, the relative bias and standard deviation (SD) was calculated, and the results are plotted in Fig. 5.3. The bias $\pm$ 1 SD of the velocity estimates in percent deviation from the true velocity is shown in the top figure, while the bias $\pm$ 1 SD of the direction estimates is shown in the bottom figure. The velocity is estimated with a relative bias of approximately -1.3%, and the SD is in average less than 0.2%. The motion direction is estimated with an average SD of 0.3%, and the bias is decreasing linearly from -1.7% at -13° to -3.2% at 13°. These results show, that the method is capable of accurately estimating the

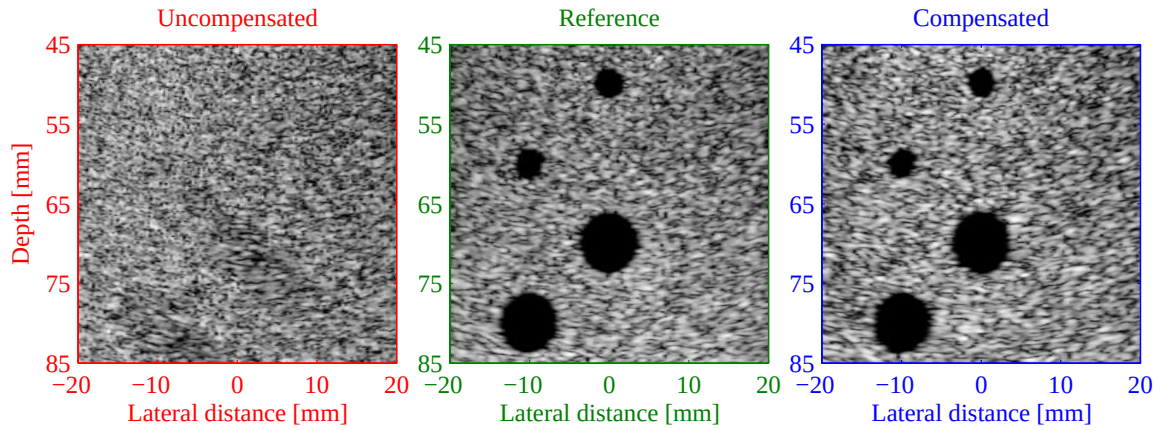

Figure 5.4: B-mode images of the simulated cyst phantom. Left: Uncompensated, Middle: Reference (stationary phantom). Right: Compensated. The dynamic range is 60 dB.

velocity and direction of the tissue motion. Sections of the reconstructed B-mode images are shown in Fig. 5.4. The motion has severely affected the image quality in the uncompensated image, where the cysts are no longer visual. After motion compensation, the image quality has been successfully regained, and, compared to the reference image, the correction is seen to be close to perfect.

Figure 5.5 shows the result of a measurement for linear array TMS imaging. The measurement was performed on a tissue mimicking phantom containing anechoic cysts, and artificial motion was imposed using a three-dimensional high precision positioning system by moving the transducer a fixed distance between each emission. For this measurement a tissue velocity of 10.6 cm/s at an angle of 68° was selected, partly due to the resolution of the positioning system. The estimation sequence was implemented using 8 E-mode emissions repeated 12 times, and the motion was estimated for every 2 mm both axially and laterally. Neglecting the false estimates from inside the cysts, the relative bias and SD of the velocity estimates was -3.24% and 5.63% averaged over all estimates, while the motion direction was estimated with relative bias of -0.14% and a SD of 1.81%. The B-mode images show, that the image quality has been successfully restored after motion compensation. The difference in contrast resolution between the reference and corrected images is 0.61% for the 4 mm cyst at 40 mm.

A similar measurement was performed for convex array TMS imaging with a tissue velocity of 5 cm/s at a 68° angle. Here, the estimation sequence was implemented using 16 E-mode emissions repeated 6 times due to the lower velocity, and the motion was estimated at 2 mm range intervals along image lines separated by 1 degree in angle as in the simulation above. The resulting B-mode images displayed in Fig. 5.6 show again, that the motion compensation achieves successful restoration of the image quality with a 3.5 % average improvement in contrast resolution for the 4 mm cysts (middle column) relative to the reference image. It is likely, however, that this difference is caused by slight variations in the speckle brightness between the two images, since the reference image is the golden standard.

To evaluate the in-vivo feasibility of the approach, a healthy volunteer was scanned abdominally using the convex array implementation. A sequence of 33 images were acquired in real-time, corresponding to approximately 2.5 seconds of data, and transducer motion was introduced by the medical doctor during the acquisition. This was done to simulate a real clinical scanning situation. The highest tissue velocity was expected to be around 5 cm/s, and, thus, the estimation

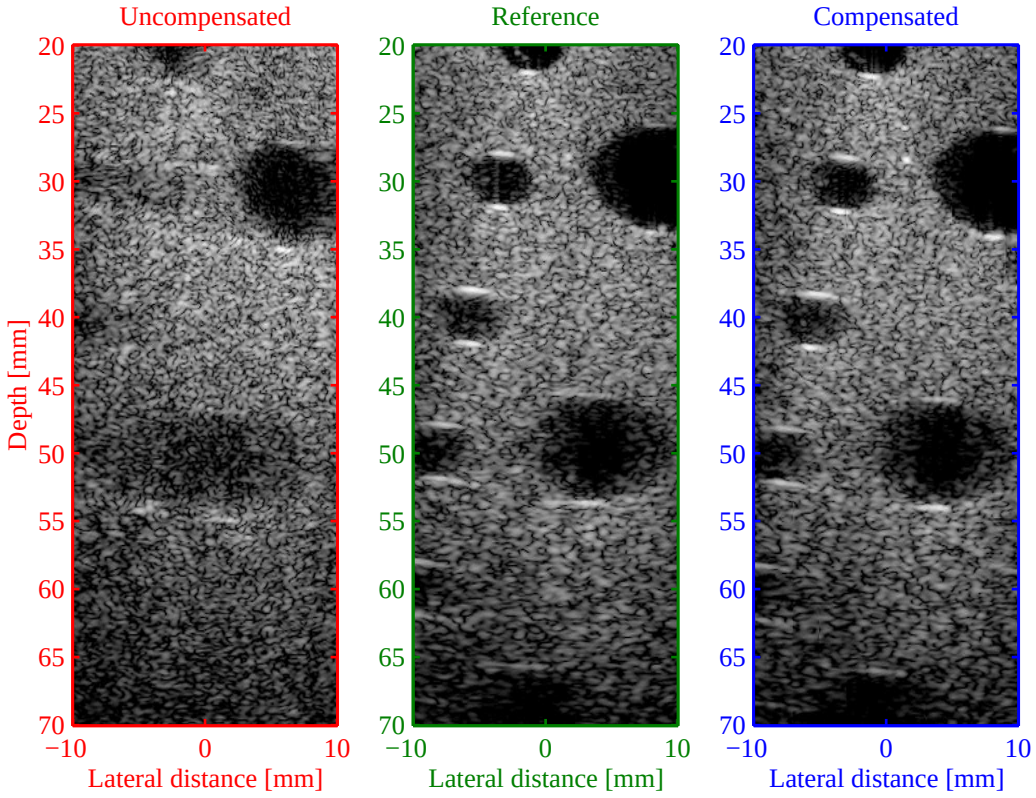

Figure 5.5: B-mode images of a tissue mimicking cyst phantom with imposed tissue motion of 10.6 cm/s at a 68° angle. This result is obtained using linear array TMS imaging. Left: Uncompensated, Middle: Reference (stationary phantom). Right: Compensated. The dynamic range is 50 dB. This is Fig. 4 in the conference paper [44].

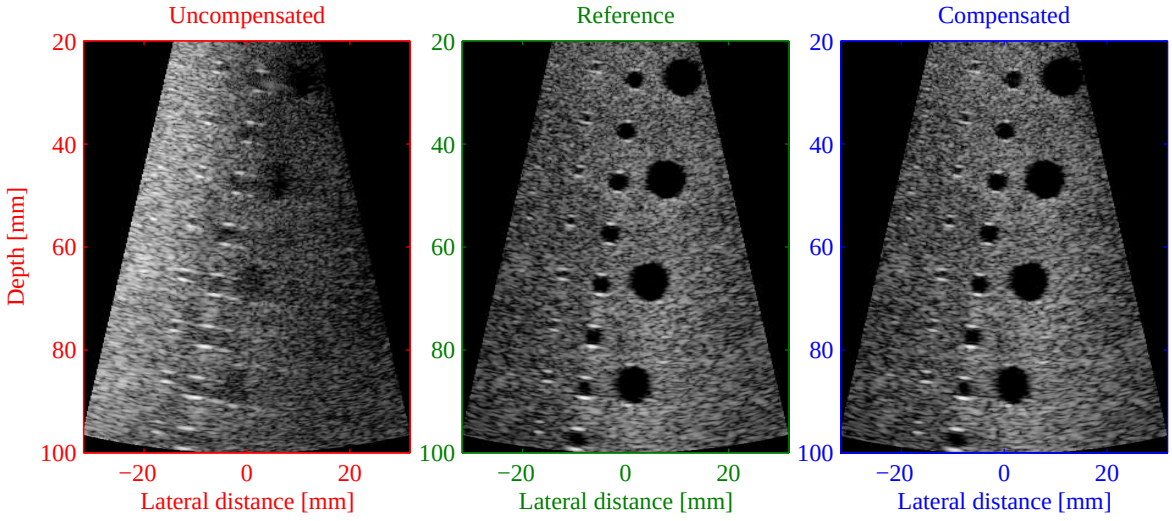

Figure 5.6: B-mode images of the scanned tissue mimicking cyst phantom with imposed tissue motion of 5 cm/s at a 68° angle. Left: Uncompensated, Middle: Reference (stationary phantom). Right: Compensated. The dynamic range is 45 dB.

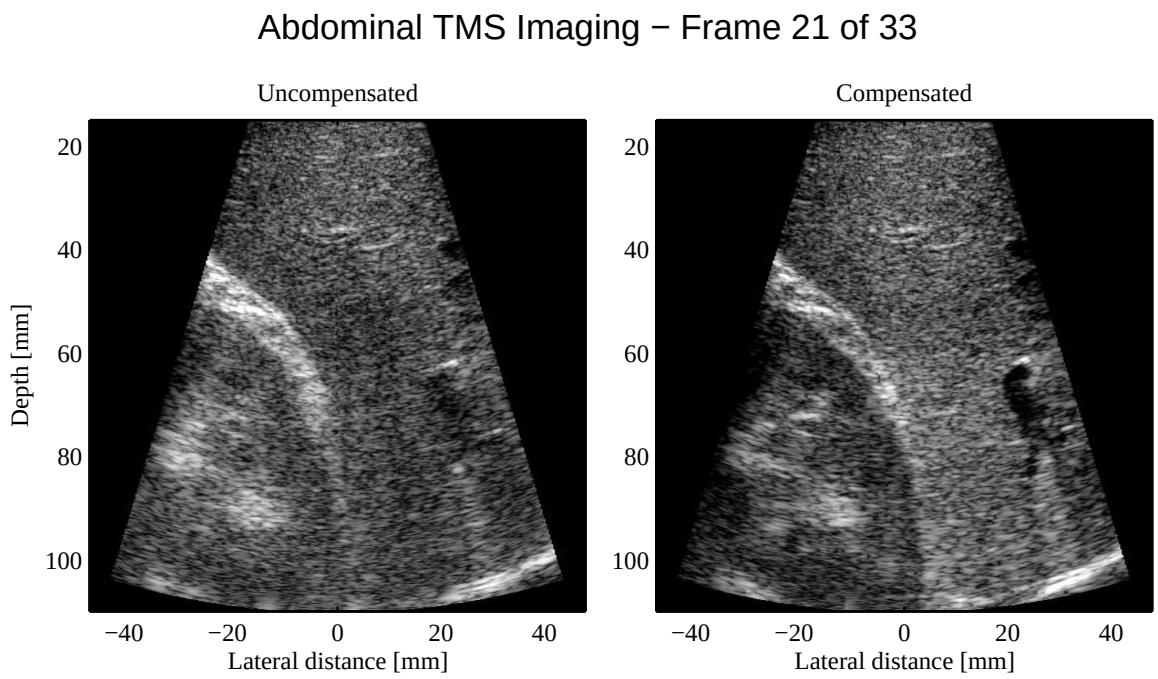

Figure 5.7: Abdominal B-mode images before (left) and after (right) motion compensation at an acquisition point with low tissue motion. The images show a longitudinal section of the right liver lobe containing a cross section view of the hepatic vein (right part), longitudinal section of a portal vein branch (top central part), the kidney, and diaphragm at the lower right corner. The dynamic range is 50 dB.

sequence was implemented using 16 E-mode emissions repeated 6 times within each B-mode sequence containing 96 emissions (see Chapter 3 for details). The motion was estimated at 4 mm range intervals along image lines separated by 1.5 degree in angle. The uncompensated and compensated B-mode images corresponding to the instance with the largest tissue velocity are displayed in Fig. 5.7 with a dynamic range of 50 dB. The images show a longitudinal section of the right liver lobe containing a cross section view of the hepatic vein (right part), longitudinal section of a portal vein branch (top central part), the kidney, and diaphragm at the lower right corner. The largest tissue velocity was estimated to 6.6 cm/s, and severe loss in image quality is seen in the uncompensated image. The hepatic vein is barely visible, and the interior of the kidney has been smeared. In the compensated image, the image quality has been fully regained, which clearly demonstrated the capability of the motion compensation approach. Furthermore, it was observed during playback of the entire movie sequence, that the flashing artifacts reported in the in-vivo study of convex array TMS imaging had been removed in the compensated sequence, which demonstrated, that these artifacts were indeed caused by tissue motion.

In conclusion, this study has shown, that severe tissue motion does have a significant influence on TMS imaging, or STA imaging in general. Using the proposed method, the motion artifacts can however be successfully eliminated, resulting in full restoration of the image quality.

CHAPTER

SIX

Conclusions

The goal of this Ph.D. study has been to improve the image quality of STA imaging to a clinically desirable level, and to show that real-time STA imaging is feasible in-vivo. Based on the research results presented in this thesis, it can be concluded, that these goals have been successfully reached.

A new method to increase the SNR in STA imaging was investigated, which employs multi-element subapertures and linearly frequency modulated (FM) signals at each emission. The subaperture was applied as a replacement of the conventional single transmit element to emulate a high power spherical wave transmitted by a virtual point source positioned behind the subaperture, and the linear FM signal replaced the conventional short excitation signal to increase the temporal energy. This approach, named *Temporally encoded Multi-element Synthetic transmit aperture (TMS) imaging*, was evaluated in detail for linear array and convex array imaging applications using simulations, and phantom and in-vivo experiments.

The application of TMS imaging for linear array geometries was investigated in Chapter 2. A detailed description of the approach was given, and it was shown, that using a 33 element subaperture and a 20 μs linear FM signal an increase in SNR of up to 17 dB could be obtained compared to conventional linear array imaging. The image quality was hereby improved on all parameters, comprising spatial resolution, image contrast, and penetration depth, due to the advantage of dynamic transmit-receive focusing and dynamic transmit-receive apodization in TMS imaging. It was explained, that the spherical wave produced by the subaperture at each emission originates from the virtual source location. This observation was shown to produce further improvements in image quality of TMS imaging. Furthermore, initial in-vivo experiments were conducted, which indicated, that TMS imaging is feasible for in-vivo imaging.

Convex array TMS imaging was presented in Chapter 3. New design considerations regarding the implementation of TMS imaging were presented, which were necessary due to the more complex aperture geometry. As for the linear array implementation, the results showed a significant increase in SNR of up to 14 dB relative to conventional convex array imaging, and phantom and in-vivo measurements showed great improvements in image quality.

An in-vivo evaluation of convex array TMS imaging for real-time abdominal imaging applications was presented in Chapter 4. The evaluation was performed as a clinical trial on 7 healthy male volunteers, and movie sequences of 3 seconds duration were acquired in real-time and analyzed by experienced medical doctors using blinded clinical evaluation. The evaluation showed a statistically significant improvement in image quality of convex array TMS imaging compared to conventional convex array imaging. Minor motion artifacts observed as subtle image brightness fluctuations were reported in TMS imaging, but these did not depreciate the

diagnostic value of the images.

A method for two-dimensional motion compensation was investigated in Chapter 5. The method was designed to estimate the velocity and direction of the tissue motion by correlating image lines beamformed along a range of motion directions and then select the direction and velocity corresponding to the highest correlation. By applying these estimates, motion compensation was introduced by tracking the location of each image pixel during the reconstruction of the low resolution images. Results of phantom experiments and real-time in-vivo measurements showed, that severe tissue motion deteriorates the image quality of STA imaging as expected, but, most importantly, that the proposed method successfully compensated for the motion, hereby retaining the image quality of TMS imaging, when scanning moving tissue.

Thus, this thesis has demonstrated, that TMS imaging is feasible for real-time in-vivo imaging with an image quality that is highly competitive with the techniques applied in current medical ultrasound scanners.

6.1 Future Directions

In this thesis, the in-vivo performance of the motion compensation approach was only evaluated using a single measurement. A natural next step would therefore be an in-vivo evaluation of convex array TMS imaging with tissue motion compensation equivalent to the clinical trial conducted for (regular) convex array TMS imaging. The outcome of this evaluation would be very interesting, because it would challenge any remaining doubts, that TMS imaging cannot be applied for real-time imaging under normal clinical conditions, and, provided success which seems likely, hopefully remove these.

As mentioned in Chapter 5, the motion compensation approach is based on a method for performing synthetic aperture blood flow imaging presented by Jensen and Nikolov in [41]. TMS imaging with motion compensation can therefore be applied for synthetic aperture flow imaging as well using its present implementation design or with only a few minor changes to the emission sequences. Thus, data obtained from an in-vivo study of TMS imaging with motion compensation can also be applied for an in-vivo study of synthetic aperture flow.

Although relatively straight forward, the implementation of TMS imaging with phased array transducers was not considered in this PhD study. Therefore, this is also an area, which should be explored in the future. Applying phased arrays enables in-vivo evaluation of TMS imaging for cardiac imaging, which is probably the most challenging application area in medical ultrasound imaging, due to the anatomical location of the heart, and the high degree of motion it involves.

Bibliography

[1] K. Nightingale, M. S. Soo, R. Nightingale, and G. Trahey, "Acoustic radiation force impulse imaging: In-vivo demonstration of clinical feasibility," *Ultrasound Med. Biol.*, vol. 28, pp. 227–235, 2002.

[2] M. A. Averkiou, D. N. Roundhill, and J. E. Powers, "A new imaging technique based on the nonlinear properties of tissues," in *Proc. IEEE Ultrason. Symp.*, 1997, vol. 2, pp. 1561–1566.

[3] M. Karaman, P. C. Li, and M. O'Donnell, "Synthetic aperture imaging for small scale systems," *IEEE Trans. Ultrason., Ferroelec., Freq. Contr.*, vol. 42, pp. 429–442, 1995.

[4] R. Y. Chiao, L. J. Thomas, and S. D. Silverstein, "Sparse array imaging with spatially-encoded transmits," in *Proc. IEEE Ultrason. Symp.*, 1997, pp. 1679–1682.

[5] L. J. Cutrona, W. E. Vivian, E. N. Leith, and G. O. Hall, "A high resolution radar combat-surveillance system," *IRE Trans. Mil. Elect.*, vol. MIL-5, no. 2, pp. 127–131, 1961.

[6] C. W. Sherwin, J. P. Ruina, and D. Rawcliffe, "Some early developements in synthetic aperture radar systems," *IRE Trans. Mil. Elect.*, vol. MIL-6, no. 2, pp. 111–115, 1962.

[7] J. C. Curlander and R. N. McDonough, *Synthetic Aperture Radar: Systems and Signal Processing*, John Wiley & Sons, Inc., 1991.

[8] B. S. Robinson, T. J. Sabourin, and C. R. Cooley, "Ultrasonic diagnostic imaging system with synthesized transmit focus," United States Patent, US 6315723 B1, Nov. 13, 2001.

[9] S. I. Nikolov, K. Gammelmark, and J. A. Jensen, "Recursive ultrasound imaging," in *Proc. IEEE Ultrason. Symp.*, 1999, vol. 2, pp. 1621–1625.

[10] G. R. Lockwood and F.S. Foster, "Design of sparse array imaging systems," in *Proc. IEEE Ultrason. Symp.*, 1995, pp. 1237–1243.

[11] G. R. Lockwood, J. R. Talman, and S. S. Brunke, "Real-time 3-D ultrasound imaging using sparse synthetic aperture beamforming," *IEEE Trans. Ultrason., Ferroelec., Freq. Contr.*, vol. 45, pp. 980–988, 1998.

[12] D. H. Johnson and D. E. Dudgeon, *Array signal processing. Concepts and techniques.*, Prentice-Hall., Englewood Cliffs, New Jersey, 1993.

[13] G. R. Lockwood, P-C. Li, M. O'Donnell, and F. S. Foster, "Optimizing the radiation pattern of sparse periodic linear arrays," *IEEE Trans. Ultrason., Ferroelec., Freq. Contr.*, vol. 43, pp. 7–14, 1996.

[14] J. J. Flaherty, K. R. Erikson, and V. M. Lund, "Synthetic aperture ultrasound imaging systems," United States Patent, US 3,548,642, 1967.

[15] C. B. Burckhardt, P-A. Grandchamp, and H. Hoffmann, "An experimental 2 MHz synthetic aperture sonar system intended for medical use," *IEEE Trans. Son. Ultrason.*, vol. 21, no. 1, pp. 1–6, January 1974.

[16] J. T. Ylitalo and H. Ermert, "Ultrasound synthetic aperture imaging: monostatic approach," *IEEE Trans. Ultrason., Ferroelec., Freq. Contr.*, vol. 41, pp. 333–339, 1994.

[17] P. D. Corl, P. M. Grant, and G. S. Kino, "A digital synthetic focus acoustic imaging system for nde," in *Proc. IEEE Ultrason. Symp.*, 1978, pp. 263–268.

[18] G. S. Kino, D. Corl, S. Bennett, and K. Peterson, "Real time synthetic aperture imaging system," in *Proc. IEEE Ultrason. Symp.*, 1980, pp. 722–731.

[19] D. K. Peterson and G. S. Kino, "Real-time digital image reconstruction: A description of imaging hardware and an analysis of quantization errors," *IEEE Trans. Son. Ultrason.*, vol. 31, pp. 337–351, 1984.

[20] K. Nagai, "A new synthetic-aperture focusing method for ultrasonic *B*-scan imaging by the fourier transform," *IEEE Trans. Son. Ultrason.*, , no. 4, pp. 531–536, 1985.

[21] M. O'Donnell and L. J. Thomas, "Efficient synthetic aperture imaging from a circular aperture with possible application to catheter-based imaging," *IEEE Trans. Ultrason., Ferroelec., Freq. Contr.*, vol. 39, pp. 366–380, 1992.

[22] M. Karaman and M. O'Donnell, "Subaperture processing for ultrasonic imaging," *IEEE Trans. Ultrason., Ferroelec., Freq. Contr.*, vol. 45, pp. 126–135, 1998.

[23] R. Y. Chiao and L. J. Thomas, "Synthetic transmit aperture using orthogonal golay coded excitation," in *Proc. IEEE Ultrason. Symp.*, 2000, pp. 1469–1472.

[24] G. E. Trahey and L. F. Nock, "Synthetic receive aperture imaging with phase correction for motion and for tissue inhomogenities - part II: effects of and correction for motion," *IEEE Trans. Ultrason., Ferroelec., Freq. Contr.*, vol. 39, pp. 496–501, 1992.

[25] H. Ş. Bilge, M. Karaman, and M. O'Donnell, "Motion estimation using common spatial frequencies in synthetic aperture imaging," in *Proc. IEEE Ultrason. Symp.*, 1996, pp. 1551–1554.

[26] M. Karaman, H. Ş. Bilge, and M. O'Donnell, "Adaptive multi-element synthetic aperture imaging with motion and phase aberation correction," *IEEE Trans. Ultrason., Ferroelec., Freq. Contr.*, vol. 42, pp. 1077–1087, 1998.

[27] C. R. Hazard and G. R. Lockwood, "Effects of motion artifacts on a synthetic aperture beamformer for real-time 3D ultrasound," in *Proc. IEEE Ultrason. Symp.*, 1999, pp. 1221–1224.

[28] J. S. Jeong, J. S. Hwang, M. H. Bae, and T. K. Song, "Effects and limitations of motion compensation in synthetic aperture techniques," in *Proc. IEEE Ultrason. Symp.*, 2000, pp. 1759 –1762.

[29] K. Gammelmark, "Multi-element synthetic transmit aperture imaging using temporal encoding," M.S. thesis, Ørsted•DTU, Technical University of Denmark, Lyngby, Denmark, 2001.

[30] K. L. Gammelmark and J. A. Jensen, "Multielement synthetic transmit aperture imaging using temporal encoding," *IEEE Trans. Med. Imag.*, vol. 22, no. 4, pp. 552–563, 2003.

[31] T. X. Misaridis and J. A. Jensen, "An effective coded excitation scheme based on a predistorted FM signal and an optimized digital filter," in *Proc. IEEE Ultrason. Symp.*, 1999, vol. 2, pp. 1589–1593.

[32] T. X. Misaridis, K. Gammelmark, C. H. Jørgensen, N. Lindberg, A. H. Thomsen, M. H. Pedersen, and J. A. Jensen, "Potential of coded excitation in medical ultrasound imaging," *Ultrasonics*, vol. 38, pp. 183–189, 2000.

[33] T. X. Misaridis, M. H. Pedersen, and J. A. Jensen, "Clinical use and evaluation of coded excitation in B-mode images," in *Proc. IEEE Ultrason. Symp.*, 2000, vol. 2, pp. 1689–1693.

[34] T. Misaridis, *Ultrasound imaging using coded signals*, Ph.D. thesis, Ørsted•DTU, Technical University of Denmark, Lyngby, Denmark, 2001.

[35] J. A. Jensen and N. B. Svendsen, "Calculation of pressure fields from arbitrarily shaped, apodized, and excited ultrasound transducers," *IEEE Trans. Ultrason., Ferroelec., Freq. Contr.*, vol. 39, pp. 262–267, 1992.

[36] J. A. Jensen, "Field: A program for simulating ultrasound systems," *Med. Biol. Eng. Comp.*, vol. 10th Nordic-Baltic Conference on Biomedical Imaging, Vol. 4, Supplement 1, Part 1, pp. 351–353, 1996b.

[37] J. A. Jensen, O. Holm, L. J. Jensen, H. Bendsen, S. I. Nikolov, B. G. Tomov, P. Munk, M. Hansen, K. Salomonsen, J. Hansen, K. Gormsen, H. M. Pedersen, and K. L. Gammelmark, "Ultrasound research scanner for real-time synthetic aperture image acquisition," *IEEE Trans. Ultrason., Ferroelec., Freq. Contr.*, p. Submitted, 2003.

[38] K. L. Gammelmark and J. A. Jensen, "Synthetic transmit aperture imaging using convex transducer arrays," *IEEE Trans. Ultrason., Ferroelec., Freq. Contr.*, p. Submitted, 2004.

[39] M. H. Pedersen, K. L. Gammelmark, and J. A. Jensen, "Preliminary in-vivo evaluation of convex array synthetic aperture imaging," in *Proc. SPIE - Progress in biomedical optics and imaging*, 2004, pp. 33–43.

[40] K. S. Kim, J. S. Hwang, J. S. Jeong, and T. K. Song, "An efficient motion estimation and compensation method for ultrasound synthetic aperture imaging," *Ultrason. Imaging*, vol. 24, pp. 91–99, 2002.

[41] J. A. Jensen and S. I. Nikolov, "Transverse flow imaging using synthetic aperture directional beamforming," in *Proc. IEEE Ultrason. Symp.*, 2002, pp. 1488–1492.

[42] J. A. Jensen, "Method for in-vivo synthetic aperture B-flow imaging," in *Proc. SPIE - Progress in biomedical optics and imaging*, 2004, p. Submitted for publication.

[43] J. A. Jensen, *Estimation of Blood Velocities Using Ultrasound: A Signal Processing Approach*, Cambridge University Press, New York, 1996.

[44] K. L. Gammelmark and J. A. Jensen, "Duplex synthetic aperture imaging with tissue motion compensation," in *Proc. IEEE Ultrason. Symp.*, 2003, pp. 1569–1573.

APPENDIX

A

Journal Articles

A.1 Multielement Synthetic Transmit Aperture Imaging using Temporal Encoding

This article was published in *IEEE Transactions on Medical Imaging*, vol. 22, no. 4, pp. 552-563, 2003.

Unfortunately, the Press at the IEEE has accidently misplaced a sentence in the paper. On page 561, left column, and last paragraph, the text starting with *"For the water SNR ...."* and ending 4 lines down in the right column with *".....improvement of TMS imaging."* is supposed to be placed above the paragraph on page 562, left column, starting with *"At the linear array...."*. On behalf of the IEEE, I apologize for the inconvenience.

Multielement Synthetic Transmit Aperture Imaging Using Temporal Encoding

Kim Løkke Gammelmark, *Student Member, IEEE,* and Jørgen Arendt Jensen, *Senior Member, IEEE*

***Abstract*—A new method to increase the signal-to-noise ratio (SNR) of synthetic transmit aperture imaging is investigated. The approach utilizes multiple elements to emulate a spherical wave, and the conventional short excitation pulse is replaced by a linear frequency-modulated (FM) signal. The approach is evaluated in terms of image quality parameters in comparison to linear array imaging. Field II simulations using an 8.5-MHz linear array transducer with 128 elements show an improvement in lateral resolution of up to 30% and up to 10.75% improvement in contrast resolution for the new approach. Measurements are performed using our experimental multichannel ultrasound scanning system, RASMUS. The designed linear FM signal obtains temporal sidelobes below −55 dB, and SNR investigations show improvements of 4–12 dB. A 30 mm (≈45%) increase in penetration depth is obtained on a multitarget phantom with 0.5 dB/[cm MHz] attenuation. Furthermore, *in vivo* images of the abdomen are presented, which demonstrate the clinical application of the new approach.**

***Index Terms*—Experimental ultrasound scanning system, Field II, linear FM signals, multielement defocusing, synthetic transmit aperture ultrasound imaging.**

I. Introduction

ONE OF the main problems in ultrasound imaging is the tradeoff between penetration depth and spatial resolution. The resolution is improved as the frequency increases, but the attenuation in soft tissue also increases with increasing frequency. Thus, to increase the penetration depth while the resolution is maintained, the transmitted energy must be increased. This can be done by increasing the amplitude and/or the duration of the excitation pulse.

The United States Food and Drug Administration (US FDA) has introduced preamendments upper limits on the acoustic output of an ultrasound scanner [1], to avoid damage to the tissue and pain to the patient. These limits concern the mechanical index (MI), the derated spatial-peak-temporal-average intensity ($I_{\mathrm{spta.3}}$), and the derated spatial-peak-pulse-average intensity ($I_{\mathrm{sppa.3}}$)[1] [1], [2]. MI is proportional to derated peak rarefraction pressure [3], while $I_{\mathrm{spta.3}}$ and $I_{\mathrm{sppa.3}}$ depend both on pulse shape and duration [2].

The peak pressure in the tissue is proportional to the peak amplitude of the excitation pulse. For the conventional imaging techniques like *linear array imaging* the peak amplitude of the short excitation pulses used can, therefore, not be increased to overcome the loss in penetration depth, when high frequencies are used. This is because the $I_{\mathrm{sppa.3}}$ limit is reached much earlier than the $I_{\mathrm{spta.3}}$ limit for these systems due to the transmit focusing. For short pulse systems in general, the $I_{\mathrm{sppa.3}}$ limit is very often reached much earlier than the $I_{\mathrm{spta.3}}$ limit, which limits the amplitude of the excitation pulse. Thus, to increase the penetration depth, the temporal energy and, thus, $I_{\mathrm{spta.3}}$, must be increased. This is done by increasing the duration of the transmitted pulse. For this purpose, the conventional pulse cannot be used, since the axial resolution is inversely proportional to the bandwidth (after matched filtering). Thus, some type of temporal encoding is necessary. This requirement is satisfied by linear frequency-modulated (FM) signals [4], [5], which have been used in radar systems for decades, because of their compression ability. These signals have recently been applied in ultrasound scanners [6]–[10], and they have shown good performance in terms of increased penetration depth, while maintaining the spatial resolution.

Generally, linear array imaging systems obtain a good spatial resolution due to the application of dynamic receive focusing. The resolution can, however, be improved by increasing the number of transmit foci. This is often done in modern ultrasound scanners at the expense of a reduction in the frame rate proportional to the number of foci. One way to obtain high spatial resolution, while keeping the frame rate high, is to use the *synthetic transmit aperture (STA) imaging* technique [11]. The inherent nature of this technique makes it possible to generate images with dynamic transmit and receive focusing using only a few transmissions. Therefore, STA imaging offers very high frame rates, which makes it suitable for real-time three-dimensional (3-D) volumetric imaging. A problem in STA imaging is, however, the low signal-to-noise ratio (SNR), due to the application of a single transmit element. This means that the penetration depth obtained by STA imaging is much lower than that obtained by linear array imaging, which significantly limits its clinical application. However, if the SNR can be increased to that of linear array imaging, images with better image quality can be generated, while maintaining a high frame rate. For this purpose the linear FM signal can be applied with great advantage. Also, previous research has shown [11], [12] that the application of multielement subapertures in STA imaging to produce a spherical wave transmission yields spatial resolution results

Manuscript received August 9, 2002; revised November 4, 2002. This work was supported in part by the Danish Science Foundation under Grant 9700883 and Grant 9700563, in part by Technical University of Denmark under Ph.D. Grant 11-3160-55173, and in part by B-K Medical A/S, Herlev, Denmark. The Associate Editor responsible for coordinating the review of this paper and recommending its publication was M. Insana. *Asterisk indicates corresponding author.*

*K. L. Gammelmark is with the Center for Fast Ultrasound Imaging, Ørsted • DTU, Building 348, Technical University of Denmark, 2800 Kgs. Lyngby, Denmark (e-mail: klg@oersted.dtu.dk).

J. A. Jensen is with the Center for Fast Ultrasound Imaging, Ørsted • DTU, Technical University of Denmark, 2800 Kgs. Lyngby, Denmark.

Digital Object Identifier 10.1109/TMI.2003.809088

[1]The thermal index (TI) has not been included in the analysis in this paper.

very close to the single element transmission, and also increases the SNR proportionally to the number of elements used in the subaperture. Another potential problem in STA imaging is tissue motion. Although this issue is not considered in this paper, an example of its influence in abdominal imaging is given in Section V using measured *in vivo* tissue velocities. The example shows, that the effects of tissue motion on the image quality are minor, and this is supported by presented abdominal *in vivo* images.

This paper investigates the combination of these two methods to increase the SNR of STA imaging. The approach utilizes a multielement subaperture to produce a spherical wave with high power, and the conventional short excitation signal is replaced by a linear FM signal. Initially, the principles of classical STA imaging is presented in Section II along with STA beamforming. Section III describes the new approach in detail and gives measures of the expected increase in SNR. Section IV presents simulation results using Field II, and Section V presents phantom and *in vivo* measurement results of the abdomen using our experimental multichannel ultrasound scanning system, RASMUS [13]. All results are compared to corresponding linear array imaging results. The paper is concluded in Section VI.

II. Synthetic Transmit Aperture Imaging

In conventional STA imaging a single element is used at each transmission to produce a spherical wave that interrogates a large region of the medium (see Fig. 1). The echoes resulting from scattering in the medium are recorded using all elements in the aperture, and the procedure is repeated until a desired number of elements have been used for transmission. For each transmission the echoes received by each element in the aperture contain information about all scatterers in the interrogated region. Since no focusing has been applied on transmit, and the exact origin of the spherical wave is known, the receive aperture can be steered in any direction and focused at any point within this region. Therefore, every point in the image can be formed independent of each other, and a full image is obtained for every transmission event with low lateral resolution due to the single transmit element. Taking into account the full path length between the transmitting element and the receive elements, when calculating the beamforming delays (as illustrated in Fig. 2), the individual low resolution images are both dynamically focused on receive, and adjusted to obtain dynamic focusing on transmit in the same operation. Dynamic focusing on transmit is then obtained subsequently by coherently summing the low resolution images which forms the final high resolution image as illustrated in Fig. 1.

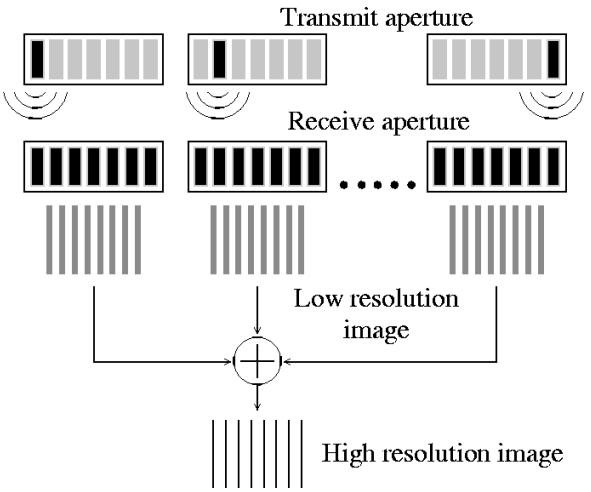

Fig. 1. Illustration of the conventional STA imaging principle. At each transmission event a single element is fired, and the echoes from the medium are collected using all elements in the receiving aperture. For each of these transmission events a complete image is beamformed, and these are subsequently summed to form the final high resolution image.

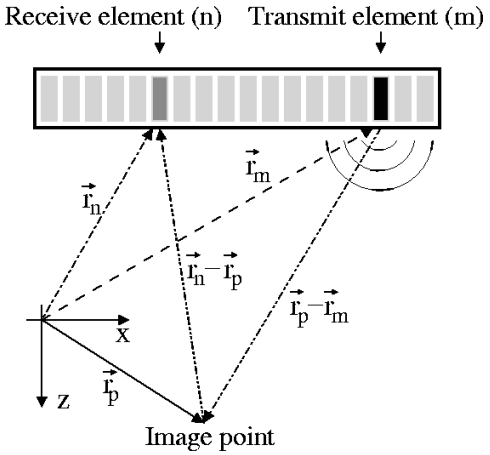

Fig. 2. Illustration of STA beamforming from a spatial view point. The time delay used for picking out the correct sample, in order to obtain transmit and receive focusing at the illustrated image point, is determined by the absolute distance between the image point and the transmit and receive elements, m and n, respectively.

A. STA Beamforming

This section describes how STA beamforming is performed and the flexibility in a STA beamformer.

Fig. 2 shows the concept of STA beamforming from a spatial point of view. The image point to be beamformed is described by the vector $\vec{r}_p$, and the vectors $\vec{r}_m$ and $\vec{r}_n$ designate the position of transmit element m and receive element n, respectively. Letting $g_{m,n}(t)$ represent the received echo signal on element n when transmitting with element m, then the low resolution image, $s_m(\vec{r}_p)$, for transmit element m is calculated by

$$s_m(\vec{r}_p) = \sum_{n=1}^{N} w_n(\vec{r}_p) g_{m,n}\left(\frac{d_{m,n}(\vec{r}_p)}{c}\right) \tag{1}$$

where $w_n(\vec{r}_p)$ is the apodization values for receive element n, c is the sound speed, and N is the number of receive channels. The total distance $d_{m,n}(\vec{r}_p)$ from the transmitting element to the image point and back to the receiving element is given by

$$d_{m,n}(\vec{r}_p) = |\vec{r}_p - \vec{r}_m| + |\vec{r}_n - \vec{r}_p| \tag{2}$$

where the individual distances are defined in Fig. 2. This distance describes the time at which the scattered signal from the image point is received at element n when transmitting with element m. Keeping the transmit element fixed, $d_{m,n}(\vec{r}_p)$ determines which samples should be picked out of the received signals in order to obtain a receive focus at the image point. However, keeping the receive element fixed and letting the transmit

element move, $d_{m,n}(\vec{r}_p)$ also determines the time shift between the received signals from different transmissions and, thus, the shift between the low resolution images. Therefore, when applying $d_{m,n}(\vec{r}_p)$ in (1) both dynamic receive focusing is obtained and $s_m(\vec{r}_p)$ is adjusted such that dynamic transmit focusing is obtained, when the low resolution images are subsequently summed. Thus, the final high resolution image, $S(\vec{r}_p)$, with both dynamic transmit and receive focusing, is obtained by summing the low resolution images (neglecting motion compensation). In particular

$$S(\vec{r}_p) = \sum_{m=1}^{M} w_m(\vec{r}_p) s_m(\vec{r}_p) \tag{3}$$

where $w_m(\vec{r}_p)$ is the apodization value for transmit element m. In general, the time at which the sample is to be picked out of the received signals, $g_{m,n}(t)$, does not correspond to an integer sample number. Therefore, interpolation is needed to find the correct sample value. If interpolation is not used, a high sampling frequency is necessary in order to limit the increase in sidelobe and grating lobe levels, due to the phase quantization [14]. An alternative to using interpolation, which can be hardware demanding, is to use phase rotation in the digital beamformer as suggested by O'Donnell and coworkers in [15].

The advantage of the above beamforming scheme is that only one interpolation operation is needed to obtain $S(\vec{r}_p)$ compared to normally two, when transmit and receive focusing is separated. This is both cost and time efficient and reduces interpolation artifacts.

The transmit and receive apodization values can be used to generate any type of dynamic aperture and dynamic apodization function in order to obtain the desired beam shape. The dynamic aperture is typically selected to grow linearly, while keeping a constant F-number. This ensures a constant beam width until the aperture is fully opened. The shape of the dynamic apodization function determines the tradeoff between sidelobe levels and lateral resolution. Note that any point in the image can be beamformed independently of all other image points using the above scheme.

III. Temporally Encoded Multielement (TMS) STA Imaging

The objective of this paper is to investigate a new approach to increase the SNR of conventional STA imaging. It is called *temporally encoded multielement* STA (TMS) imaging, and it is based on the combination of multielement STA imaging with linear FM waveforms. These two techniques are described briefly in the following.

A. Multielement STA Imaging

The major drawback of STA imaging is the low SNR. Since a single element is used at each transmission the SNR is very low compared to, e.g., linear array imaging, which significantly limits its clinical application. To overcome this, a subaperture consisting of multiple grouped elements can be used to emulate the radiation pattern of a (virtual) high power point source, i.e., a spherical wave, and hereby increase the SNR. This concept is called *multielement synthetic transmit aperture imaging*, and it has previously been investigated by Karaman and coworkers [11] with respect to application in hand-held scanners, and by Lockwood and coworkers [16] with the purpose of 3-D ultrasound imaging. Both groups show that by properly delaying the individual elements in the subaperture, good approximation to a spherical wave can be obtained along with a significant improvement in SNR.

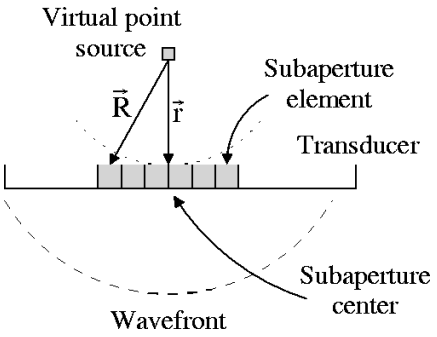

Fig. 3. Illustration of the setup used when calculating the transmit delays for emulating a spherical wave emitted from a virtual high power point source positioned behind the subaperture.

The defocusing delay for each subaperture element can be calculated as illustrated in Fig. 3. The position of a virtual point source is selected behind the center of the subaperture with a certain axial distance selected, e.g., as a fraction of the subaperture size. Given the subaperture elements coordinates and the center of the subaperture, the defocusing delay τ_d for a specific element is then calculated by

$$\tau_d = \frac{\left|\vec{R}\right| - |\vec{r}|}{c} \tag{4}$$

where $\vec{R}$ is the vector from the virtual point source to the element, and $\vec{r}$ is the vector from the virtual point source to the subaperture center.

The position of the virtual point source, which produces the best emulation of the spherical wave, is not straight forward to calculate, because it depends on the interference between the waves from the individual subaperture elements and their radiation patterns. If the virtual source is moved away from the subaperture, the beam will become increasingly flat and narrow, and at some point yield a nearly plane wave for the given subaperture. The virtual element cannot be moved too close to the subaperture either, because the difference between the transmit delays becomes too large to obtain a coherent wavefront. Therefore, the proper location of the virtual point source should be investigated through simulations. These results are presented in Section IV.

B. Temporal Encoding Using Linear FM Signals

Linear FM signals have been used in radars for decades because of their distinctive feature of serving as both a long emitted and a short compressed pulse simultaneously. In medical ultrasound imaging, one of the first frameworks for using coded signals to improve the penetration-resolution problem was described by Takeuchi in 1979 [6]. Since then several authors have investigated different approaches and schemes to fully utilize their capabilities and improve their performance (e.g., [7], [10], and [17]–[19]).

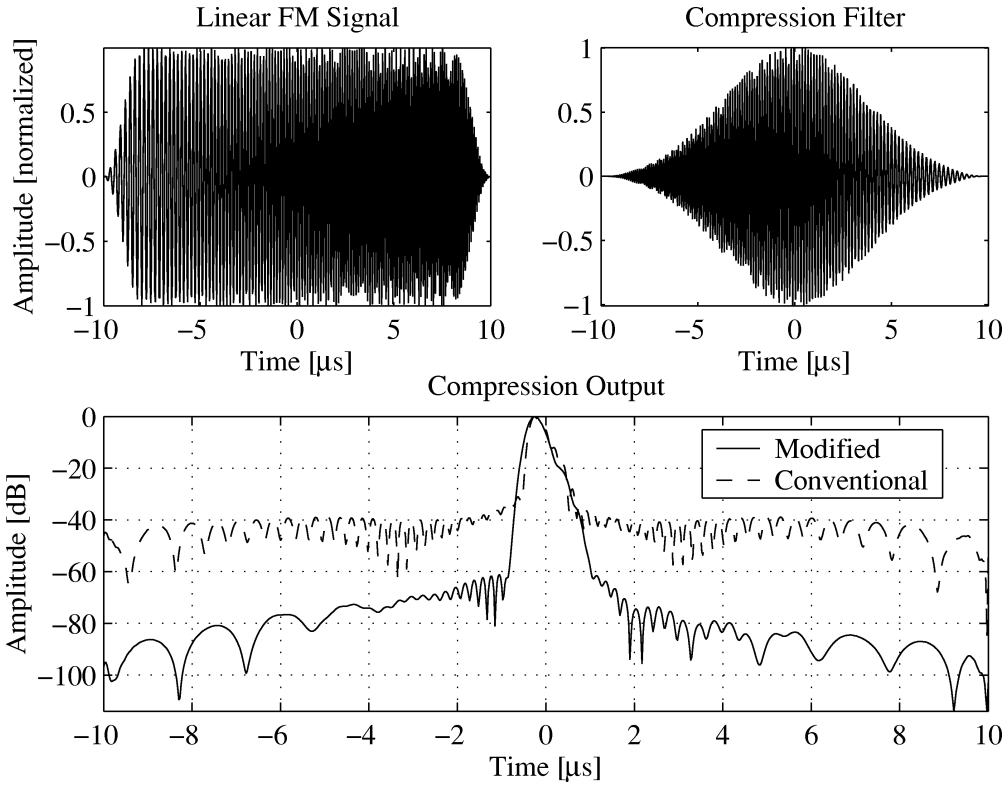

Fig. 4. Top left: Modified linear FM signal with a 7-MHz center frequency and 7-MHz bandwidth. A Tukey window with a duration of 10% has been applied. Top right: Modified compression filter using a Chebychev window with 70 dB relative sidelobe attenuation. Bottom: Compression output for the conventional FM signal (dashed) and the modified FM signal (solid). The effect of a linear array transducer has been introduced in the compression outputs.

The conventional linear FM signal is described in [4] as

$$p(t) = b\cos\left(2\pi\left[f_c t + \frac{B_s}{2\tau_s}t^2\right]\right), \qquad |t| \le \frac{\tau_s}{2} \tag{5}$$

where b is the amplitude, f_c is the center frequency, B_s is the frequency sweep (the bandwidth), and τ_s is the duration of the signal. The matched filter to $p(t)$ in (5) is given by

$$\begin{aligned} h_m(t) &= p(-t) \\ &= b\cos\left(2\pi\left[f_c t - \frac{B_s}{2\tau_s}t^2\right]\right), \qquad |t| \le \frac{\tau_s}{2}. \end{aligned} \tag{6}$$

Assuming $p(t)$ is the waveform received from a point target, the compressed radio-frequency signal becomes [4]

$$\begin{aligned} g(t) &= p(t) * h_m(t) \\ &= \frac{b^2\tau_s}{2}\,\frac{\sin\left(\pi D\frac{t}{\tau_s}\left(1-\frac{|t|}{\tau_s}\right)\right)}{\pi D\frac{t}{\tau_s}}\cos\left(2\pi f_c t\right) \end{aligned} \tag{7}$$

where $D = \tau_s B_s$ is the time-bandwidth product, $|t| \le \tau_s$, and higher frequency terms have been neglected. Considering only the envelope of $g(t)$, this has approximately the shape of a sinc-function. Assuming D is large (generally above 20 as mentioned by Blinchikoff and Zverev [4]), the envelope of $g(t)$, $\hat{g}(t)$, becomes a sinc-function

$$\hat{g}(t) \approx |g(t)| \approx \frac{b^2\tau_s}{2}\,\frac{\sin\left(\pi D\frac{t}{\tau_s}\right)}{\pi D\frac{t}{\tau_s}}, \qquad |t| \le \tau_s. \tag{8}$$

The $2/\pi \approx -4$ dB width of this function is $\delta t = 1/B_s$, which shows that the temporal (axial) resolution can be improved by increasing the bandwidth. This is advantageous when using high bandwidth transducers.

An example of the compression result in (8) is shown as the dashed curve in Fig. 4 (bottom). The influence of an 8.5-MHz linear array transducer has been introduced, and the parameters for $p(t)$ and $h_m(t)$ are $f_c = 7$ MHz, $B_s \simeq 7$ MHz, and $\tau_s = 20$ μs. As seen the temporal sidelobes are around -40 dB, which is not sufficient for medical imaging. To reduce the sidelobes, previous research has shown that this can effectively be done by applying amplitude weighting on the linear FM signal and compression filter [8], [19], [20]. In this study, a Tukey window with a 10% duration is applied on the linear FM signal, and a Chebychev window with 70 dB relative sidelobe attenuation is applied on the compression filter $h_m(t)$. The modified linear FM signal and compression filter are shown in the left and right parts of Fig. 4, respectively. The same parameters as given above have been used. The compression output is shown as the solid curve in bottom figure. As seen the temporal sidelobes have been reduced below -60 dB, which is adequate for clinical imaging.

C. Signal-to-Noise-Ratio

The (peak) SNR after matched filtering is proportional to the energy in the received signal [4]. Also, the peak compression output is proportional to the energy in the linear FM signal as seen in (8). Thus, the analysis can be simplified by only considering the energy, when comparing the SNRs obtained by linear array imaging and TMS imaging.

The noise in the system includes both analog electronics noise produced in the front-end of the system, and the quantization

noise generated by the analog-to-digital converters (ADC) on each channel. These noise sources are assumed to be white and uncorrelated between channels. The quantization noise power is determined by the resolution of the ADC, and it is independent of the input signal and the imaging technique. Therefore, the influence of the quantization noise can be discarded under the assumption, that the input signal fills a significant part of the ADC input range, which is generally achieved in practical systems. Thus, only the analog electronics noise is considered in the analysis.

It is assumed, that the received signals from each channel are perfectly phase aligned. In this case there is no difference between transmitting with the same aperture M times or with M different apertures with the same size. Thus, the beamformer can be regarded as simply averaging the received channel signals. Furthermore, attenuation and diffraction effects are not included in this analysis, and it is assumed that no amplitude weighting is applied to the transmitted waveforms and receive filters. Using these assumptions a simple model for the improvement in SNR can be established. For linear array imaging, the energy in the received signal for a single element E_{R_L} from a point target at the acoustic focus can be approximated by the number of transmit elements N_{T_L} squared times the duration of the transmitted pulse τ_l

$$E_{R_L} \sim N_{T_L}^2 \tau_l. \tag{9}$$

As shown experimentally by Karaman and coworkers [11], the amplitude of the wavefront created by the defocused subaperture consisting of N_{T_S} elements is proportional to $\sqrt{N_{T_S}}$. Thus, the energy in the received signal for a single element E_{R_S} for TMS imaging is

$$E_{R_S} \sim N_{T_S} \tau_s \tag{10}$$

where τ_s is the duration of the transmitted FM signal. As mentioned above the beamformer is considered as simply averaging the individual channel signals. Denoting the number of receive channels for linear array imaging N_{R_L}, the SNR in the linear array image is proportional to

$$\mathrm{SNR}_{B_L} \sim N_{R_L} N_{T_L}^2 \tau_l \tag{11}$$

since the noise is white and uncorrelated between channels. From the description of STA beamforming, (3) in combination with (1) states that in TMS imaging averaging is done over N_{R_S} receive channels and M transmit events. Thus, the SNR in the TMS image is proportional to

$$\mathrm{SNR}_{B_S} \sim M N_{R_S} N_{T_S} \tau_s. \tag{12}$$

The ratio between (12) and (11) gives the improvement I_B in SNR

$$I_B = \frac{\mathrm{SNR}_{B_S}}{\mathrm{SNR}_{B_L}} \sim \frac{M N_{T_S}}{N_{T_L}^2} \frac{N_{R_S}}{N_{R_L}} \frac{\tau_s}{\tau_l}. \tag{13}$$

This assumes that the noise is stationary and described by the same probability density function for both systems. If a better SNR is to be obtained by TMS imaging, this ratio needs to be greater than 1.

In this study, a subaperture of $N_{T_S} = 33$ elements will be used. The applied FM signal has a duration of $\tau_s = 20$ μs, and the transducer has 128 transmit and receive elements, which results in $M = 96$ transmissions. Using (13) and a linear array imaging setup of $N_{T_L} = 64$, $N_{R_L} = N_{R_S} = 128$, and a 2 cycle sinusoid excitation at 7 MHz, it is found that $I_B \simeq 54.2 \approx 17.3$ dB. This indicates that a significant increase in SNR is to be expected.

In general, the energy in the waveform received from a point target is not directly related to the duration of the transmitted pulse. Rather, it depends on both the duration and the shape. The approximation used to obtain (9) and (10) holds if the received waveform has a rectangular envelope, but under normal conditions this is not obtained due to the finite bandwidth of the transducer. Also, as mentioned previously, amplitude weighting is applied on the linear FM signal and compression filter for temporal sidelobe reduction. Therefore, the actual improvement in SNR may differ slightly from result above, because these factors have not been included in the model for simplicity. Their influence is investigated further in the next section.

IV. Simulations

Simulations are done using Field II [21], [22] to compare the performance of TMS imaging to linear array imaging on a theoretical basis in terms of spatial and contrast resolution.

The transducer model used is a 128-element linear array aperture with a center frequency of 8.5 MHz and a relative bandwidth of 60%. The pitch is 0.208 mm and the element height is 4.5 mm. The transducer has an elevation lens with a focal point at 25 mm. The impulse response of the receive elements is set to the pulse-echo response *measured* from a plane reflector in water using a delta excitation for the transducer used for the measurements in Section V. Thus, the impulse response of the transmit aperture is set to a Dirac delta function. In this way, the simulation model resembles the true situation more accurately.

For linear array imaging a 64-element aperture is used for transmission and all 128 elements are used in receive. A two-cycle sinusoid at 7 MHz weighted with a Hanning window is used as excitation signal, and no transmit apodization is applied. The received signals are filtered using a matched filter, and beamformed using dynamic receive focusing with updated delay curves for every second sample. The number of lines in the image and their spacing is calculated from the highest spatial frequency of the point spread function (PSF) to satisfy the spatial Nyquist theorem. This results in images with line counts between 132 and 165 for transmit foci at 50 and 40 mm, respectively.

TMS imaging is done using a 33 element subaperture and 128 receive elements, which results in 96 emissions. The excitation signal is the linear FM signal displayed in Fig. 4 (top, left). It has a duration of 20 μs, a center frequency of 7 MHz, and a bandwidth of approximately 7 MHz. The FM signal has been weighted with a Tukey window to reduce the temporal sidelobes. The corresponding compression filter is also shown in Fig. 4 (top, right). A Chebychev window has been applied to reduce the temporal sidelobes in the compression output. The position of the virtual point source is chosen such that the distance to the subaperture is equal to the size of the subaperture. This has been determined through wavefront simulations [23]. A Tukey like window function is applied on the subaperture to reduce the influence of edge waves on the PSF. The resulting PSF is shown in Fig. 5 (top), and the corresponding PSF when

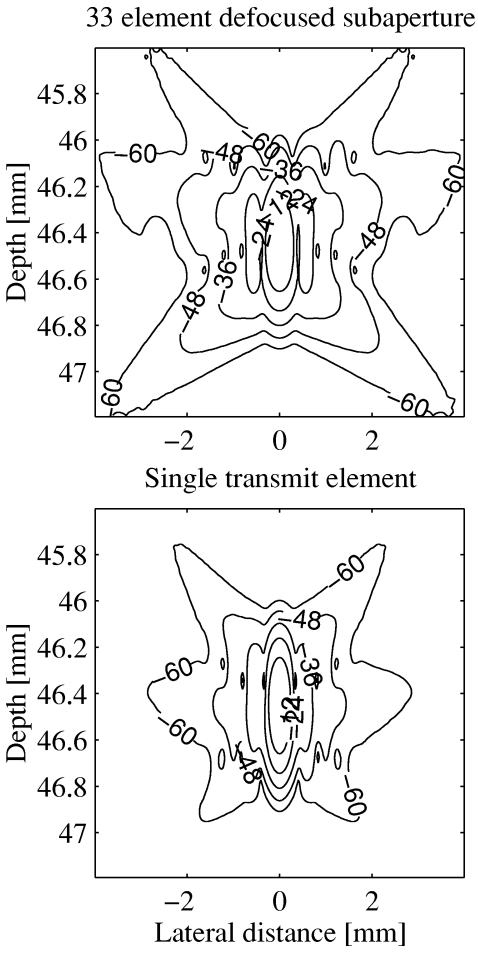

Fig. 5. PSFs obtained when using a defocused 33 element subaperture (top) and a single transmit element (bottom). The virtual point source for the multi element subaperture is placed behind the center of aperture at a distance equal to the size of the subaperture itself. The distance between the contours is 12 dB. Notice the slightly wider multi element PSF, which indicates a slight degradation in lateral resolution compared to the single element transmission.

using a single transmit element is shown in the bottom part of the figure. As seen, the two PSFs are very similar, but the multielement PSF is a bit wider in the lateral direction, which indicates a slightly degraded lateral resolution. STA Beamforming is done with dynamic transmit and receive focusing as explained previously in Section II-A, and the received echo signals on each channel are compressed prior to beamformation. For both linear array imaging and TMS imaging, a dynamic receive aperture is used with an expanding modified Hamming window with edge levels at -12 dB. The aperture opens at an F-number of 2.

A. Acoustic Output and SNR Simulations

When comparing two imaging techniques it is important that both their acoustic outputs are within the official limits. The US FDA has set pre-Amendments upper limits on the acoustic outputs which may occur in the human body. These are: $I_{\mathrm{spta.3}} \leq 720$ mW/cm^2, $I_{\mathrm{sppa.3}} \leq 190$ W/cm^2, and $\mathrm{MI} \leq 1.9$ [1]. The measurement of these parameters are done following the guidelines set by the American Institute of Ultrasound in Medicine (AIUM) [2]. A simulation can, however, be done following the same guidelines to give a theoretical measure of the acoustic output. The US FDA limits are global maximum values. MI and $I_{\mathrm{sppa.3}}$ are taken at the spatial location, where the derated pulse intensity integral ($PII_{.3}$) is maximum, while $I_{\mathrm{spta.3}}$ is taken at the spatial location of its global maximum [2]. For both linear array and TMS imaging this will occur on-axis of the transducer, but at different depths. For TMS imaging $PII_{.3,\,\mathrm{max}}$ and $I_{\mathrm{spta.3,\,max}}$ occur at the acoustic focus of the elevation lens at 17 mm. For linear array imaging $PII_{.3,\,\mathrm{max}}$ occurs at the lateral acoustic focus at 38 mm (geometric focal point at 40 mm), while $I_{\mathrm{spta.3,\,max}}$ occurs at the acoustic focus of the elevation lens at 17 mm. To ease the comparison, the amplitudes of both excitation signals have been set equal and scaled such that linear array imaging reaches the $I_{\mathrm{sppa.3}}$ limit. In this case the obtained values are for linear array imaging: $I_{\mathrm{sppa.3}} = 190$ W/cm^2, $I_{\mathrm{spta.3}} = 62.7$ mW/cm^2, $\mathrm{MI} = 1.07$, and for TMS imaging: $I_{\mathrm{sppa.3}} = 35.9$ W/cm^2, $I_{\mathrm{spta.3}} = 1749.2$ mW/cm^2, $\mathrm{MI} = 0.45$. As seen, MI and $I_{\mathrm{sppa.3}}$ are lower for TMS imaging due to the linear array transmit focus, and $I_{\mathrm{spta.3}}$ for TMS imaging is significantly higher than linear array imaging. Compared to the US FDA limits, however, $I_{\mathrm{spta.3}}$ for TMS imaging is a factor of 2.4 larger than the FDA limit, while both MI and $I_{\mathrm{sppa.3}}$ are significantly below the limits. Since the acoustic output of a scanner must comply with all the limits, the excitation voltage for TMS imaging needs to be reduced by a factor of $\sqrt{2.4} \simeq 1.55$ compared to the linear array excitation voltage in order to satisfy the requirements. This reduction will affect all the output measures. Alternatively, the duration of the linear FM signal can be reduced by a factor of 2.4, which will only affect $I_{\mathrm{spta.3}}$. It should be noted, that nonlinear effects are not included in this analysis as well as measurement noise, hydrophone effects, etc. Also, this analysis assumes that it is possible to apply excitation voltages in the scanner to reach the $I_{\mathrm{sppa.3}}$ FDA limit, which will depend on the front-end electronics and transducer, and, thus, the limit might not be reachable in linear array imaging. This is investigated in further detail in Section V.

It was shown in Section III-C that a significant improvement in SNR for TMS imaging is to be expected using the imaging setup described above. The model proposed model does, however, not account for the deviation from a rectangular envelope of the excitations and matched filters, and it does not include the influence of the transducer impulse response and acoustical effects, e.g., diffraction. Thus, a Field II simulation is used to take these factors into account and get a closer estimate. The excitation voltages are set equal for both methods in the analysis. If, however, the scaling of 1.55 was used, the results presented below would be reduced by $10 \log 1.55^2 \simeq 3.81$ dB. The simulation is done by calculating the received echo response from a set of wires displaced in the axial dimension. The wires are located on-axis of the transducer at 20–90 mm with 5-mm spacing. The line corresponding to the position of the wires is then beamformed for both linear array imaging and TMS imaging. The ratio between the peak responses for TMS and linear array imaging is then taken for each wire, and the results are plotted in Fig. 6. The dashed curve is the result, when no amplitude weighting of the excitation signals, matched filters, and receive apertures (no fixed or dynamic apodization) are used. In this case the difference between the SNR model described in Section III-C and the simulation is the influence of the transducer and the acoustics. The linear array data are beamformed using dynamic receive focusing, and the TMS data are beamformed using dynamic transmit and receive focusing.

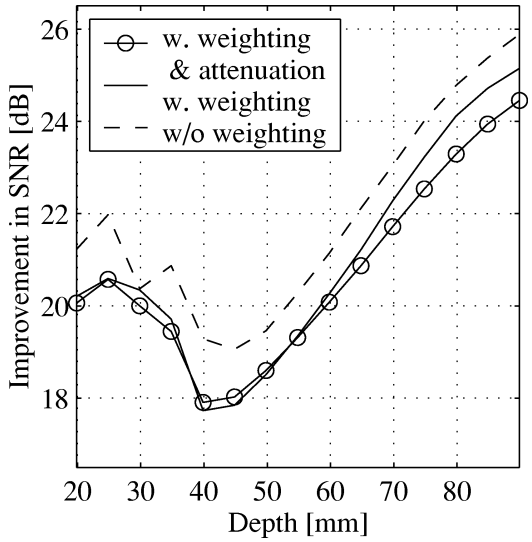

Fig. 6. Simulated SNR improvement results with (solid) and without (dashed) the application of amplitude weighting on the excitation pulses, matched filters, and the receive apertures (no dynamic aperture and expanding apodization function). The solid curve with circles is for the case when both weighting and attenuation is used. The attenuation is 0.5 dB/[cm MHz].

The improvement in SNR at 40 mm is 19 dB, which is close to the 17.3 dB predicted by the model. This result shows that the model is useful to gain a simple understanding of the parameters, which affect the SNR. It is noted that away from the linear array focus the improvement increases, which is due to the application of dynamic transmit focusing in TMS imaging. The solid curve is the result using amplitude weighting of the excitation signals and matched filters are used, and when dynamic apodization is applied in the beamforming. At 40 mm the improvement in SNR has decreased to 17.7 dB, which again is very close to the SNR model. The solid curve with circles shows the case when both weighting and attenuation is applied. The attenuation is 0.5 dB/[cm MHz]. It can be seen that the attenuation does not have a significant effect until after 60 mm, where the improvement starts to decrease compared to the case with no attenuation.

B. Spatial Resolution

To investigate the spatial resolution performance, a wire phantom is simulated with wires located at 20 mm to 120 mm with 5 mm spacing. The transmit focal point for linear array imaging was set to 50 mm. Fig. 7 shows the -6 dB lateral (top) and axial resolutions (bottom) as a function of depth for linear array imaging (dashed) and TMS imaging (solid), respectively. The lateral resolution is approximately constant until the aperture is fully opened at 53 mm. Beyond this depth the lateral performance of TMS imaging is better due dynamic transmit focusing. At 120 mm the lateral resolution has improved by approximately 30%. The performance of the axial resolutions is seen to be close, but the compression mechanism of the linear FM signal is more stable with depth.

C. Contrast Resolution

The contrast resolution is evaluated by simulating a cyst phantom containing sixteen anechoic cysts placed in two columns with a start depth at 30 mm. The cysts have a diameter

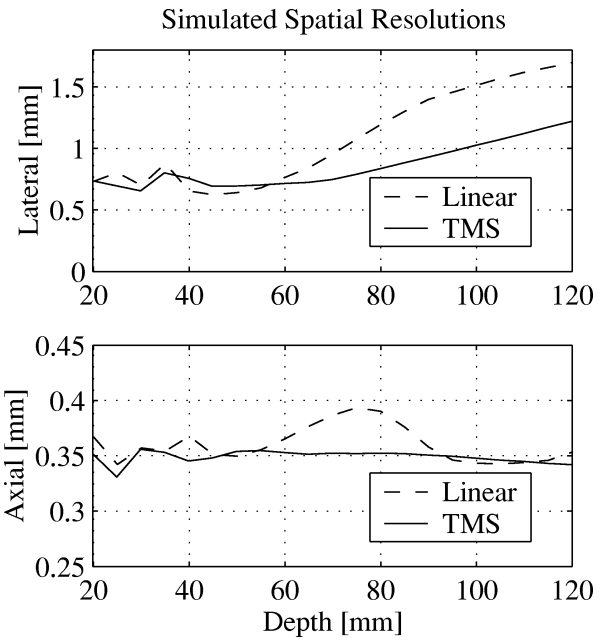

Fig. 7. (top) Lateral and (bottom) axial (-6 dB) resolution for linear array imaging (dashed) and TMS imaging (solid), respectively. The results are obtained from a simulated wire phantom with 5-mm spacing between the wires. The transmit focal length for linear array imaging was set to 50 mm.

of 4 mm, and they are separated by 10 mm in depth and 5 mm laterally. All cysts have an amplitude of -40 dB compared to the surrounding speckle. The linear array transmit focus was again set to 50 mm, and no attenuation effects are included. The results are shown in Fig. 8. To enhance the visualization of the results each image has been divided into two parts as seen. The left part of the figure shows the results from 25 mm to 65 mm, and the right part shows the results from 65 mm to 105 mm. The latter clearly shows the improvement in lateral resolution for TMS imaging as described in the previous section. This has a positive effect on the contrast resolution which is improved for TMS imaging at depths beyond 70 mm. From the images in the left part of the figure no conspicuous difference in image quality is seen.

As a measure of the contrast resolution (CR), the following equation is used:

$$\mathrm{CR} = 1 - \frac{I_c}{I_s} \tag{14}$$

where I_c is the intensity inside the cyst, and I_s is the intensity of the speckle within a region of the same size as the cyst and at the same depth. This equation gives results between zero and one, where one corresponds to perfect contrast resolution.

When calculating CR, the original size of the cyst in used and not the size of the dark region displayed in the images. This is done to take into account both the influence of the lateral resolution and the sidelobes and grating lobes. The calculated CRs are summarized in Table I. For each imaging method the numbers have been averaged for each depth. In general, these numbers show an overall improvement in contrast resolution for TMS imaging. The lowest improvement is about 1% and it is obtained for the cyst at 60 mm. This is also the first cyst for which the receive aperture is fully opened. Beyond this depth the contrast resolution improves and at 100 mm the improvement is 10.75%.

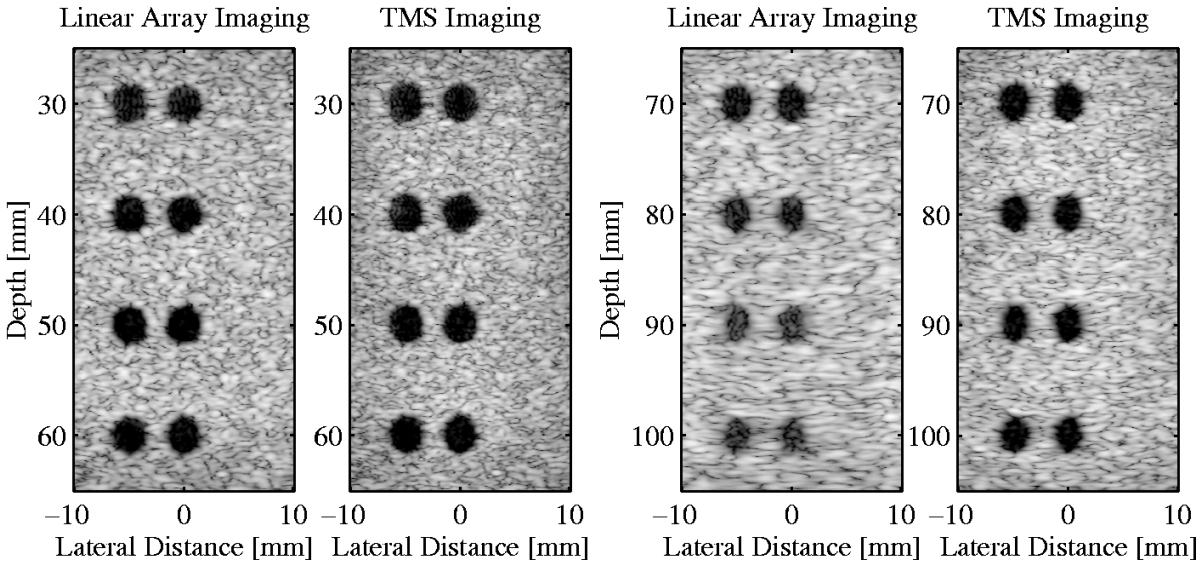

Fig. 8. Images of the simulated cyst phantom. The images have been divided into two parts with the region 25 mm to 65 mm displayed in the left part of the figure, and the region 65 mm to 105 mm is shown to the right. In both parts of the figure, the linear array image is shown to the left and the TMS image to the right. No attenuation effects are included in the simulation.

TABLE I
CALCULATED CONTRASTS FOR THE SIMULATED CYST PHANTOMS

Cyst	Depth	Linear Array Imaging	TMS Imaging	Improvement in %
1	30 mm	0.92	0.98	5.64
2	40 mm	0.91	0.95	3.75
3	50 mm	0.94	0.97	2.77
4	60 mm	0.92	0.92	1.06
5	70 mm	0.94	0.96	2.30
6	80 mm	0.88	0.95	7.57
7	90 mm	0.86	0.95	10.31
8	100 mm	0.86	0.95	10.75

Above 60 mm the contrast resolution has also improved. This is also expected due to the dynamic transmit focusing.

V. MEASUREMENTS

The measurements are performed using the experimental multichannel ultrasound scanning system, RASMUS [13]. The system has 128 individually programmable transmitters capable of sending arbitrary coded waveforms with a precision of 12 bits at 40 MHz. Sixty-four receive channels can be simultaneously sampled at 12 bits and 40 MHz, and the 2 to 1 multiplexing in the system enables acquisition of 128 channels in real-time over two transmissions. The RASMUS system is remotely accessible and programmed through a developed Matlab/C-library interface. The system is build using a slightly modified commercial front-end, which is limited to a supply voltage of ± 100 V. In practice, however, ± 50 V or 100 Vpp is used. Thus, the system represents a commercially available scanner.

The transducer used for the measurements has the same parameters as the transducer used for the simulations. Also, the measurement setups for linear array imaging and TMS imaging are the same as those used for the simulations. This has been chosen to enable direct comparison between the measurements and the simulations. The filters used for matched filtering and compression of the received signals have been normalized equally for both methods to enable a fair comparison, and the beamforming of the measured data is also done as for the simulated data.

A. Acoustic Output Measurements

According to the acoustic output simulations presented in Section IV, the excitation voltage used in TMS imaging needs to be reduced a factor of 1.55 compared to the linear array excitation voltage to comply with the FDA limits. This analysis assumed that the excitation voltage could be increased to reach the $I_{\mathrm{sppa.3}}$ FDA limit. However, in the RASMUS system, this might not be achievable due to limitations of the front-end electronics and heating of the transducer. Also, the simulations did not account for several practical effects, such as the nonlinear effects, the influence of the hydrophone, noise, etc., which also will influence the output quantities. Therefore, the acoustic output should be measured to obtain a direct relation to the FDA requirements.

Due to current limitations of our measurement setup only MI and $I_{\mathrm{sppa.3}}$ have been measured. The measurements were done in a water tank according to the guidelines in [2] for both linear array and TMS imaging. $PII_{.3,\,\mathrm{max}}$ was found on-axis for both methods, but at 17 mm for TMS imaging and at 40 mm for linear array imaging (geometric focal point at 40 mm). For linear array imaging the measured quantities were: $\mathrm{MI} = 0.12$ and $I_{\mathrm{sppa.3}} = 10.0$ W/cm^2, and TMS imaging: $\mathrm{MI} = 0.10$ and $I_{\mathrm{sppa.3}} = 1.94$ W/cm^2. As seen all quantities are significantly below the FDA limits. In particular, $I_{\mathrm{sppa.3}}$ for linear array imaging is 19 times less than the FDA limit. Thus, the excitation voltage in the RASMUS system can be increased $\sqrt{19} \simeq 4.4$ times for linear array imaging, assuming a linear relation between the excitation voltage and the pressure, to reach

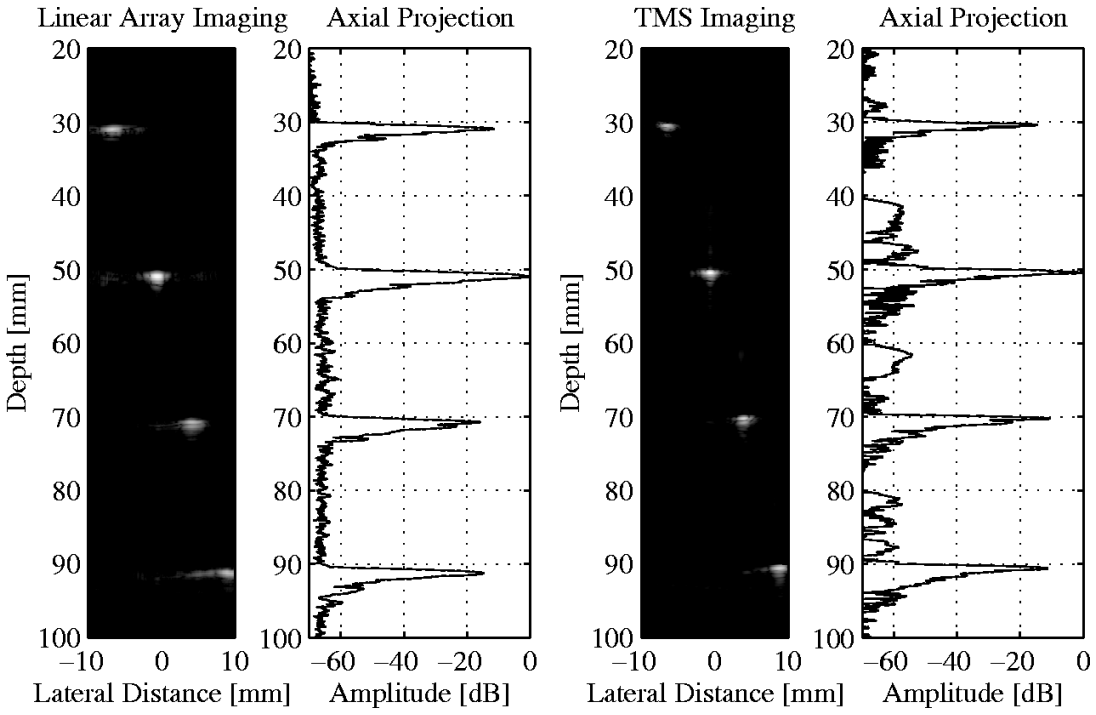

Fig. 9. Measured B-mode images and axial projections of a scanned wire phantom using linear array imaging (left) and TMS imaging (right). The phantom contains four laterally and axially spaced copper wires and water, and the dynamic range in the B-mode image is 60 dB. As seen in the projection image for TMS imaging, the applied linear FM signal and compression filter yields temporal sidelobes below -55 dB.

the FDA limit. This results in an excitation voltage of approximately ± 220 V, which significantly exceeds the limitations of the front-end and the transducer. The companion excitation voltage for TMS imaging would be $(\pm 220\,\mathrm{V})/1.55 \simeq \pm 142$ V, which likewise exceeds the limitation in the front-end. If the excitation voltage is increased to ± 100 V, the acoustic output for TMS imaging will still be below the FDA limit. Keeping the excitation voltages equal for both methods, therefore, does not violate the basis for a fair comparison. Thus, the excitation voltage is ± 50 V for all measurements. It should be mentioned, however, that if the power supply voltage could be increased beyond ± 142 V, the excitation voltages would have to be different for TMS and linear array imaging to comply with the FDA regulations and to make the comparison fair.

B. Phantom Measurements

The linear FM signal used in both the simulations and measurements has been designed to obtain temporal sidelobe levels at approximately -60 dB. To evaluate this, a wire phantom containing four wires in water has been scanned. Fig. 9 shows the B-mode images and axial projections for linear array imaging (left) and TMS imaging (right). The axial projections are obtained by taking the maximum at each depth in the images. The dynamic range in the B-mode images is 60 dB. As seen the temporal sidelobes have been reduced to approximately -55 dB, which is adequate for clinical imaging. Also, it is noticed, that the lateral sidelobe levels are lower both above and below the linear array transmit focus. This observation is inspected more closely in Fig. 10, which shows the lateral projections of the PSF at depth 70 mm in both B-mode images. The lateral projection

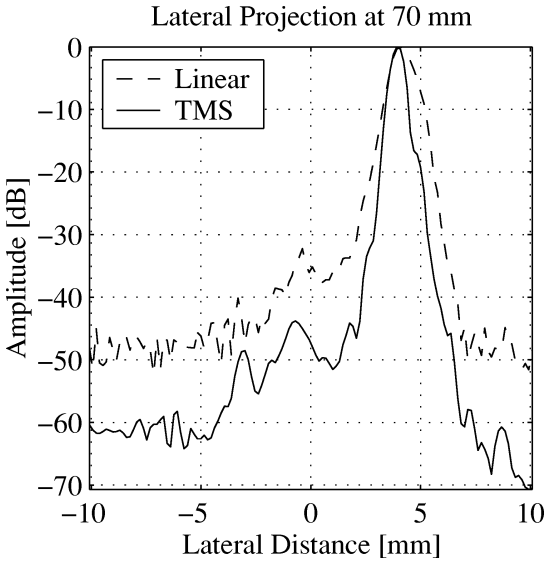

Fig. 10. Lateral projection of the PSFs at depth 70 mm in Fig. 9. The dashed line is linear array imaging and the solid line is TMS imaging.

is obtained by taking the maximum of each line within the region containing the PSF. The reduction in sidelobe levels is up to 15 dB.

The spatial resolution and SNR performance of TMS imaging is evaluated in the presence of attenuation using a multitarget phantom with 0.5 dB/[cm MHz] attenuation. Fig. 11 shows the linear array image (left) and TMS image (right) of a scanned region containing twisted nylon wires spaced axially by 1 cm. The dynamic range is 50 dB in both images. The penetration depth has been increased roughly 3 cm using TMS imaging.

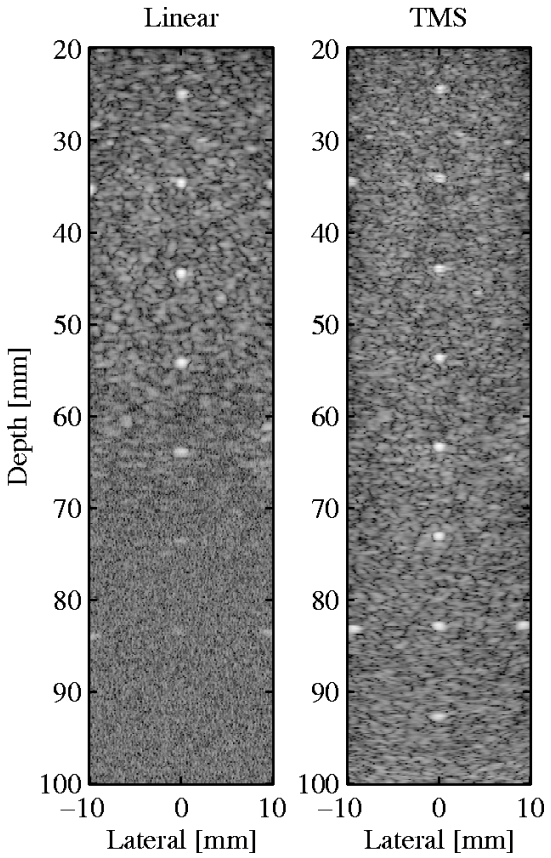

Fig. 11. Measured linear array image (left) and TMS image (right) on a multitarget phantom with 0.5 dB/[cm MHz] attenuation. The scanned section contains twisted nylon wires spaced axially by 1 cm throughout the imaged region. The dynamic range in the images is 50 dB.

The linear array image has a very low SNR after 70 mm, and the wires are not visible in this region. No apparent noise is present in the TMS image, and the wires are, thus, fully visible throughout the imaged region.

The -6 dB lateral and axial resolutions are evaluated for each wire in both images in Fig. 11. The results are shown in Fig. 12, where the lateral resolution is displayed in the top figure and the axial resolution in the bottom figure. TMS imaging has a better lateral performance at distances after the linear array transmit focus due to dynamic transmit focusing. Compared to the simulation results in Fig. 7, it is noted that the lateral resolutions follow the same trends, but it is a bit higher in the measurements due to the presence of attenuation. The axial resolution is better for TMS imaging throughout the imaged region. This shows that the linear FM signal has a better axial performance in the presence of attenuation than the conventional short excitation pulse. The axial resolution for linear array imaging can, however, be improved by applying a shorter excitation pulse instead of the two cycles pulse used in this study. This will though result in less transmitted energy and, thus, lower penetration and SNR.

For the water SNR the linear array transmit focus was set to 50 mm, and at this depth the SNR improvement is 8 dB. This result does not compare exactly to the SNR model proposed earlier and the simulations, which showed an improvement of approximately 18 dB. There are, however, many factors which cannot be included in a model and in the simulations. One of these factors

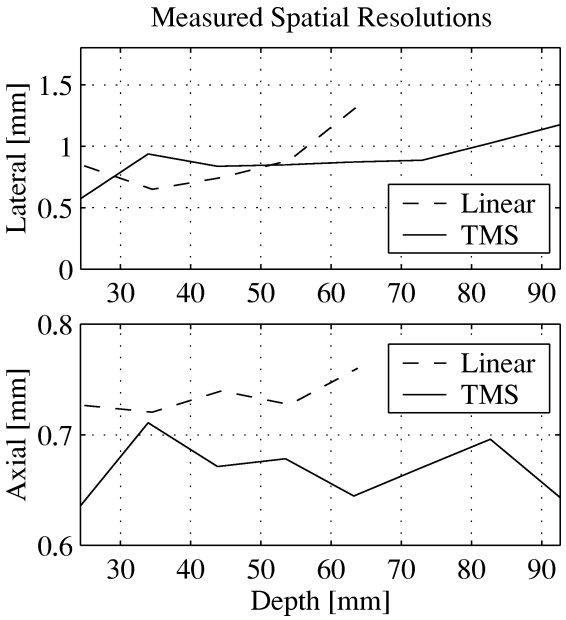

Fig. 12. Lateral (top) and axial (bottom) resolution curves for linear array imaging (dashed) and TMS imaging (solid). The curves have been obtained by calculating the spatial resolutions for each wire in Fig. 11.

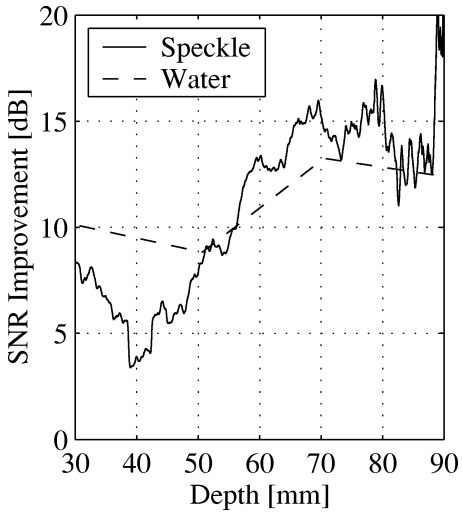

Fig. 13. Calculated SNR improvement obtained by TMS imaging in water (dashed) and in a tissue mimicking phantom (solid).

is inefficiency of the measurement system. Therefore, the deviation between the simulation and the measurement result should be looked upon as a place of possible improvement of TMS imaging.The improvement in SNR obtained by TMS imaging in water and for a tissue mimicking phantom is shown in Fig. 13. The SNR for water was obtained using the wire phantom data from Fig. 9. For each image and depth the power was calculated resulting in two signal power vectors. The noise power in the system generated by each imaging method was obtained by scanning a water bath with no reflections. For each imaging method the power of the resulting noise images was calculated, resulting in a noise power vector. Taking the ratio between the signal power vectors and the noise power vectors yields the SNR for each imaging method, and the difference between these SNR curves at the wire locations is the SNR improvement shown as

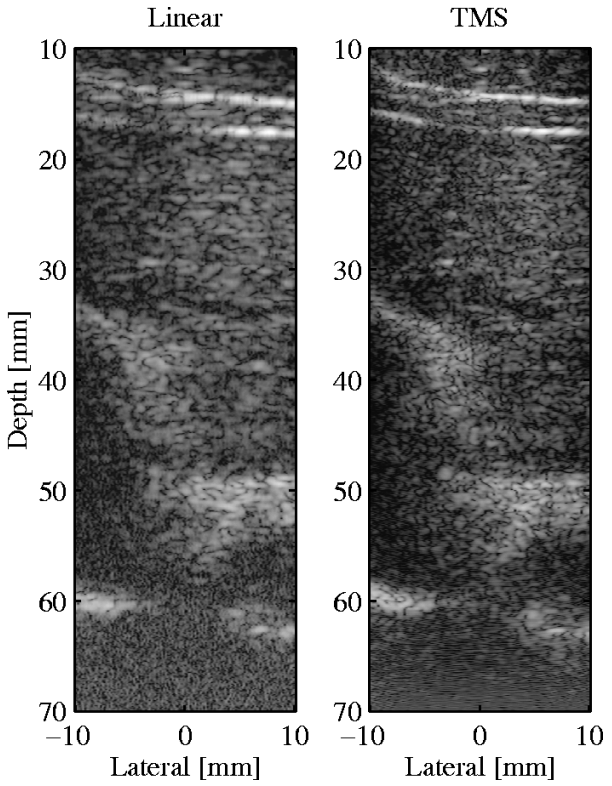

Fig. 14. *In-vivo* images of the abdomen using linear array imaging (left) and TMS imaging (right). The dynamic range in the image is 50 dB.

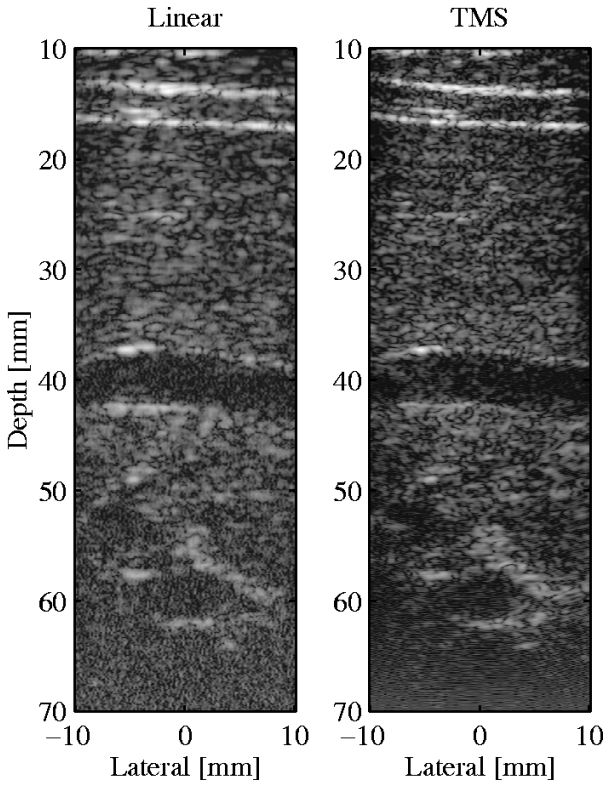

Fig. 15. Same as Fig. 14 but of a different abdominal location. The dynamic range in the image is 40 dB.

the dashed curve in Fig. 13. Since only one image was used for calculating the signal power vector, this vector contains noise. Therefore, the noise power was subtracted from the signal power vector before taking the ratio. Thus, for a given depth

$$\mathrm{SNR} = \frac{P_{\mathrm{signal}} - P_{\mathrm{noise}}}{P_{\mathrm{noise}}} \tag{15}$$

where P_{signal} is the signal power, and P_{noise} is the noise power. The SNR improvement in the tissue mimicking phantom was obtained using the parts of Fig. 11 not containing wires and the generated noise vectors from the water bath. The SNR improvement was evaluated at each depth throughout the image, and the result is shown as the solid curve in Fig. 13. A low-pass filter has been applied on the curve to make it more smooth.

At the linear array focal point in the phantom (40 mm) the improvement in SNR is about 4 dB, but it is significantly larger before and after the focus. At 80 mm, an improvement of 15 dB is obtained and at approximately 90 mm, the SNR of linear array imaging is so low that the correct values can no longer be obtained. In general, the SNR follows the same trend as the simulations, but the curve has been shifted downwards.

C. In-Vivo Measurements

To demonstrate the clinical feasibility of TMS imaging, *in vivo* measurements on the abdomen of a 27-year-old male were performed. The measurement setups for both linear array imaging and TMS imaging are the same as those used for the phantom measurements with the linear array transmit focal depth set to 50 mm. The RASMUS system is setup in an interleaved mode such that the linear array and TMS scannings are performed in one long sequence. Thus, data from exactly the same abdominal position are obtained at the same time, which enables direct comparison of the images. Figs. 14 and 15 show the results of two scannings at different abdominal locations. The dynamic range is 50 dB in Fig. 14 and 40 dB in Fig. 15, and the linear array and TMS images are shown to the left and right, respectively. The TMS images have both better spatial resolution and contrast resolution.

When comparing the linear array and TMS images there are no visible motion artifacts. This may seem surprising since TMS imaging in theory is more sensitive to tissue motion, because a complete image is formed at each transmission event and the images are summed in the end as explained in Section II. As reported by Trahey and Nock [24], axial tissue motion is the dominant factor in image quality degradation. Thus, in the following example only axial motion is considered. Using a pulse repetition frequency (f_{prf}) of 5 kHz, the TMS imaging system described here will have a frame rate FR of approximately 25 frames/s, due to the 96 emissions and the 2-to-1 multiplexing. Schlaikjer and coworkers [25] have reported measured tissue velocities around the Hepatic vein of 10 mm/s over a cardiac cycle. Using this velocity as the axial velocity v_z of a tissue region, the total displacement Δz of the tissue from the first to the last transmission, i.e., the whole frame, is

$$\Delta z = \frac{v_z}{FR} = \frac{10\ \mathrm{mm/s}}{25\ \mathrm{frames/s}} = 400\ \mu\mathrm{m/frame}. \tag{16}$$

This is compared to an acoustic wavelength λ of 220 μm, assuming a sound speed of 1540 m/s and a center frequency of 7 MHz. Thus, the tissue moves approximately 2λ during the acquisition of a full high resolution TMS image. This motion will

occur gradually over the whole acquisition, if the velocity is assumed constant. The displacement between two low resolution images is, therefore, about 4 μm, which is less than 2% of the wavelength, and the correlation between the images is, therefore, high. Also, the axial resolution is observed to be approximately 3λ in Fig. 12. Therefore, it can be concluded that tissue motion in this case will not have a significant influence on the image quality of the TMS image, which is also supported by the abdominal *in vivo* images, that show no visual motion artifacts.

VI. Conclusion

In this paper a new approach to increase the SNR of STA imaging has been investigated. The approach combines multielement STA imaging with the application of linear FM signals, and it is called TMS imaging. Several simulations using Field II and phantom and *in vivo* measurements were performed to investigate the performance of TMS imaging compared to linear array imaging. The overall performance of TMS imaging is better than linear array imaging. The simulations showed an improvement in lateral resolution of up to 30% at a depth of 120 mm, and general improvements in contrast resolution of up to approximately 11% were obtained. The phantom measurements showed an increase in penetration depth of 3 cm on a tissue-mimicking phantom with 0.5 dB/[cm MHz] attenuation. This corresponds to an increase of approximately 45%. The corresponding increase in SNR was 4–12 dB. The *in vivo* measurements of the abdomen showed better contrast and spatial resolution for TMS imaging and no visual distortion of the images due to tissue motion.

This paper has shown that the SNR of STA imaging can be increased to exceed that obtained by linear array imaging. The result is images with overall better image quality obtained using fewer transmission events than linear array imaging.

References

[1] "Information for manufacturers seeking marketing clearance of diagnostic ultrasound systems and transducers," United States Food and Drug Administration (FDA) and Center for Devices and Radiological Health, Tech. Rep., 1997.

[2] "Acoustic output measurement standard for diagnostic ultrasound equipment," Amer. Inst. Ultrasound in Medicine and Nat. Electrical Manufacturers Assoc. (AIUM), Tech. Rep., May 1998.

[3] J. G. Abbott, "Rationale and derivation of MI and TI—A review," *Ultrasound Med. Biol.*, vol. 25, pp. 431–441, 1999.

[4] H. J. Blinchikoff and A. I. Zverev, *Filtering in the Time and Frequency Domains*. New York: Wiley, 1976.

[5] D. R. Wehner, *High Resolution Radar*, 2nd ed. Norwood, MA: Artech House, 1996.

[6] Y. Takeuchi, "An investigation of a spread energy method for medical ultrasound systems—Pt. I: Theory and investigations," *Ultrasonics*, pp. 175–182, 1979.

[7] M. O'Donnell, "Coded excitation system for improving the penetration of real-time phased-array imaging systems," *IEEE Trans. Ultrason., Ferroelect., Freq. Contr.*, vol. 39, pp. 341–351, May 1992.

[8] T. X. Misaridis, K. Gammelmark, C. H. Jørgensen, N. Lindberg, A. H. Thomsen, M. H. Pedersen, and J. A. Jensen, "Potential of coded excitation in medical ultrasound imaging," *Ultrasonics*, vol. 38, pp. 183–189, 2000.

[9] T. X. Misaridis, M. H. Pedersen, and J. A. Jensen, "Clinical use and evaluation of coded excitation in B-mode images," in *Proc. IEEE Ultrason. Symp.*, vol. 2, 2000, pp. 1689–1693.

[10] T. Misaridis, "Ultrasound imaging using coded signals," Ph.D. dissertation, Ørsted • DTU, Tech. Univ. Denmark, Lyngby, Denmark, 2001.

[11] M. Karaman, P. C. Li, and M. O'Donnell, "Synthetic aperture imaging for small scale systems," *IEEE Trans. Ultrason., Ferroelect., Freq. Contr.*, vol. 42, pp. 429–442, May 1995.

[12] S. I. Nikolov, K. Gammelmark, and J. A. Jensen, "Recursive ultrasound imaging," in *Proc. IEEE Ultrason. Symp.*, vol. 2, 1999, pp. 1621–1625.

[13] J. A. Jensen, O. Holm, L. J. Jensen, H. Bendsen, H. M. Pedersen, K. Salomonsen, J. Hansen, and S. Nikolov, "Experimental ultrasound system for real-time synthetic imaging," in *Proc. IEEE Ultrason. Symp.*, vol. 2, 1999, pp. 1595–1599.

[14] S. Holm and K. Kristoffersen, "Analysis of worst-case phase quantization sidelobes in focused beamforming," *IEEE Trans. Ultrason., Ferroelect., Freq. Contr.*, vol. 39, pp. 593–599, Sept. 1992.

[15] M. O'Donnell, W. E. Engeler, J. T. Pedicone, A. M. Itani, S. E. Noujaim, R. J. Dunki-Jacobs, W. M. Leue, C. L. Chalek, L. S. Smith, J. E. Piel, R. L. Harris, K. B. Welles, and W. L. Hinrichs, "Real-time phased array imaging using digital beam forming and autonomous channel control," in *Proc. IEEE Ultrason. Symp.*, 1990, pp. 1499–1502.

[16] G. R. Lockwood, J. R. Talman, and S. S. Brunke, "Real-time 3-D ultrasound imaging using sparse synthetic aperture beamforming," *IEEE Trans. Ultrason., Ferroelect., Freq. Contr.*, vol. 45, pp. 980–988, July 1998.

[17] P. Li, E. Ebbini, and M. O'Donnell, "A new filter design technique for coded excitation systems," *IEEE Trans. Ultrason., Ferroelect., Freq. Contr.*, vol. 39, pp. 693–699, Nov 1992.

[18] J. Shen and E. S. Ebbini, "A new coded-excitation ultrasound imaging system—Pt. I: Basic principles," *IEEE Trans. Ultrason., Ferroelect., Freq. Contr.*, vol. 43, pp. 131–140, Jan. 1996.

[19] T. X. Misaridis and J. A. Jensen, "An effective coded excitation scheme based on a predistorted FM signal and an optimized digital filter," in *Proc. IEEE Ultrason. Symp.*, vol. 2, 1999, pp. 1589–1593.

[20] Y. Takeuchi, "Chirped excitation for <-100dB time sidelobe echo sounding," in *Proc. IEEE Ultrason. Symp.*, 1995, pp. 1309–1314.

[21] J. A. Jensen and N. B. Svendsen, "Calculation of pressure fields from arbitrarily shaped, apodized, and excited ultrasound transducers," *IEEE Trans. Ultrason., Ferroelect., Freq. Contr.*, vol. 39, pp. 262–267, Mar. 1992.

[22] J. A. Jensen, "Field: A program for simulating ultrasound systems," in *Med. Biol. Eng. Comp.*, vol. 4, Suppl. 1, Pt. 1, vol. 10th Nordic-Baltic Conference on Biomedical Imaging, 1996b, pp. 351–353.

[23] K. Gammelmark, "Multi-element synthetic transmit aperture imaging using temporal encoding," M.S. thesis, Ørsted • DTU, Tech. Univ. Denmark, Lyngby, Denmark, 2001.

[24] G. E. Trahey and L. F. Nock, "Synthetic receive aperture imaging with phase correction for motion and for tissue inhomogenities—Pt. II: Effects of and correction for motion," *IEEE Trans. Ultrason., Ferroelec., Freq. Contr.*, vol. 39, pp. 496–501, July 1992.

[25] M. Schlaikjer, S. Torp-Pedersen, J. A. Jensen, and P. F. Stetson, "Tissue motion in blood velocity estimation and its simulation," in *Proc. IEEE Ultrason. Symp.*, 1998, pp. 1495–1499.

A.2 Synthetic Transmit Aperture Imaging using Convex Transducer Arrays

This article was submitted to *IEEE Transactions on Ultrasonics, Ferroelectrics, and Frequency Control* in April 2004.

Synthetic Transmit Aperture Imaging using Convex Transducer Arrays

Kim Løkke Gammelmark, *Student Member, IEEE*, and Jørgen Arendt Jensen, *Senior Member, IEEE*

Abstract

Studies of synthetic transmit aperture (STA) imaging has primarily been performed using phased and linear array transducers. This paper investigates the feasibility of performing STA imaging using convex array transducers. The convex array geometry is more complicated than the linear array geometries, which introduces new design considerations regarding transmission scheme and image reconstruction. The paper describes these considerations in detail, and it revisits methods for improving the signal-to-noise ratio. Experimental phantom and in-vivo results obtained using the RASMUS research scanner and a commercial 5.5 MHz convex array transducer are presented to evaluate the performance and feasibility of STA convex array imaging in comparison to conventional convex array imaging. The SNR of STA imaging was increased by applying multi-element apertures and a linear FM signal at each transmission. The results showed improvements in spatial resolution, and the contrast resolution was improved by up to 42.7%. An improvement of 14 dB in SNR was obtained after the conventional imaging focal point, and in-vivo images of the abdomen and right kidney showed a significant overall improvement in image quality of STA imaging in terms of sharper images with better contrast and structure definitions. Two in-vivo movie sequences of 2.5 sec duration were also acquired and showed no visual artifacts from tissue motion.

I. Introduction

In modern medical ultrasound scanners, linear and phased array techniques are used to generate the displayed images. These techniques build up the images over a number of transmit events by transmitting focused beams in distinctive directions in the medium. For each direction the received echoes are focused along the same direction, and the produced scan lines are stacked together to create the displayed image. These techniques are intuitive and easy to implement, and they achieve good penetration because of the high peak intensity produced at the transmit focal point.

The frame rate obtained by modern systems is dependent on the number of lines required for adequate spatial sampling of the medium. In general, this number depends on the spatial resolution in the transverse direction (lateral or angular) and the size of the image. The number of lines can thus become high, resulting in low frame rates.

The received echoes are focused dynamically along the transmit direction, which produces the best possible receive beam pattern. The overall spatial resolution is, however, compromised by the single transmit focal point. Thus, the spatial resolution is only optimal at the transmit focal point. To minimize this effect, compound imaging is often applied, which composes each line from several transmissions, each having a different transmit focus location. This, however, reduces the frame rate by the number of transmit zones.

Synthetic transmit aperture (STA) imaging is a technique which relies on principles quite the reverse of the conventional techniques. Here, each transmit event produces an unfocused wave, which propagates in all directions in the medium, and the recorded echoes for all transmit events are processed in such a way that both the receive aperture and (synthesized) transmit aperture are focused at every image point. This produces ultrasound images with improvements in both spatial resolution and image contrast.

Traditionally, STA imaging has been considered for phased array applications [1] and recently linear array imaging [2]. However, few studies on the application of STA imaging using convex array transducers has been published [3]. Convex array transducers are generally used for abdominal imaging because of their large field of view and good penetration depth. Extending STA imaging to convex apertures requires some new design considerations, because of the more complicated aperture geometry.

This study investigates STA imaging using convex transducer arrays in comparison to conventional convex array imaging. The purpose is to show, that although the convex aperture geometry may not be the ideal geometry for STA imaging, these can be integrated successfully to produce high abdominal image quality. A detailed introduction to STA imaging is given in Section II, which also describes the impacts on image reconstruction of the convex aperture geometry. The experimental setup is described in Section III, and the results in terms of signal-to-noise ratio, spatial- and contrast resolution, and in-vivo image quality are presented in Section IV. A discussion of these results are given in Section V, and the paper is concluded in Section VI.

Kim L. Gammelmark (klg@oersted.dtu.dk) and Jørgen A. Jensen (jaj@oersted.dtu.dk) are both from the Center for Fast Ultrasound Imaging, Ørsted•DTU, Building 348, Technical University of Denmark, 2800 Kgs. Lyngby, Denmark

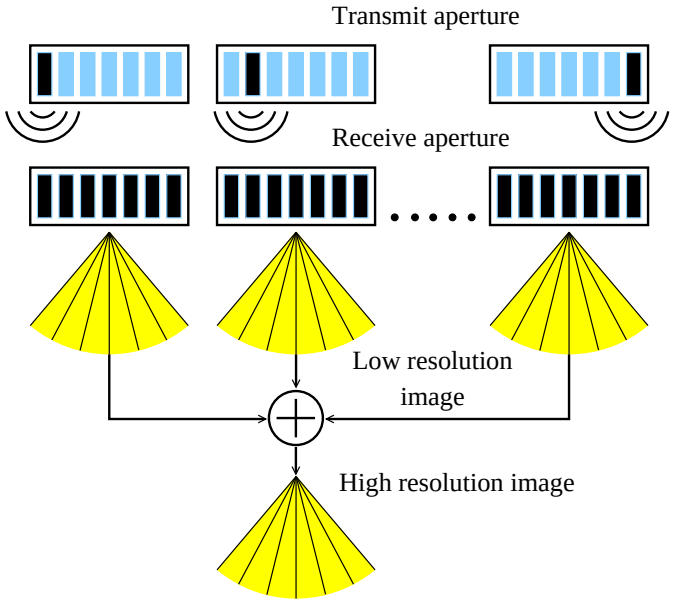

Fig. 1. Illustration of the conventional STA imaging principle. At each transmission event a single element is fired, and the echoes from the medium are collected using all elements in the receiving aperture. For each of these transmission events a complete image is beamformed, and these are subsequently summed to form the final high resolution image.

II. Synthetic Transmit Aperture Imaging

Synthetic aperture imaging is a method, which has been investigated for medical ultrasound imaging applications since early 1970 [4], [5]. The technique was originally developed for radar systems (synthetic aperture radar) in the 1950's with the purpose of improving the lateral/azimuthal resolution of side-looking radars. In ultrasound imaging, the same monostatic approach was initially investigated, and later extended to array transducers when these emerged in the 1980's.

The concept of synthetic transmit aperture (STA) imaging is explained in Fig. 1. At each transmit event a single element is excited, which transmits a spherical wave, that spreads out in all directions in the tissue. The echoes are recorded using all elements in the receive aperture, and this transmit-receive process is repeated until all or a desired number of elements in the array have been excited.

Reconstruction of each pixel in the ultrasound image is performed by coherently summing the echoes received from a point target located at the center of each pixel for all transmissions. This is possible because the origin and shape of the transmitted wave is known. The origin is determined by the location of the transmitting element, and the wavefront is spherical due to the small aperture elements. Assuming the speed of sound in the medium is known, the arrival time of the echo from a given point target for a specific transmit and receive element pair can be calculated exactly using the geometric relations illustrated in Fig. 2. Performing this calculation for all transmit-receive element pairs, picking out the corresponding samples of the recorded echoes, and finally summing these samples, both the transmit and the receive apertures are focused at the point target location, producing an optimally focused image point. This process is repeated for all points or pixels in the ultrasound image. Mathematically, the reconstruction is performed by

$$S(\vec{r}_p) = \sum_{m=1}^{M} \sum_{n=1}^{N} w_m(\vec{r}_p) w_n(\vec{r}_p) g_{n,m} \left(\frac{|\vec{r}_n - \vec{r}_p| + |\vec{r}_p - \vec{r}_m|}{c} \right) \tag{1}$$

where $S(\vec{r}_p)$ is the reconstructed image, $a_T(\vec{r}_m, \vec{r}_p)$ is the dynamic apodization for transmit element m, $a_R(\vec{r}_n, \vec{r}_p)$ is the dynamic apodization for receive element n, $g_{n,m}(t)$ is the recorded echo data, and M and N are the number of transmit and receive elements, respectively. Note, that the image points are independent from each other, enabling parallel processing.

In practice, the image reconstruction process is performed sequentially. After each emission event a complete ultrasound image is formed by focusing the receive aperture at all image points based on the transmit element location (Fig. 1). The produced image is called a low (lateral) resolution image, because the image is created using a single transmit element. This is repeated after each emission, and the individual low resolution images are finally summed to produce the displayed high resolution image. In this way, the transmit aperture is synthesized over several transmissions, and the ultrasound image is build up sequentially.

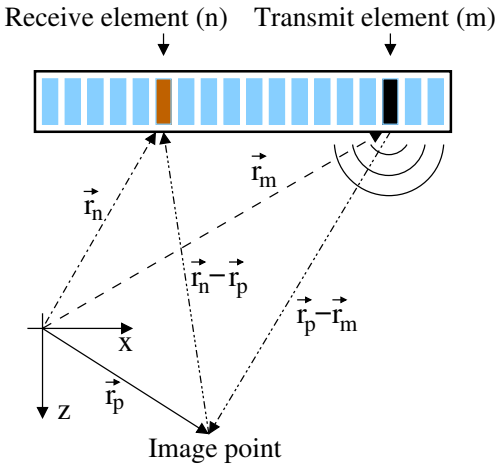

Fig. 2. Geometrical illustration of STA beamforming. The core principle is the known origin and shape (spherical) of the emitted wave. Based on this and the knowledge of the speed of sound, the arrival time of the echo from a given point target can be calculated exactly.

Clinical implementation of STA imaging has primarily been limited by a low signal-to-noise ratio (SNR). The low SNR is obtained because the energy produced by the single transmit element is limited, which again is caused by hardware and transducer heating limitations. This results in low penetration depth, and thus limited in-vivo application. Another issue is the influence of tissue motion on STA imaging. Tissue motion causes the scatterers to move between consecutive firings, resulting in incoherent summation of the low resolution images. For high tissue velocities this will produce an unfocused, smeared image with poor image quality, and STA imaging is thus more susceptible to motion than conventional imaging. Although the influence of tissue motion and compensation thereof is out of the scope of this study, we will revisit this subject briefly in the discussion in Section V.

The SNR can be improved by increasing the transmitted energy. This can be done in several ways, which will affect either the peak intensity (the peak pressure) or the temporal intensity in the tissue.

A. Increasing Peak Intensity

Producing a higher peak intensity means increasing the peak pressure. This can be obtained by increasing the amplitude of the transmitted signal, but hardware limitations in the front-end and to some extend problems with internal heating in the transducer generally excludes this solution. A more suitable strategy is to use more elements at each emission to emulate the spherical wave transmitted by the single element. This technique was first applied by O'Donnell and Thomas [6] in a catheter based ultrasound system using a circular aperture, and later extended to plane apertures by Karaman and coworkers [1]. The approach is to use a subaperture with proper time delays to produce a defocused wave with a limited spherical wave extend. The delays are calculated geometrically based on the position of a virtual point source positioned behind the subaperture as illustrated in Fig. 3(a) and the element coordinates. In particular, the delay $\tau(n)$ of element n is

$$\tau(n) \quad = \quad \frac{d(n) - r}{c}, \tag{2}$$

where $d(n)$ is the distance between the virtual point source and element n, r is the distance between the virtual point source and the subaperture center, and c is the speed of sound.

The position of the virtual point source determines the angular extend α over which the transmitted wavefront is spherical. This determines the beam characteristics of the virtual point source or rather virtual transmit element. The angular sensitivity of each virtual element in the synthesized transmit aperture can therefore be controlled by changing the location of the associated virtual point sources. This is advantageous because the energy can be concentrated within a controllable band ($\pm\alpha$), which increases the peak wavefront pressure and thus SNR. It however puts a limit on the minimum transmit f-number applicable when reconstructing the ultrasound image.

When transmitting from the outer parts of the convex array, the geometry will cause a significant part of the wave to propagate outside the region to be imaged. Therefore, it may be advantageous to change the propagation direction of the wavefront towards the region where the image is reconstructed. Angled transmissions are obtained by moving the virtual point source to the side as illustrated in Fig. 3(b). The maximum propagation angle that can be obtained is influenced by the directivity of the subaperture elements, and any propagation angle can thus not be selected.

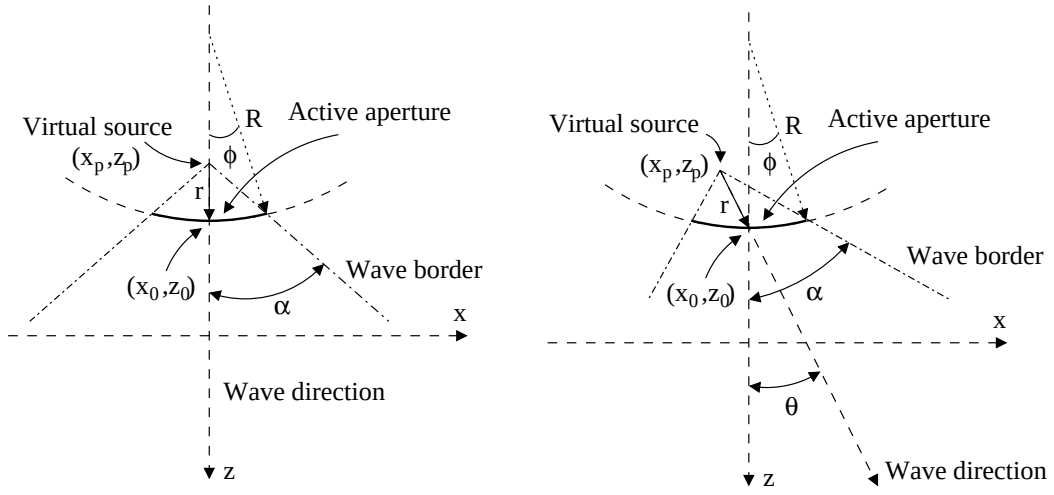

(a) Conventional application where the virtual point source is placed behind the center of the subaperture to produce a sym- metric spherical wave.

(b) Angled transmission where the virtual point source is placed such that the spherical wave propagates at an angle θ.

Fig. 3. Illustration of two methods for applying multi-element STA imaging to convex arrays.

With reference to Fig. 3(b), the location (x_p, z_p) of the virtual point source is, in general, calculated by

$$\begin{bmatrix} z_p \\ x_p \end{bmatrix} = \begin{bmatrix} z_0 - r \cdot \cos\theta \\ x_0 - r \cdot \sin\theta \end{bmatrix}, \tag{3}$$

where r is calculated by

$$r = R\left(\frac{\sin\phi - \tan\alpha\,(\cos\phi - 1)}{\tan\alpha\cos|\theta| - \sin|\theta|}\right), \tag{4}$$

and ϕ is half the angular size of the subaperture, θ is the propagation direction of the spherical wavefront, and R is the radius of the convex aperture. Note, that α and ϕ are always positive, and that the coordinate system used here moves with the subaperture across the array. Also, the subaperture elements are assumed to be point sources for simplicity. The directivity of the elements will have an influence on shape of the wavefront. The actual angular extend of the spherical wavefront will, thus, differ slightly from the specified value, which can be studied through simulations, e.g. using Field II [7], [8].

The increase in the wavefront pressure is dependent on the number of elements used in the subaperture and the chosen spherical wave extend. Karaman and coworkers [1] has shown, that for an angular extend $\alpha = 45°$ the wavefront pressure is proportional to $\sqrt{N}$, where N is the number of subaperture elements. When α decreases e.g. to $27°$, this number increases by approximately 40%. In general, however, it can be assumed, that the wavefront pressure increases with $\sqrt{N}$ relative to the single element transmission.

B. Increasing Temporal Intensity

Increasing the temporal intensity means transmitting a longer waveform. For this purpose linear frequency modulated (FM) signals have proven to be very advantageous, because they can act as both a long and a short signal simultaneously. When the linear FM signal is transmitted it has a long duration and large bandwidth, while pulse compression techniques (matched filtering) are used upon reception to compress the signal to a short duration. Thus, linear FM signals enables the possibility of transmitting more (temporal) energy, while maintaining temporal or axial resolution. The lateral resolution is not affected by the use of linear FM signals.

Several studies of applying linear FM signals in medical ultrasound imaging have been published (e.g. [9], [10], [11], [12]), which have resulted in improved penetration while maintaining spatial resolution. The gain in SNR relative to a conventional short excitation pulse is $GSNR = \frac{T_c}{T_p}$, where T_c is the duration of the linear FM signal, T_p is the duration of the pulse, and both waveforms are assumed to have a square envelope.

In a recent study [2] we explored the feasibility of combining multi-element defocusing with linear FM signals in STA imaging. The results showed that this approach produces a significant increase in SNR, leading to an image quality of STA imaging highly feasible for in-vivo application. The same approach, denoted TMS imaging[1], is applied in this study to increase the SNR of STA imaging, but with the new design considerations given above.

[1] Temporally encoded Multi-element Synthetic transmit aperture imaging

III. Experimental Setup

The purpose of this study is, as mentioned previously, to compare convex TMS imaging with conventional convex array imaging in terms of image quality. The evaluation is based on both phantom and in-vivo experiments, and the equipment and imaging modes and processing strategies are described below.

A. Equipment

The measurements were performed using the experimental multi-channel ultrasound scanning system, *RASMUS* [13]. The system has 128 individually programmable transmitters capable of sending arbitrary coded waveforms with a precision of 12 bits at 40 MHz. Sixty-four receive channels can be sampled simultaneously at 12 bits and 40 MHz, and the 2-to-1 multiplexing in the system enables acquisition of 128 channels in real-time over two transmissions. The system has 16 Gbytes of storage memory in the receivers, which enables the acquisition of several seconds of RF data. The transmission voltage is ± 50V, and RASMUS is remotely accessible and programmable through a developed Matlab/C-library interface.

The transducer used for the measurements was a commercial 5.5 MHz convex array transducer with 192 elements and λ pitch. The bandwidth of the elements is 60% relative to the center frequency, and the convex radius of the aperture is 41 mm. The height of the elements is 8 mm, and the array has a lens in the elevation dimension with a fixed focus at 40 mm. Due to the limitation of the RASMUS system, only the central 128 elements of the array were used.

B. Imaging Modes

Conventional imaging was implemented using a 64 elements transmit aperture focused at 70 mm, and each element was excited by a 1.5 cycle sinusoid weighted by a Hanning window. All 128 elements in the aperture were used on receive to record the echoes from the tissue using the multiplexors. Thus, two transmissions were performed for each beam. The number of beams are determined by the spatial Nyquist theorem, which requires that the spatial sampling rate is at least twice the highest lateral spatial frequency. This can be determined using k-space theory [14], and it is found that the angular separation $\delta\theta$ between the beams is

$$\delta\theta \leq \arcsin\left(\frac{\lambda}{\left(1+\frac{B_{rel}}{2}\right)D_{eff}}\right) \tag{5}$$

where λ is the wavelength, B_{rel} is the relative -6dB bandwidth, and D_{eff} is the size of the effective aperture, which is determined by the convolution of the transmit and receive apertures [15]. The angular size of the image is limited to approx. 26 degrees, and the number of beams in each image should then be at least 105. To ensure proper sampling, the actual number of beams is increased to 142, resulting in 284 emissions per frame.

TMS imaging was implemented using a 33 element aperture and a 20 μs tapered linear FM signal. The center of the transmit aperture was stepped one element at a time, resulting in 96 transmit positions, and all 128 elements were used on receive to record the echoes. Due to the application of the multiplexors, a total of 192 emissions was used for each frame. At each emission the wavefront was directed to propagate parallel to the z-axis. With reference to Fig. 3(b), this means that for each emission the propagation angle θ was set equal to the angle of the transmit aperture center, but with opposite sign. The beam spread angle α was decreased linearly from 40 degrees for the first emission to 30 degrees for the center emission, and then increased linearly to 40 degrees for the last emission. This was done to increase the energy transmitted into the image area, and thus increase SNR as explained previously. The linear FM signal had a center frequency of 5.5 MHz and a relative bandwidth of approx. 95%. The signal envelope was weighted by a Tukey window to reduce the ripples in its Fourier spectrum and thus attenuate the distant temporal sidelobes in the compression result[11].

C. Data Acquisition

Data acquisition was done in real-time. Initially, the RF data were stored in the internal memory of RASMUS, and subsequently transferred to a Linux cluster network for off-line processing.

To enable direct comparison of the imaging methods, the frames of both methods were interleaved, when data were recorded. This means that one frame of conventional imaging was followed directly by one frame of TMS imaging. This was especially important during the in-vivo scannings to obtain images of the exact same anatomical slice. The depth of all scans was 16 cm, resulting in an interleaved frame rate of approx. 12 frames/sec.

D. Data Processing

The processing was done off-line on a 40 cpu Linux cluster using Matlab. To reduce the number of calculations, a pixel based processing strategy was applied in both imaging methods. The method reduces the number of points to be processed along each line by utilizing the complex RF channel data. This lowers the requirement to the spatial sampling distance δR from

$$\delta R \leq \frac{\lambda}{4\left(1+\frac{B_{rel}}{2}\right)} \tag{6}$$

to

$$\delta R \leq \frac{\lambda}{2B_{rel}} \tag{7}$$

where λ is the wavelength, and B_{rel} is the relative -6 dB bandwidth. For a relative bandwidth of say 50% this results in a reduction of a factor of 6 in the number of range image points to be beamformed.

For conventional imaging, the RF channel data were bandpass filtered using a matched filter and Hilbert transformed to form the complex RF data. The beamforming scheme described above was then applied to process the required number of image points along each line using dynamic focusing and dynamic apodization keeping the F-number$= 2$. The expanding apodization function was a modified Hamming window with the edge levels raised to -12 dB.

The TMS data were filtered using a mismatch baseband filter to compress the linear FM signal and recover the range resolution. The mismatch filter was designed based on the transmitted linear FM signal by applying a Chebychev window with a relative sidelobe reduction of 70 dB[11]. This was done to reduce the temporal sidelobes below -60dB. For each emission a complete image was reconstructed using the method described in Section II. It was chosen to use the same image format as that obtained in conventional imaging to enable direct comparison of the results. Thus, 142 lines were reconstructed in each low resolution image although any image geometry and number of image points can be chosen. The pixel based processing method was applied, and dynamic apodization was applied on both the receive aperture and the synthesized transmit aperture using the same apodization window as for conventional imaging. Each image point was perfectly focused corresponding to dynamic transmit and receive focusing as explained in Section II.

When using convex array geometries it is important to take into account the relation between the image point location and the sensitivity of the aperture elements. In fact, all elements may not contribute coherent information when processing a given image point, specifically if the image point is located outside the sensitivity regions of some elements defined by their acceptance angles. For a given image line, the minimum depth $R(i)$ at which aperture element i can be enabled in the beamformer is given by

$$R(i) = R_c \frac{\sin\alpha}{\sin\left(\alpha - |\beta(i) - \theta|\right)} \tag{8}$$

where R_c is the radius of the convex aperture, α is the acceptance angle of the elements, $\beta(i)$ is the angular position of element i, and θ is the angle of the image line to be processed. The numerical signs are introduced to account for the symmetry property of the aperture.

In this study, the acceptance angle of the receive aperture elements was set to $\pm 50^\circ$, while the acceptance for the virtual sources in TMS imaging was set to $\pm 30^\circ$ for all sources, although it ranged between 40° and 30°.

1) Influence of Virtual Element Location: Another factor, which needs to be taken into account when processing the TMS data, is the location of the virtual sources. The wavefront of the limited spherical wave produced at each emission will have its origin at the virtual source and not at the zero phase center of the subaperture used to generate the wavefront. With reference to Fig. 2 this means that $\vec{r}_m$ points to the virtual source location and not to the center of the transmit aperture. Furthermore, the RF data must be adjusted to compensate for the distance between the virtual source and the first transmitting element in the subaperture for the correction to be fully implemented. This is specifically important when using convex arrays due to the geometry.

Figure 4 shows the effect of not taking into account the location of the virtual source. Obviously, neglecting the actual origin of the limited spherical wavefront results in phase errors, which defocuses the reconstruction of the point target.

IV. RESULTS

The experimental results are shown below. In all figures the conventional image is shown to the left and the TMS image is shown to the right, unless indicated otherwise.

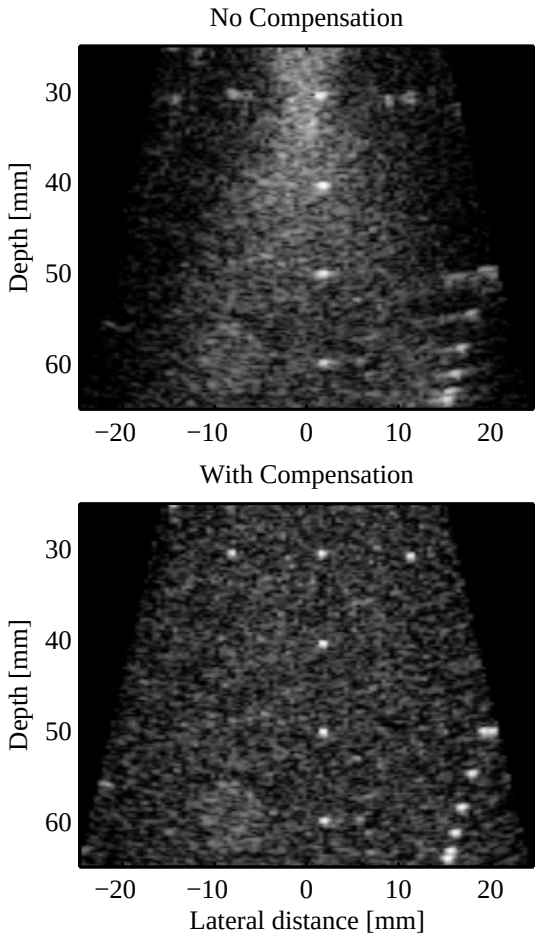

Fig. 4. Effect of compensation for the virtual source location.

A. Spatial Resolution

Spatial resolution determines the ability to differentiate point targets in the image, and it generally divided into range (axial) and angular (lateral) resolution. The range resolution is inversely proportional to the bandwidth of the transmitted waveform (after matched filtration), while the angular resolution depends on frequency, bandwidth, and aperture size.

The spatial resolution is evaluated using a tissue mimicking phantom containing thin, twisted nylon wires by calculating the -6 dB axial and lateral widths of each wire. The B-mode images are shown in Fig. 5, and the attenuation is 0.5 dB/[cm MHz]. A clear improvement in lateral resolution is observed, and the penetration depth has also been increased. The noise becomes dominant in the conventional image after approximately 100 mm, while no noise seems present in the TMS image, indicating improvement in SNR. Evaluation of SNR is revisited later in this section.

The spatial resolutions were measured for the column of wires located at lateral position -7mm. The results are plotted in Fig. 6. As expected the lateral resolution in TMS imaging is generally better than conventional imaging due to the perfect focusing of the transmit aperture. The axial resolution is, however, better for conventional imaging. This is surprising, and it indicates that the design of the linear FM signal and corresponding compression filter has not been performed carefully enough. The design thus needs to be revised. One possible and obvious reason could be, that the transducer bandwidth is not utilized fully. The source of this would be either the bandwidth of the transmitted linear FM signal or the bandwidth of the compression filter (or both), which may be less than the transducer bandwidth.

B. Contrast Resolution

The contrast resolution is a measure of the detectability of small and low scattering structures from the background texture (speckle) in the image. It is generally dependent on pulse-echo beam characteristics, such as the ratio of mainlobe to sidelobes energy and spatial resolution, but it is also affected by the SNR.

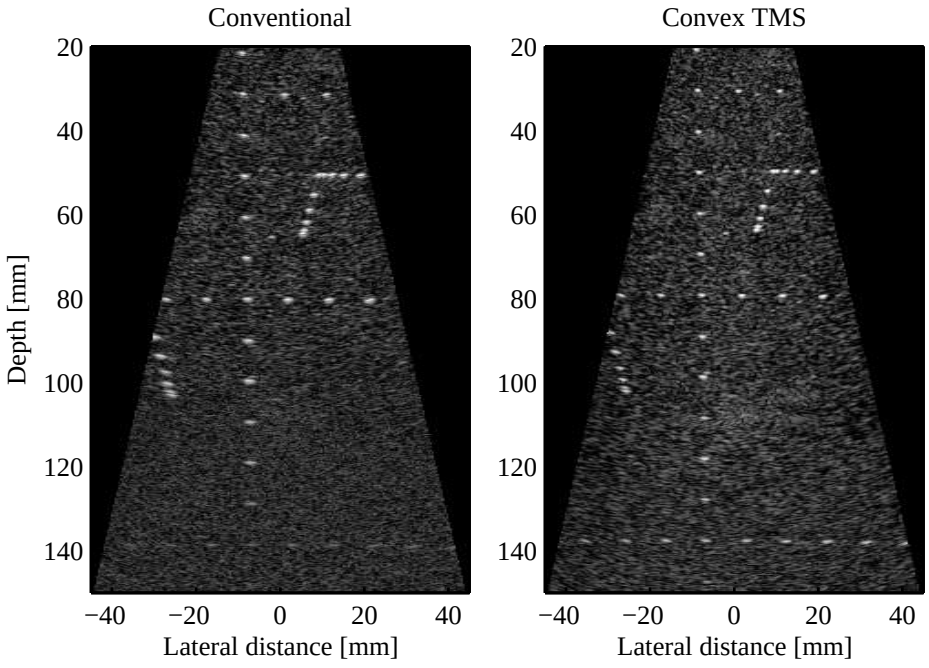

Fig. 5. Images of a multi target tissue mimicking phantom containing twisted nylon wires with 0.5 dB/[cm MHz] attenuation. A clear improvement in penetration depth and speckle size is observed.

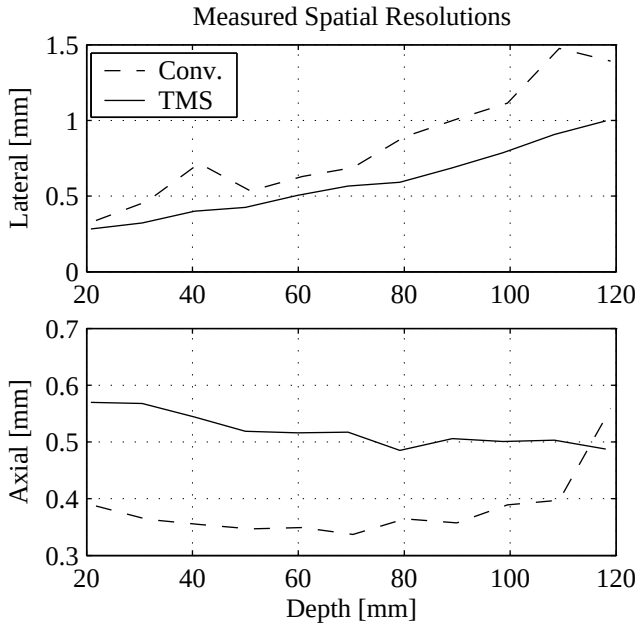

Fig. 6. Lateral (top) and axial (bottom) resolution measured as the -6 dB widths of the wires in Fig. 5 positioned at lateral distance -7mm.

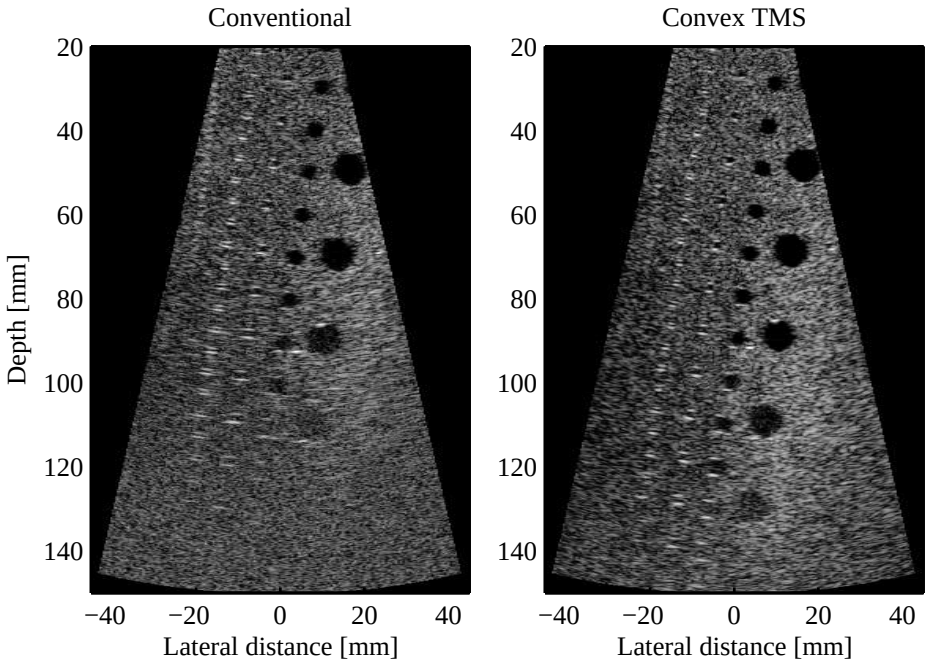

Fig. 7. Images of a tissue mimicking phantom containing anechoic cylinders placed in angled columns with diameters of $0.5, 1, 2, 4, 8$ mm from left to right.

The contrast resolution was characterized by scanning a tissue mimicking phantom containing anechoic cysts of different sizes. In the resulting image the interior of these cysts should ideally be black, i.e. no scatter energy should be present. By calculating the intensity inside these cysts relative to the intensity of the surrounding speckle, a measure of the detectability is thus obtained. Based on this, the contrast resolution CR is calculated by

$$CR = 1 - \frac{I_c}{I_s} \tag{9}$$

where I_c is the intensity inside the cysts, and I_s is the intensity of the surrounding speckle within a region of equal size.

In Fig. 7 the images of a tissue mimicking phantom containing 5 columns of anechoic cylinders with diameters of $0.5, 1, 2, 4, 8$ mm (from left to right) are shown. A clear improvement in contrast resolution is observed, especially at depths beyond 80 mm, and an increase in penetration of approximately 2 cm has been obtained. Fig. 8 shows an expanded view of the lower part of Fig. 7 to further illustrate the improvement. The cysts at 105 mm are barely visible in the conventional image, but easily detected in the TMS image.

Tables I and II presents the calculated contrast resolutions for the 4 mm and 8 mm cysts. These numbers support the visual findings in Figs. 7 and 8, and they show that the contrast resolution of TMS imaging improves significantly after 80 mm. In particular, the difference between the 4 mm cysts at 100 mm is approximately 33%, which demonstrates the advantage of dynamic transmit focusing obtained in TMS imaging.

C. Signal-to-Noise Ratio

The change in SNR with depth can be used to measure the penetration depth. The SNR is calculated from the beamformed data by taking the ratio of the signal energy and the noise power spectral density assuming that matched filtering of the RF data has been utilized. The SNR is measured in two ways; either the point SNR, which can be obtained e.g. using wire targets, or the speckle SNR obtained from pure speckle generating targets.

Here, the speckle SNR was measured by scanning a homogeneous phantom solely containing randomly distributed scatterers. To separate the signal and noise components, 25 frames were acquired. By averaging these images a noise free image was obtained, which represented the pure signal image. This image was subtracted from the original images producing 25 new images containing only noise. The final noise power image was then obtained by taking the mean, square value of these noise images. The SNR is then calculated by the ratio of the squared signal image and the noise power image, producing an image of the SNR.

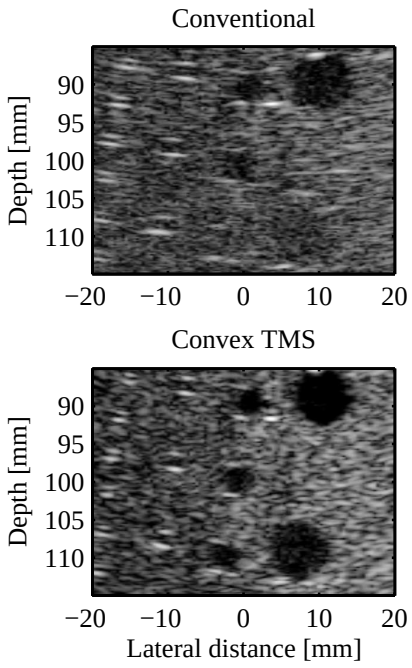

Fig. 8. Expanded (1:1) view of a selected area in Fig. 7 to illustrate the improvement in contrast resolution.

Depth	Conventional	TMS	Improvement in %
40 mm	0.95	0.99	3.3
60 mm	0.96	0.99	2.6
80 mm	0.90	0.99	9.1
100 mm	0.69	0.92	32.8
120 mm	-	0.82	-

TABLE I

CALCULATED CONTRAST RESOLUTIONS FOR THE 4 MM CYSTS SHOWN IN FIG. 7.

Depth	Conventional	TMS	Improvement in %
50 mm	0.99	1.00	0.9
70 mm	0.97	1.00	2.6
90 mm	0.90	0.98	8.7
110 mm	0.67	0.95	42.7
130 mm	-	0.79	-

TABLE II

CALCULATED CONTRAST RESOLUTIONS FOR THE 8 MM CYSTS SHOWN IN FIG. 7.

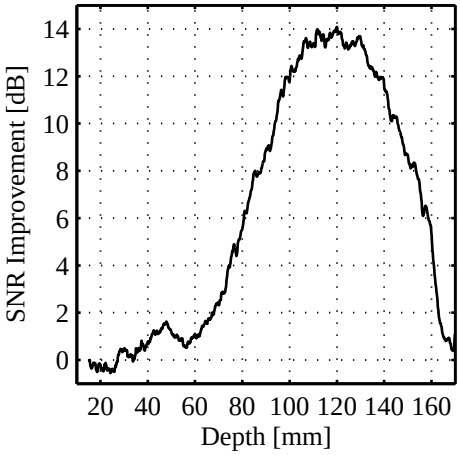

Fig. 9. The calculated improvement in speckle SNR from a homogeneous phantom containing only randomly distributed scatterers. The SNR of TMS imaging relative to conventional imaging improves rapidly after 60 mm and peaks at 120 mm with a 14 dB increase in SNR. The attenuation was 0.5 dB/[MHz,cm].

Mathematically, the SNR at image point $\vec{r}_p$ was calculated by

$$SNR(\vec{r}_p) = \frac{\left[\frac{1}{N}\sum_{n=1}^{N} S_n(\vec{r}_p)\right]^2}{\frac{1}{N}\sum_{n=1}^{N}\left[S_n(\vec{r}_p) - \bar{S}(\vec{r}_p)\right]^2} \tag{10}$$

where N is the number of images, $S_n(\vec{r}_p)$ is image n, and $\bar{S}(\vec{r}_p)$ is the mean image.

The improvement in SNR of TMS imaging relative to conventional imaging is displayed in Fig. 9. The result is plotted as the average SNR improvement for each depth, and the curve has been filtered using a lowpass filter to produce a more smooth appearance. It is noted that the SNR of TMS imaging improves rapidly after the geometric focal point of conventional imaging at 60 mm, reaching a maximum of 14 dB at 120 mm. At 130 mm the SNR starts to decay and reaches 0 dB at approximately 170 mm.

D. Acoustic Output

Prior to conducting the in-vivo measurements the acoustic outputs of the ultrasound scanner were measured for the two imaging modes. The measured intensities need to satisfy preamendments upper limits regulated by the United States Food and Drug Administration (FDA) [16], which have been introduced as safety guides to avoid damage to the tissue and pain to the patient. These limits concern the mechanical index, MI$\leq$ 1.9, the derated spatial-peak-temporal-average intensity, $\mathrm{I_{spta.3}} \leq 720\,\mathrm{mW/cm^2}$, and the derated spatial-peak-pulse-average intensity $\mathrm{I_{sppa.3}} \leq 190\,\mathrm{W/cm^2}$ [16].

The acoustic outputs were measured in a water tank using a high precision 3-dimensional positioning system and a miniature PVDF hydrophone (Force Technology, Denmark, model: MH28-4) by following the guidelines given by the American Institute of Ultrasound in Medicine (AIUM) [17]. The levels obtained are listed in Table III. These values are considerably lower than the FDA limits and in-vivo scanning is therefore safe using the present imaging modes.

The calculation of $\mathrm{I_{spta.3}}$ was based on the interleaved implementation of the methods with a scan repetition frequency (frame rate) of 12 frames/sec.

E. In-Vivo Image Quality

Two in-vivo acquisition sequences each containing 30 frames (2.5 sec. scan duration) at abdominal locations on two healthy male volunteers were scanned by an experienced sonographer to evaluate the feasibility of TMS imaging in-vivo. At each scanning the patient was asked to hold his breath to remove respiratory motion and improve the anatomic visibility. No other motion compensation was applied.

The images in Fig. 10 are two snapshots of the processed movie sequence from the first scanning. They show transverse sections of the right liver lobe containing hepatic vein branches, cross sections of portal vein branches,

	Conventional	TMS	Unit
$I_{sppa.3}$	26.28	7.93	W/cm^2
$I_{spta.3}$	3.66	72.94	mW/cm^2
MI	0.41	0.27	-

TABLE III

ULTRASOUND INTENSITIES AND MECHANICAL INDEX (MI) USED IN CONVENTIONAL AND TMS IMAGING RESPECTIVELY. THE VALUES ARE DERATED IN-SITU VALUES,AND THEY HAVE BEEN MEASURED ACCORDING TO THE GUIDELINES GIVEN BY AIUM.

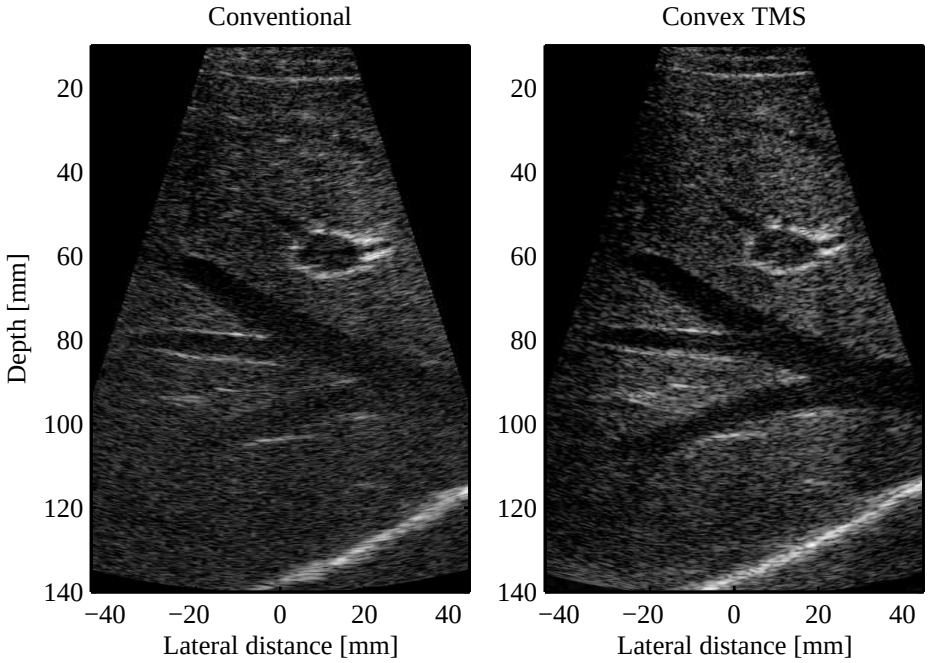

Fig. 10. The images show transverse sections of the right liver lobe containing hepatic vein branches, cross sections of portal vein branches, and the diaphragm in the lower part of the images.

and the diaphragm in the lower part of the images. Note, the improvement in vessel contrast in the TMS image, which is obtained due to the improvements in both contrast resolution and spatial resolution.

The images in Fig. 11 are snapshots from the second scanning. These show a longitudinal section of the right liver lobe showing cross sections of hepatic vein branches, longitudinal section of a portal vein branch (upper left part), the kidney, and the diaphragm at the bottom. The improvement in spatial resolution is clearly observable, and the boarder of the kidney and its inside structures are better defined.

The movie sequences were used to evaluate real-time feasibility. These included tissue motion from heart beating, resulting in organ and vessel wall motion. No motion artifacts were observed, which indicates that tissue motion is not a significant problem in abdominal STA imaging. Furthermore, it was noticed, that when breathing motion was removed the motion of the structures in TMS imaging was more independent. This was observed especially for the kidney, which appeared as an independent organ rather than bounded to the surrounding tissue as in conventional imaging. In other words, the motion in TMS imaging is more realistic, because TMS imaging takes a snapshot image of the tissue.

V. DISCUSSION

TMS imaging holds several advantages over conventional imaging, such as higher frame rates, better focusing, and continuous blood flow imaging. The frame rate of TMS imaging is directly proportional to the number of emissions applied to build the high resolution image, and it is therefore independent of the image format, neglecting real-time implementation issues. Thus, the frame rate can be increased by simply reducing the number of emissions, at the expense of SNR and to some extend presence of grating lobes depending on the spacing between the virtual

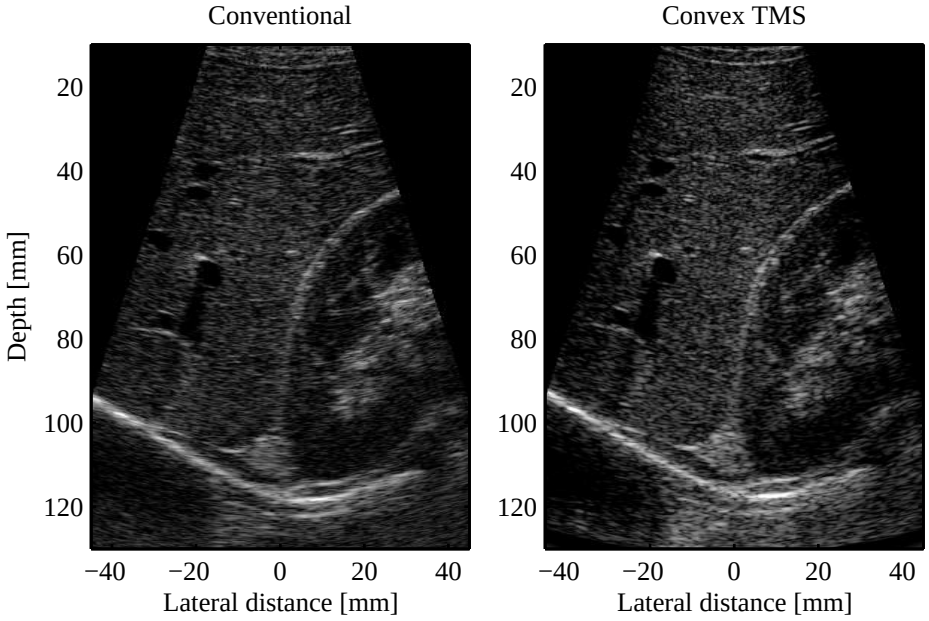

Fig. 11. Longitudinal section of right liver lobe showing cross sections of hepatic vein branches, longitudinal section of a portal vein branch (upper left part), the kidney, and diaphragm at the bottom.

sources. This could be beneficial e.g. when imaging a region with significant tissue motion or for 3D imaging. As explained in Section II both the transmit and receive apertures are focused in the best possible manner at every image point, corresponding to dynamic transmit and receive focusing in a conventional imaging system. Synthesizing the transmit aperture provides the freedom of better control of the transmit beam pattern using dynamic apodization algorithms, which is beneficial in terms of improving the contrast resolution and more generally the image appearance. Recently, it has also been shown, that STA imaging can be applied to perform accurate blood flow imaging continuously at all flow angles including pure transverse flow [18], [19], [20].

It may seem surprising that the in-vivo images and movie sequences did not show any visible effects of tissue motion on the TMS image quality, especially since the method is more susceptible to motion as explained previously. Several authors have reported that axial tissue motion is the dominant factor in image degradation [21], [22], due to the much higher spatial frequency in this dimension. As a worst case scenario, to avoid incoherent summation of the low resolution images, the axial tissue displacement should be less than $\lambda/2$ over the acquisition of a whole frame. The tissue velocity v_t should therefore be limited to

$$v_t < \frac{c}{2}\frac{f_{prf}}{f_0}\frac{1}{M} \tag{11}$$

where c is the speed of sound, f_{prf} is the pulse repetition frequency, f_0 is the center frequency, and M is the number of transmissions. Based on the imaging parameters used for this study and a scan depth of 16 cm, the demand on v_t becomes

$$v_t < \frac{1540}{2}\frac{\frac{1540}{2\cdot 0.16}}{5.5\cdot 10^6}\frac{1}{96} \simeq 7\mathrm{mm/sec} \tag{12}$$

Schlaikjer and coworkers [23] have reported abdominal tissue velocities of up to 10 mm/sec over a cardiac cycle around the Hepatic vein. Considering this estimate as the average abdominal tissue velocity, the TMS images should have shown some motion artifacts. There are however several reasons why this is not the case. First of all, the above calculation is valid only for a narrow band pulse, which means that complete cancellation will only occur at the center frequency. The system is, however, highly broadband to obtain good range resolution, and thus a specific tissue velocity will only affect a small frequency range. Secondly and more importantly, the calculation was based solely on axial motion, which rarely occurs in-vivo. Tissue motion is commonly 3-dimensional, and this means that it is the 3-dimensional characteristics of the point spread function, which determines the effects. A more detailed analysis of the influence of tissue motion and methods for compensation is out of the scope of this study, but it is the topic of ongoing research [24], [25]. Based on the results presented here, it is concluded that tissue motion does not objectively seem to have a significant influence on the image quality of abdominal TMS imaging.

VI. Conclusion

This paper presented a feasibility study of performing STA imaging using convex array transducers. STA imaging was implemented using a previously published method called TMS imaging to increase the SNR to a clinically satisfactory level. This method was described in details and some essential design considerations introduced by the more complex geometry of the convex aperture was presented and solved.

An experimental evaluation of convex TMS imaging was performed through both phantom and in-vivo measurements using the RASMUS research scanner, and the results were compared to a conventional application of the convex array in a commercial scanner using focused beams.

The phantom results showed clear improvements in image quality in terms of both spatial resolution, contrast resolution and signal-to-noise ratio (SNR). In particular, the contrast resolution was improved for TMS imaging by more than 30% after the focal depth of conventional imaging, and an increase of up to 14 dB in SNR was obtained, which translated into better image contrast and a 2 cm increase in penetration depth approximately.

In-vivo movie sequences with a 2.5 sec. duration of the abdomen and right kidney were acquired and evaluated. Image snapshots of these movies were presented and they showed the same improvements obtained in the phantom measurements, thus supporting these results. No visual tissue motion artifacts were present in the images, and this observation was also supported by the evaluation of the movie clips. Furthermore, it was noticed, that the motion of the structures in the TMS imaging sequences due to heart beating and vessel pulsation was more independent of each other. In particular, the kidney seemed to be moving independent of the surrounding tissue, which was noticed especially around its borders.

In conclusion, this paper has shown that application of TMS imaging with convex array transducers is possible and in-vivo TMS imaging seems feasible.

Acknowledgments

This work was supported by grants 9700883 and 9700563 from the Danish Science Foundation, by Ph.D. grant 11-3160-55173 from the Technical University of Denmark, and by B-K Medical A/S, Herlev, Denmark.

References

[1] M. Karaman, P. C. Li, and M. O'Donnell, "Synthetic aperture imaging for small scale systems," *IEEE Trans. Ultrason., Ferroelec., Freq. Contr.*, vol. 42, pp. 429–442, 1995.

[2] K. L. Gammelmark and J. A. Jensen, "Multielement synthetic transmit aperture imaging using temporal encoding," *IEEE Trans. Med. Imag.*, vol. 22, no. 4, pp. 552–563, 2003.

[3] J. T. Ylitalo, "Synthetic aperture ultrasound imaging using a convex array," in *Proc. IEEE Ultrason. Symp.*, 1995, pp. 1337–1340.

[4] D. W. Prine, "Synthetic aperture ultrasonic imaging," in *Proceedings of the Engineering Applications of Holography Symposium*, 1972, pp. 287–294.

[5] C. B. Burckhardt, P-A. Grandchamp, and H. Hoffmann, "An experimental 2 MHz synthetic aperture sonar system intended for medical use," *IEEE Trans. Son. Ultrason.*, vol. 21, no. 1, pp. 1–6, January 1974.

[6] M. O'Donnell and L. J. Thomas, "Efficient synthetic aperture imaging from a circular aperture with possible application to catheter-based imaging," *IEEE Trans. Ultrason., Ferroelec., Freq. Contr.*, vol. 39, pp. 366–380, 1992.

[7] J. A. Jensen and N. B. Svendsen, "Calculation of pressure fields from arbitrarily shaped, apodized, and excited ultrasound transducers," *IEEE Trans. Ultrason., Ferroelec., Freq. Contr.*, vol. 39, pp. 262–267, 1992.

[8] J. A. Jensen, "Field: A program for simulating ultrasound systems," *Med. Biol. Eng. Comp.*, vol. 10th Nordic-Baltic Conference on Biomedical Imaging, Vol. 4, Supplement 1, Part 1, pp. 351–353, 1996b.

[9] Y. Takeuchi, "An investigation of a spread energy method for medical ultrasound systems - part one: theory and investigations.," *Ultrasonics*, pp. 175–182, 1979.

[10] M. O'Donnell, "Coded excitation system for improving the penetration of real-time phased-array imaging systems," *IEEE Trans. Ultrason., Ferroelec., Freq. Contr.*, vol. 39, pp. 341–351, 1992.

[11] T. X. Misaridis and J. A. Jensen, "An effective coded excitation scheme based on a predistorted FM signal and an optimized digital filter," in *Proc. IEEE Ultrason. Symp.*, 1999, vol. 2, pp. 1589–1593.

[12] M. H. Pedersen, T. X. Misaridis, and J. A. Jensen, "Clinical evaluation of chirp-coded excitation in medical ultrasound," *Ultrasound Med. Biol.*, vol. 29, no. 6, pp. 895–905, 2003.

[13] J. A. Jensen, O. Holm, L. J. Jensen, H. Bendsen, H. M. Pedersen, K. Salomonsen, J. Hansen, and S. Nikolov, "Experimental ultrasound system for real-time synthetic imaging," in *Proc. IEEE Ultrason. Symp.*, 1999, vol. 2, pp. 1595–1599.

[14] W. F. Walker and G. E. Trahey, "The application of k-space in pulse echo ultrasound," *IEEE Trans. Ultrason., Ferroelec., Freq. Contr.*, vol. 45, pp. 541–558, 1998.

[15] G. R. Lockwood and F.S. Foster, "Design of sparse array imaging systems," in *Proc. IEEE Ultrason. Symp.*, 1995, pp. 1237–1243.

[16] FDA, "Information for manufacturers seeking marketing clearance of diagnostic ultrasound systems and transducers," Tech. Rep., Center for Devices and Radiological Health, United States Food and Drug Administration, 1997.

[17] AIUM, "Acoustic output measurement standard for diagnostic ultrasound equipment," Tech. Rep., American Institute of Ultrasound in Medicine & National Electrical Manufacturers Association, May 1998.

[18] S. I. Nikolov and J. A. Jensen, "Velocity estimation using synthetic aperture imaging," in *Proc. IEEE Ultrason. Symp.*, 2001, pp. 1409–1412.

[19] J. A. Jensen and S. I. Nikolov, "Transverse flow imaging using synthetic aperture directional beamforming," in *Proc. IEEE Ultrason. Symp.*, 2002, pp. 1488–1492.

[20] S. I. Nikolov and J. A. Jensen, "In-vivo synthetic aperture flow imaging in medical ultrasound," *IEEE Trans. Ultrason., Ferroelec., Freq. Contr.*, pp. 848–856, 2003.

[21] G. E. Trahey and L. F. Nock, "Synthetic receive aperture imaging with phase correction for motion and for tissue inhomogenities - part II: effects of and correction for motion," *IEEE Trans. Ultrason., Ferroelec., Freq. Contr.*, vol. 39, pp. 496–501, 1992.

[22] C. R. Hazard and G. R. Lockwood, "Theoretical assessment of a synthetic aperture beamformer for real-time 3-D imaging," *IEEE Trans. Ultrason., Ferroelec., Freq. Contr.*, vol. 46, pp. 972–980, 1999.
[23] M. Schlaikjer, S. Torp-Pedersen, J. A. Jensen, and P. F. Stetson, "Tissue motion in blood velocity estimation and its simulation," in *Proc. IEEE Ultrason. Symp.*, 1998, pp. 1495–1499.
[24] K. S. Kim, J. S. Hwang, J. S. Jeong, and T. K. Song, "An efficient motion estimation and compensation method for ultrasound synthetic aperture imaging," *Ultrason. Imaging*, vol. 24, pp. 91–99, 2002.
[25] K. L. Gammelmark and J. A. Jensen, "Duplex synthetic aperture imaging with tissue motion compensation," in *Proc. IEEE Ultrason. Symp.*, 2003, pp. 1569–1573.

A.3 In-Vivo Evaluation of Convex Array Synthetic Aperture Imaging

This article was submitted to *Ultrasound in Medicine and Biology* in July 2004.

In-vivo Evaluation of Convex Array Synthetic Aperture Imaging

Morten H. Pedersen, Kim L. Gammelmark and Jørgen A. Jensen
Center for Fast Ultrasound Imaging, Ørsted•DTU, Build. 348,
Technical University of Denmark, DK-2800 Kgs. Lyngby, Denmark

September 9, 2004

Abstract

This paper presents an in-vivo study of STA imaging in comparison to conventional imaging, evaluating whether STA imaging is feasible in-vivo, and whether the image quality obtained is comparable to traditional scanned imaging in terms of penetration depth, spatial resolution, contrast resolution, and artifacts.

Acquisition was performed using our research scanner RASMUS and a 5.5 MHz convex array transducer. STA imaging was acquired using circular wave emulation by 33-element subapertures and a 20 μs linear FM signal as excitation pulse. For conventional imaging a 64 element aperture was used in transmit and receive with a 1.5 cycle sinusoid excitation pulse.

Conventional and STA images were acquired interleaved ensuring that the exact same anatomical location was scanned. Image sequences were recorded in real-time and processed off-line. Seven male volunteers were scanned abdominally, and resulting images were compared by three medical doctors using randomized blinded presentation. Penetration and image quality were scored and evaluated statistically. Results showed slightly but significantly (0.48 cm, p=0.008) increased penetration using STA. Image quality was also highly significantly ($P<0.001$) increased. Results show that in-vivo ultrasound imaging using STA is feasible for abdominal imaging without severe motion artifacts.

Introduction

Conventional ultrasound scanning emits focused beams in one direction at a time, sequentially building up an image of consecutive scan lines. This is a technically intuitive and easy implementable solution to ultrasound imaging, imposed by the limits of analog electronics at the birth of medical ultrasound in the 1950's. The emergence of array element transducers has introduced dynamic receive focusing, which yields an optimal lateral focus at all depths in the image for this method. Synthetic transmit aperture (STA) imaging, a technique originally adapted from radar, offers the same optimal resolution at all depths in transmit as well as receive, with the potential of increasing the overall spatial and contrast resolution.

Simulation and phantom studies of STA imaging have been published with good results (Karaman et al. 1995; Gammelmark and Jensen 2002, 2003b). The viability of the technique in-vivo is, however, yet to be proven, and doubts have been uttered, stating that tissue motion will probably make the coherent summation of temporally separated signals break down.

In this study an implementation of STA imaging using multi element defocused circular wave emissions and linearly frequency modulated signals (Gammelmark and Jensen 2002) will be tested in a clinical setting on healthy volunteers. The method is investigated for abdominal imaging using a convex array transducer, and it is compared to conventional convex array imaging measured under the exact same conditions at the same time and anatomical location. This is ensured by our experimental ultrasound scanning system, which can produce simultaneous ultrasound acquisitions of the exact same location using two or more different techniques. Images will be rated by blinded evaluation by ultrasound specialists (medical doctors).

The following two null hypotheses are tested:

1. STA imaging has no effect on penetration depth.
2. STA imaging has no effect on image quality.

Additionally, this paper gives a short technical introduction to STA imaging.

Synthetic Transmit Aperture Imaging

The traditional ultrasound scanning method transmits sound in one direction at a time, hence the term scanning. The signals received by multiple receive elements of the transducer are used to reconstruct part of an image corresponding to the scan line. In the following, linear arrays will be used for simplicity. Since each transducer element transmits a more or less circular wave in the image plane, a line shaped emission field is approximated by delaying the emissions from each element individually, so that the wavefronts arrive simultaneously at a desired focal point. Hereby the energy is focused in the focal point, and also, although to lesser degree, along the scan line as shown in Fig. 1(a), where the lateral elements emit earlier than central elements. Assuming a constant sound speed, the travel time between points

is given as the geometric distance divided by the speed of sound. To compensate for a longer distance a delay is imposed on elements closer to the focal point. The emission delays (d_T) of each transmit element (T) located at x_T is:

$$d_T(n) = \frac{z_F - \sqrt{z_F^2 + (x_T(n) - x_F)^2}}{c}, \qquad (1)$$

where (x_F, z_F) is the position of the focal point, c is speed of sound, and x_T is the lateral position of the transmit elements (Fig. 2). To reconstruct the line in the image, it is assumed, that energy is transmitted along the scan line only (the line $\overrightarrow{LF}$ in Fig. 3) defined by the center of emission and the focal point. To reconstruct an image line, signals from all receive elements are delayed and summed dynamically during reception, i.e. the focal point moves along the scan line during reception, as shown in Fig. 1(b). The focused scan line signal $I_L(z)$ as a function of depth (z) is:

$$I_L(x_F, z) = \sum_{n=1}^{N_R} s_n \left(\frac{|\overrightarrow{LP}| + |\overrightarrow{PR_n}|}{c} \right), \qquad (2)$$

where

$$|\overrightarrow{LP}| = z$$
$$|\overrightarrow{PR_n}| = \sqrt{(x_F - x_R(n))^2 + z^2}$$

and $s_n(t)$ is the signal received by element no. n, N_R is the number of receive elements, x_F is the lateral position of the focal point, P is the image point (x_F, z_P), and $x_R(n)$ is the lateral position of the element (Fig. 3). To achieve a full image with N_L lines, one must perform N_L emissions.

In synthetic transmit aperture imaging a different approach is taken. Here a single element is used at each transmission to generate a circular (i.e. defocused) wave in the image plane, which ideally spreads out in all directions. This way a single well-defined wavefront propagates through the medium. To reconstruct the image point $P = I(x_P, z_P)$, the signal value $s_n(t)$ is taken at the time:

$$t = \frac{|\overrightarrow{TP}| + |\overrightarrow{PR}|}{c}, \qquad (3)$$

where

$$|\overrightarrow{TP}| = \sqrt{(x - x_T)^2 + z^2}$$
$$|\overrightarrow{PR}| = \sqrt{(x - x_R)^2 + z^2}.$$

The signal at the time t is the integral of the scattering signal along an ellipse defined by the transmit element located at $T = (x_T, 0)$ and the receive element at $R = (x_R, 0)$ as focal points, and $c \cdot t$ as major axis (see Fig. 4). By combining the signals from multiple receive elements, intersecting ellipses extracts the information from a single point (Fig. 5). In this way a full image can be obtained from a single transmission event:

$$I(x, z) = \sum_{n=1}^{N_R} s_n \left(\frac{|\overrightarrow{TP_{x,z}}| + |\overrightarrow{P_{x,z}R_n}|}{c} \right), \qquad (4)$$

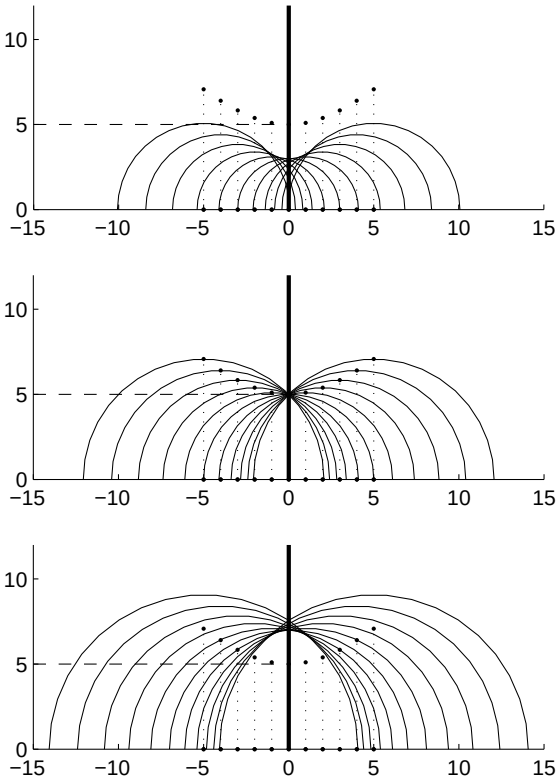

(a) Transmit focus in conventional system, where the geometrical circular wavefronts from each element only intersects perfectly in the transmit focal point (dashed line at depth 5). Three different points in time are shown.

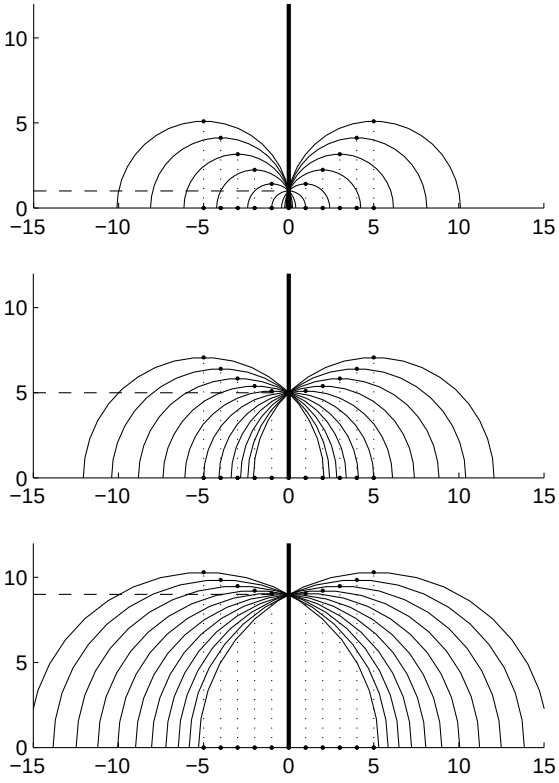

(b) In dynamic receive focus, the signal delays used for summing, are adjusted during reception, so perfect receive focusing is achieved along the scan line, i.e. the circles, that represents the positions contributing to the received signal at a given time instance, intersect perfectly

Figure 1: Conventional transmit and receive focus.

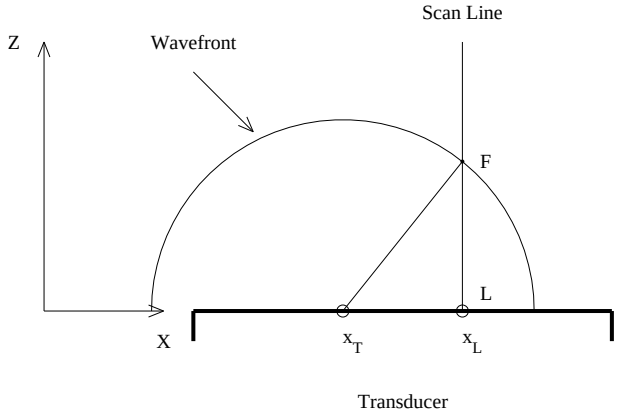

Figure 2: The geometry of transmission from a single element T located at $(x_T, 0)$. The focal point F is located at $(x_F, z_F))$.

compared to the single line of an image one obtains for each transmission in conventional scanning. By adding the result of several (N_T) transmissions with different transmission elements:

$$I(x,z) = \sum_{m=1}^{N_t} \sum_{n=1}^{N_r} s_{n,m} \left(\frac{|\overrightarrow{T_m P_{x,z}}| + |\overrightarrow{P_{x,z} R_n}|}{c} \right), \quad (5)$$

one obtains even better focusing yielding a higher resolution. In Fig. 6 the difference between focusing in a conventional system and STA is shown using three (for simplicity) transmit and receive elements.

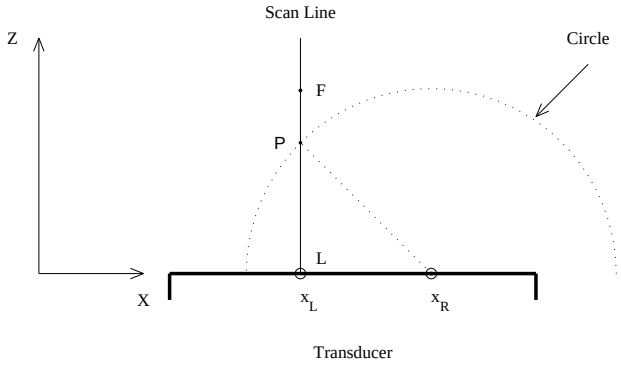

Figure 3: Assumed scan line parallel with Z-axis defined by focal point (F) used for reconstructing image in conventional scanning.

To perform the acquisition, the scattered echoes are recorded using all elements in the receive aperture without any beam formation during reception. The transmit-receive procedure is repeated until all elements in the transmit aperture have been used for transmission. Calculation of image points are independent from each other, which enables parallel processing. In practice, the image reconstruction process is performed sequentially. After each emission event a complete ultrasound image is formed by focusing the receive aperture at all image points based on the transmit element location (Fig. 7). The produced image is called a low (lateral) resolution image, because the image is created using a single transmit element. This is repeated after each emission, and the individual low resolution images are finally summed to produce the displayed high resolution image. In this way, the transmit aperture is synthesized over several transmissions, and the ultrasound image is build up sequentially. Hence the term synthetic aperture imaging.

Since a single element is applied at each transmission, the emitted energy is low, which results in a low signal-to-noise ratio (SNR) and, thus, low penetration. To increase the SNR a recent study of STA imaging (Gammelmark and Jensen

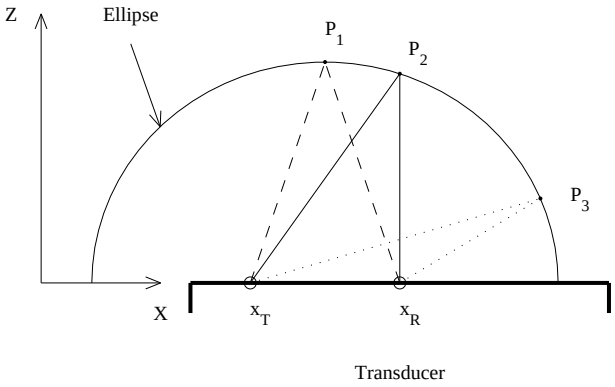

Figure 4: Ellipse with major axis equalling $c \cdot t$ for a given transmission and reception element, that describes the source of the scattering information summed in the received signal at time t.

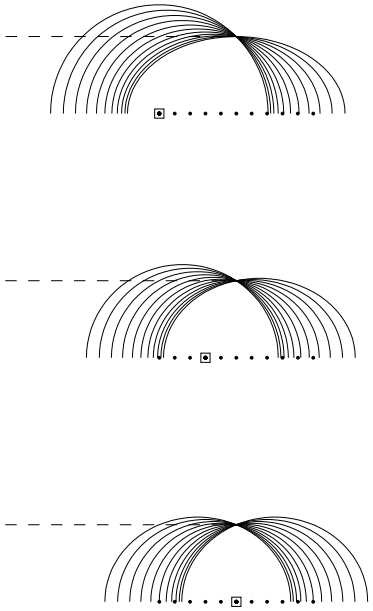

Figure 5: Focusing is obtained by intersecting the ellipses of for each receive element at the point of interest. Eleven receive elements (red dots) are used with a single transmission element (red). Three different figures, with different transmission elements are shown.

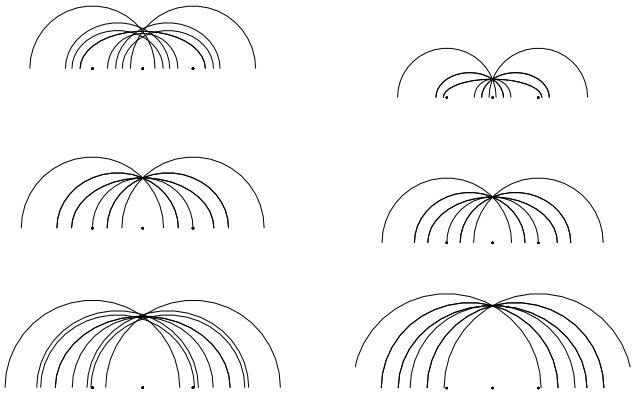

(a) In a conventional system the ellipses for each transmit-receive element pair only intersect perfectly in the transmit focal point.

(b) In an STA system, the ellipses intersect perfectly in all points in the image.

Figure 6: Intersection of geometrical representation of signal samples in conventional and STA imaging in a system with three transmit and receive elements

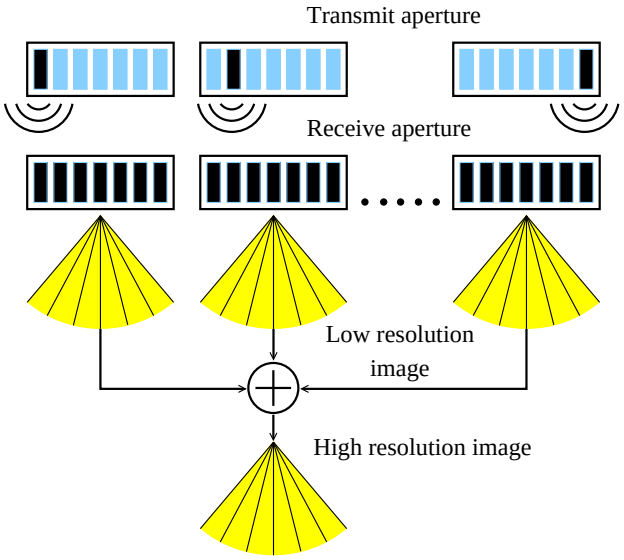

Figure 7: Schematic illustration of STA imaging. At each emission event a spherical wave is transmitted from a single element, and the echoes are recorded by all receive aperture elements. The echoes from each emission are focused at each pixel in the image producing low resolution images, and these images are finally summed coherently to form the displayed high resolution image.

2003b) has shown, that the combination of multi-element subapertures, used at each emission to increase the intensity of the emitted spherical wave (O'Donnell and Thomas 1992; Karaman et al. 1995), with linear FM signals (Misaridis and Jensen 1999) can be used to increase the SNR of STA imaging beyond that of conventional images.

Material and Methods

Seven healthy male volunteers were scanned in supine position by an experienced sonographer. Mean age was 32.5 (from 26.5 to 43.5) years, mean weight 82 (from 70 to 96) kg and mean body mass index (BMI) was 25.2 (23.7 to 28.1).

Equipment

The measurements were performed using the experimental multi-channel ultrasound scanning system RASMUS (Jensen et al. 1999). The system has 128 individually programmable transmitters capable of sending arbitrary coded waveforms with a precision of 12 bits at 40 MHz. Sixty-four receive channels can be sampled simultaneously at 12 bits and 40 MHz, and the 2-to-1 multiplexing in the system enables acquisition of 128 channels in real-time over two transmissions. The system has 16 Gbytes of storage memory in the receivers, which enables the acquisition of several seconds of real-time RF data, and it is remotely accessible and programmable through a developed Matlab/C-library interface. The front-end in RASMUS is build by slightly modifying a commercial front-end. The analog electronics in the system is, thus, comparable to a commercially available ultrasound scanner.

The transducer used for this study was a commercial 5.5 MHz convex array transducer with 192 elements and λ pitch. The bandwidth of the elements is 60% relative to the center frequency, and the convex radius of the aperture is 41 mm. The height of the elements is 8 mm, and the array has a lens in the elevation dimension with a fixed focus at 40 mm. Due to the limitation of the RASMUS system, only the central 128 elements of the array are accessible.

Imaging Setup

For conventional imaging a 64 elements transmit and receive aperture was used with a fixed focus at 70 mm. A 1.5 cycle sinusoid with a center frequency of 5.5 MHz and Hanning apodization was used as excitation. The number of lines in each frame was determined by the spatial Nyquist theorem. For the present imaging setup and the above convex array geometry, this resulted in 195 lines per frame.

For STA imaging a 33 element subaperture was used to emulate the high power spherical wave transmission, and 64 elements equally spaced over the full 128 element aperture were used on receive. The transmit aperture was moved one element after each transmission producing a total of 96 emissions for each frame. A 20 μs linear FM signal with a center frequency of 5.5 MHz and 90% bandwidth was used as excitation signal. The FM signal had been weighted with a Tukey window to reduce the temporal sidelobes (Misaridis and Jensen 1999). As explained previously, this combination was used to increase the SNR of STA imaging.

The imaging modes were interleaved such that one frame from one mode followed directly after the other. Hereby,

images from exactly the same in-vivo view were obtained, enabling direct comparison of the methods. The depth of each scan was 13-16 cm, and the interleaved frame rate was set to 12 frames/sec, i.e. 12 conventional and 12 synthetic frames per second.

The excitation voltage was the same for both conventional and STA imaging (± 50 V), and it was not changed during acquisition.

Acoustic Output

Prior to conducting in-vivo experiments, the acoustic outputs of the ultrasound scanner were measured for the imaging modes under investigation. The measured intensities need to satisfy preamendments upper limits regulated by the United States Food and Drug Administration (FDA 1997), which have been introduced as safety guides to avoid damage to the tissue and pain to the patient. These limits concern the mechanical index, MI$\leq$ 1.9, the derated spatial-peak-temporal-average intensity, $\mathrm{I_{sppa.3}} \leq 190\,\mathrm{W/cm^2}$, and the derated spatial-peak-pulse-average intensity $\mathrm{I_{spta.3}} \leq 720\,\mathrm{mW/cm^2}$ (FDA 1997).

The acoustic outputs were measured in a water tank using a high precision 3-dimensional position system and a miniature PVDF hydrophone (Force Technology, Denmark, model: MH28-4) by following the guidelines given by the American Institute of Ultrasound in Medicine (AIUM 1998). The levels obtained for both imaging methods are listed in Table 1. These values are considerably lower than the FDA limits and in-vivo scanning is therefore safe using the present imaging modes.

Acquisition

Two different locations (Fig. 8) were scanned in each person. Both upper abdominal views of the liver in some cases including the right kidney. Hereby, two acquisitions, with the two imaging techniques were made in seven volunteers yielding 28 cine-loop sequences (14 paired sequences), each of approximately 3 seconds duration.

A scout image to initially locate the transducer was obtained using the transducer on a commercial scanner (B-K Medical, Hawk 2102) immediately before the acquisition. The volunteer was asked to hold his breath and an interleaved sequence of 3 seconds (36 frames) duration was recorded. The acquired RF data were then transferred to a computer cluster for subsequent off-line processing.

Data Processing

The conventional data were beamformed using dynamic receive focusing. The RF signals were filtered using a matched filter, and dynamic apodization using a modified Hamming window with -12 dB edge levels was applied, which kept the receive f-number=2 until the receive aperture was fully opened.

	Conventional	STA	Unit
$I_{sppa.3}$	26.28	7.93	W/cm^2
$I_{spta.3}$	3.66	72.94	mW/cm^2
MI	0.41	0.27	-

Table 1: Ultrasound intensities and mechanical index (MI) used in conventional and STA imaging respectively. The values are derated in-situ values.

The STA data were processed using dynamic transmit and receive focusing as described earlier. A designed compression filter with a center frequency of 5.5 MHz and 90% bandwidth was used to filter the RF data and perform the pulse compression. The filter was weighted with a Chebychev window to reduce the near and distant temporal sidelobes in the compression output (Misaridis and Jensen 1999; Gammelmark and Jensen 2003b). Dynamic apodization was applied in both transmit and receive using a modified Hamming window with -12 dB edge levels, and both F-numbers were kept constant at 2 until the apertures were fully opened. The number of beamformed image lines was the same as the number of scanned lines in conventional imaging, i.e. 195 beams. Note, however, that any number of scan lines or image points could have been beamformed for STA imaging, from the acquired data.

When both sets of data were beamformed the element sensitivity (O'Donnell and Thomas 1992) was taken into account. The angular sensitivity of each aperture element

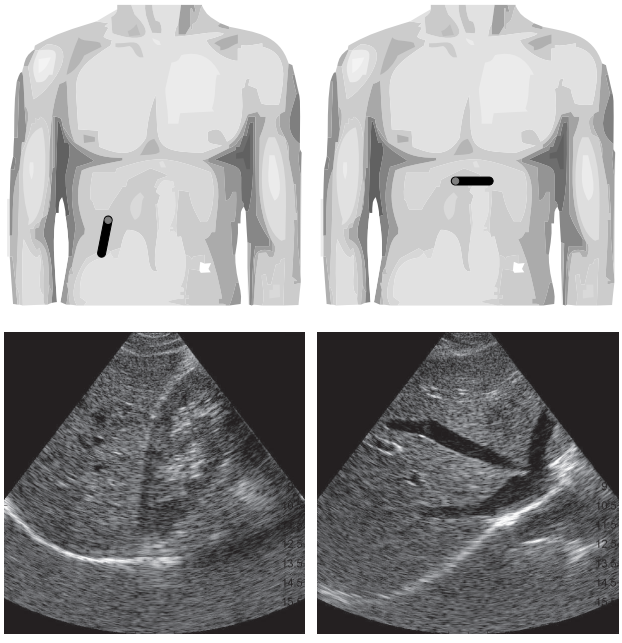

(a) Sub-costal sagittal view (b) Sub-xiphoid transverse view

Figure 8: Two typical scanning locations

was set to ± 50 degrees (corresponding to the -6 dB sensitivity limit), and an element was not applied in the beamformer until the image point to be beamformed occurred inside its acceptance angle.

Automatic TGC Post-Correction

Before scan-line conversion, the TGC was corrected according to depth to obtain homegenous images suitable for comparison. The automatic correction method is described by Pedersen et al (2003). The method automatically simulates the TGC adjustments performed by a sonographer, eliminating the possible bias from human intervention.

After envelope detection and log-compression the median value of all lines for all depths in the first recorded frame was found. The resulting curve was fitted (cubic spline) to eight control points found from the average value of the median curve in eight evenly distributed along the depth axis. The resulting fitted curve was then subtracted from all lines in alle frames. In Fig. 9 an example of the correction is depicted. A dynamic range of 50 dB was used.

Movie Generation

Scan line conversion and movie generation were done in MATLAB (MathWorks Inc., Natick, Mass., USA). Movies consisting of 3 s recordings, swinging forwards and backwards, to avoid annoying temporal discontinuities, were created with both single and paired images. In the single image movies only conventional or synthetic acquisitions were shown. In paired movies both conventional and synthetic images were shown side-by-side. Two versions of the paired movies were made, with the conventional image to the left and to the right respectively. The movies were compressed using the loss-less Huffyuv CODEC v2.1.1[1] to generate Windows™ AVI files.

[1]by Ben Rudiak-Gould, Berkeley University, USA (`http://web.archive.org/web/20020202101504/http://www.math.berkeley.edu/~benrg/huffyuv.html`

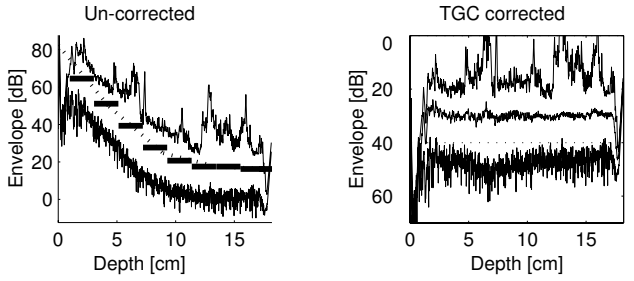

Figure 9: Automatic TGC post-correction of logarithmic envelope. The left graph shows the maximum and minimum log-dB values as a function of depth. Between the maximum and minimum curves the fitted median curve and the control point levels (horizontal bars) are shown. The right graph shows the min, max, and median values after TGC correction.

Image Assessment

Three medical doctors (ultrasound specialists) evaluated the movie clips. None of the three were involved in the project, nor had they any prior knowledge about the details of synthetic aperture imaging, or seen any of the images beforehand. Evaluations were done blinded and independently of each other.

Penetration depth comparison were done by presenting the 28 sequences, as shown in Fig. 10(a), in random order to each doctor without any information on the type of technique used. He was asked: ”At what depth [cm] does the image quality decrease significantly?”, to estimate the perceived penetration depth. The differences between depths in matching image pairs (conventional and STA) were used for the statistical analysis to avoid the bias from different examiners, who undoubtedly have different opinions on how to answer the posed question.

Image quality comparison of conventional and STA images were performed by displaying matching pairs side-by-side in random order and with random left-right placement of the conventional image. This resulted in 28 presentations of the 14 pairs. The doctors were asked to score which of the two presented images (movies) was better on a visual analog scale (Altman 1997) (VAS), see Fig. 11(a). Before the scoring the VAS scale was explained using Fig. 11(b). The figure instructs the doctor on how to interpret the scale when performing the evaluation. To avoid categorized data and get a smoother distribution, this explanatory scale is not shown during the actual evaluation (scoring).

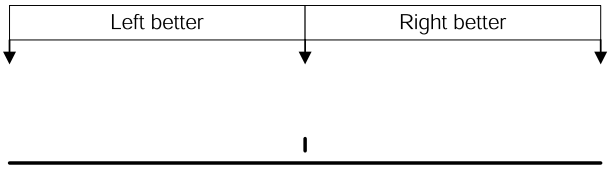

(a) Visual Analog Scale (VAS) used to compare left and right image.

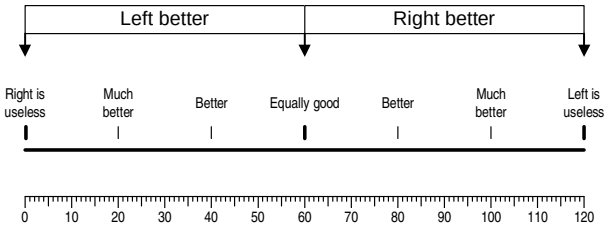

(b) Explanation of VAS shown to medical doctors before scoring images. The lower scale was used to read scored values.

Figure 11: Visual analog scale for image quality comparison

(a) Synthetic aperture image / movie clip used for penetration depth estimation.

(b) Image of movie with both conventional (left) and STA (right) images for comparison.

Figure 10: Single and double image presentation. The presented images are transverse sections of the right liver lobe containing hepatic vein branches, cross sections of portal vein branches, and the diaphragm in the lower part of the images. The depth indications are in cm.

Statistical Analysis

The statistical data analysis language R[2] was used for statistical computations. Student's (one sample) t-test was used on the resulting differences in *penetration depth*, assuming normal distribution supported by Fig. 12. Two-sided tests were used.

Since each evaluating doctor most likely has his own interpretation of the visual analog scale and show different degrees of attraction to the center point (Fig. 13) in side-by-side *image quality comparisons*, no assumptions of normal distributed data were made. Consequently, Wilcoxon signed rank test with continuity correction was used on the VAS results. The P values of the pooled data from all three examiners were corrected for multiple comparison using the Bonferroni method (Altman 1997).

[2] `http://www.r-project.org/`

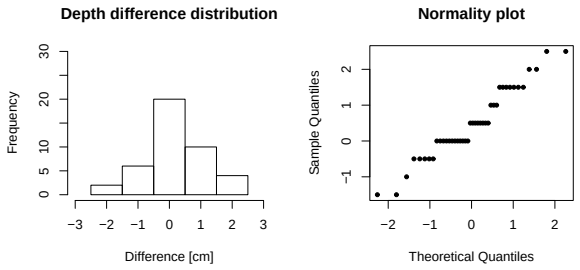

Figure 12: Histograms and normality plots of perceived penetration depth differences ($d_{STA} - d_{Conv.}$). The normality plot supports the assumption of normally distributed data.

Results

The STA images were generally good and undoubtedly applicable in clinical imaging. Examples are shown in Fig. 10 and Fig. 14.

New features

Synthetic aperture images clearly had a more uniform lateral resolution than the conventional, undoubtedly due to the optimal focusing at all depths, which resulted in sharper images with more well-defined structure borders. Additionally, movement during acquisition seemed to be rendered differently compared to conventional images. Moving organs seems to be moving more *en bloc*, i.e. without the warping that occurs in conventional ultrasound imaging. This remains to be evaluated further, though.

Limitations and Artifacts

An artifact appeared just above strong specular reflectors (the diaphragm) in a few images, due to saturation (Fig. 10(a)). The harmonic components introduced hereby result in an extra 'match' when performing the matched filtering producing a bright spot above the reflector. The artifact is described and shown in Pedersen et. al (2003).

A subtle, but clearly noticeable, flashing artifact was seen in some of the STA images during movement. It was not visible in the individual images, only during movie playback. It had no visible influence on image quality, and was not mentioned by the evaluating doctors.

Penetration

The differences in penetration depths between the two techniques are shown in Table 2 and the distribution is depicted in Fig. 12. As seen, there is only a slight but significant (P=0.008) difference in penetration depth; STA images on

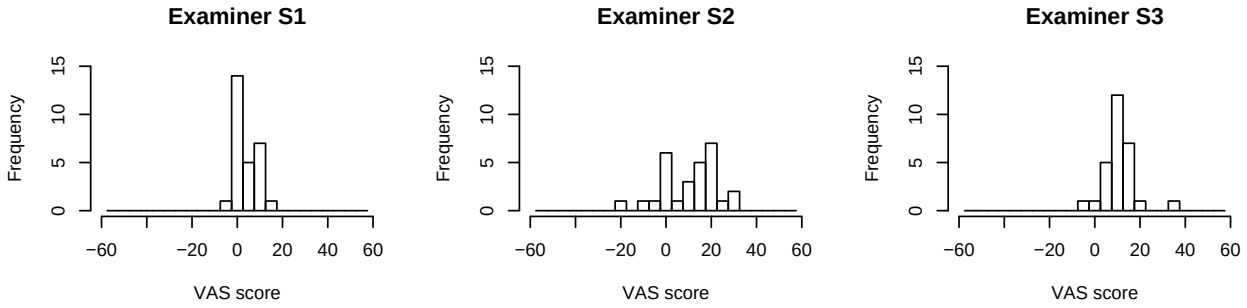

Figure 13: Distribution of answers to image comparisons. Positive values mean that the STA image is better. Data are shown for the three doctors (S1-S3) individually.

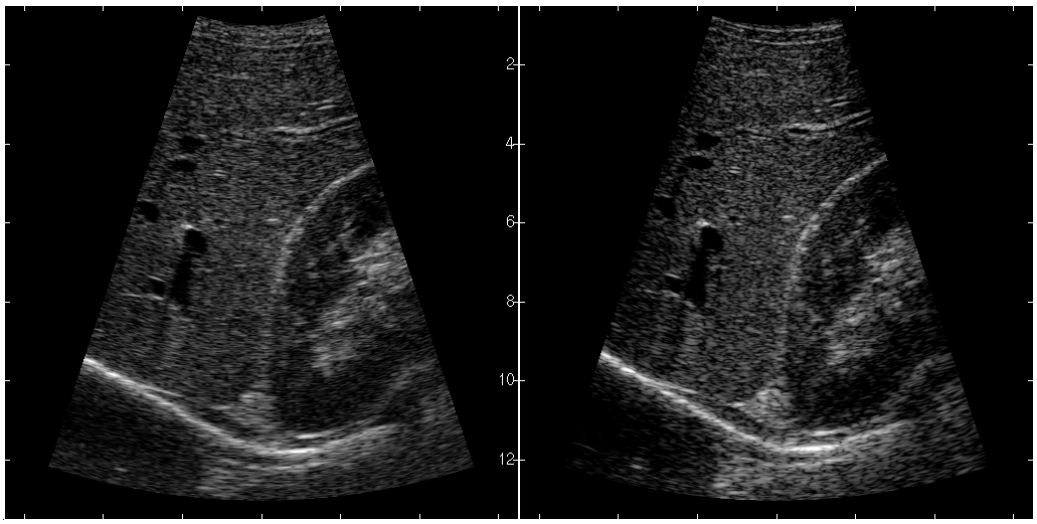

(a) Longitudinal section of right liver lobe showing cross sections of hepatic vein branches, longitudinal section of a portal a vein branch (upper left part), the kidney, and diaphragm at the bottom.

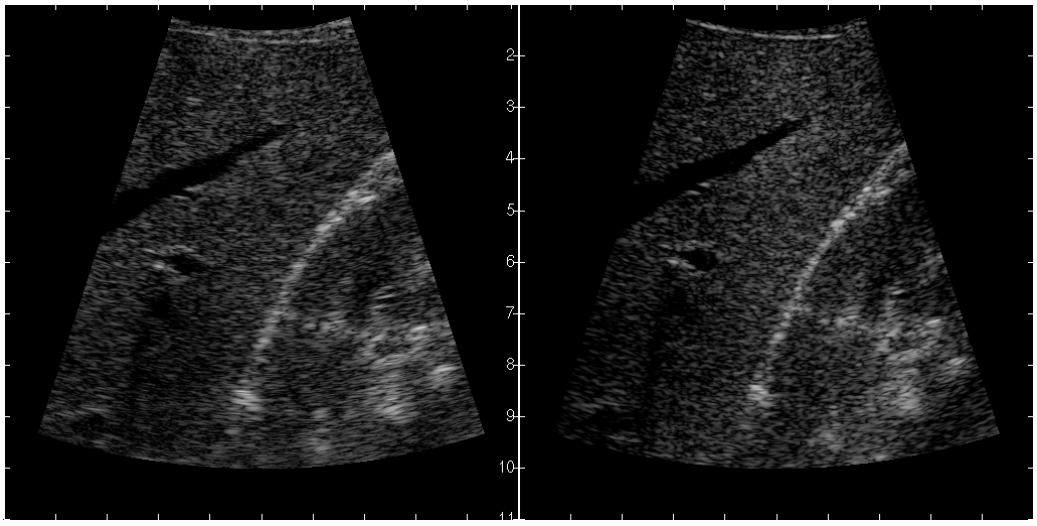

(b) Longitudinal section through right liver lobe including the right kidney. A hepatic vein branch is seen as a dark excavation in the liver.

Figure 14: Some examples of the produced in-vivo images. Left part is the conventional and right is the STA image.

average had 0.48 cm more penetration. The first examiner, though, did not perceive any significant difference in penetration depth. The utilized signals and intensities were deliberately chosen to match penetration ability in conventional and STA imaging within the given safety limits. This shows that STA imaging is fully capable of producing images to at least the same depth as conventional ultrasound imaging.

Image Quality

The distributions and results of the image quality scoring are shown in Fig. 13 and Table 3, respectively. All three examiners scored a significant better image quality in STA images yielding a highly significant ($P<0.001$) image quality improvement based on the pooled answers. The mean VAS score from all three examiners is not calculated, since it really makes no sense to do that. Also, one should be careful to interpret the absolute VAS averages of each examiner, since the values heavily depend on that persons interpretation of the scale.

Examiner	Conventional (cm)	STA (cm)	Difference (cm)	P value
S1	8.86	9.04	0.18	0.477
S2	8.21	8.79	0.57	0.076
S3	9.36	10.04	0.68	0.012
Pooled	8.81	9,29	0.48	0.008

Table 2: Results of answers to "At what depth [cm] does the image quality decrease significantly?"

Sonographer	Difference (VAS)	P value
S1	10.75	0.0011
S2	10.6	0.014
S3	3.64	0.0025
Pooled		< 0.001

Table 3: Mean VAS differences between conventional and STA images for each examiner. Positive values mean STA is better.

Discussion

The results significantly show, that synthetic transmit aperture imaging can be used in medical ultrasound. We believe this is the first published study that make a clinical comparison of conventional and synthetic aperture ultrasound imaging. The worry, that tissue motion would make coherent summation of samples, and thereby image formation, impossible, can be discarded for these abdominal images. Motion does introduce minor flash artifacts, though, which we expect to be able to remove by motion compensation in future works (Gammelmark and Jensen 2003a). The synthetic aperture technique heavily depend on coded (chirp) excitation to obtain sufficient signal-to-noise ratio and therefore exhibits the same minor artifacts in our current implementation as described in earlier work (Pedersen et al. 2003).

The clinical evaluation performed by the medical doctors shows a minute (0.48 cm) but significant (P=0.008) increase in penetration depth using synthetic aperture with coded excitation. Since the two techniques are totally different with regards to excitation method, aperture use, and pulse design, this value is not that interesting. Based on the statistical results, hypothesis one is rejected, and we conclude that STA imaging can obtain satisfying penetration within the current intensity limits. In the present case penetration is actually improved.

Image quality evaluation showed highly significant improvement in STA images compared to conventional images, which was also expected by the authors due to the apparent improved resolution throughout the STA images. Therefore, also hypothesis number two was rejected. One should be careful about interpreting the absolute VAS values, since the inter-observer variation in VAS scale interpretation is always large.

Conclusion

Synthetic aperture ultrasound imaging has been demonstrated and evaluated in-vivo. The clinical evaluation showed improved image quality in side-by-side comparison to conventional ultrasound imaging. This finding is very important to future real-time three-dimensional imaging methods based on synthetic aperture techniques (Nikolov et al. 2003; Hazard and Lockwood 1999). Especially two- and three-dimensional vectorial flow estimation methods (Jensen and Nikolov 2003), which heavily depend on the high acquisition rate delivered by STA imaging.

Acknowledgments

Thanks to M.D. Dr.Med. Torben Larsen, M.D. Nis Nørgaard, and M.D. Bjørn Skjoldbye for evaluating the ultrasound images, and to the volunteers for participating.

This work is sponsored by grant 9700883 and 9700563 from the Danish Science Foundation, by Engineer Frode V. Nyegaard and wife's Foundation, by Ph.D. grant 11-3160-55173 from the Technical University of Denmark, and by B-K Medical A/S, Herlev, Denmark.

References

AIUM (1998). Acoustic output measurement standard for diagnostic ultrasound equipment. Technical report, American Institute of Ultrasound in Medicine & National Electrical Manufacturers Association.

Altman, D. G. (1997). *Practical Statistics for Medical Research*, volume 14. Chapman and Hall / CRC, London.

FDA (1997). Information for manufacturers seeking marketing clearance of diagnostic ultrasound systems and transducers. Technical report, Center for Devices and Radiological Health, United States Food and Drug Administration.

Gammelmark, K. L. and Jensen, J. A. (2002). Experimental study of convex coded synthetic transmit aperture imaging. In *Proc. IEEE Ultrason. Symp.*, pages 1573–1576.

Gammelmark, K. L. and Jensen, J. A. (2003a). Duplex synthetic aperture imaging with tissue motion compensation. In *Proc. IEEE Ultrason. Symp.*, pages 1569–1573.

Gammelmark, K. L. and Jensen, J. A. (2003b). Multielement synthetic transmit aperture imaging using temporal encoding. *IEEE Trans. Med. Imag.*, 22(4):552–563.

Hazard, C. R. and Lockwood, G. R. (1999). Theoretical assessment of a synthetic aperture beamformer for real-time 3-D imaging. *IEEE Trans. Ultrason., Ferroelec., Freq. Contr.*, 46:972–980.

Jensen, J. A., Holm, O., Jensen, L. J., Bendsen, H., Pedersen, H. M., Salomonsen, K., Hansen, J., and Nikolov, S. (1999). Experimental ultrasound system for real-time synthetic imaging. In *Proc. IEEE Ultrason. Symp.*, volume 2, pages 1595–1599.

Jensen, J. A. and Nikolov, S. I. (2003). A method for real-time three-dimensional vector velocity imaging. In *Proc. IEEE Ultrason. Symp.*, pages 1582–1585.

Karaman, M., Li, P. C., and O'Donnell, M. (1995). Synthetic aperture imaging for small scale systems. *IEEE Trans. Ultrason., Ferroelec., Freq. Contr.*, 42:429–442.

Misaridis, T. X. and Jensen, J. A. (1999). An effective coded excitation scheme based on a predistorted FM signal and an optimized digital filter. In *Proc. IEEE Ultrason. Symp.*, volume 2, pages 1589–1593.

Nikolov, S. I., Tomov, B., Gran, F., Dufait, R., and Jensen, J. A. (2003). Further development of synthetic aperture real-time 3d scanning with a rotating phased array. In *Proc. IEEE Ultrason. Symp.*, pages 1899–1902.

O'Donnell, M. and Thomas, L. J. (1992). Efficient synthetic aperture imaging from a circular aperture with possible application to catheter-based imaging. *IEEE Trans. Ultrason., Ferroelec., Freq. Contr.*, 39:366–380.

Pedersen, M. H., Misaridis, T. X., and Jensen, J. A. (2003). Clinical evaluation of chirp-coded excitation in medical ultrasound. *Ultrasound Med. Biol.*, 29(6):895–905.

A.4 2D Tissue Motion Compensation of Synthetic Aperture Images

This article was submitted to *IEEE Transactions on Medical Imaging* in August 2004.

2D Tissue Motion Compensation of Synthetic Transmit Aperture Images

Kim Løkke Gammelmark, *Student Member, IEEE,* and Jørgen Arendt Jensen, *Senior Member, IEEE*

Abstract

Synthetic Transmit Aperture (STA) Imaging is by nature more susceptible to tissue motion than traditional scanning techniques, due to the summation of low resolution images to create the displayed high resolution image. Methods for motion estimation and correction of STA images, which have previously been investigated, have primarily been concerned about axial motion. Lateral motion will, however, degrade the lateral resolution and contrast resolution, and, thus, two dimensional (2D) motion compensation is necessary to retain the advantages of STA imaging. This paper presents a method for 2D tissue motion correction in STA imaging. The method utilizes the high correlation that exists between high resolution images recorded using the same emission sequence. The velocity and direction of the motion is found at selected image points by cross-correlating short high resolution lines beamformed along selected angles. For each point the angle with the highest correlation coefficient gives the direction of the motion, and for this direction the velocity is calculated. The method is interleaved with the regular B-mode emissions in STA imaging, and the motion compensation is performed by tracking each pixel in the reconstructed image using the estimated velocity and direction. The method was primarily evaluated using phantom and in-vivo experiments. The phantom results generally showed that the direction and velocity can be estimated with low bias and standard deviation for both high and low tissue velocities, resulting in almost perfect recovery of the image quality. For a tissue velocity of 15 cm/s at a 45 degrees angle, the velocity was estimated with a relative bias and standard deviation of -6.9% and 5.4%, while the motion direction was estimated with a relative bias and standard deviation of -8.4% and 6.6%, respectively. The contrast resolution in the corrected image was -0.65% lower than the reference image. The in-vivo experiment performed abdominally, with transducer motion produced by the sonographer, demonstrated that severe tissue motion is indeed a problem in STA imaging, and that the presented method is capable of perfect motion compensation producing a significant increase in image quality.

I. Introduction

Traditional medical ultrasound images are measured by sequentially transmitting a focused ultrasound beam in different directions in the tissue and simultaneously steering and focusing the receive field in the same directions. This produces a set of scan lines, which are stacked together to generate the displayed image.

Synthetic Transmit Aperture (STA) imaging is a relatively new imaging technique, originally adapted from radar, which exploits a somewhat different approach to building up the ultrasound image [1], [2]. Instead of limiting the transmitted ultrasound field to a narrow beam in a particular direction, the basic principle in STA imaging is to transmit a spherical wave using a single element, which propagates in all directions in the tissue simultaneously. The echoes recorded by the receive elements contain information about every scatterer in the illuminated region, and the received signals are then processed by steering and focusing at all image points to form a complete image after one emission [3]. This process is repeated by consecutively exciting all elements in the transmit aperture, and the individual low resolution images are finally summed to generate the displayed high resolution image. No focusing is applied at each transmission and, since the origin of the beam is known, the transmit aperture is also steered and focused at every image point. This produces images with dynamic transmit and receive focusing, which are improved compared to the traditional ultrasound scanners with a single transmit focus.

The application of a single transmit element produces a clinically insufficient signal-to-noise ratio (SNR), because the transmitted energy is limited due to hardware limitations and transducer heating problems. Recent work has shown that the SNR can be increased by employing a subaperture at each emission to emulate the spherical wave transmitted by the single element [1], [2], and by replacing the conventional short excitation signal by a linear frequency modulated (FM) signal [4], [5], [6]. Using this approach, denoted TMS imaging[1] [3], [7], the SNR is increased to a clinically suitable level enabling successful in-vivo application. This was demonstrated in a recently published clinical study comparing TMS imaging to conventional convex array imaging in abdominal imaging [8], [9].

Since STA images are produced by adding low resolution images obtained over several emissions, it inherently relies on coherent summation, i.e. the images are phase aligned when summed. If the low resolution images are summed incoherently, the displayed STA image will be unfocused with a smeared appearance, resulting in loss

Kim L. Gammelmark (klg@oersted.dtu.dk) and Jørgen A. Jensen (jaj@oersted.dtu.dk) are both with the Center for Fast Ultrasound Imaging, Ørsted•DTU, Building 348, Technical University of Denmark, 2800 Kgs. Lyngby, Denmark.

[1] Temporally encoded Multi-element Synthetic transmit aperture imaging.

in image quality. Presently, the most important factor considered to cause phased misalignment is tissue motion, which is primarily produced by the beating heart, blood pulsation, respiration, and transducer motion. The latter is produced by the sonographer while scanning. The degree of loss in image quality will depend on how severe the motion is, and therefore it will depend on the anatomical location being scanned. Compared to the traditional ultrasound scanners, where motion artifacts occur as distortions of the tissue structures rather than loss in spatial and contrast resolutions, STA imaging is clearly more susceptible to motion. In general, it may therefore be necessary to compensate for tissue motion to fully retain the advantages of STA imaging.

Several methods have previously been investigated for tissue motion estimation in STA imaging [10], [11], [12], [13]. Commonly it is reported that axial motion is the dominant factor causing image degradation due to the significantly higher spatial frequency in this dimension. There are though a significant shortcoming to solely performing axial compensation. If 2D motion is present, and only the axial motion component is compensated for, the resulting images will have degraded lateral and contrast resolutions compared to the case of perfect 2D compensation, hereby loosing the advantage of better image quality in STA imaging as shown on Fig. 3 in [13] (as an example hereof). Since tissue motion is inherently three dimensional, it is therefore evident that full utilization of the advantages of STA imaging requires at least two dimensional (2D) motion correction to compensate successfully for scan plane tissue motion.

Generally, motion estimation methods are based on time-domain cross-correlation of reference signals to find the shift in position of the tissue. The degree of success of such methods depends on the correlation between the reference signals, which again depends on the degree of common spatial frequencies used to generate the reference signals. This property was used by Karaman and colleagues in [12] to find axial motion by cross-correlating segments of low resolution images obtained by solely using common spatial frequencies. Another method to obtain highly correlated reference signals is to use high resolution images. These will be completely correlated, if they are acquired using the exact same emission sequence and receive aperture setup. This property has been used by Nikolov and Jensen [14], [15] to generate synthetic aperture flow images for all flow angles. Here the blood flow velocity is estimated by cross-correlating high resolution lines beamformed along the flow direction using a sparse implementation of TMS imaging with a few emissions per high resolution image.

In this paper a method for 2D tissue motion compensation is presented for convex array TMS imaging. The concept of convex TMS imaging has been studied by the authors previously in [7], [16] for B-mode imaging, and a detailed description of this approach can therefore be found in these references. The motion compensation approach is based on the same principles for finding the tissue velocity as the synthetic aperture flow method mentioned above applied to find the blood flow velocity. As an extension, the direction of the motion needs to be found as well, which is done by correlating high resolution lines for multiple angles at each estimation point and selecting the angle at which the correlation is highest. This direction estimation method has been investigated by Jensen in [17] for automatic flow angle estimation. The method for convex arrays is described in full detail in Section II, and the experimental setup used for the phantom and in-vivo measurements performed using the RASMUS research scanner [18] are presented in Section III along with the applied signal processing strategies. The results are presented in Section IV, and finally the paper is concluded in Section V.

II. Directional Motion Estimation

The motion estimation method utilizes the high correlation that exists between high resolution images acquired using the same emission sequence and receive aperture setup, and the fact that for a given emission any set of image points within the interrogated region can be processed using STA beamforming [14]. The method seeks to find the tissue motion at a given image point by first estimating the direction in which the scatterers have moved and secondly estimating the velocity with which they moved. This is possible because the motion distortion in high resolution images acquired using the same emission sequence will be identical, if the tissue velocity and direction is constant during the acquisition [15].

To simplify matters initially, the method is illustrated in Fig. 1 using two emissions. For a given location in the image $\vec{r}_p$ at which the motion is to be estimated, a set of low resolution lines along selected angles θ_l, $l = 1, 2, \ldots, L$, are beamformed for each emission. This is illustrated in detail in Fig. 2. For each set of consecutive emissions, here $[m, m+1]$, $[m+1, m+2]$, $[m+2, m+3]$, ..., the lines corresponding to the same angle are summed to form high resolution lines $g_m(n, l)$, $g_{m+1}(n, l)$, $g_{m+2}(n, l)$,..., where n, $n = 1, 2, \ldots, N$, is the sample number, and l is the angle index. Thus, $g_m(n, l)$ is a 2D data set, where each column is a directional line. Assuming a constant tissue velocity during the acquisition, the motion distortion in $g_m(n, l)$ and $g_{m+2}(n, l)$ will be the same and the only difference should be the shift in position of the scatterers [15]. This is true only for the angle corresponding to the direction of the motion, and the correlation between the high resolution lines will therefore be highest for this angle. By correlating $g_m(n, l)$ and $g_{m+2}(n, l)$ for all angles, i.e. column by column, the direction of the motion is then found for the angle at which the normalized covariance is maximum. For this angle the shift in position of the correlation peak can be found and, thus, the tissue velocity.

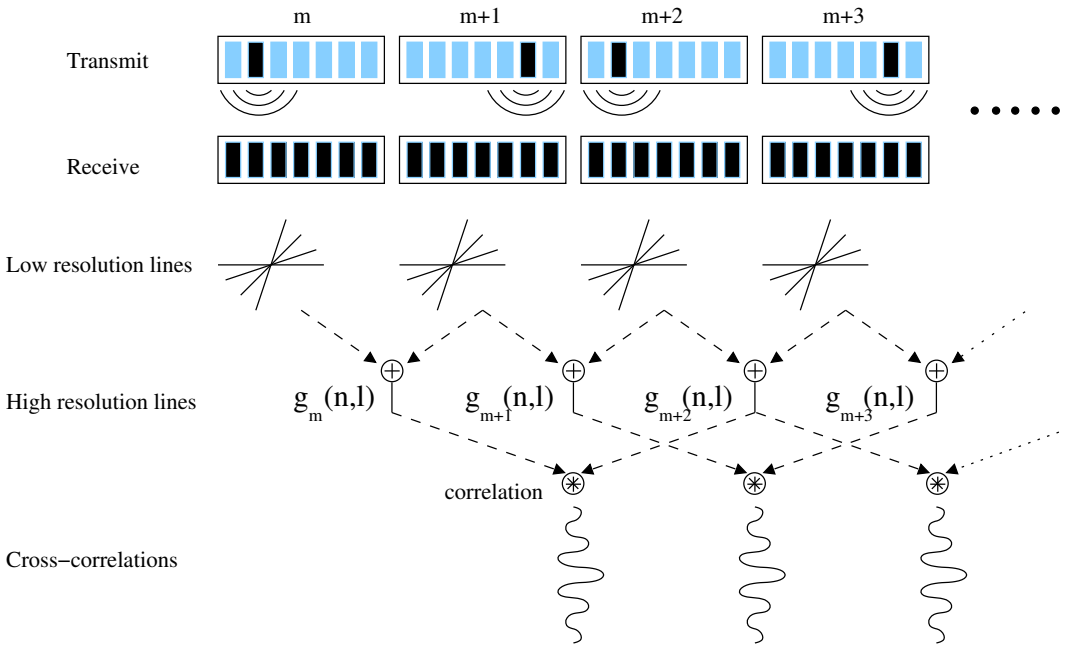

Fig. 1. Illustration of the tissue velocity estimation approach using two repeating emissions. For each emission and each estimation point a set of low resolution lines are beamformed for selected angles. These lines are summed angle by angle for consecutive emissions, $[m, m+1]$, $[m+1, m+2]$, $[m+2, m+3]$,. . ., to form high resolution lines $g_m(n,l)$, $g_{m+1}(n,l)$, $g_{m+2}(n,l)$,. . .. The lines from idetical emissions sets are then correlated to find the direction of the motion and the velocity.

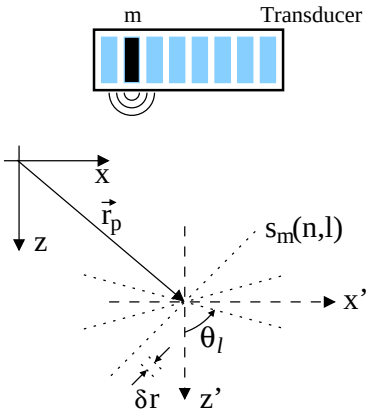

Fig. 2. Detailed illustration of the directional lines beamformed at each emission and used for the direction and velocity estimation. The vector $\vec{r}_p$ denotes the image point location, θ_l is the angle of the l'th directional line, δr is the sample spacing, and $s_m(n,l)$ is the directional line for emission m.

The shift in position between high resolution lines $g_{m+1}(n,l)$ and $g_{m+3}(n,l)$ will be equal to that between $g_m(n,l)$ and $g_{m+2}(n,l)$, again assuming that the tissue velocity is constant during the acquisition interval [15]. Thus, the peak in the covariance functions will be located at the same lag, and they can be averaged to improve the velocity estimate. This averaging can be applied for as long as the velocity can be assumed constant.

Going into more details, M emissions spaced over the full aperture will, in general, be used to create each high resolution line and they are repeated N_{seq} times, resulting in a total of $M \cdot N_{seq}$ emissions. The i'th high resolution line is obtained from

$$g_i(n,l) = \sum_{m=1}^{M} s_{m+i}(n,l), \tag{1}$$

where $i = 0, 1, \ldots, M(N_{seq}-1)$, and $s_m(n,l)$ is the low resolution line for emission m with zero mean. The normalized covariance [19] is obtained for each angle by cross-correlating the high resolution lines corresponding

to the same angle as explained previously. Thus,

$$\rho_j(k,l) = \frac{\frac{1}{N}\sum_{n=1}^{N} g_j(n,l) g_{j+M}(n+k,l)}{\sqrt{\sigma_j^2 \sigma_{j+M}^2}}, \tag{2}$$

where $j = 0, 1, \ldots, M(N_{seq} - 2)$, k is the lag, and σ_j^2 and σ_{j+M}^2 are the variances of the high resolution lines $g_j(n,l)$ and $g_{j+M}(n,l)$, respectively, adjusted to have zero mean.

The peaks in the $M(N_{seq} - 2) + 1$ correlation functions will be located at the same position for the angle in which the motion occurs. The estimate of the tissue velocity can therefore be improved by averaging the covariance functions [20]

$$\bar{\rho}(k,l) = \frac{1}{M(N_{seq} - 2)} \sum_{j=0}^{M(N_{seq}-2)} \rho_j(k,l). \tag{3}$$

The direction of the motion is found at the angle $\hat{\theta}_{l_{max}}$ where l_{max} is the index for which $\bar{\rho}(k,l)$ is maximum for all values of k and l. The velocity magnitude $\hat{v}$ of the motion is then calculated for this angle by

$$\hat{v} = \frac{k_{max} \delta r f_{prf}}{M}, \tag{4}$$

where k_{max} is the lag of the correlation peak in $\bar{\rho}(k, l_{max})$, δr is the sample spacing in meters, and f_{prf} is the pulse repetition frequency.

The direction estimate will in general be too coarse due to the discrete set of angles, and the velocity estimate will therefore be inaccurate. The estimates can be improved using interpolation around the correlation peak. Here, this is done over two steps by first interpolating the angle estimate l_{max} and secondly finding the interpolated velocity estimate along the new direction. Following the approach in [21], the interpolated motion direction is $\hat{\theta}_{l_{int}}$, where

$$l_{int} = l_{max} - \frac{\bar{\rho}_m(l_{max} + 1) - \bar{\rho}_m(l_{max} - 1)}{2(\bar{\rho}_m(l_{max} + 1) - 2\bar{\rho}_m(l_{max}) + \bar{\rho}_m(l_{max} - 1))}, \tag{5}$$

and $\bar{\rho}_m(l)$ is the maximum correlation for each angle

$$\bar{\rho}_m(l) = \max_k \bar{\rho}(k,l). \tag{6}$$

For this angle, the lag of the correlation peak is found using the same interpolation method. Thus,

$$k_{int} = k_{max} - \frac{\bar{\rho}(k_{max} + 1, l_{int}) - \bar{\rho}(k_{max} - 1, l_{int})}{2(\bar{\rho}(k_{max} + 1, l_{int}) - 2\bar{\rho}(k_{max}, l_{int}) + \bar{\rho}(k_{max} - 1, l_{int}))}, \tag{7}$$

and the velocity estimate becomes

$$\hat{v} = \frac{k_{int} \delta r f_{prf}}{M}. \tag{8}$$

A. Implementation with TMS Imaging

To obtain continuous imaging, the emissions in the estimation approach are interleaved with the B-mode emissions normally used in TMS imaging. This is illustrated in Fig. 3 for a 1-to-1 ratio, where the motion estimation emissions are denoted E-mode emissions. Hereby, the tissue velocity is estimated continuously. Using the 1-to-1 ratio, the tissue velocity estimate in (8) becomes

$$\hat{v} = \frac{k_{int} \delta r f_{prf}}{2M}, \tag{9}$$

because the time between the E-mode emissions is now twice the pulse repetition period.

The velocity and angle estimates are used to compensate the low resolution B-mode images by recalculating the location of the image points to be reconstructed. In particular, each pixel in the motion compensated B-mode image $S(\vec{r}_p)$ is reconstructed by

$$S(\vec{r}_p) = \sum_{m=1}^{N_{xmt}} w_m(\vec{r}_p) \sum_{n=1}^{N_{rcv}} w_n(\vec{r}_p)\, g_{m,n}\left(\frac{d_{m,n}(\vec{r}_t(m))}{c}\right), \tag{10}$$

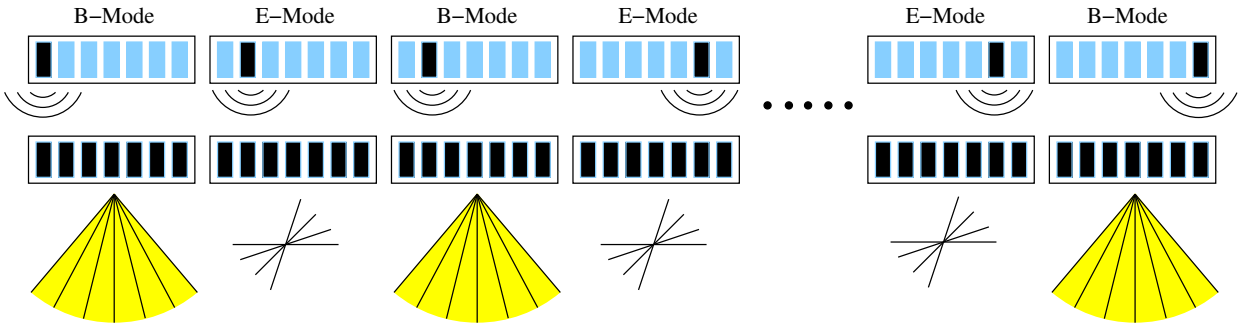

Fig. 3. Illustration of the implementation used to obtain continuous motion compensation and B-mode imaging. The estimation emissions, denoted E-mode emissions, are interleaved with the regular B-mode emissions with a 1-to-1 ratio.

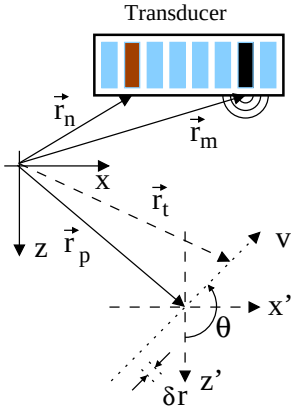

Fig. 4. Definition of geometric variables used for the motion compensation. The vectors $\vec{r}_m$, $\vec{r}_n$, and $\vec{r}_t(m)$ denote the locations of transmit element m, receive element n, and the tracked pixel for emission m, respectively.

where $w_n(\vec{r}_p)$ is the apodization values for receive element n, $w_m(\vec{r}_p)$ is the apodization value for (virtual) transmit element m, c is the sound speed, and N_{xmt} and N_{rcv} are the number of emissions and receive channels, respectively. The total distance $d_{m,n}(\vec{r}_t(m))$ from transmission center m to the tracked image point and back to receive element n is given by

$$d_{m,n}(\vec{r}_t(m)) \quad = \quad |\vec{r}_t(m) - \vec{r}_m| + |\vec{r}_n - \vec{r}_t(m)|\,, \tag{11}$$

where $\vec{r}_t(m)$ is the location of the tracked image point

$$\vec{r}_t(m) = [\sin\hat{\theta}_{l_{int}}, 0, \cos\hat{\theta}_{l_{int}}] \cdot \frac{2\hat{v}}{f_{prf}}(m-1) + \vec{r}_p. \tag{12}$$

The vectors are defined geometrically in Fig. 4.

B. Parameters of Interest

The theory presented above gives an overview of the motion estimation method and its implementation with TMS imaging to continuously obtain motion compensated images. There are though some parameters in the estimation algorithm, which requires further attention to fully understand the approach. These are the sample distance δr, the length of the directional lines $N \cdot \delta r$, and the number of repeated emissions M.

The distance between the samples in a directional line will in general be dependent on its angle. Creating a directional line at a given location in the image corresponds to sampling the medium in that particular direction. To comply with the spatial Nyquist theorem, the spatial sampling frequency must therefore be at least twice the highest spatial frequency in that direction. The K-space magnitude spectrum obtained by Fourier transforming a 2D speckle region [22] determines the spatial frequencies of the speckle region around the directional line. For an angle θ_l the highest spatial frequency is found by rotating the K-space spectrum along the same angle and projecting it onto the axial frequency axis, which is cumbersome to calculate. For all angles the highest spatial frequency will be in

the axial direction. This means that, the Nyquist theorem can be satisfied for all angles by solely using the axial sampling frequency. Therefore, the sample spacing δr is determined by [7]

$$\delta r \leq \frac{\lambda}{4\left(1+\frac{B_{rel}}{2}\right)}, \tag{13}$$

where λ is the wavelength, and B_{rel} is the -6dB relative bandwidth of the transmitted pulse.

The length of the directional lines are determined by several factors, where the tissue velocity, the variance on the velocity estimate, and the assumed area of constant tissue velocity are the most important ones. It is clear that the line needs to be long enough, so that the motion of the scatterers can be estimated. This puts an interdependence on the line length and the maximum detectable tissue velocity. The variance on the velocity estimate is inversely proportional to the length of the line [19], and therefore the variance is decreased, when the line length is increased. However, it is assumed in the model that the velocity is constant, and the line length is therefore limited by the size of the tissue region over which the velocity can be assumed constant.

Although not a direct requirement, it is preferred that the number of repeated E-mode emissions M is an integer fraction of the number of B-mode emissions used per TMS image. This is to ensure that the estimation sequence is repeated an integer number of times within one B-mode sequence. In other words, M and N_{seq} should be integers and $M \cdot N_{seq} = N_{xmt}$. This therefore puts some restrictions on the design of the estimation sequence.

III. Experimental Setup

The measurements were performed using the experimental multi-channel ultrasound scanning system, *RASMUS* [18]. The system has 128 individually programmable transmitters capable of sending arbitrary coded waveforms with a precision of 12 bits at 40 MHz. Sixty-four receive channels can be sampled simultaneously at 12 bits and 40 MHz, and the 2-to-1 multiplexing in the system enables acquisition of 128 channels in real-time over two transmissions. The system has 16 Gbytes of storage memory in the receivers, which enables acquisition of several seconds of RF data in real-time. The transmission voltage is ± 50V, and RASMUS is remotely accessible and programmable through a developed Matlab/C-library interface.

The transducer used for the measurements was a commercial 5.5 MHz convex array transducer with 192 elements and λ pitch. The bandwidth of the elements is approximately 60% relative to the center frequency, and the convex radius of the aperture is 41 mm. The height of the elements is 8 mm, and the array has a lens in the elevation dimension with a fixed focus at 40 mm. Due to the limitation of the RASMUS system, only the central 128 elements of the array were used.

A. Imaging Setup

As explained in Section II the motion compensation approach is composed of two interleaved sequences: 1) the regular TMS B-mode emissions, and 2) the E-mode emissions used for motion estimation.

TMS imaging was implemented using a 33 element subaperture at each emission to emulate a spherical wave emanating from a virtual point source located behind the subaperture. As explained in [7] the transmitted wavefront was directed to propagate parallel to the z-axis at each emission to increase the energy transmitted into the image area, and thus increase the SNR. The excitation signal used was a 20μs linear FM signal with 5.5 MHz center frequency and a relative bandwidth of approximately 95%. The signal envelope was weighted by a Tukey window with a 16% duration to reduce the ripples in the chirps Fourier spectrum, and, thus, attenuate the distant temporal sidelobes in the compression result [6]. The subaperture was stepped over the 128 elements array one element at a time, resulting in $N_{xmt} = 96$ transmit positions. Using the 2-to-1 multiplexing all 128 elements in the array were recorded on receive, and the total number of B-mode emissions used per high resolution image was 192. This implementation is identical to the setup applied in previous studies of convex TMS imaging in [7], [8].

The setup used for each of the E-mode emissions was the same as that used for each of the B-mode emissions described above. The estimation sequence was tested using two implementations: 1) M=8 and N_{seq}=12, and 2) M=16 and N_{seq}=6. These are in accordance with the preferred implementation requirements mentioned in the previous section, and the number of E-mode emissions were 192 using the multiplexing. The total number of emissions in the combined sequence was therefore 384. For these two implementation sequences the number of averaged covariance functions $M(N_{seq}-2)+1$ was 81 and 65, respectively (see Section II for details).

B. Data Acquisition

Both phantom and in-vivo measurements were done to investigate the performance of the approach. The phantom measurements were performed to test the method in a fairly controllable environment. A custom made three dimensional positioning system was used to move the transducer a fixed distance between each emission to impose

a constant tissue velocity and motion direction. The positioning system is using stepper motors for accurate motion and it has a resolution of $12.5\mu m$ in the lateral and elevation direction and $5\mu m$ in the axial direction. The data were acquired by performing one emission at a time and after each emission moving the transducer according to the desired motion. The tissue mimicking phantom contained small anechoic cysts with diameters between 1 and 8 mm, and both the 8 and 16 emissions implementations mentioned above were evaluated.

An abdominal measurement of the right kidney was performed on a healthy male volunteer to evaluate the method in-vivo. The measurement was done by an experienced sonographer using the 16 emissions implementation, and freehand motion was applied during data acquisition to simulate a true clinical scanning situation. A 2.5 sec data sequence was acquired with a frame rate of 13 frames/sec and a scanning depth of 12 cm.

C. Data Processing

The processing was done off-line on a 70 cpu Linux cluster using Matlab. The RF channel data from each B-mode and E-mode emission were filtered using a mismatch baseband filter to compress the linear FM signal and recover the range resolution. The mismatch filter was designed based on the transmitted linear FM signal by applying a Chebychev window with a relative sidelobe reduction of 70 dB [6]. This was done to reduce the temporal sidelobes below -60 dB. Subsequently, the RF channel data were Hilbert transformed to form complex data sets.

The elastic properties of tissue tend to make the tissue move in approximately the same direction within a certain region. It is therefore only necessary to perform the estimation at discrete points within the image area and not at every point being reconstructed in the B-mode images. For the phantom measurements the tissue velocity and direction were estimated for every 2 mm in range along lines separated by 1 degree in angle covering the whole image area. At each estimation point, directional lines were created over a 30 degrees angular extend around the true motion direction with a separation of 1 degrees between the lines. This was only possible because the true direction was known. For the in-vivo measurement the resolution was 4 mm in range and 1.5 degrees in angle. Since the direction of the tissue motion in-vivo is unknown, directional lines with 2 degrees separation were created here over the full 180 degrees angular span. In all cases the length of the directional lines was 25λ corresponding to 7 mm, and the sample distance was approximately $\lambda/10$.

After velocity and direction estimation the B-mode images were reconstructed using the tracking method described in Section II. Since the estimates only exist at discrete points, each image point was processed using the velocity and angle from the closest estimation point. Prior to compensation the estimates were filtered using a 2D vector based median filter. This filter adjusts the estimated velocity and direction at each point by calculating the median velocity and angle using the neighboring estimates. This was done to remove false estimates and to smooth the estimates according to the elasticity property of tissue mentioned above. The filter had a geometric extend of 8 by 8 mm in the lateral and axial directions, respectively.

The motion compensated images were reconstructed using the same approach as that applied in the previous investigations of convex TMS imaging in [7], [8], except that for each emission the image points were tracked using the approach described in the previous section. The images were created using the conventional convex array image format with an angular size of 26° and 142 lines in the phantom images, and 34° and 183 lines in the in-vivo images. The transmit and receive apertures were focused at every image point as explained in Section II, producing perfectly focused images, and dynamic apodization was applied to keep the f-number constant at 2. The window function used was a modified Hamming window with the edge levels raised to -12 dB.

When reconstructing each line in the motion compensated images, the number of calculations were reduced using the pixel based approach introduced in [23]. In particular, this method lowers the requirement on the spatial sampling distance along each line to

$$\delta R \leq \frac{\lambda}{2B_{rel}} \tag{14}$$

where λ is the wavelength, and B_{rel} is the relative -6 dB bandwidth.

IV. RESULTS

In this section the results of the measurements are presented. Unless otherwise noted, the dynamic range in the displayed B-mode images is 45dB.

A. Field II Simulation

Initially, a simulation using Field II [24], [25] of a tissue mimicking phantom with a scatterer density of 10 scatterers per resolution cell (fully developed speckle) and 4 anechoic cysts was performed to test the method theoretically. The cysts were created as two pairs of cylinders with diameters of 4 mm and 8 mm, respectively. A tissue

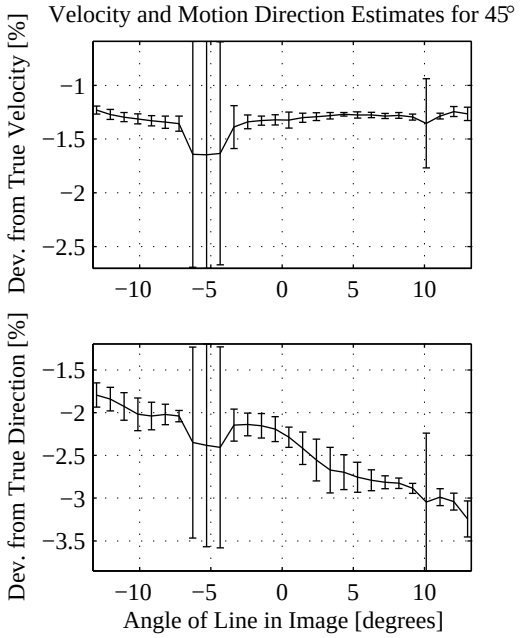

Fig. 5. Results of the velocity and direction estimation in the simulation. The top figure shows the relative bias $\pm$ 1 SD of the velocity estimation in percent deviation from the true velocity, and the bottom figure shows the relative bias $\pm$ 1 SD of the motion direction estimate ($\hat{\theta}_{l_{int}}$) in percent deviation from the true motion angle. The figures are obtained by calculating the bias and SD for each line in the image, and the x-axis is therefore image angle. This applies to all figures of the same type within this paper. (Note: Dev. is an abbreviation for deviation.)

velocity of 15 cm/s at an angle of 45 degrees was imposed by moving the scatterers between each emission, and the estimation sequence with 8 E-mode emissions repeated 12 times was used. As for the phantom measurements presented next, the velocity and direction was estimated at 2 mm range intervals along lines covering the whole image area separated by 1 degree in angle. The size of the simulated phantom was 10 cm starting at 2 cm with an angular size of 26°. Thus, the motion was estimated along 27 lines each with 41 estimation points.

The relative bias and standard deviation (SD) were calculated for both the velocity and direction estimates for each image line along which the motion was estimated. The results are shown in Fig. 5. The top figure shows the relative bias $\pm$ 1 SD of the velocity estimation in percent deviation from the true velocity, and the bottom figure shows the relative bias $\pm$ 1 SD of the motion direction estimates ($\hat{\theta}_{l_{int}}$) in percent deviation from the true angle. These figures therefore present the performance of the approach as a function of different image angles.

The velocity is estimated with a relative bias of approximately -1.3%, and the SD is in average less than 0.2%. The motion direction is estimated with an average SD of 0.3%, and the bias is decreasing linearly from -1.7% at -13° to -3.2% at 13°. These results show that the method is capable of accurately estimating the velocity and direction of the tissue motion. The linear decrease in the direction estimate indicates the algorithm is slightly dependent on imaging angle. Also it should be noted that the higher SD around -5° is caused by a few false estimates in the bottom of the image. False peaks are likely to occur due to the finite window length and decorrelation of the signals being correlated [19], [20].

A section of the reconstructed B-mode images are shown in Fig. 6. The figure shows the uncompensated (left) and compensated (right) images in comparison to the reference image (middle) in which the scatterers were stationary during the entire acquisition. As shown the image quality in the uncompensated image is lost completely, and the cysts are nowhere present in this image. After motion compensation, the image quality has successfully been recovered with only minimal distortion of the cysts.

The simulation results presented above show that the method can accurately estimate the velocity and direction of the tissue motion, and the image quality can be fully recovered when these estimates are used to compensate the B-mode image. It should be noted though, that these results are obtained without the presence of receiver noise. To evaluate the performance in presence of noise, the estimation was performed on the same data while adding -20 dB Gaussian noise to the RF channel data. Since 128 elements are used on receive, this corresponds to approximately a 0 dB SNR in the directional lines, when no motion is present. The results of the velocity and direction estimation in this case are shown in Fig. 7. As expected, the performance drops, when the SNR decreases, since the variance of the correlation estimate is inversely proportional to SNR [19]. For the velocity estimation, the relative bias has increased to -1.9% in average and the average SD is 2%, while the relative bias and SD of the direction estimates

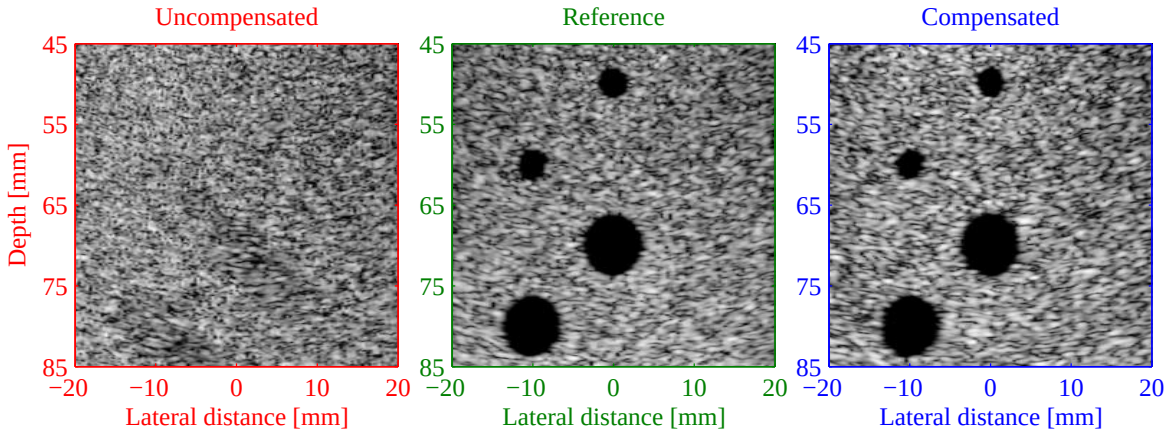

Fig. 6. B-mode images of the simulated cyst phantom with 15 cm/s motion at a $45°$ angle. Left: Uncompensated, Middle: Reference (stationary phantom). Right: Compensated. The dynamic range is 60 dB.

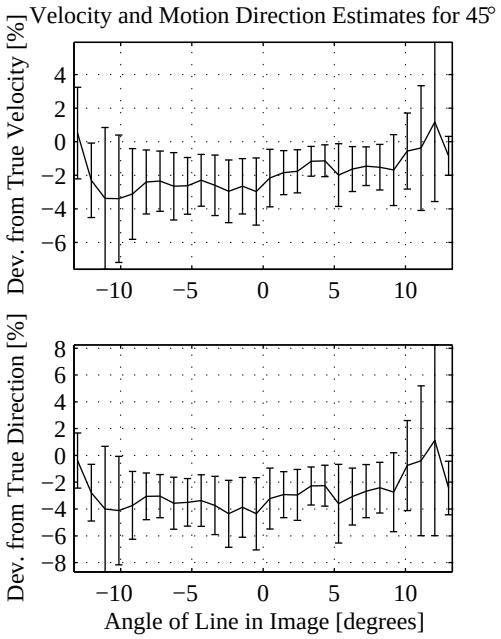

Fig. 7. Results of the velocity and direction estimation in the presence of -20dB Gaussian channel noise. The top figure shows the relative bias $\pm$ 1 SD of the velocity estimation, and the bottom figure shows the relative bias $\pm$ 1 SD of the direction estimate ($\hat{\theta}_{l_{int}}$). Both figures are plottet as a function of image angle.

are -2.8% and 2.6%, respectively.

B. Phantom Experiments

In comparison to the simulation presented above a phantom measurements was done with an imposed velocity of approximately 15 cm/s at a 45° angle. The motion was applied to the phantom using the positioning system as explained in Section III, and the estimation scheme with 8 E-mode emissions repeated 12 times was employed as in the simulation. The angular size of the image area was 26° starting at a depth of 2 cm until 10 cm. As explained previously the motion was estimated at 2 mm range intervals along lines within the whole image area separated by 1 degree. This therefore corresponds to 41 estimation points along 27 lines.

The results of the velocity and direction estimation are plotted in Fig. 8. The average bias of the velocity estimate is -6.9% and the average SD is 5.4%. The direction is found with a bias of -8.4% and a SD of 6.6%. These numbers are based on the 41 independent estimates along each line.

The reconstructed B-mode images are shown in Fig. 9, where the uncompensated image is shown to the left, the reference image (stationary target) is displayed in the middle, and the compensated image is presented to the right.

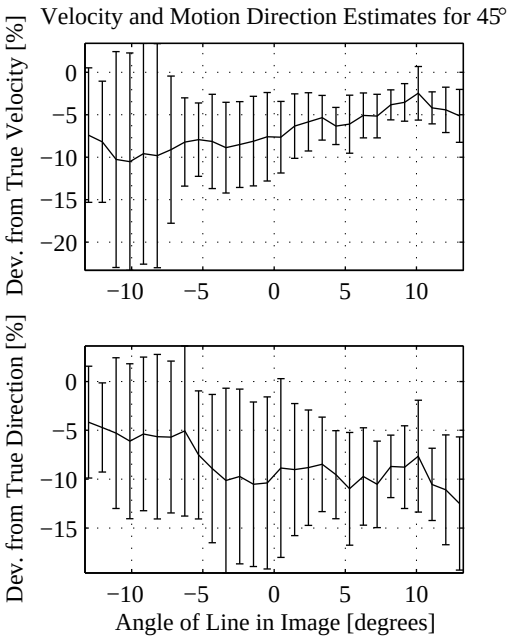

Fig. 8. Results of the velocity and direction estimation for the phantom measurement with true velocity and motion direction of 15 cm/s and 45°, respectively. The top figure shows the relative bias ± 1 SD of the velocity estimation in percent deviation from the true velocity, and the bottom figure shows the relative bias ± 1 SD of the direction estimate ($\hat{\theta}_{l_{int}}$) in percent deviation from the true angle. Both figures are plottet as a function of image angle.

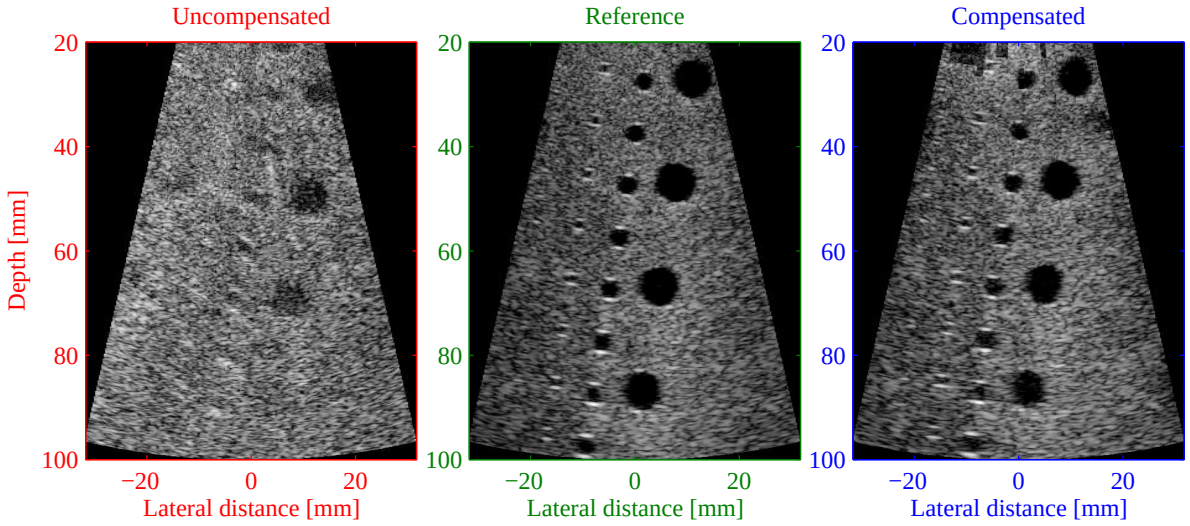

Fig. 9. B-mode images of the scanned tissue mimicking cyst phantom with imposed tissue motion of 15 cm/s at a $45°$ angle. Left: Uncompensated, Middle: Reference (stationary phantom). Right: Compensated.

Clearly, the motion has destroyed the image quality in the uncompensated image, since the motion has caused the low resolution images to be summed incoherently. Comparing the reference image and the compensated image a significant portion of the image quality has been recovered after motion compensation. There are some artifacts in the beginning of the image, which are due to false estimates, and at depths beyond 80 mm the contrast resolution has not been entirely recovered. The difference in contrast resolution between the reference and corrected image is on average -0.65% for the 4 mm cysts, where the contrast resolution CR was calculated by

$$CR = 1 - \frac{I_c}{I_s} \tag{15}$$

where I_c is the intensity inside the cyst, and I_s is the intensity of the surrounding speckle within a region of the

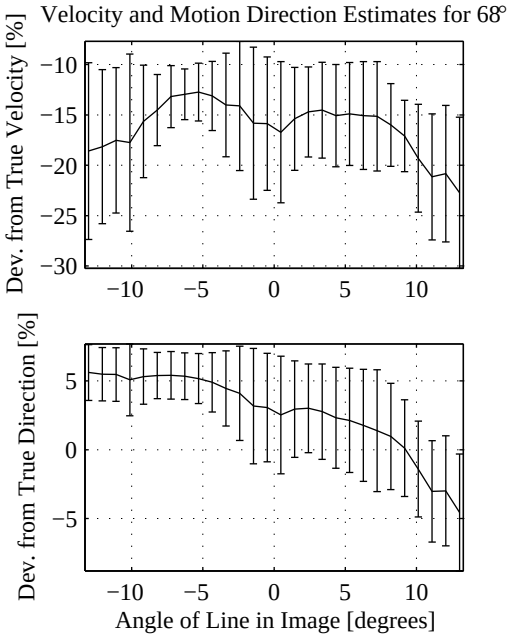

Fig. 10. Velocity and direction estimates for the phantom measurement with tissue velocity of 5 cm/s and direction of 68°. The top figure shows the relative bias ± 1 SD of the velocity estimation, and the bottom figure shows the relative bias ± 1 SD of the direction estimate ($\hat{\theta}_{l_{int}}$). Both figures are plottet as a function of estimation angle.

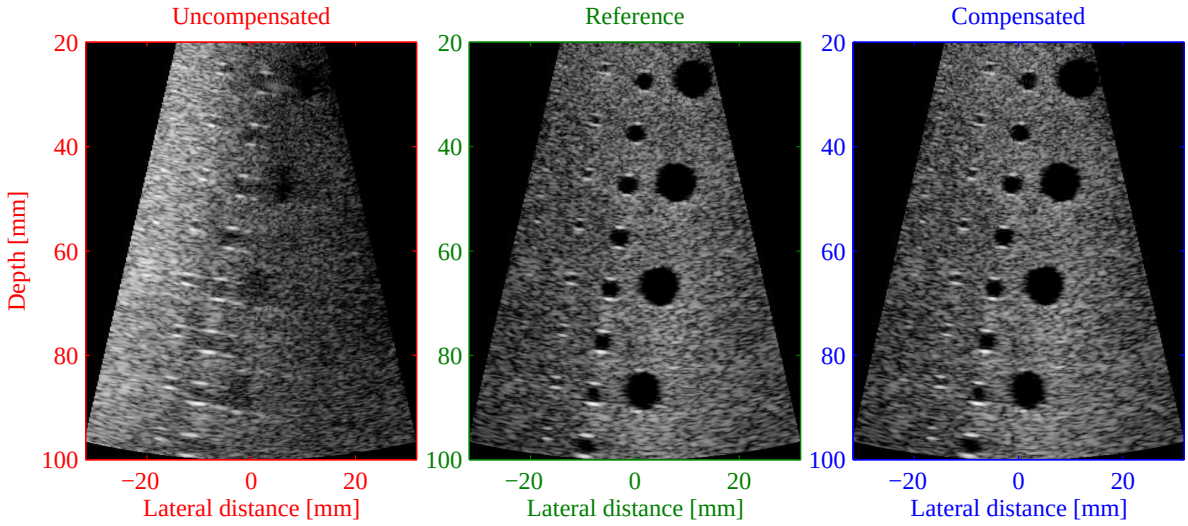

Fig. 11. B-mode images of the scanned tissue mimicking cyst phantom with imposed tissue motion of 5 cm/s at a 68° angle. Left: Uncompensated, Middle: Reference (stationary phantom). Right: Compensated.

same size as the cyst. Thus, the contrast resolution is on average slightly lower in the corrected image.

Tissue velocities up to 15 cm/s would possibly be observed in cardiac imaging applications. In abdominal imaging, the velocity will, however, be significantly lower. To evaluate the performance of the approach at a lower tissue velocity, a second phantom experiment was done. The smallest step size of the positioning system was applied (see Section III for details) and with a pulse repetition frequency of 4 kHz this corresponds to a velocity and direction of approximately 5 cm/s and 68°, respectively. Since the velocity is lower, the scatterers will also move less, and thus more E-mode emissions can be used to increase the SNR of the directional lines. Thus, 16 E-mode emissions were used with the number of repetitions N_{seq} equal to 6.

The bias and SD of the velocity and direction estimation are plotted in Fig. 10, and the reconstructed B-mode images are shown in Fig. 11. The average bias of the estimated velocities is -16% and the average SD is 5.5%, while the bias of the direction estimates ranges from 5% to -5% with an average SD of 3.1%. It is likely that this

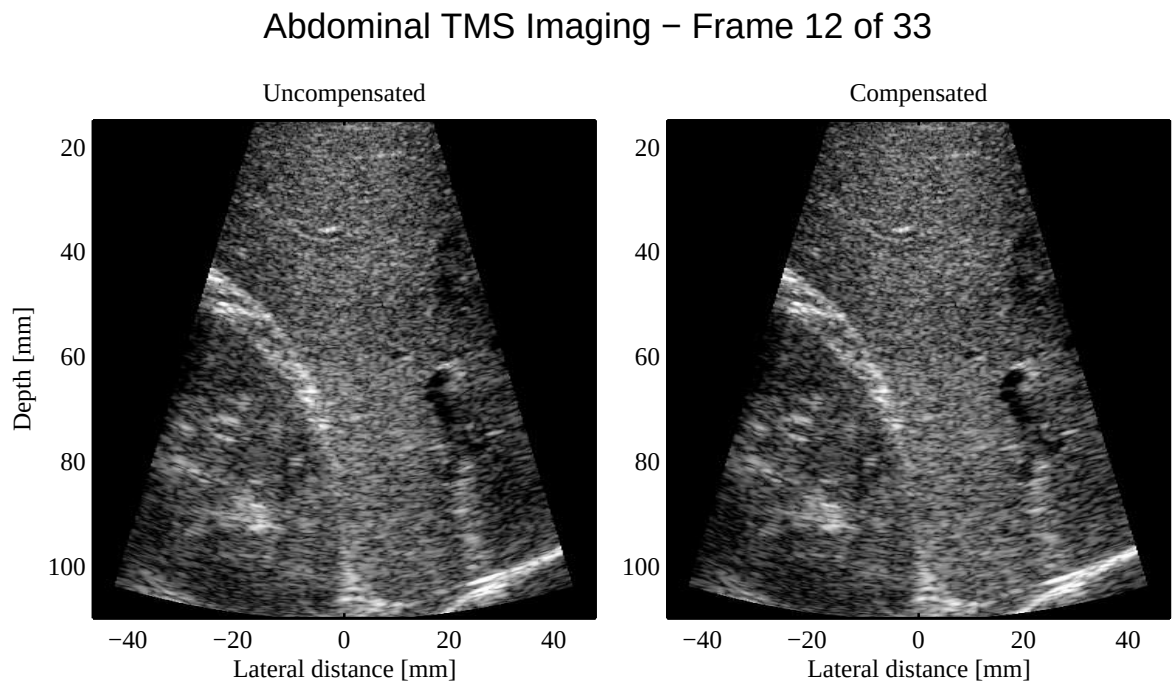

Fig. 12. Abdominal B-mode images before (left) and after (right) motion compensation at an acquisition point with low tissue motion. The images show a longitudinal section of the right liver lobe containing a cross section view of the hepatic vein (right part), longitudinal section of a portal vein branch (top central part), the kidney, and diaphragm at the lower right corner.

underestimation of the velocity and overestimation of the direction is caused by misalignment of the transducer with the phantom. Although the transducer was mounted in a holder which contained markers matched to the transducer, some degrees of freedom was still present and accurate alignment had to be done by eye. Therefore, the transducer could easily have been rotated a couple of degrees. Nevertheless, the reconstructed B-mode images show that the direction and velocity found by the estimator is correct, and the image quality has been fully recovered in the compensated image. This gives further support to the misalignment argument. The difference in contrast resolution between the reference and corrected image is on average 3.5% for the 4 mm cysts, which indicated a slightly better contrast resolution in the corrected image. In general, it should not be possible to improve the contrast resolution beyond the reference image. Thus, it is likely that the difference is caused by slight variations in the speckle brightness between the two images.

C. In-Vivo Experiments

The phantom measurements presented above showed that the velocity and direction of the tissue motion can be estimated, and that the estimates were accurate enough to fully recover the image quality after motion compensation.

In a clinical study of convex TMS imaging published by the authors recently [8], it was observed that tissue motion in abdominal scannings did not have a significant impact on the image quality. In particular, the acquired movie sequences showed no obvious motion artifacts. Some flashing artifacts were reported, which were believed to be caused by tissue motion, but the diagnostic value of the images was not directly affected by these according to the medical doctors who evaluated the results. These abdominal measurements only contained tissue motion created naturally by the patient, and the transducer was therefore kept steady by medical doctor during the scannings. To make the imaging situation more realistic in a clinical sense, the abdominal measurement performed here included freehand motion of the transducer as mentioned previously. Even with freehand motion during scanning the maximum velocity was expected to be around 5 cm/s, and thus the estimation sequence with 16 E-mode emissions was used.

Figures 12 and 13 show two frames from the acquired movie sequence, where the uncompensated images are shown to the left and the corrected images to the right. The images show a longitudinal section of the right liver lobe containing a cross section view of the hepatic vein (right part), longitudinal section of a portal vein branch (top central part), the kidney, and diaphragm at the lower right corner.

Fig. 12 correspond to the point in the acquisition at which the tissue velocity was smallest. The highest velocity was estimated to 3.1 cm/s. The image quality of both images is comparable, indicating that motion did not have

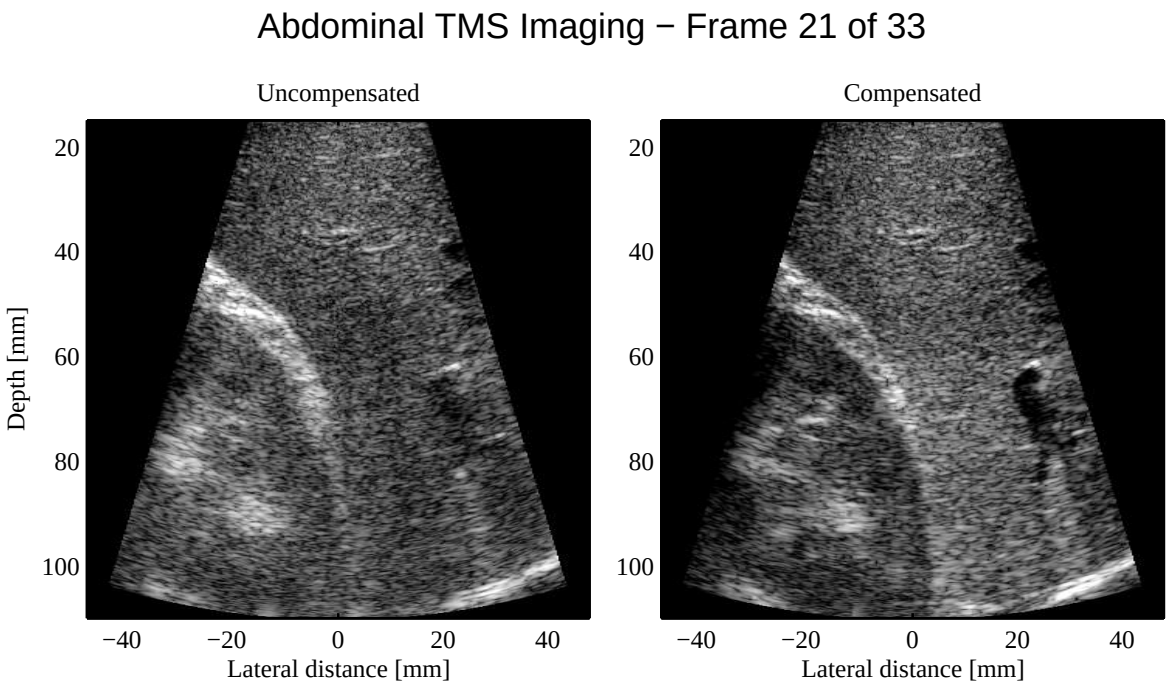

Fig. 13. Abdominal B-mode images before (left) and after (right) motion compensation at an acquisition point with high tissue motion. The images show the same structures as described in Fig. 12.

a significant influence here, but the compensated image has a sharper appearance with improved detail resolution. This is especially noticed along the kidney boarder and by comparing the areas containing the hepatic vein in the right part of the images.

Fig. 13 shows the images corresponding to the point with the largest tissue velocities, which was estimated to 6.6 cm/s. Here, significant loss in image quality is observed in the uncompensated image, where the hepatic vein has almost disappeared and the kidney has a smeared appearance. In the corrected image, the shape of the vessel has been regained and the interior of the kidney including its boarders are fully re-established. Thus, the image quality has been successfully recovered, which demonstrated the capabilities of the motion compensation approach.

When evaluating the entire movie sequence it was observed that the flashing artifacts reported in the clinical study have been removed after motion compensation. Thus, it can be concluded that these flashes, which occurred as fluctuations in the image intensity between uncompensated images, are indeed caused by incoherent summation due to tissue motion.

V. Conclusion

This paper presented a method for 2D tissue motion compensation of STA images. The method was designed to find the tissue velocity and motion direction by utilizing the high correlation that exists between high resolution images acquired using the same emission sequence. By cross-correlating lines beamformed along different angular directions at each image point, the tissue velocity and motion direction was found for the angle at which the highest correlation was observed. To obtain continuous imaging, the motion estimation sequence was interleaved with the B-mode emission sequence used in normal STA imaging. Motion correction was performed by tracking the position of the image pixels in each low resolution image using the estimated velocities and directions, hereby obtaining coherent summation of the low resolution images.

The performance of the approach was evaluated primarily using phantom and in-vivo measurements using the experimental ultrasound scanner RASMUS. The phantom measurements were performed by imposing artificial tissue motion using a three dimensional positioning system. Two situations were investigated with tissue velocities of 15 cm/s and 5 cm/s at motion angles of 45 degrees and 68 degrees, respectively. The results showed that the velocity and motion direction can be estimated in both cases, and that the image quality can be fully recovered after motion compensation. Compared to the reference image, the improvement in contrast resolution after correction was -0.65% and 3.54% for the two cases, respectively. The in-vivo measurement was performed abdominally and included freehand transducer motion applied by the medical doctor during the acquisition to emulate a real clinical situation. The results showed that tissue motion does in fact have a significant influence on the image quality of

STA images, if the motion is severe. Using the estimated velocities and motion directions, the image quality was fully restored after motion compensation, resulting in improvements in both image contrast and image sharpness.

It is worth noting that since the motion estimation approach presented here is based on the same principles as those applied for synthetic aperture blood flow imaging in [15], it can also be used for continuous blood flow imaging with none or only slight modifications to the emission sequence. This is the topic of future research.

Based on the results presented here it is concluded that the presented approach can be applied to perform successful 2D tissue motion compensation, and, thus, it can retain the advantages of synthetic aperture imaging when scanning moving targets.

ACKNOWLEDGMENTS

This work was supported by grants 9700883 and 9700563 from the Danish Science Foundation, by Ph.D. grant 11-3160-55173 from the Technical University of Denmark, and by B-K Medical A/S, Herlev, Denmark. The authors would like to thank M.D. Morten Høgholm Pedersen for performing the in-vivo scanning.

REFERENCES

[1] M. O'Donnell and L. J. Thomas, "Efficient synthetic aperture imaging from a circular aperture with possible application to catheter-based imaging," *IEEE Trans. Ultrason., Ferroelec., Freq. Contr.*, vol. 39, pp. 366–380, 1992.

[2] M. Karaman, P. C. Li, and M. O'Donnell, "Synthetic aperture imaging for small scale systems," *IEEE Trans. Ultrason., Ferroelec., Freq. Contr.*, vol. 42, pp. 429–442, 1995.

[3] K. L. Gammelmark and J. A. Jensen, "Multielement synthetic transmit aperture imaging using temporal encoding," *IEEE Trans. Med. Imag.*, vol. 22, no. 4, pp. 552–563, 2003.

[4] Y. Takeuchi, "An investigation of a spread energy method for medical ultrasound systems - part one: theory and investigations.," *Ultrasonics*, pp. 175–182, 1979.

[5] M. O'Donnell, "Coded excitation system for improving the penetration of real-time phased-array imaging systems," *IEEE Trans. Ultrason., Ferroelec., Freq. Contr.*, vol. 39, pp. 341–351, 1992.

[6] T. X. Misaridis and J. A. Jensen, "An effective coded excitation scheme based on a predistorted FM signal and an optimized digital filter," in *Proc. IEEE Ultrason. Symp.*, 1999, vol. 2, pp. 1589–1593.

[7] K. L. Gammelmark and J. A. Jensen, "Synthetic transmit aperture imaging using convex transducer arrays," *IEEE Trans. Ultrason., Ferroelec., Freq. Contr.*, p. Submitted, 2004.

[8] M. H. Pedersen, K. L. Gammelmark, and J. A. Jensen, "Preliminary in-vivo evaluation of convex array synthetic aperture imaging," in *Proc. SPIE - Progress in biomedical optics and imaging*, 2004, pp. 33–43.

[9] M. H. Pedersen, K. L. Gammelmark, and J. A. Jensen, "In-vivo evaluation of convex array synthetic aperture imaging," *Ultrasound Med. Biol.*, p. Submitted, 2004.

[10] G. E. Trahey and L. F. Nock, "Synthetic receive aperture imaging with phase correction for motion and for tissue inhomogenities - part II: effects of and correction for motion," *IEEE Trans. Ultrason., Ferroelec., Freq. Contr.*, vol. 39, pp. 496–501, 1992.

[11] H. Ş. Bilge, M. Karaman, and M. O'Donnell, "Motion estimation using common spatial frequencies in synthetic aperture imaging," in *Proc. IEEE Ultrason. Symp.*, 1996, pp. 1551–1554.

[12] M. Karaman, H. Ş. Bilge, and M. O'Donnell, "Adaptive multi-element synthetic aperture imaging with motion and phase aberation correction," *IEEE Trans. Ultrason., Ferroelec., Freq. Contr.*, vol. 42, pp. 1077–1087, 1998.

[13] K. S. Kim, J. S. Hwang, J. S. Jeong, and T. K. Song, "An efficient motion estimation and compensation method for ultrasound synthetic aperture imaging," *Ultrason. Imaging*, vol. 24, pp. 91–99, 2002.

[14] S. I. Nikolov and J. A. Jensen, "Velocity estimation using synthetic aperture imaging," in *Proc. IEEE Ultrason. Symp.*, 2001, pp. 1409–1412.

[15] J. A. Jensen and S. I. Nikolov, "Transverse flow imaging using synthetic aperture directional beamforming," in *Proc. IEEE Ultrason. Symp.*, 2002, pp. 1488–1492.

[16] K. L. Gammelmark and J. A. Jensen, "Experimental study of convex coded synthetic transmit aperture imaging," in *Proc. IEEE Ultrason. Symp.*, 2002, pp. 1573–1576.

[17] J. A. Jensen, "Velocity vector estimation in synthetic aperture flow and B-mode imaging," in *IEEE International Symposium on Biomedical imaging from nano to macro*, 2004, pp. 32–35.

[18] J. A. Jensen, O. Holm, L. J. Jensen, H. Bendsen, H. M. Pedersen, K. Salomonsen, J. Hansen, and S. Nikolov, "Experimental ultrasound system for real-time synthetic imaging," in *Proc. IEEE Ultrason. Symp.*, 1999, vol. 2, pp. 1595–1599.

[19] W. F. Walker and G. E. Trahey, "A fundamental limit on delay estimation using partially correlated speckle signals," *IEEE Trans. Ultrason., Ferroelec., Freq. Contr.*, vol. 42, no. 2, pp. 301–308, March 1995.

[20] J. A. Jensen, *Estimation of Blood Velocities Using Ultrasound: A Signal Processing Approach*, Cambridge University Press, New York, 1996.

[21] S. G. Foster, P. M. Embree, and W. D. O'Brien, "Flow velocity profile via time-domain correlation: Error analysis and computer simulation," *IEEE Trans. Ultrason., Ferroelec., Freq. Contr.*, vol. 37, pp. 164–175, 1990.

[22] W. F. Walker and G. E. Trahey, "The application of k-space in pulse echo ultrasound," *IEEE Trans. Ultrason., Ferroelec., Freq. Contr.*, vol. 45, pp. 541–558, 1998.

[23] M. Karaman, A. Atalar, and H. Köymen, "VLSI circuits for adaptive digital beamforming in ultrasound imaging," *IEEE Trans. Med. Imag.*, vol. 12, pp. 711–720, 1993.

[24] J. A. Jensen and N. B. Svendsen, "Calculation of pressure fields from arbitrarily shaped, apodized, and excited ultrasound transducers," *IEEE Trans. Ultrason., Ferroelec., Freq. Contr.*, vol. 39, pp. 262–267, 1992.

[25] J. A. Jensen, "Field: A program for simulating ultrasound systems," *Med. Biol. Eng. Comp.*, vol. 10th Nordic-Baltic Conference on Biomedical Imaging, Vol. 4, Supplement 1, Part 1, pp. 351–353, 1996b.

APPENDIX

B

Conference Articles

B.1 Multi-Element Synthetic Transmit Aperture Imaging using Temporal Encoding

This paper was presented at the conference *SPIE - Progress in biomedical optics and imaging* in San Diego, California, February 2002, and published in the corresponding proceedings on pages 25-36.

Multi-Element Synthetic Transmit Aperture Imaging using Temporal Encoding

Kim L. Gammelmark and Jørgen A. Jensen

Center for Fast Ultrasound Imaging, Ørsted•DTU, Build. 348,
Technical University of Denmark, 2800 Kgs. Lyngby, Denmark

ABSTRACT

A new method to increase the signal-to-noise-ratio (SNR) of synthetic transmit aperture (STA) imaging is investigated. The new approach is called temporally Encoded Multi-Element STA imaging (EMESTA). It utilizes multiple elements to emulate a single transmit element, and the conventional short excitation pulses are replaced by linear FM signals. Simulations using Field II and measurements are compared to linear array imaging. A theoretical analysis shows a possible improvement in SNR of 17 dB. Simulations are done using an 8.5 MHz linear array transducer with 128 elements. Spatial resolution results show better performance for EMESTA imaging after the linear array focus. Both methods have similar contrast performance. Measurements are performed using our experimental multi-channel ultrasound scanning system, *RASMUS*. The designed linear FM signal obtains temporal sidelobes below -55 dB, and SNR investigations show improvements of 4-12 dB. The depth performance is investigated using a multi-target phantom. Results show a 30 mm increase in penetration depth with improved spatial resolution. In conclusion, EMESTA imaging significantly increases the SNR of STA imaging, exceeding that of linear array imaging.

Keywords: Ultrasound, linear array imaging, synthetic transmit aperture imaging, multi-element defocusing, linear FM signals, temporal sidelobe reduction, Field II, experimental ultrasound scanning system.

1. INTRODUCTION

One of the main problems in ultrasound imaging is the tradeoff between penetration depth and spatial resolution. The resolution is improved as the frequency increases, but the attenuation in soft tissue also increases with increasing frequency. Increasing the peak pressure is not possible since the Food and Drug Administration (FDA) has introduced restrictions on the maximum intensities, which may occur in the body, to avoid damage to the tissue and pain to the patient. For the conventional imaging techniques like *linear array imaging* the peak amplitude of the short excitation pulses used can, therefore, not be increased infinitely to overcome the loss in penetration depth, when high frequency transducers are used. This is because the spatial-peak-temporal-peak intensity (I_{sptp}) is much higher than the spatial-peak-temporal-average intensity (I_{spta}) for these systems due to the transmit focusing. For B-mode imaging, the I_{sptp} limit is very often reached much earlier than the I_{spta} limit for these systems, which limits the amplitude of the excitation pulse. To increase the penetration depth, I_{spta} must be increased. This is done by increasing the length of the transmitted pulse. For this purpose the conventional pulse cannot be used, since the axial resolution is directly proportional to the pulse length (for short pulse systems). Thus, some type of temporal encoding is necessary. This is offered by the linear FM signal, which has been used in radars for decades, because of its compression ability. These signals have recently been applied in ultrasound scanners, and they have shown good performance in terms of increasing the penetration depth, while maintaining the spatial resolution.[1–3]

Generally, linear array imaging systems obtain good spatial resolution due to the application of dynamic receive focusing. The resolution can, however, be improved by increasing the number of transmit foci. This is often done in modern ultrasound scanners at the expense of a reduction in the frame rate proportional to the number of foci. One way to obtain high spatial resolution, while keeping the frame rate high, is to use the *synthetic transmit aperture (STA) imaging* technique. The inherent nature of this technique makes it possible

Send correspondence to Kim L. Gammelmark, E-mail: klg@oersted.dtu.dk

to generate images with dynamic transmit and receive focusing using only a few transmissions. Therefore, STA imaging offers very high frame rates, which makes it suitable for real-time 3-D volumetric imaging. A problem in STA imaging is, however, the low signal-to-noise-ratio (SNR), due to the application of a single transmit element*. This means that the penetration depth obtained by STA imaging is much lower than that obtained by linear array imaging, which significantly limits its clinical application. However, if the SNR can be increased to that of linear array imaging, images with better image quality can be generated, while keeping a high frame rate. For this purpose the linear FM signal can be applied with great advantage. Since no focusing is applied in transmit, I_{sptp} is no longer the main problem, and therefore the amplitude can be increased. Also, previous research has shown[4–6] that the application of multi-element subapertures in STA imaging to emulate a single element transmission yields good spatial resolution results and also increases the SNR proportional to the number of elements used in the subaperture. Therefore, the purpose of this study is to investigate the application of both these techniques in STA imaging and make a comparison to linear array imaging. Both simulations using Field II and measurements using our experimental multi-channel ultrasound scanner are used for the investigation.

2. SYNTHETIC TRANSMIT APERTURE IMAGING

In conventional STA imaging a single element is used at each transmission to produce a broad beam that interrogates a large region of the medium. The echoes resulting from scattering in the medium are recorded using all elements in the aperture, and the procedure is repeated until a desired number of element have been used for transmission. For each transmission the echoes received by each element in the aperture contain information about all scatterers in the interrogated region, and since no focusing has been applied on transmit, the receive aperture can be steered in any direction and focused at any point within this region. That is, a complete set of dynamically focused receive beams can be formed (simultaneously) in all directions in the region. These lines constitute a full image with low lateral resolution due to the single transmit element. The individual images are dynamically focused on transmit in a similar manner and subsequently summed to form the final high resolution image.

2.1. STA Beamforming

To describe STA beamforming in more detail, let $r_{mn}(k)$ be the digitized signal received by element n when transmitting with element m. Also, let $\tau_n^l(k)$ be the dynamic focusing times for receive element n and line l in the low resolution image. Then, each line in the low resolution image for transmit element m is calculated by

$$s_m^l(k) = \sum_{n=1}^{N} W_n(k)\, r_{mn}\big(k - \tau_n^l(k) f_s\big)\,, \qquad l = 1, 2, 3, \ldots, L \tag{1}$$

where $W_n(k)$ is the dynamic apodization values for receive element n, N is the number of receive channels, and L is the number of lines in the image. This is a formulation of the conventional *delay-and-sum beamformer*. If the product $\tau_n^l(k) f_s$ is not an integer, interpolation is needed to find the correct value.

After the low resolution images for all M transmit elements have been beamformed, the final high resolution image is created by delaying and summing the corresponding lines from each low resolution image. In particular,

$$\begin{aligned} S^l(k) &= \sum_{m=1}^{M} W_m(k)\, s_m^l\big(k - \tau_m^l(k) f_s\big) \\ &= \sum_{m=1}^{M} W_m(k) \sum_{n=1}^{N} W_n(k)\, r_{mn}\big(k - \tau_n^l(k) f_s - \tau_m^l(k) f_s\big) \\ &= \sum_{m=1}^{M} \sum_{n=1}^{N} W_m(k) W_n(k)\, r_{mn}\big(k - \tau_n^l(k) f_s - \tau_m^l(k) f_s\big)\,, \qquad l = 1, 2, 3, \ldots, L \end{aligned} \tag{2}$$

*Another problem can be motion artifacts, but this is not considered here.

where $W_m(k)$ is the apodization value for transmit element m, and $\tau_m^l(k)$ is the dynamic focusing times for transmit element m and line l. Since motion compensation is assumed unnecessary, (2) suggests that the high resolution lines can be composed sequentially as the individual transmissions are acquired.

3. TEMPORALLY ENCODED MULTI-ELEMENT STA IMAGING

The objective of this study is to investigate a new approach to increase the SNR of conventional STA imaging. It is called *temporally Encoded Multi-Element STA imaging* (EMESTA), and it is based on the combination of multi-element STA imaging with coded excitation waveforms. These two approaches are described briefly in turn in the following.

3.1. Multi-Element STA Imaging

The major drawback of the STA imaging approach is the SNR. Since a single element is used at each transmission the SNR is very low compared to e.g. linear array imaging, which significantly limits its clinical application. To overcome this, a subaperture consisting of multiple grouped elements can be used to emulate the radiation pattern of a single (virtual) element, and hereby increase the SNR. This concept is called *Multi-Element Synthetic Transmit Aperture imaging* (MESTA), and has previously been investigated by Karaman et al. with respect to application in hand-held scanners,[4] and by Lockwood et al. with the purpose of 3-D ultrasound imaging.[5] Both groups show that by properly delaying the individual elements in the subaperture, good approximation to the single element beam can be obtained along with a significant improvement in SNR.

The defocusing delay for each subaperture element can be calculated as illustrated in Fig. 1. A virtual

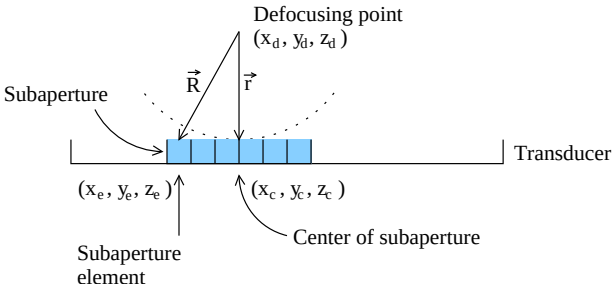

Figure 1. Definition of variables used for calculating the defocusing delays to emulate the radiation pattern of a virtual single element positioned behind the subaperture center.

element position or defocusing point is selected with a certain axial distance to the center of the subaperture, e.g. as a fraction of the subaperture size. Given the element coordinates and the center of the subaperture, the defocusing delay τ_d for a specific element is then calculated by

$$\tau_d = \frac{\left|\vec{R}\right| - |\vec{r}|}{c}, \tag{3}$$

where $\vec{R}$ is the vector from the defocusing point to the element, $\vec{r}$ is the vector from the defocusing point to the subaperture center, and c is the sound speed. The lengths of the two vectors are calculated from Fig. 1 as

$$\left|\vec{R}\right| = \sqrt{(x_e - x_d)^2 + (y_e - y_d)^2 + (z_e - z_d)^2} \tag{4}$$

$$|\vec{r}| = \sqrt{(x_c - x_d)^2 + (y_c - y_d)^2 + (z_c - z_d)^2}. \tag{5}$$

The position of the defocusing point, which produces the best emulation of the single element radiation pattern, is not straight forward to calculate, because it depends on the interference between the waves from the individual

elements and their radiation patterns. On one hand, if the defocusing point is moved away from the subaperture, the beam will become increasingly flat and narrow, and at some point yield a plane wave approximation. But, the defocusing point cannot be moved too close to the subaperture either, because the difference between the transmit delays becomes too large to obtain a coherent wavefront. Therefore, the location of a proper defocusing point should be investigated through simulations. Different apodization schemes can be applied on the subaperture to attenuate certain elements and obtain a better approximation.[7]

3.2. Temporal Encoding using Linear FM Signals

Linear frequency modulated (FM) signals have been used in radars for decades because of their distinctive feature of serving as both a long and a short pulse simultaneously. In medical ultrasound imaging, the first framework for using coded signals to increase the penetration depth in phased array imaging was described by O'Donnell[1] in 1992.

The conventional linear FM signal is given by[8]

$$s(t) = b\cos\left(2\pi\left[f_c t + \frac{B_s}{2\tau_s}t^2\right]\right), \qquad |t| \leq \frac{\tau_s}{2}, \tag{6}$$

where b is the amplitude, f_c is the center frequency, B_s is the -6 dB bandwidth, and τ_s is the duration of the signal. The matched filter to $s(t)$ in (6) is given by

$$h_m(t) = s(-t) = b\cos\left(2\pi\left[f_c t - \frac{B_s}{2\tau_s}t^2\right]\right), \qquad |t| \leq \frac{\tau_s}{2}, \tag{7}$$

Assuming $s(t)$ is the waveform received from a point target, the compressed rf signal becomes[8]

$$r(t) = s(t) * h_m(t) = \frac{b^2\tau_s}{2}\frac{\sin\left(\pi D\frac{t}{\tau_s}\left(1-\frac{|t|}{\tau_s}\right)\right)}{\pi D\frac{t}{\tau_s}}\cos\left(2\pi f_c t\right), \qquad |t| \leq \tau_s \tag{8}$$

where D is the time-bandwidth product. Considering only the envelope of $r(t)$, this has approximately the shape of a sinc-function. Assuming D is large (generally above 20 as mentioned by Blinchikoff and Zverev[8]), the envelope of $r(t)$, $r_e(t)$, becomes a sinc-function

$$r_e(t) = |r(t)| = \frac{b^2\tau_s}{2}\frac{\sin\left(\pi D\frac{t}{\tau_s}\right)}{\pi D\frac{t}{\tau_s}}, \qquad |t| \leq \tau_s, \qquad D > 20. \tag{9}$$

The $\frac{2}{\pi} \approx -4$ dB width of this function is $\delta t = \frac{1}{B_s}$, which shows that the temporal (axial) resolution can be improved by increasing the bandwidth. This is advantageous when applying high bandwidth transducers.

An example of the compression result in (9) is shown as the dashed curve in Fig. 2 (bottom). The influence of a typical 8.5 MHz linear array transducer has been introduced, and the parameters for $s(t)$ and $h_m(t)$ are $f_c = 7$ MHz, $B_s \simeq 7$ MHz, and $\tau_s = 20$ μs. As seen the temporal sidelobes are around -40 dB, which is not sufficient for medical imaging. To reduce the sidelobes, previous research has shown that this can effectively be done by applying amplitude weighting on the linear FM signal and compression filter.[2,9] In this study, a Tukey window with a 10% duration is applied on the linear FM signal, and a Chebychev window with 70 dB relative sidelobe attenuation is applied on the compression filter ($h_m(t)$). The modified linear FM signal and compression filter are shown in the left and right parts of Fig. 2, respectively. The same parameters as given above have been used. The compression output is shown as the solid curve in bottom figure. As seen the temporal sidelobes have been reduced below -60 dB, which is adequate for clinical imaging.

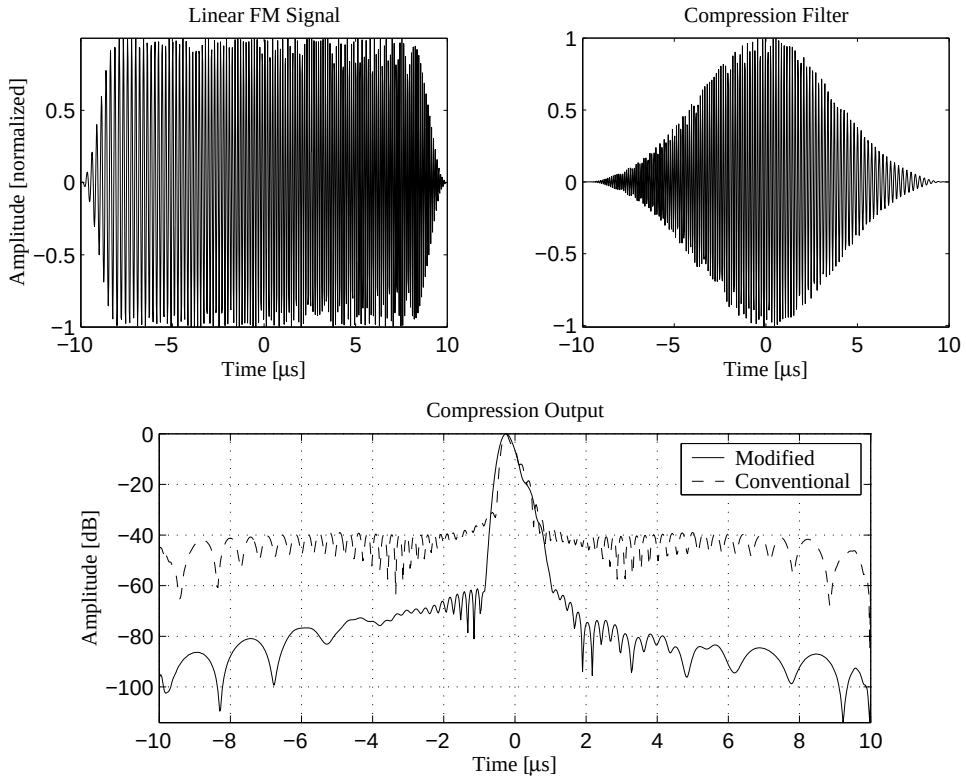

Figure 2. Top left: Modified linear FM signal with a 7 MHz center frequency and 7 MHz bandwidth. A Tukey window with a duration of 10% has been applied. Top right: Modified compression filter using a Chebychev window with 70 dB relative sidelobe attenuation. Bottom: Compression output for the conventional FM signal (dashed) and the modified FM signal (solid). The effect of a typical linear array transducer has been introduced in the compression outputs.

3.3. Signal-to-Noise-Ratio

The (peak) SNR after matched filtering is directly proportional to the energy in the received signal. Also, the peak compression output in (8) is proportional to the energy in the linear FM signal. Thus, the analysis can be simplified by only considering the energy, when comparing the SNR obtained by linear array imaging and EMESTA imaging. Also, the noise in the system is assumed white and uncorrelated, and the received signals from each channel are perfectly phase aligned. In this case there is no difference between transmitting with the same aperture M times or with M different apertures with the same size. Thus, the beamformer can be regarded as simply averaging the received channel signals. Furthermore, attenuation and diffraction effects are not included in this analysis, and it is assumed that no amplitude weighting is applied to the transmitted waveforms and receive filters.

For linear array imaging the energy in the received signal for a single element E_{R_L} from a point target at the acoustic focus is proportional to the number of transmit element N_T squared and the duration of the transmitted pulse τ_l

$$E_{R_L} \sim N_T^2 \tau_l. \tag{10}$$

As showed experimentally by Karaman and coworkers[4] the amplitude of the wavefront created by the defocused subaperture consisting of A_T elements is proportional to $\sqrt{A_T}$. Thus, the energy in the received signal for a single element E_{R_S} for EMESTA imaging is

$$E_{R_S} \sim A_T \tau_s, \tag{11}$$

where τ_s is the duration of the transmitted FM signal. As mentioned above the beamformer is considered as simply averaging the individual channel signals. Let the number of receive channel be N_R, then the SNR in the linear array image is proportional to

$$SNR_{B_L} \sim N_R N_T^2 \tau_l, \tag{12}$$

since the noise is white and uncorrelated between channels. From the description of STA beamforming, (2) states that in EMESTA imaging averaging is done over N_R receive channels and M transmit events. Thus, the SNR in the EMESTA image is proportional to

$$SNR_{B_S} \sim M N_R A_T \tau_s. \tag{13}$$

Taking the ratio between (13) and (12) yields

$$I_B = \frac{SNR_{B_S}}{SNR_{B_L}} \sim \frac{M A_T}{N_T^2} \frac{\tau_s}{\tau_l}. \tag{14}$$

This assumes that the noise is stationary and described by the same probability density function for both systems. If a better SNR is to be obtained, this ratio needs to be greater than 1, thus

$$\tau_s \geq \frac{N_T^2}{M A_T} \tau_l. \tag{15}$$

In this study, a subaperture of $A_T = 33$ elements will be used. The applied FM signal has a duration of $\tau_s = 20$ μs, and the transducer has 128 transmit and receive elements, and thus the number of transmissions will be $M = 96$. Using (14) and a linear array imaging setup of $N_T = 64$, $N_R = 128$, and a 2 cycle sinusoid at 7 MHz, it is found that $I_B \simeq 54.2 \approx 17$ dB. This indicates that a significant increase in SNR is to be expected.

4. SIMULATIONS

The simulations are done using Field II[10] to compare the performance of EMESTA imaging to linear array imaging on a theoretical basis in terms of spatial and contrast resolution.

The transducer model used was a 128 element linear array aperture with a center frequency of 8.5 MHz and a relative bandwidth of 60 %. The pitch is 0.208 mm and the element height is 4.5 mm. The transducer has an elevation lens with a focal point at 25 mm. The impulse response of the receive elements is set to the pulse-echo response measured from a plane reflector using a delta excitation. Thus, the impulse response of the transmit aperture is set to a Dirac delta function.

In linear array imaging a 64 element aperture is used for transmission and all 128 elements are used in receive. A 2 cycles sinusoid at 7 MHz weighted with a Hanning window is used as excitation signal, and no transmit apodization is applied. The received signals are filtered using a matched filter, and beamformed using dynamic receive focusing with updated delay curves for every second sample. The number of lines in the image and their spacing is calculated from the highest spatial frequency of the medium to satisfy the spatial Nyquist theorem.

EMESTA imaging is done using a 33 element subaperture and 128 receive elements, which results in 96 emissions. The excitation signal is the linear FM signal displayed in Fig. 2 (top, left). It has a duration of 20 μs, a center frequency of 7 MHz, and a bandwidth of approximately 7 MHz. The FM signal has been weighted with a Tukey window to reduce the temporal sidelobes. The corresponding compression filter is also shown in Fig. 2 (top, right). A Chebychev window has been applied to reduce the temporal sidelobes in the compression output. The defocusing point is set to $(x_d, y_d, z_d) = (x_c, y_c, d_s)$, where d_s is the size of the subaperture, which has been determined through wavefront simulations.[7] Transmit apodization is applied on the subaperture to reduce the influence of edge waves on the point spread function (PSF). Beamforming is done using dynamic transmit and receive focusing. In both linear array imaging and EMESTA imaging, a modified Hamming window with edge levels at -12 dB is applied as receive apodization.

A wire phantom is simulated to investigate the spatial resolution performance. The wires are located at 20 mm to 120 mm with 5 mm spacing. The transmit focal point for linear array imaging was set to 50 mm. Figure 3 shows the -6 dB lateral (top) and axial resolutions (bottom) as a function of depth for linear array imaging (dashed) and EMESTA imaging (solid) respectively. As expected the lateral performance of EMESTA imaging

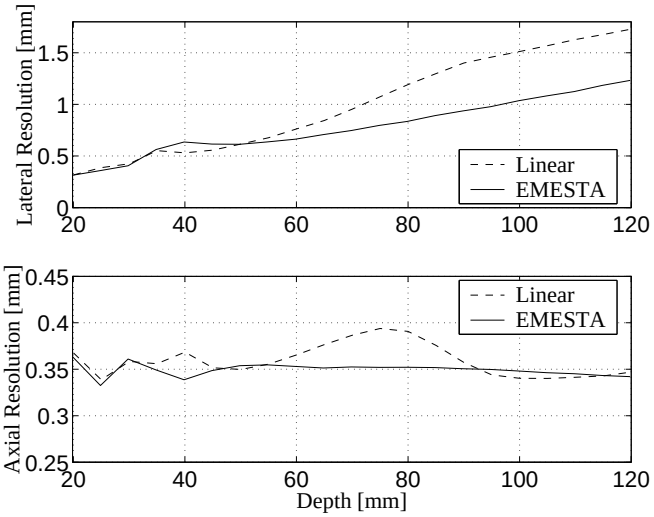

Figure 3. -6dB lateral (top) and axial (bottom) resolution for linear array imaging (dashed) and EMESTA imaging (solid) respectively. The results are obtained from a simulated wire phantom with 5mm spacing between the wires. The transmit focal length for linear array imaging was set to 50mm.

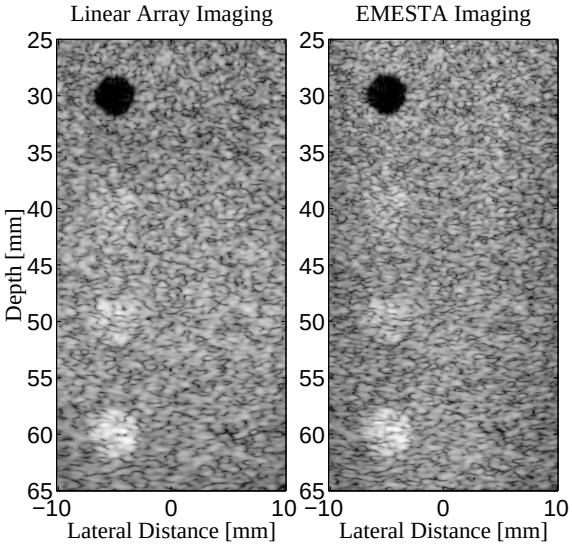

Figure 4. Simulated cyst phantom for linear array imaging (left) and EMESTA imaging (right) containing four cysts at depth 30, 40, 50, and 60 mm with amplitudes -40, 4, 6, and 12 dB above the surrounding speckle respectively. No attenuation effects are included.

is better after the linear array transmit focus, and it improves with depth due to the application of dynamic transmit focusing. At 120mm the lateral resolution has improved by approximately 30%. The performance of the axial resolutions is seen to be close, but the compression mechanism of the linear FM signal is more stable with depth.

The contrast resolution is evaluated by simulating a cyst phantom containing four cysts at depths of 30, 40, 50, and 60 mm with amplitudes of -40, 4, 6, and 12 dB above the surrounding speckle, respectively. No attenuation effects are included. The results are shown in Fig. 4 for linear array imaging (left) and EMESTA imaging (right). The linear array transmit focus was again set to 50mm.

As a measure of the contrast resolution the *contrast-to-noise ratio* (CNR) is used as proposed by Ucar and Karaman[11]

$$CNR = \frac{|\mu_c - \mu_s|}{\sqrt{0.5\left(\sigma_c^2 + \sigma_s^2\right)}}, \tag{16}$$

where μ_c and σ_c^2 are the mean and variance of the intensity inside the target, and μ_s and σ_s^2 are the mean and variance of the intensity within the speckle at the same depth as the target. Figure 4 shows no conspicuous difference, and this observation is also supported by the calculated CNRs, which are summerized in Table 1. From Fig. 4, no significant difference in the speckle size is observed, which is also in accordance with the results in Fig. 3.

Based on the results presented above, it is concluded that the EMESTA imaging and linear array imaging have equal contrast performance, and EMESTA imaging obtains better lateral resolution after the linear array focal point.

5. MEASUREMENTS

The measurements are performed using the experimental multi-channel ultrasound scanning system, *the RASMUS system*, developed at our center. The system has 128 individually programmable transmitters capable of sending arbitrary coded waveforms with a precision of 12 bits at 40 MHz. Sixty-four receive channels can be simultaneously sampled at 12 bits and 40 MHz, and the 2 to 1 multiplexing in the system enables acquisition of 128 channels in real-time over two transmissions. The RASMUS system is remotely accessible and programmed through a developed Matlab interface.

For the measurements a 8.5 MHz linear array transducer is used with 128 elements. The relative bandwidth is approximately 60%, and the pitch is 0.208 mm. The transducer elements have a height of 4.5 mm and an elevation lens with a geometric focal point at 25 mm.

The measurement setups for linear array imaging and EMESTA imaging are the same as those used for the simulations. This has been chosen to enable direct comparison between the measurements and the simulations. The same transmit voltage is used for both linear array imaging and EMESTA imaging, and the filters used for matched filtering and compression of the received signals have been normalized equally to enable a fair comparison.

The linear FM signal used in both the simulations and measurements has been designed to obtain temporal sidelobe levels at approximately -60dB. To evaluate this, a wire phantom containing four wires and water has been scanned. Figures 5 and 6 show the B-mode images and axial projections for linear array imaging and EMESTA imaging respectively. The dynamic range in the B-mode images is 60 dB. As seen the temporal sidelobes have been reduced to approximately -55dB, which is adequate for clinical imaging.

The spatial resolution and SNR performance of EMESTA imaging is evaluated in the presence of attenuation using a multi-target phantom with 0.5 dB/[cm MHz] attenuation. Figure 7 shows the linear array image (left) and EMESTA image (right) of a scanned region containing twisted nylon wires spaced axially by 1 cm. The dynamic range is 50 dB in both images. As seen the penetration depth has significantly been increased using EMESTA imaging. The linear array image has a very low SNR after 70 mm, and the wires are not visible in this region. No apparent noise is present in the EMESTA image, and the wires are thus fully visible throughout the imaged region. This indicates an increase in penetration depth of more than 3 cm.

The lateral and axial resolutions are evaluated for each wire in both images in Fig. 7. The results are shown in Fig. 8, where the lateral resolution is displayed left and the axial resolution in the right figure. As seen EMESTA imaging has a better lateral performance at distances after the linear array transmit focus due to dynamic transmit focusing. Compared to the simulation results in Fig. 3, it is noted that the lateral resolutions follow the same trends, but it is a bit higher in the measurements due to the presence of attenuation. The axial resolution is better for EMESTA imaging throughout the imaged region. This shows that the linear FM signal has a better axial performance in the presence of attenuation than the conventional short excitation pulse. This observation has been reported previously by Misaridis.[12]

The improvement in SNR obtained by EMESTA imaging in water and for a tissue mimicking phantom is shown in Fig. 9. The SNR for water was obtained using the wire phantom data from Figs. 5 and 6. For each image and depth the rms value was calculated resulting in two signal vectors. The noise in the system generated by each imaging method was obtained by scanning a water bath with no reflections. For each imaging method the rms value of the resulting noise images was calculated, resulting in two noise vectors. Taking the ratio

Cyst	Linear Array Imaging	EMESTA Imaging
-40dB	1.9241	1.8151
4dB	0.7420	0.7430
6dB	1.0950	1.1305
12dB	1.9801	1.7992

Table 1: Calculated CNR for simulated cyst phantoms.

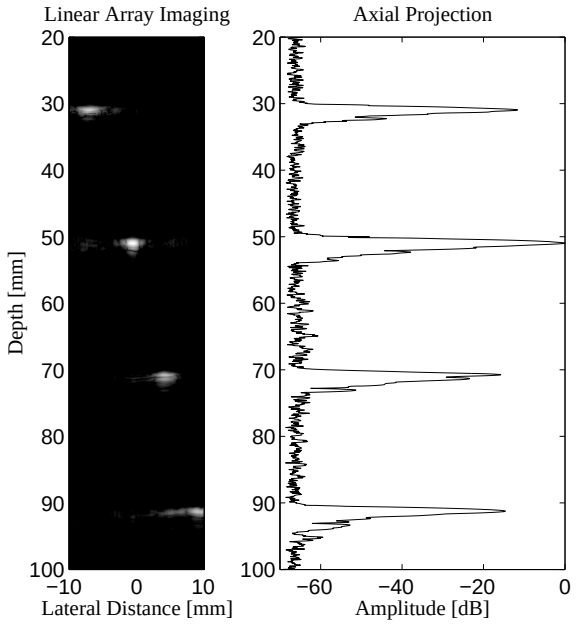

Figure 5. B-mode image and axial projection of scanned wire phantom using linear array imaging. The phantom contains four laterally and axially spaced copper wires and water, and the dynamic range in the B-mode image is 60 dB.

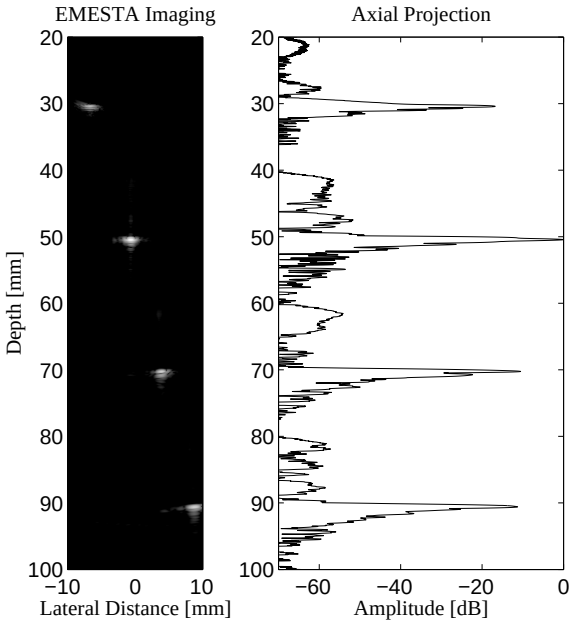

Figure 6. Same as Fig. 5 but for EMESTA imaging. As seen the applied linear FM signal and compression filter yields temporal sidelobes below -55 dB.

between the signal vectors and the noise vectors yields the SNR for each imaging method, and the difference between these SNR curves at the wire locations is the SNR improvement shown as the dashed curve in Fig. 9. The SNR improvement in the tissue mimicking phantom was obtained using the parts of Fig. 7 not containing wires and the generated noise vectors from the water bath. The SNR improvement was evaluated at each depth throughout the image, and the result is shown as the solid curve in Fig. 9. A lowpass filter has been applied on the curve to make it more smooth.

For the water SNR the linear array transmit focus was set to 50 mm, and at this depth the SNR improvement is 8 dB. Compared to the theoretical model proposed earlier, this result does no compare exactly. However, this model did not account for diffraction and amplitude weighting of the FM signal and compression filter. Thus, to obtain a closer correspondance to the measurements, these parameters should be included in the model.

At the linear array focal point in the phantom (40 mm) the improvement in SNR is about 4 dB, but it is significantly larger before and after the focus. At 60 mm an improvement of 12 dB is obtained, and then the ratio starts to decrease approximately linearly until it reaches zero at 95 mm. Note, that the SNR can be improved simply by extending the duration of the linear FM signal. This, however, also extends the dead zone in the beginning of the image, since the transmitters are turned on longer.

To evaluate the contrast resolution of EMESTA imaging, a section of the multi-target phantom containing a +3 dB cyst was scanned. The resulting images are shown in Fig. 10 for linear array imaging (left) and EMESTA imaging (right). The cyst has a 4 mm diameter, and it is located approximately at 65 mm. Because of the reduced penetration depth in the linear array image the cyst is not visible here, but for EMESTA imaging the cyst is slightly visible. This indicates that EMESTA imaging has a slightly better contrast resolution in the presence of attenuation, but this is, however, difficult to determine from this single image and cyst. Therefore, more measurements using a more appropriate phantom are necessary to evaluate the contrast performance.

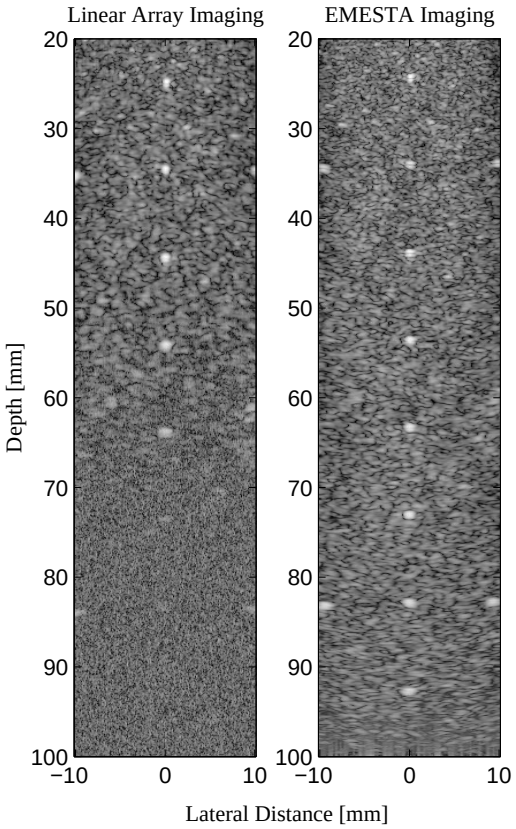

Figure 7. Linear array image (left) and EMESTA image (right) of a scanned multi-target phantom with 0.5 dB/[cm MHz] attenuation. The scanned section contains twisted nylon wires spaced axially by 1 cm throughout the imaged region. The dynamic range is 50 dB.

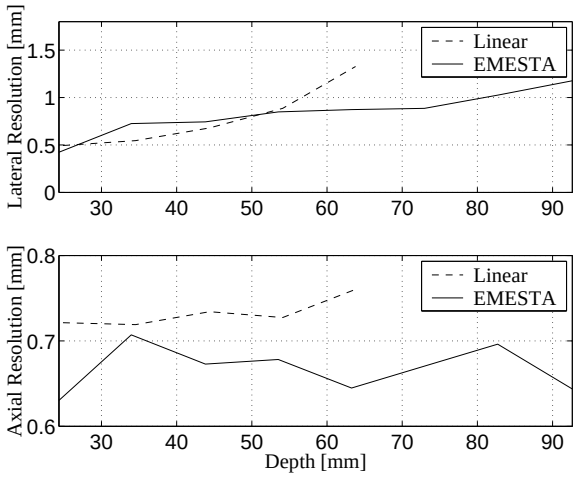

Figure 8. Lateral (top) and axial (bottom) resolution curves for linear array imaging (dashed) and EMESTA imaging (solid). The curves have been obtained by calculating the spatial resolutions for each wire in Fig. 7.

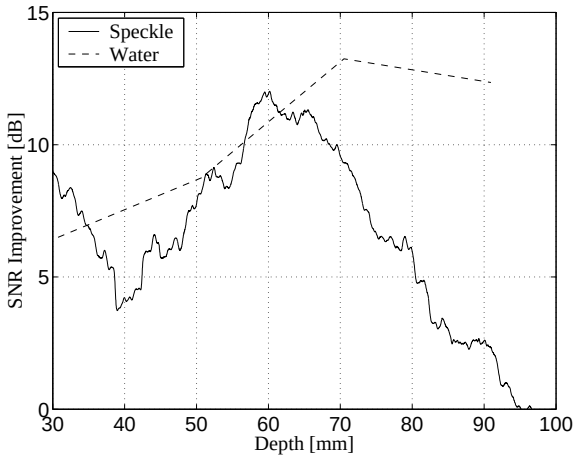

Figure 9. Calculated SNR improvement obtained by EMESTA imaging in water (dashed) and in a tissue mimicking phantom (solid).

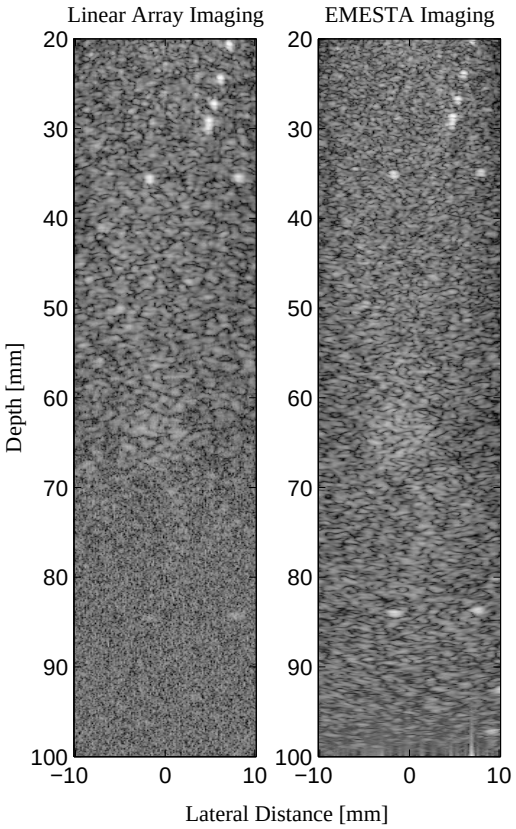

Figure 10. Scanned multi-target phantom containing wires and a +3 dB cyst at 65 mm. The linear array image is shown left and the EMESTA image is shown right. Notice again the improvement in penetration depth.

6. CONCLUSION

In this study, a new approach to increase the SNR of conventional STA imaging has been proposed and investigated. The new imaging approach, EMESTA imaging, utilizes a multiple-elements subaperture to emulate a single transmit element by making a defocused transmission. Furthermore, the conventional short excitation pulses are replaced by linear FM signals with amplitude tapering to reduce the temporal sidelobes resulting from the compression on receive. The approach was compared to linear array imaging, and a theoretical analysis showed that a SNR improvement of 17 dB was possible. Simulations with Field II were done using a 128 linear array with 8.5 MHz center frequency and 60 % bandwidth. The EMESTA approach was setup to use a 33 element subaperture for transmission and a 20 μs modified linear FM signal. In linear array imaging a transmit aperture of 64 element and a 2 cycles sinusoid with Hanning weighting was used. The simulation results showed similar axial resolutions, but the lateral resolution was improved for EMESTA imaging due to the application of dynamic transmit focusing.

An analysis of the contrast resolution showed similar performance. Measurements were performed using our experimental multi-channel ultrasound scanning system, *RASMUS*. The results here showed an improvement in SNR between 4 to 12 dB, and a corresponding increase in penetration depth of more than 3 cm. This was obtained while maintaining a better spatial resolution performance.

In conclusion, the EMESTA imaging approach has shown the capability of significantly improving the SNR, and thus the penetration depth, of conventional STA imaging, exceeding that of linear array imaging. This makes this new approach feasible for clinical imaging and possibly real-time 3D volumetric imaging.

ACKNOWLEDGMENTS

This work was supported by grant 9700883 and 9700563 from the Danish Science Foundation and by B-K Medical A/S, Gentofte, Denmark.

REFERENCES

1. M. O'Donnell, "Coded excitation system for improving the penetration of real-time phased-array imaging systems," *IEEE Trans. Ultrason., Ferroelec., Freq. Contr.* **39**, pp. 341–351, 1992.
2. T. X. Misaridis, K. Gammelmark, C. H. Jørgensen, N. Lindberg, A. H. Thomsen, M. H. Pedersen, and J. A. Jensen, "Potential of coded excitation in medical ultrasound imaging," *Ultrasonics* **38**, pp. 183–189, 2000.
3. T. X. Misaridis, M. H. Pedersen, and J. A. Jensen, "Clinical use and evaluation of coded excitation in B-mode images," in *Proc. IEEE Ultrason. Symp.*, **2**, pp. 1689–1693, 2000.
4. M. Karaman, P. C. Li, and M. O'Donnell, "Synthetic aperture imaging for small scale systems," *IEEE Trans. Ultrason., Ferroelec., Freq. Contr.* **42**, pp. 429–442, 1995.
5. G. R. Lockwood, J. R. Talman, and S. S. Brunke, "Real-time 3-D ultrasound imaging using sparse synthetic aperture beamforming," *IEEE Trans. Ultrason., Ferroelec., Freq. Contr.* **45**, pp. 980–988, 1998.
6. S. I. Nikolov, K. Gammelmark, and J. A. Jensen, "Recursive ultrasound imaging," in *Proc. IEEE Ultrason. Symp.*, **2**, pp. 1621–1625, 1999.
7. K. Gammelmark, "Multi-element synthetic transmit aperture imaging using temporal encoding," Master's thesis, Ørsted•DTU, Technical University of Denmark, Lyngby, Denmark, 2001.
8. H. J. Blinchikoff and A. Zverev, *Filtering in the time and frequency domains*, Wiley, 1976.
9. T. X. Misaridis and J. A. Jensen, "An effective coded excitation scheme based on a predistorted FM signal and an optimized digital filter," in *Proc. IEEE Ultrason. Symp.*, **2**, pp. 1589–1593, 1999.
10. J. A. Jensen, "Field: A program for simulating ultrasound systems," *Med. Biol. Eng. Comp.* **10th Nordic-Baltic Conference on Biomedical Imaging, Vol. 4, Supplement 1, Part 1**, pp. 351–353, 1996b.
11. F. N. Ucar and M. Karaman, "Beam space processing for low-cost scanners," in *Proc. IEEE Ultrason. Symp.*, pp. 1349–1352, 1996.
12. T. Misaridis, *Ultrasound imaging using coded signals.* PhD thesis, Ørsted•DTU, Technical University of Denmark, Lyngby, Denmark, 2001.

B.2 Experimental Study of Convex Coded Synthetic Transmit Aperture Imaging

This paper was presented at the *IEEE International Ultrasonics Symposium* in Münich, Germany, October 2002, and published in the corresponding proceedings on pages 1573-1576.

Experimental Study of Convex Coded Synthetic Transmit Aperture Imaging

Kim Løkke Gammelmark and Jørgen Arendt Jensen*
Center for Fast Ultrasound Imaging, Ørsted•DTU, Build. 348,
Technical University of Denmark, 2800 Kgs. Lyngby, Denmark

Abstract **-** Synthetic transmit aperture imaging is investigated using a convex array transducer. To increase the signal-to-noise ratio, a multi-element subaperture is used to emulate the spherical wave transmission, and the conventional short excitation pulse is replaced by a linear FM signal. The approach is compared to the conventional application of the convex array in commercial scanners. The array used is a commercial 5.5 MHz, 128 element array with 60% bandwidth and λ pitch. For conventional imaging a 64 element transmit aperture is used with a 2 cycle temporally weighted sinusoid as excitation signal. For synthetic aperture imaging an 11 element transmit aperture is used with a 20 μs linear FM signal as excitation. For both methods, 128 elements are used on receive. Measurements are done using our experimental multi-channel ultrasound scanner, RASMUS. Wire phantom measurements show an improvement in lateral resolution of about 30% throughout the image with lower near and far field sidelobe levels. Results from a cyst phantom show big improvements in contrast resolution, and an increase in penetration depth of about 2 cm. In-vivo images of the abdomen of a healthy 27 year old male show slight improvements in image quality, especially in the near field.

I Introduction

It is widely accepted that synthetic transmit aperture (STA) imaging can be used to obtain images with better image quality compared to conventional techniques like phased and linear array imaging. The reason for this is that both transmit and receive beamforming can be applied in STA imaging, while only a single transmit focus combined with receive beamforming is used in the traditional imaging techniques. Consequently, STA beamforming is done using dynamic focusing and apodization in both transmit and receive, which gives better control of the beam shape. However, it is also well known that STA imaging suffers from a low signal-to-noise ratio (SNR) due to the single element transmissions. Recent research has though shown [1] that the combination of existing techniques of multi-element subapertures and temporal encoding can be utilized to increase the SNR to exceed that of the conventional imaging techniques.

Traditionally, STA imaging has been considered for phased array applications [2] and recently linear array imaging [1]. However, only little research on the application of STA imaging with convex array transducers has been published in the open literature [3]. Convex array transducers are generally used for abdominal imaging because of their large field of view and good penetration depth. Extending STA imaging to convex apertures requires some new design considerations because of the more complicated aperture geometry. The advantage is, however, better abdominal images than those obtained by linear and phased arrays, because the convex array is designed specifically for this application.

This paper investigates STA imaging using multi-element subapertures and temporal encoding for a convex transducer array. The method is described in Section II, and the setup for the measurement using our experimental multi-channel ultrasound scanner, RASMUS, are described in Section III. The measurement results for both phantom objects and *in-vivo* imaging are presented in Section IV.

II Theory

In conventional STA imaging a single element is used at each transmission to produce a spherical wave that interrogates a large region of the medium. The echoes are recorded using all elements in the aperture, and the procedure is repeated until a desired number of elements have been used for transmission. For each transmission, the received echoes contain information about all scatterers in the interrogated region. Since no focusing has been applied on transmit, and the exact origin of the spherical wave is known, the receive aperture can be steered in any direction and focused at any point within this region. Therefore, every point in the image can be formed independent of each other, and a full image is obtained for every transmission event with low lateral resolution due to the single transmit element. Taking into account

*This work was supported by grants 9700883 and 9700563 from the Danish Science Foundation, by Ph.D. grant 11-3160-55173 from the Technical University of Denmark, and by B-K Medical A/S, Herlev, Denmark.

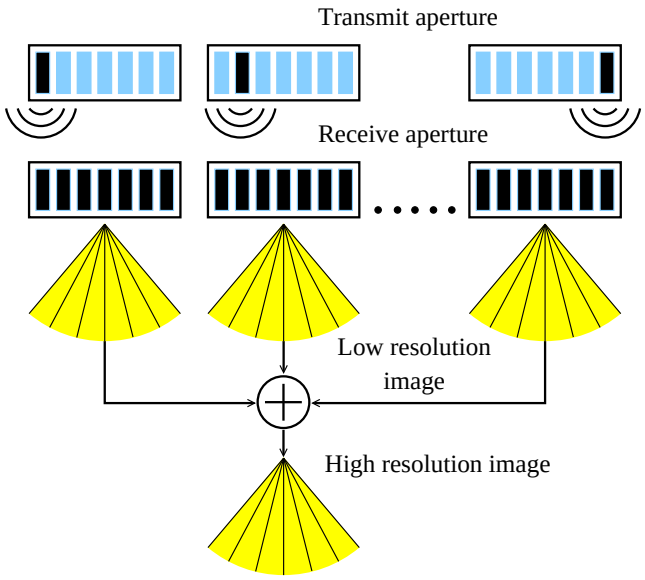

Figure 1: Illustration of the conventional STA imaging principle. At each transmission event a single element is fired, and the echoes from the medium are collected using all elements in the receiving aperture. For each of these transmission events a complete image is beamformed, and these are subsequently summed to form the final high resolution image.

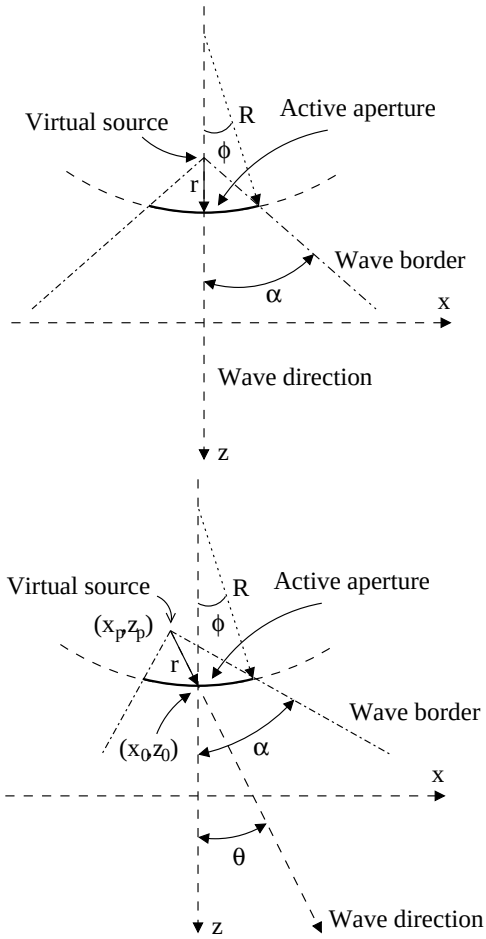

Figure 2: Illustration of two methods for applying multi-element STA imaging to convex arrays. Top: Conventional application where the virtual point source is placed behind the center of the subaperture to produce a symmetric spherical wave. Bottom: Angled transmission where the virtual point source is placed such that the spherical wave propagates at an angle θ.

the full path length between the transmitting element and the receive elements, when calculating the beamforming delays, the individual low resolution images are both dynamically focused on receive, and adjusted to obtain dynamic focusing on transmit in the same operation. Dynamic focusing on transmit is then obtained subsequently by coherently summing the low resolution images which forms the final high resolution image as illustrated in Fig. 1.

The STA imaging approach investigated in this paper combines multi-element STA imaging and linear FM signals with a convex array transducer. This approach has recently been investigated using linear array transducers [1], where the results showed significant improvements in both spatial and contrast resolution. In general, the concept of STA imaging does not depend on the array type, however, the more complicated geometry of the convex array makes it necessary to redesign the use of multi-element subapertures. This is described below.

The multi-element subaperture is utilized to produce a high power spherical wave over a limited angular extend. Traditionally, this is done by placing a virtual point source at a distance r behind the center of the subaperture as illustrated in the top part of Fig. 2. The spherical wave produced is symmetric with an angular extend α, which is determined by r.

Due to the geometry of the array and the shape of the convex array images, a significant part of the energy in the spherical wave will propagate outside the image area when the outer subapertures are used. Thus, to limit the amount of wasted energy, the transmissions can be angled as illustrated in the bottom part of Fig. 2. Here, the virtual point source is moved to the side to obtain a wave direction θ, and at the same time increase α. It is noted, that the wave is no longer symmetric and that the angular extend of the wave α is larger in the direction of the beam. The position of the virtual point source is calculated geometrically as

$$\begin{bmatrix} z_p \\ x_p \end{bmatrix} = \begin{bmatrix} z_0 - r \cdot \cos\theta \\ x_0 - r \cdot \sin\theta \end{bmatrix}, \tag{1}$$

where r is the radial distance to the virtual source given by

$$r = R\left(\frac{\sin\phi - \tan\alpha\,(\cos\phi - 1)}{\tan\alpha\cos|\theta| - \sin|\theta|}\right), \qquad (2)$$

and ϕ is half the angular size of the subaperture. Note, that α and ϕ are always positive, and that the coordinate system used here moves with the subaperture. Also, the directivity pattern of the individual elements will have an influence on the shape of the wave, but this has not been included in the model at this point.

Using this approach the individual transmissions can be directed such that the spherical wave interrogates a larger region of the image, and thus more image points can be beamformed for each transmission. In this study, the wave direction for each transmission is chosen such that the center of the spherical wave travels parallel to the axis of the transducer, i.e. straight down.

III Measurement Setup

The measurements are performed using the experimental multi-channel ultrasound scanning system, *RASMUS* [4]. The system has 128 individually programmable transmitters capable of sending arbitrary coded waveforms with a precision of 12 bits at 40 MHz. Sixty-four receive channels can be sampled simultaneously at 12 bits and 40 MHz, and the 2-to-1 multiplexing in the system enables acquisition of 128 channels in real-time over two transmissions. The system has 16 Gbytes of storage memory in the receivers, which enables the acquisition of several seconds of RF data. The RASMUS system is remotely accessible and programmed through a developed Matlab/C-library interface.

The transducer used for the measurements is a commercial 5.5 MHz convex array transducer with 192 elements and λ pitch. The bandwidth of the elements is 60% relative to the center frequency, and the convex radius of the aperture is 41 mm. The height of the elements is 8 mm, and the array has a lens in the elevation dimension with a fixed focus at 40 mm. Due to the limitation of the RASMUS system, only the central 128 elements of the array are used.

For conventional imaging a 64 elements, Hamming weighted, transmit aperture is used with a fixed focus at 70 mm. A 2 cycle sinusoid at 5.5 MHz weighted with a Hanning window is used as the excitation pulse, and all 128 elements are used on receive and for the subsequent beamformation. For synthetic imaging an 11 element subaperture is used to emulate the spherical wave transmission, and all 128 elements in the aperture are used on receive. The center of the transmit aperture is moved one element after each transmission, which results in a total of 118 emissions. A 20 μs linear FM signal with a center frequency of 5.5 MHz and 90% bandwidth is used as excitation signal. The FM signal has been weighted with a Tukey window to reduce the temporal sidelobes [5].

The conventional data are beamformed using dynamic receive focusing with delay updates for each sample. The RF signals are filtered using a matched filter, and dynamic Hamming apodization is applied which opens the receive aperture at a f-number of 2. The edge level of the Hamming window is raised to -12 dB. The synthetic data are processed using dynamic transmit and receive focusing. A designed compression filter with a center frequency of 5.5 MHz and 90% bandwidth is used to filter the RF data. The filter is weighted with a Chebychev window to reduce the near and distant temporal sidelobes in the compressed signal [5, 1]. Dynamic Hamming apodization is applied in both transmit and receive with -12 dB edge levels, and both apertures are opened at a f-number equal to 2. When beamforming both sets of data the element sensitivity is taken into account. The acceptance angle [6] is set to $\pm$50 degrees for each element, and, thus, an element is not applied in the beamformer until the point to be beamformed lies inside its acceptance angle.

IV Results & Conclusion

A wire phantom with an attenuation of 0.5 dB/[MHz·cm] was scanned to investigate the spatial resolution and penetration depth of the approach. The results are shown in Fig. 3 for conventional scanning to the left and synthetic imaging to the right. The dynamic range in both images is 45 dB. The improvement in lateral resolution for synthetic imaging is noticed throughout the image, especially at the group of wires at 90 mm. The row of wires at 140 mm is barely visible in the synthetic image but not in the conventional image, which indicates a slight improvement in penetration depth. The axial resolution has, however, been slightly degraded in the synthetic image. Thus, the design of the linear FM signal and the corresponding compression filter needs to be revised, since the bandwidth and weighting functions highly affect the compression efficiency [7].

To investigate the contrast resolution a cyst phantom was scanned. The phantom contains tissue mimicking material with an attenuation of 0.5 dB/[MHz·cm] and 5 columns of anechoic cysts. The cysts in the different columns have diameters of 16, 8, 4, 2, 1 mm from left to right, and the columns are placed at an angle of 15 degrees. The attenuation in the phantom is 0.5 dB/[MHz·cm]. The results are shown in Fig. 4 for conventional imaging (left) and synthetic imaging (right). The improvement in both contrast resolution and penetration depth is evident and significant improvements are obtained below 90 mm.

In-vivo images of the abdomen of a healthy 27 year old male volunteer were obtained to investigate clinical improvements in spatial and contrast resolution. The results are shown in Fig. 5 with the conventional method displayed to

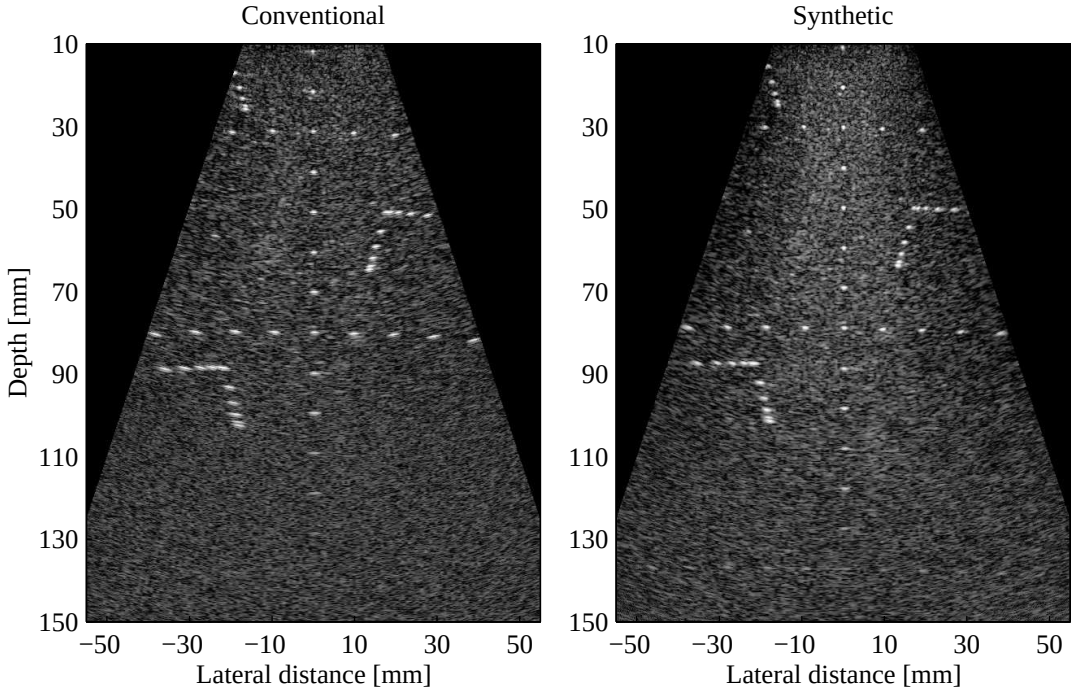

Figure 3: Measured images of a wire phantom with an attenuation of 0.5 dB/[MHz·cm]. The conventional image is displayed to the left and the synthetic image to the right. The dynamic range in both images is 45 dB.

the left and the synthetic approach to the right. The dynamic range in both images is 40 dB. The portal vein branch is seen in the center of the image with the hepatic vein located above to the left and the caval vein below to the right with respect to the portal vein. A slightly better spatial and contrast resolution seems to have been obtained. This is especially noticed at the small vessels in the center of the image. There are, however, also small distortions in the synthetic image as seen at the caval vein in the left part of the image. This may be due to the influence of tissue motion and phase aberration to which STA imaging is more susceptible than conventional imaging. These issues have not been addressed in this study and, thus, they need to be considered in the future work to obtain the image quality improvements shown in the phantom images.

V REFERENCES

[1] K. L. Gammelmark and J. A. Jensen, "Multi-element synthetic transmit aperture imaging using temporal encoding," in *Proc. SPIE: Progress in biomedical optics and imaging*, 2002, vol. 3, pp. 25–36.

[2] M. Karaman, P. C. Li, and M. O'Donnell, "Synthetic aperture imaging for small scale systems," *IEEE Trans. Ultrason., Ferroelec., Freq. Contr.*, vol. 42, pp. 429–442, 1995.

[3] J. T. Ylitalo, "Synthetic aperture ultrasound imaging using a convex array," in *Proc. IEEE Ultrason. Symp.*, 1995, pp. 1337–1340.

[4] J. A. Jensen, O. Holm, L. J. Jensen, H. Bendsen, H. M. Pedersen, K. Salomonsen, J. Hansen, and S. Nikolov, "Experimental ultrasound system for real-time synthetic imaging," in *Proc. IEEE Ultrason. Symp.*, 1999, vol. 2, pp. 1595–1599.

[5] T. X. Misaridis and J. A. Jensen, "An effective coded excitation scheme based on a predistorted FM signal and an optimized digital filter," in *Proc. IEEE Ultrason. Symp.*, 1999, vol. 2, pp. 1589–1593.

[6] M. O'Donnell and L. J. Thomas, "Efficient synthetic aperture imaging from a circular aperture with possible application to catheter-based imaging," *IEEE Trans. Ultrason., Ferroelec., Freq. Contr.*, vol. 39, pp. 366–380, 1992.

[7] T. Misaridis, *Ultrasound imaging using coded signals*, Ph.D. thesis, Ørsted•DTU, Technical University of Denmark, Lyngby, Denmark, 2001.

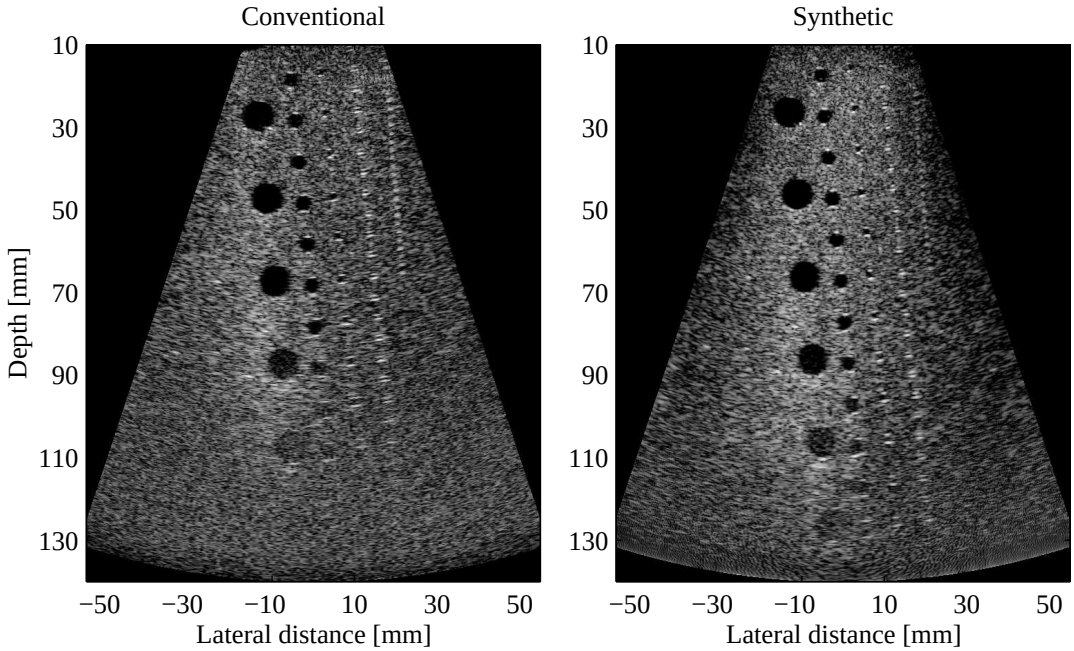

Figure 4: Measured images of a cyst phantom with an attenuation of 0.5 dB/[MHz·cm]. The conventional image is displayed to the left and the synthetic image to the right. The dynamic range in both images is 40 dB.

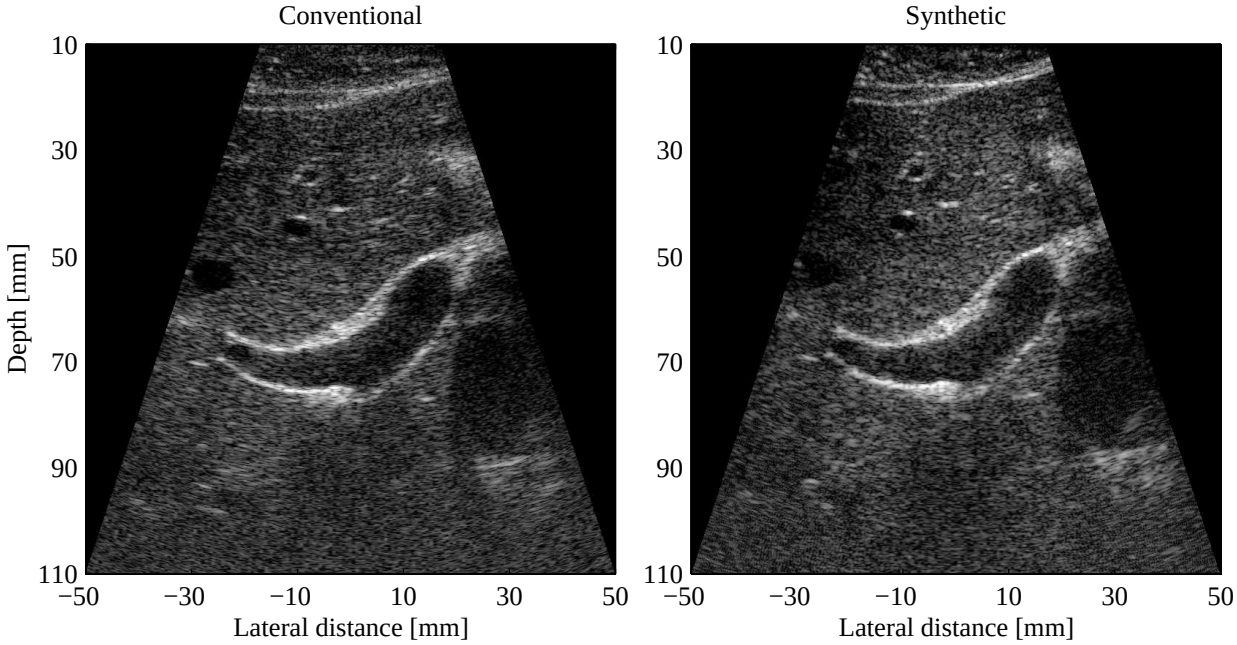

Figure 5: Measured images of the abdomen of a healthy 27 year old volunteer. The portal vein branch is seen in the center of the images, and the hepatic and caval veins are located to the left and right of the portal vein, respectively. The conventional image is shown to the left, and the synthetic image is shown to the right. The dynamic range is 40 dB in both images.

B.3 Duplex Synthetic Aperture Imaging with Tissue Motion Compensation

This paper was presented at the *IEEE International Ultrasonics Symposium* in Honolulu, Hawaii, October 2003, and published in the corresponding proceedings on pages 552-563.

Duplex Synthetic Aperture Imaging with Tissue Motion Compensation

Kim Løkke Gammelmark and Jørgen Arendt Jensen*
Center for Fast Ultrasound Imaging, Ørsted•DTU, Build. 348,
Technical University of Denmark, 2800 Kgs. Lyngby, Denmark

Abstract **-** This paper investigates a method for tissue motion estimation and compensation in synthetic transmit aperture imaging. The approach finds the tissue velocity and the direction of the motion at every tissue region by cross-correlating high resolution lines beamformed along multiple directions at each image points. Compensation is applied in the beamformer by tracking the image points using the velocity and angle estimates from the closest estimation point. Simulation results using Field II show nearly perfect motion compensation with no appreciable difference in contrast resolution after compensation. Phantom measurements show similar performance with differences in contrast resolution of 29% and 0.61% before and after compensation, respectively.

I Introduction

Synthetic transmit aperture (STA) imaging has been investigated by several research groups over the last decade, e.g. [1, 2]. The results presented have in general shown that STA imaging has the potential to improve image quality beyond that obtained by the traditional imaging techniques like linear/phased array imaging. So far, however, in-vivo implementation of STA imaging has generally been limited by two main problems: 1) Low signal-to-noise ratio (SNR), and 2) Susceptibility to tissue motion.

The low SNR arises due to the classic application of a single transmit element. This limits the penetration of the ultrasound beam in the presence of attenuation, which is a general property of biological tissue, and thus minimizes the clinical utility of the approach. In recent papers [1, 3] it has however been shown, that the loss in SNR can be overcome by replacing the single transmit element with a subaperture defocused to emulate a high power spherical wave, and at the same time replace the traditional short excitation with a long linear frequency modulated (FM) waveform [4]. This approach, denoted *TMS imaging*[1], increases the SNR by several dB compared to e.g. linear array imaging, which makes in-vivo imaging possible. Thus, the short penetration depth is no longer an issue, which requires attention.

STA imaging relies on the coherent summation of sequentially acquired and beam formed low resolution images. Thus, STA imaging is susceptible to tissue motion, because this will cause the low resolution images to be incoherently summed, resulting in an unfocused image. This susceptibility is more pronounced for STA imaging compared to traditional imaging, because the latter techniques build up the image line by line. Tissue motion therefore distorts the structures in the traditional images rather than degrading the spatial and contrast resolutions. If tissue motion is severe, successful STA imaging requires motion compensation. This is especially the case, if several emissions are used for each high resolution image.

This paper presents a method for tissue motion compensation in STA imaging based on cross-correlation of high resolution image lines beamformed along the direction of the motion. The method and acquisition strategy is described in Section II, and simulations with Field II used to theoretically investigate the approach are presented in Section III. Phantom measurement results obtained using the RASMUS research scanner are presented in Section IV, and the paper is concluded in Section V.

II Motion Compensation

Coherent summation of the low resolution images beamformed after each emission in STA imaging is necessary in order to fully utilize the advantages of the method. If these images are not phase aligned, incoherent summation will occur which produces an unfocused, smeared high resolution image. This affects the SNR, spatial resolution, and contrast resolution. Such phase misalignment is produced by target motion, where the tissue moves between each emission. Thus, it is necessary to estimate this motion and compensate for it in order to maintain image quality.

Different methods for motion estimation and compensation have been studied for synthetic aperture ultrasound imaging previously, e.g. [5, 6]. As reported in these papers, the dominant factor in image degradation is axial motion due to the significantly higher spatial frequency in this direction. Lateral motion will however also have a significant impact on the

*This work is sponsored by grant 9700883 and 9700563 from the Danish Science Foundation, by Ph.D. grant 11-3160-55173 from the Technical University of Denmark, and by B-K Medical A/S, Gentofte, Denmark.

[1] Temporally encoded Multi-element Synthetic transmit aperture (TMS) imaging

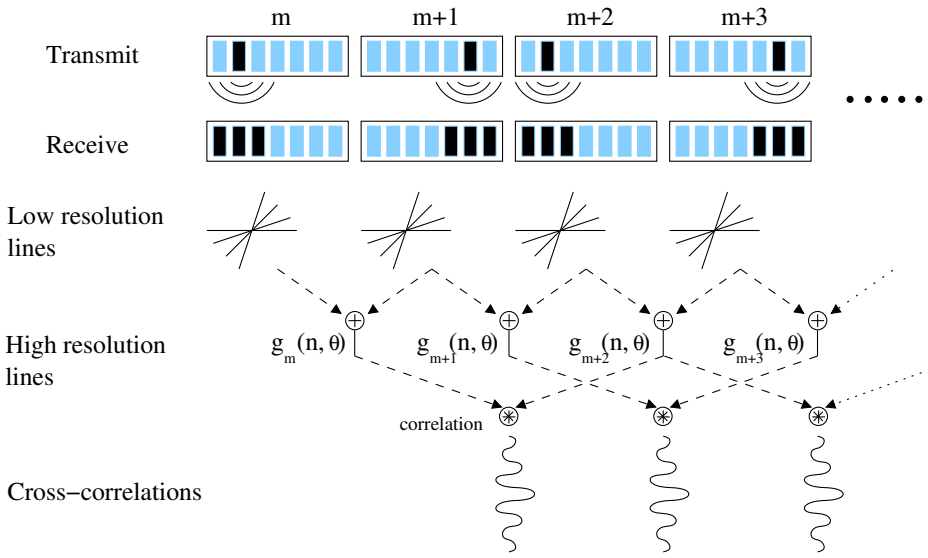

Figure 1: Illustration of the tissue velocity estimation approach.

image quality. This is especially the case, if many emissions are used, because the motion artifacts build up. Therefore, two dimensional motion compensation is necessary.

Generally, motion estimation methods are based on cross-correlation of reference signals to find the shift in position or phase of the tissue. The degree of success of such methods depends on the correlation between the reference signals, which again depends on the degree of common spatial frequencies used to generate the reference signals. One method to obtain highly correlated reference signals is to use high resolution images. These will be completely correlated, if they are acquired in exactly the same way. This property has recently been used to generate synthetic aperture flow images in [7, 8], where the blood flow velocity is estimated by cross-correlating high resolution lines acquired using TMS imaging with few emissions and beamformed along the flow direction.

The motion estimation and compensation method presented here is based on the synthetic aperture flow method mentioned above. The approach utilizes the high correlation between the high resolution images and the fact that for a given emission any set of image points within the interrogated region can be created using STA beamforming [7]. The method is illustrated in Fig. 1 using two emissions. For a given image point at which tissue motion is to be estimated, a set of low resolution lines along selected directions are beam formed for each emission. For each set of consecutive emissions, here $[m, m+1]$, $[m+1, m+2]$, $[m+2, m+3]$, etc., the corresponding lines for each angle θ are then summed to form high resolution lines $g_m(n,\theta)$, $g_{m+1}(n,\theta)$, $g_{m+2}(n,\theta)$, etc., where n is the sample number. Assuming a constant tissue velocity during the acquisition, the distortion in $g_m(n,\theta)$ and $g_{m+2}(n,\theta)$ will be the same and the only difference is the shift in position of the scatterers. The correlation for the different angles will be highest in the direction of the motion. By cross-correlating $g_m(n,\theta)$ and $g_{m+2}(n,\theta)$ for all angles, the direction of the motion is therefore found at the angle for which the normalized correlation coefficient is maximum. For this angle the shift in position can be found and thus the velocity.

The shift in position between high resolution lines $g_{m+1}(n,\theta)$ and $g_{m+3}(n,\theta)$ will be equal to that between $g_m(n,\theta)$ and $g_{m+2}(n,\theta)$, if the tissue velocity is assumed constant. Thus, the peak in the cross-correlation functions will be located at the same lag, and they can be averaged to improve the velocity estimate. This averaging can be applied for as long as the velocity can be assumed constant.

In general, M emissions, denoted flow mode emissions or F-mode emissions, are used, and the emission sequence is repeated N_{seq} times. The i'th high resolution line is created by

$$g_i(n,\theta,\vec{r}_p) = \sum_{m=1}^{M} s_{m+i}(n,\theta,\vec{r}_p), \tag{1}$$

where n, $n = 1,2,\ldots,N$, is the sample number along the line, θ is the angular direction of the line, and $\vec{r}_p$ denotes the location of the point being investigated (see Fig. 2). The signal $s_m(n,\theta,\vec{r}_p)$ is the low resolution line for emission m, and $i = 1,2,\ldots,M(N_{seq}-1)$. The number of samples N in the directional lines and the sampling interval δr are determined by several parameters, e.g. the spatial frequency at the given angle θ, and the maximum tissue velocity.

The normalized cross-correlation is obtained by

$$\rho_{i,i+M}(k,\theta,\vec{r}_p) = \frac{E\left\{g_i(n,\theta,\vec{r}_p)g_{i+M}(n+k,\theta,\vec{r}_p)\right\}}{\sqrt{\sigma_i^2\sigma_{i+M}^2}}, \tag{2}$$

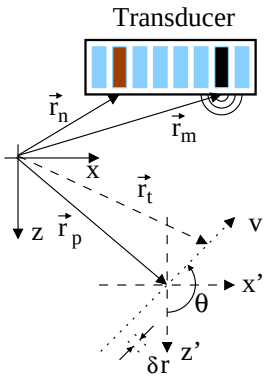

Figure 2: Definition of geometric variables.

where k is the lag, and σ_i^2 and σ_{i+M}^2 are the variances of $g_i(n,\theta,\vec{r}_p)$ and $g_{i+M}(n,\theta,\vec{r}_p)$, respectively. Using the average cross-correlation function

$$\bar{\rho}(k,\theta,\vec{r}_p) = \frac{1}{M(N_{seq}-1)} \sum_{i=1}^{M(N_{seq}-1)} \rho_{i,i+M}(k,\theta,\vec{r}_p) \qquad (3)$$

the direction of the motion is found at the angle $\hat{\theta}(\vec{r}_p)$ for which $\bar{\rho}(k,\theta,\vec{r}_p)$ is maximum as explained previously. The velocity magnitude $v_m(\vec{r}_p)$ of the motion is then calculated by

$$\hat{v}(\vec{r}_p) = \frac{k_{max}(\hat{\theta}(\vec{r}_p))\delta r\, f_{prf}}{M}, \qquad (4)$$

where $k_{max}(\hat{\theta},\vec{r}_p)$ is lag of the cross-correlation peak, and f_{prf} is the pulse repetition frequency.

To obtain continuous B-mode and flow imaging, the TMS imaging emissions and the F-mode emissions are interleaved such that every second emission is an F-mode emission. Hereby, the motion can be estimated continuously. The velocity and angle estimates are used to compensate the low resolution B-mode images by recalculating the location of the image points to beamform. With reference to Fig. 2, the high resolution B-mode image is created by

$$S(\vec{r}_p) = \sum_{m=1}^{N_{xmt}} w_m(\vec{r}_p) \sum_{n=1}^{N_{rcv}} w_n(\vec{r}_p)\, g_{m,n}\left(\frac{d_{m,n}(\vec{r}_t(m))}{c}\right), \qquad (5)$$

where $w_n(\vec{r}_p)$ is the apodization values for receive element n, $w_m(\vec{r})$ is the apodization value for transmit element m, c is the sound speed, and N_{xmt} and N_{rcv} are the number of emissions and receive channels, respectively. The total distance $d_{m,n}(\vec{r}_t(m))$ from transmission center m to the tracked image point and back to receive element n is given by

$$d_{m,n}(\vec{r}_t(m)) = |\vec{r}_t(m) - \vec{r}_m| + |\vec{r}_n - \vec{r}_t(m)|, \qquad (6)$$

where

$$\vec{r}_t(m) = [\sin\hat{\theta}, 0, \cos\hat{\theta}] \cdot \frac{2\hat{v}}{f_{prf}}(m-1) \qquad (7)$$

Note, that this approach can also be used for continuous B-mode and blood flow TMS imaging.

III Simulations

To investigate the method described in the previous section theoretically, a simulation using Field II has been performed [9, 10]. A commercial 128 element 7 MHz linear array transducer with element spacing on the order of a wavelength (λ) was used. Each emission is performed using a 33 element subaperture and with a 20 μs linear FM signal as excitation waveform. The linear FM signal and the corresponding compression filter have both been amplitude weighted to reduce the near and distant temporal sidelobes [4, 3]. Each acquisition sequence consists of 96 B-mode emissions and 12 motion sequences each with 8 F-mode emissions. This results in a total of 192 emissions in each acquisition and 89 cross-correlation estimates. The B-mode and F-mode emissions are interleaved with ratio 1-to-1 as explained above. For every B-mode emission 64 receive elements spaced by 2λ were used (i.e. every second transducer element). For the F-mode emissions the 64 element receive aperture was centered around the transmit subaperture.

A tissue mimicking phantom containing an anechoic cyst with a diameter of 4 mm centered on-axis and 25 mm away from the transducer was used as target. Uniform tissue motion was simulated by changing the position of the scatterers between each emission event. The velocity of the motion was 0.15 m/s, and the scatterers were moved at an angle θ = 110° relative to the z-axis, see Fig. 2.

The velocity magnitude and angle were estimated for every 2 mm in both the lateral and axial direction. The relative bias and standard deviation (STD) of the velocity estimate obtained were -4.40% and 0.85%, respectively, while the relative bias and STD of the estimated angle were 1.08% and 0.20%, respectively. The resulting images are shown in Fig. 3. Clearly the motion completely destroys the image quality in the uncompensated image, while the image quality has been fully recovered after motion compensation.

The degradation in contrast resolution CR_{rel} in percent relative to the reference phantom is calculated by

$$CR_{rel} = \frac{CR_{ref} - CR_{obj}}{CR_{ref}} \cdot 100, \qquad (8)$$

where CR_{ref} is the contrast resolution of the reference phantom, and CR_{obj} is the contrast resolution of the object being analyzed. The contrast resolution CR is calculated by [3]

$$CR = 1 - \frac{I_C}{I_S}, \qquad (9)$$

where I_C is the intensity inside the cyst, and I_S is the intensity of the speckle. Using these equations, the contrast resolution before compensation is degraded by 48%, while no appreciable difference is present after motion compensation.

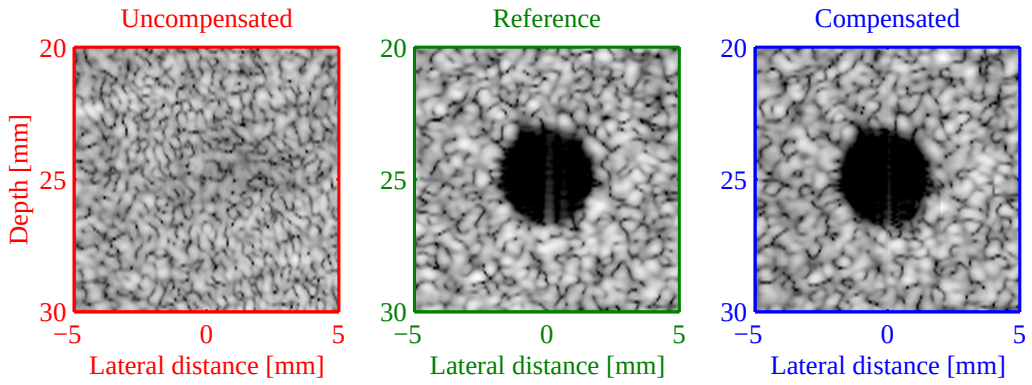

Figure 3: Image results of tissue motion simulation. Left: Uncompensated, Middle: Reference (stationary phantom). Right: Compensated. The dynamic range is 40 dB.

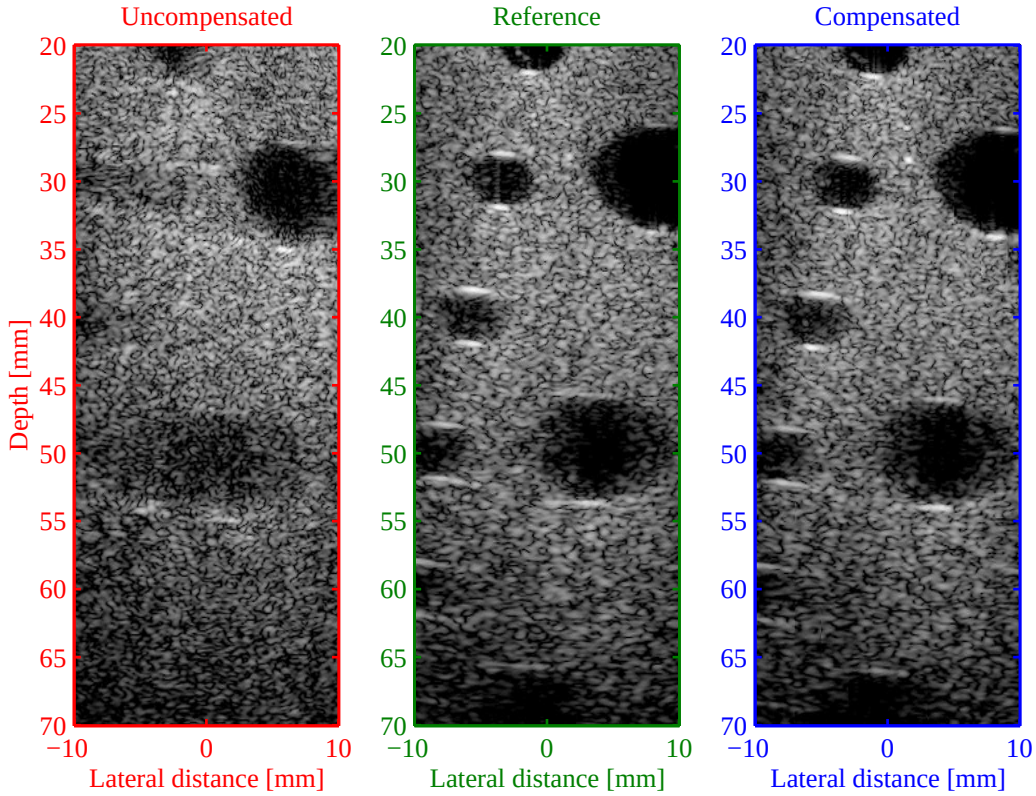

Figure 4: Left: Uncompensated, Middle: Reference (stationary phantom). Right: Compensated. The dynamic range is 50 dB.

IV Measurements

Measurements were performed using the RASMUS research scanner developed at our center [11]. This system has 128 individually programmable transmitters capable of sending arbitrary coded waveforms with a precision of 12 bits at 40 MHz. Sixty-four receive channels are sampled simultaneously with a resolution of 12 bits and 40 MHz, and the 2-to-1

multiplexing in the system enables acquisition of 128 channels in real-time over two transmissions.

An anechoic cyst phantom containing water filled cylinders with diameters of 4 mm and 8 mm was scanned. The applied acquisition and processing strategies were identical to those used in the simulation described in the previous section to enable direct comparison of the results. Uniform scatterer motion was emulated by moving the transducer between each emission using a high precision translation stage. The velocity and direction of the imposed motion was 0.106 m/s and -68.2°, respectively.

The tissue velocity and motion direction was estimated for every 2 mm in both the lateral and axial direction, and the angular separation between the directionally beam formed lines was 1°.

The relative bias and STD of the velocity estimate obtained were -7.23% and 15.84%, respectively, while the relative bias and STD of the estimated angle were 1.11% and 4.65%, respectively. These numbers are higher than those obtained in the simulation, because they contain the false estimates from inside the cysts. These can be avoided by using a proper discriminator between noise and tissue. Neglecting the false estimates from inside the cysts, the relative bias and STD of the estimated velocity becomes -3.24% and 5.63%, while the angle estimates change to -0.14% and 1.81%.

The uncompensated, compensated, and reference B-mode images are shown in Fig. 4. As seen, a significant improvement in image quality has been obtained although the variance of the motion estimates is relatively high. The difference in contrast before and after compensation is 29% and 0.61%, respectively, for the cyst located at depth 40 mm.

V Conclusion

A new method for tissue motion compensation was presented. The method estimated the velocity and direction of the tissue motion at every tissue region using cross-correlation of high resolution lines beam formed along multiple direction. The direction of the motion is determined by the angle for which the correlation is maximized, and the velocity is found using conventional cross-correlation techniques. Compensation is performed using the velocity and angle estimates by recalculating the location of the image points, when beamforming the compensated low resolution images.

The simulation results showed nearly perfect motion compensation using the method. The difference in contrast resolution before and after compensation was 48% and approximately 0%, respectively. The measurement results showed, that successful motion compensation can be obtained using the method in a noisy environment with only a 0.61% difference in contrast resolution after compensation.

VI References

[1] M. Karaman, P. C. Li, and M. O'Donnell, "Synthetic aperture imaging for small scale systems," *IEEE Trans. Ultrason., Ferroelec., Freq. Contr.*, vol. 42, pp. 429–442, 1995.

[2] G. R. Lockwood, J. R. Talman, and S. S. Brunke, "Real-time 3-D ultrasound imaging using sparse synthetic aperture beamforming," *IEEE Trans. Ultrason., Ferroelec., Freq. Contr.*, vol. 45, pp. 980–988, 1998.

[3] K. L. Gammelmark and J. A. Jensen, "Multielement synthetic transmit aperture imaging using temporal encoding," *IEEE Trans. Med. Imag.*, vol. 22, no. 4, pp. 552–563, 2003.

[4] T. X. Misaridis and J. A. Jensen, "An effective coded excitation scheme based on a predistorted FM signal and an optimized digital filter," in *Proc. IEEE Ultrason. Symp.*, 1999, vol. 2, pp. 1589–1593.

[5] G. E. Trahey and L. F. Nock, "Synthetic receive aperture imaging with phase correction for motion and for tissue inhomogenities - part II: effects of and correction for motion," *IEEE Trans. Ultrason., Ferroelec., Freq. Contr.*, vol. 39, pp. 496–501, 1992.

[6] M. Karaman, H. Ş. Bilge, and M. O'Donnell, "Adaptive multi-element synthetic aperture imaging with motion and phase aberation correction," *IEEE Trans. Ultrason., Ferroelec., Freq. Contr.*, vol. 42, pp. 1077–1087, 1998.

[7] S. I. Nikolov and J. A. Jensen, "Velocity estimation using synthetic aperture imaging," in *Proc. IEEE Ultrason. Symp.*, 2001, pp. 1409–1412.

[8] J. A. Jensen and S. I. Nikolov, "Transverse flow imaging using synthetic aperture directional beamforming," in *Proc. IEEE Ultrason. Symp.*, 2002, pp. 1488–1492.

[9] J. A. Jensen and N. B. Svendsen, "Calculation of pressure fields from arbitrarily shaped, apodized, and excited ultrasound transducers," *IEEE Trans. Ultrason., Ferroelec., Freq. Contr.*, vol. 39, pp. 262–267, 1992.

[10] J. A. Jensen, "Field: A program for simulating ultrasound systems," *Med. Biol. Eng. Comp.*, vol. 10th Nordic-Baltic Conference on Biomedical Imaging, Vol. 4, Supplement 1, Part 1, pp. 351–353, 1996b.

[11] J. A. Jensen, O. Holm, L. J. Jensen, H. Bendsen, H. M. Pedersen, K. Salomonsen, J. Hansen, and S. Nikolov, "Experimental ultrasound system for real-time synthetic imaging," in *Proc. IEEE Ultrason. Symp.*, 1999, vol. 2, pp. 1595–1599.

B.4 Preliminary In-Vivo Evaluation of Convex Array Synthetic Aperture Imaging

This paper was presented at *SPIE - Progress in biomedical optics and imaging* in San Diego, California, February 2004, and published in the corresponding proceedings on pages 33-43.

Preliminary In-Vivo Evaluation of Convex Array Synthetic Aperture Imaging

Morten H. Pedersen, Kim L. Gammelmark, and Jørgen A. Jensen

Center for Fast Ultrasound Imaging, Ørsted•DTU, Build. 348,
Technical University of Denmark, DK-2800 Kgs. Lyngby, Denmark

ABSTRACT

Synthetic transmit aperture (STA) imaging has previously been investigated and compared to traditional imaging techniques in simulations and phantom studies. However, a full in-vivo study evaluating its clinical potential has yet to be conducted. This paper presents a preliminary in-vivo study of STA imaging in comparison to conventional imaging. The purpose is to evaluate whether STA imaging is feasible in-vivo, and whether the image quality obtained is comparable to traditional scanned imaging in terms of penetration depth, spatial resolution, contrast resolution, and artifacts. Acquisition was done using our RASMUS research scanner and a 5.5 MHz convex array transducer. STA imaging applies spherical wave emulation using multi-element subapertures and a 20 μs linear FM signal as excitation pulse. For conventional imaging a 64 element aperture was used in transmit and receive with a 1.5 cycle sinusoid excitation pulse. Conventional and STA images were acquired interleaved yielding ensuring exact same anatomical location. Image sequences were recorded in real-time, and processing was done offline. Male volunteers were scanned abdominally, and resulting images were compared by medical doctors using randomized blinded presentation. Penetration and image quality were scored and evaluated statistically. Results show that in-vivo imaging using STA imaging is feasible with improved image quality compared to conventional imaging.

Keywords: Synthetic aperture imaging, Medical ultrasound, Clinical evaluation, Image comparison

1. INTRODUCTION

Conventional ultrasound scanning employs emission of focused beams in one direction at a time, thereby building up an image of consecutive scan lines. This is a technically intuitive and easy implementable solution to ultrasound imaging, imposed by the limits of analog electronics at the birth of medical ultrasound in the 1950'ies. The emergence of array element transducers has introduced dynamic receive focusing, which yields an optimal lateral focus at all depths in the image for this method. Synthetic transmit aperture (STA) imaging, a technique originally adapted from radar, offers the same optimal resolution at all depths in transmit as well as receive, with the potential of increasing the overall spatial and contrast ultrasound image resolution.

Simulation and phantom studies of STA imaging have been published with good results.[1–3] The viability of the technique in-vivo is, however, yet to be proven and doubts have been uttered, stating that tissue motion will probably make the coherent summation of temporally separated signals break down.

In this study an implementation of STA imaging using multi element defocused spherical wave emissions and linear FM signals[2] will be tested in a clinical setting on healthy volunteers and evaluated by ultrasound specialists (medical doctors). The method is investigated for abdominal imaging using a convex array transducer, and it is compared to conventional convex array imaging measured under the exact same conditions at the same time and anatomical location.

Further author information: Send correspondence to Morten H Pedersen, Ørsted•DTU, Ørsteds Plads Build. 348, DK-2800 Lyngby, Denmark. E-mail: mhp@dadlnet.dk

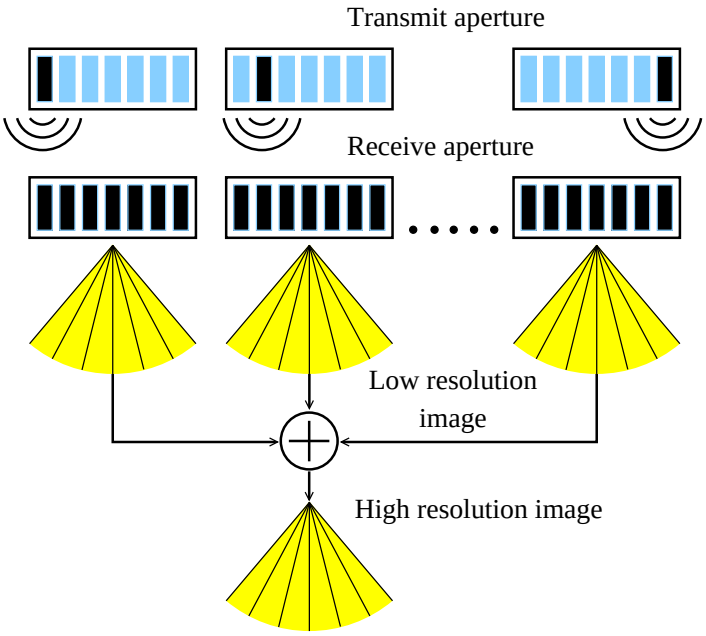

Figure 1. Illustration of the principle behind STA imaging. At each emission event a spherical wave is transmitted from a single element, and the echoes are recorded by all receive aperture elements. The echoes from each emission are focused at each pixel in the image producing low resolution images, and these images are finally summed coherently to form the displayed high resolution image.

1.1. Aim

The purpose of the study is to evaluate the performance of STA imaging in-vivo by blinded clinical evaluation of ultrasound scanning using both conventional and STA imaging. An experimental ultrasound scanning system capable of producing simultaneous recordings of the exact same locations using both techniques is used.

The following two null hypotheses are tested:

1. STA imaging has no effect on penetration depth.
2. STA imaging has no effect on image quality (spatial resolution and image contrast).

Additionally, this paper gives a short technical introduction to STA imaging in Section 2, and the data acquisition and processing strategies are described in Section 3. Section 4 presents the results of the statistical analysis along with the in-vivo images, i.e. their general appearance and artifacts. Results are discussed and conclusions are drawn in Section 5.

2. SYNTHETIC TRANSMIT APERTURE IMAGING

Traditional linear and phased array imaging methods perform ultrasound scanning by transmitting focused beams in one direction at a time. The echoes received by the aperture elements are recorded and focused dynamically along the transmit direction to form a scan line. These scan lines are stacked together to form the displayed ultrasound image.

In STA imaging the reverse of traditional imaging is performed. Here, as illustrated in Fig. 2, a single element is used at each transmission to generate a spherical (i.e. defocused) wave, which spreads out in all directions in the medium. The scattered echoes are recorded using all elements in the receive aperture, and the transmit-receive procedure is repeated until all elements in the transmit aperture have been used for transmission.

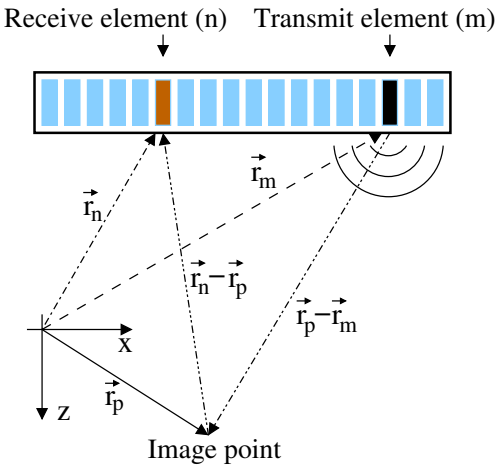

Figure 2. Geometrical illustration of STA beamforming. The core principle is the known origin and shape (spherical) of the emitted wave. Based on this and the knowledge of the speed of sound, the arrival time of the echo from a given point target can be calculated exactly.

Reconstruction of each pixel in the ultrasound image is performed by coherently summing the echoes received from a point target located at the center of each pixel for all transmissions. This is possible because the origin and shape of the transmitted wave is known. The origin is determined by the location of the transmitting element, and the wavefront is spherical due to the small aperture elements. Assuming the speed of sound in the medium is known, the arrival time of the echo from a given point target for a specific transmit and receive element pair can be calculated exactly using the geometric relations illustrated in Fig. 2. Performing this calculation for all transmit-receive element pairs, picking out the corresponding samples of the recorded echoes, and finally summing these samples both the transmit and the receive apertures are focused at the point target location, producing an optimally focused image point. This process is repeated for all points or pixels in the ultrasound image. Note, however, that the image points are independent from each other, enabling parallel processing.

In practice, the image reconstruction process is performed sequentially. After each emission event a complete ultrasound image is formed by focusing the receive aperture at all image points based on the transmit element location (Fig. 2). The produced image is called a low (lateral) resolution image, because the image is created using a single transmit element. This is repeated after each emission, and the individual low resolution images are finally summed to produce the displayed high resolution image. In this way, the transmit aperture is synthesized over several transmissions, and the ultrasound image is build up sequentially.

Since a single element is applied at each transmission, the emitted energy is low, which results in a low signal-to-noise ratio (SNR) and, thus, low penetration. To increase the SNR a recent study of STA imaging[3] has shown, that the combination of multi-element subapertures, used at each emission to increase the intensity of the emitted spherical wave,[1,4] with linear FM signals[5] can be used to increase the SNR of STA imaging.

3. MATERIAL AND METHODS

Seven healthy male volunteers were scanned in supine position by an experienced sonographer. Mean age was 32.5 (from 26.5 to 43.5) years, mean weight 82 (from 70 to 96) kg and mean body mass index (BMI) was 25.2 (23.7 to 28.1).

3.1. Equipment

The measurements were performed using the experimental multi-channel ultrasound scanning system *RASMUS*.[6] The system has 128 individually programmable transmitters capable of sending arbitrary coded waveforms with a precision of 12 bits at 40 MHz. Sixty-four receive channels can be sampled simultaneously at 12

bits and 40 MHz, and the 2-to-1 multiplexing in the system enables acquisition of 128 channels in real-time over two transmissions. The system has 16 Gbytes of storage memory in the receivers, which enables the acquisition of several seconds of real-time RF data, and it is remotely accessible and programmable through a developed Matlab/C-library interface. The front-end in RASMUS is build by slightly modifying a commercial front-end. The analog electronics in the system is, thus, comparable to a commercially available ultrasound scanner.

The transducer used for this study was a commercial 5.5 MHz convex array transducer with 192 elements and λ pitch. The bandwidth of the elements is 60% relative to the center frequency, and the convex radius of the aperture is 41 mm. The height of the elements is 8 mm, and the array has a lens in the elevation dimension with a fixed focus at 40 mm. Due to the limitation of the RASMUS system, only the central 128 elements of the array are accessible.

3.2. Imaging Setup

For conventional imaging a 64 elements transmit and receive aperture was used with a fixed focus at 70 mm. A 1.5 cycle sinusoid with a center frequency of 5.5 MHz and Hanning apodization was used as excitation. The number of lines in each frame was determined by the spatial Nyquist theorem. For the present imaging setup and the above convex array geometry, this resulted in 195 lines per frame.

For STA imaging a 33 element subaperture was used to emulate the high power spherical wave transmission, and 64 elements equally spaced over the full 128 element aperture were used on receive. The transmit aperture was moved one element after each transmission producing a total of 96 emissions for each frame. A 20 μs linear FM signal with a center frequency of 5.5 MHz and 90% bandwidth was used as excitation signal. The FM signal had been weighted with a Tukey window to reduce the temporal sidelobes.[5] As explained previously, this combination was used to increase the SNR of STA imaging.

The imaging modes were interleaved such that one frame from one mode followed directly after the other. Hereby, images from exactly the same in-vivo view were obtained, enabling direct comparison of the methods. The depth of each scan was 13-16 cm, and the interleaved frame rate was set to 12 frames/sec, i.e. 12 conventional and 12 synthetic frames per second.

The excitation voltage was the same for both conventional and STA imaging ($\pm$50 V), and it was not changed during acquisition.

3.3. Acoustic Output

Prior to conducting in-vivo experiments the acoustic outputs of the ultrasound scanner were measured for the imaging modes under investigation. The measured intensities need to satisfy preamendments upper limits regulated by the United States Food and Drug Administration (FDA),[7] which have been introduced as safety guides to avoid damage to the tissue and pain to the patient. These limits concern the mechanical index, MI$\leq$ 1.9, the derated spatial-peak-temporal-average intensity, $I_{spta.3} \leq 190$ W/cm^2, and the derated spatial-peak-pulse-average intensity $I_{sppa.3} \leq 720$ mW/cm^2.[7]

The acoustic outputs were measured in a water tank using a high precision 3-dimensional position system and a miniature PVDF hydrophone (Force Technology, Denmark, model: MH28-4) by following the guidelines given by the American Institute of Ultrasound in Medicine (AIUM).[8] The levels obtained for conventional imaging are listed in Table 1. These values are considerably lower than the FDA limits and in-vivo scanning is therefore safe using the present imaging modes.

3.4. Acquisition

Two different locations were scanned in each person. Both upper abdominal views of the liver in some cases including the right kidney. Hereby, two acquisitions, with the two imaging techniques were made in seven volunteers yielding 28 cine-loop sequences (14 paired sequences), each of approx. 3 seconds duration.

A scout image to initially locate the transducer was obtained using the transducer on a commercial scanner (B-K Medical, Hawk 2102) immediately before the acquisition. The volunteer was asked to hold his breath and an interleaved sequence of 3 seconds (36 frames) duration was recorded. The acquired rf-data were then transferred to a computer cluster for subsequent off-line processing.

	Conventional	STA	Unit
$I_{sppa.3}$	26.28	7.93	W/cm^2
$I_{spta.3}$	3.66	72.94	mW/cm^2
MI	0.41	0.27	-

Table 1. Ultrasound intensities and mechanical index (MI) used in conventional and STA imaging respectively. The values are derated in-situ values.

3.5. Data Processing

The conventional data were beamformed using dynamic receive focusing. The RF signals were filtered using a matched filter, and dynamic apodization using a modified Hamming window with -12 dB edge levels was applied, which kept the receive f-number=2 until the receive aperture was fully opened.

The STA data were processed using dynamic transmit and receive focusing as described in Section 2. A designed compression filter with a center frequency of 5.5 MHz and 90% bandwidth was used to filter the RF data and perform the pulse compression. The filter was weighted with a Chebychev window to reduce the near and distant temporal sidelobes in the compression output.[3,5] Dynamic apodization was applied in both transmit and receive using a modified Hamming window with -12 dB edge levels, and both f-numbers were kept constant at 2 until the apertures were fully opened. The number of beamformed image lines was the same as the number of scanned lines in conventional imaging, i.e. 195 beams. Note, however, that any number of scan lines or image points could have been beamformed for STA imaging.

When both sets of data were beamformed the element sensitivity[4] was taken into account. The angular sensitivity of each aperture element was set to ± 50 degrees, and an element was not applied in the beamformer until the image point to be beamformed occurred inside its acceptance angle.

3.6. Automatic TGC Post-Correction

Before scan-line conversion, the TGC was corrected according to depth to obtain homegenous images suitable for comparison. The automatic correction method is described by Pedersen et al (2003). The method automatically simulates the TGC adjustments performed by a sonographer, eliminating the possible bias from human intervention.

After envelope detection and log-compression the median value of all lines for all depths in the first recorded frame was found. The resulting curve was fitted (cubic spline) to eight control points found from the average value of the median curve in eight evenly distributed along the depth axis. The resulting fitted curve was then subtracted from all lines in alle frames. In Fig. 3 an example of the correction is depicted. A dynamic range of 50 dB was used.

3.7. Movie Generation

Scan line conversion and movie generation were done in MATLAB (MathWorks Inc., Natick, Mass., USA). Movies consisting of 3 sec recordings, swinging forwards and backwards to avoid annoying temporal discontinuities were created with both single and paired images. In the single image movies only conventional or synthetic acquisitions were shown. In paired movies both conventional and synthetic images were shown side-by-side. Two versions of the paired movies were made, with the conventional image to the left and to the right respectively. The movies were compressed using the loss-less Huffyuv CODEC v2.1.1 for Windows AVI-file generation*

3.8. Image Assessment

Three medical doctors (ultrasound specialists) evaluated the movie clips. None of the three were involved in the project, nor had they any prior knowledge about the details of synthetic aperture imaging, or seen any of the images beforehand. Evaluations were done blinded and independently of each other.

*The Huffyuv codec was made by Ben Rudiak-Gould at Berkeley University, USA. `http://web.archive.org/web/20020202101504/http://www.math.berkeley.edu/~benrg/huffyuv.html`

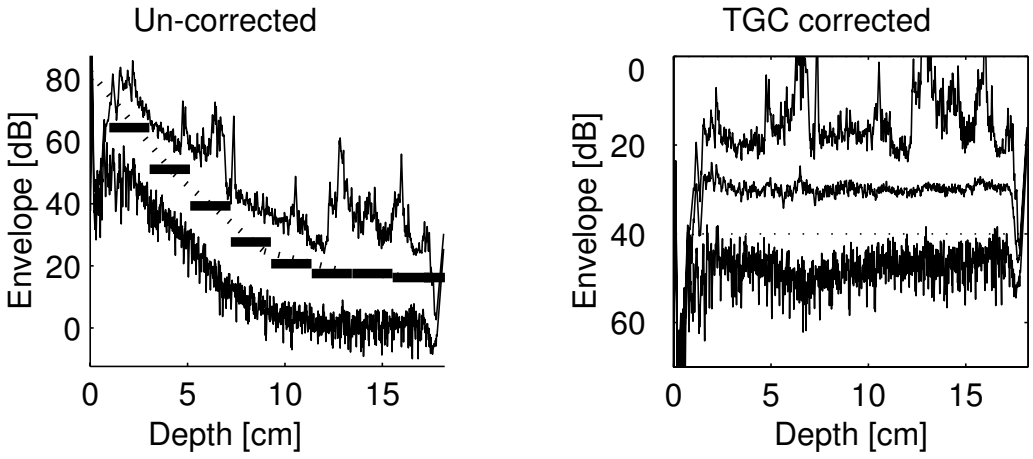

Figure 3. Automatic TGC post-correction of logarithmic envelope. The left graph shows the maximum and minimum log-dB values as a function of depth. Between the maximum and minimum curves the fitted median curve and the control point levels (horizontal bars) are shown. The right graph shows the min, max, and median values after TGC correction.

(a) Synthetic aperture image / movie clip used for penetration depth estimation.

(b) Image of movie with both conventional (left) and STA (right) images for comparison.

Figure 4. Single and double image presentation. The presented images are transverse sections of the right liver lobe containing hepatic vein branches, cross sections of portal vein branches, and the diaphragm in the lower part of the images.

Penetration depth comparison were done by presenting the 28 sequences in random order to each doctor without any information on the type of technique used, as shown in Fig. 4(a). He was asked: "At what depth [cm] does the image quality decrease significantly?", to estimate the perceived penetration depth. The differences between depths in matching image pairs (conventional and STA) were used for the statistical analysis to avoid the bias from different examiners, who undoubtedly have different opinions on how to answer the posed question.

Image quality comparison of conventional and STA images were performed by displaying matching pairs side-by-side in random order and with random left-right placement of the conventional image. This resulted in 28 presentations of the 14 pairs. The doctors were asked to score which of the two presented images (movies) was better on a visual analog scale[10] (VAS), see Fig. 5(a). Before the scoring the VAS scale was explained using

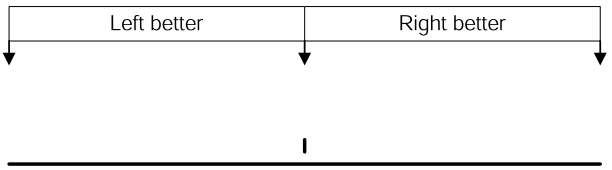

(a) Visual Analog Scale (VAS) used to compare left and right image.

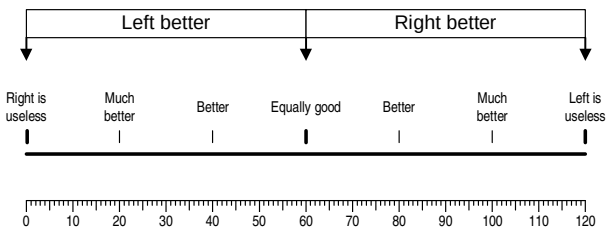

(b) Explanation of VAS shown to medical doctors before scoring images. The lower scale was used to read scored values.

Figure 5: Visual analog scale for image quality comparison

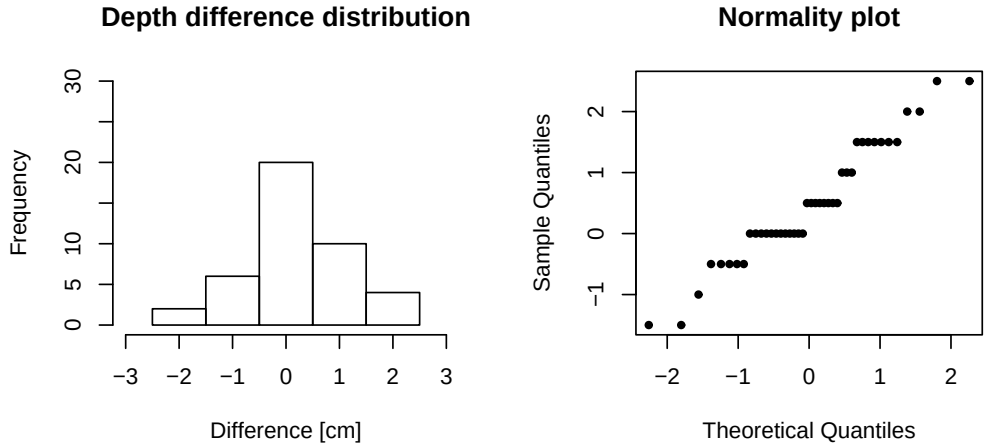

Figure 6. Histograms and normality plots of perceived penetration depth differences ($depth_{STA} - depth_{Conventional}$). The normality plot supports the assumption of normally distributed data.

Fig. 5(b). The figure instructs the doctor on how to interpret the scale when performing the evaluation. To avoid categorized data and get a smoother distribution, this explanatory scale is not shown during the actual evaluation (scoring).

3.9. Statistical Analysis

The statistical data analysis language R[†] was used for statistical computations. Student's (one sample) t-test was used on the resulting differences in *penetration depth*, assuming normal distribution supported by Fig. 6. Two-sided tests were used.

Since each evaluating doctor most likely has his own interpretation of the visual analog scale and show different degrees of attraction to the center point (Fig. 7) in side-by-side *image quality comparisons*, no assumptions of normal distributed data were made. Consequently, Wilcoxon signed rank test with continuity correction was used on the VAS results. The P values of the pooled data from all three examiners were corrected for multiple comparison using the Bonferroni method.[10]

[†] `http://www.r-project.org/`

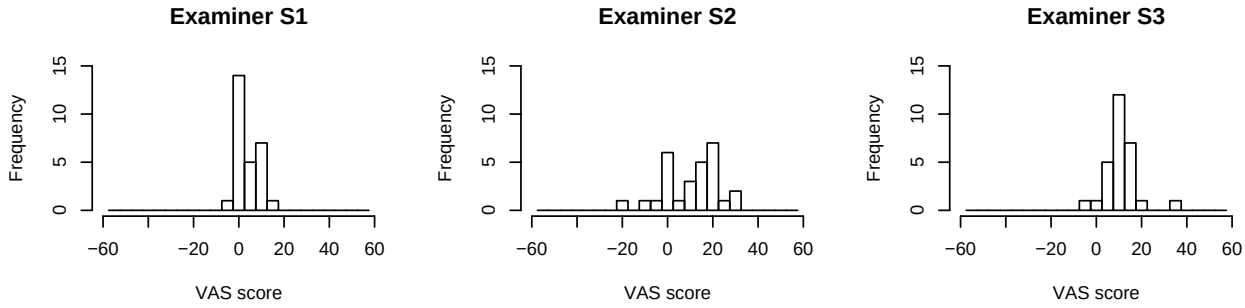

Figure 7. Distribution of answers to image comparisons. Positive values mean that the STA image is better. Data are shown for the three doctors (S1-S3) individually.

4. RESULTS

The STA images were generally good and undoubtedly applicable in clinical imaging. Examples are shown in Fig. 4 and Fig. 8.

4.1. New features

Synthetic aperture images clearly had a more uniform lateral resolution than the conventional, undoubtedly due to the optimal focusing at all depths, which resulted in sharper images with more well-defined structure borders.

Additionally, movement during acquisition seemed to be rendered differently compared to conventional images. Moving organs seems to be moving more *en bloc*, i.e. without the warping that occurs in conventional ultrasound imaging. This remains to be evaluated further, though.

4.2. Limitations and Artifacts

An artifact appeared just above strong specular reflectors (the diaphragm) in a few images, due to saturation (Fig. 4(a)). The harmonic components introduced hereby result in an extra 'match' when performing the matched filtering producing a bright spot above the reflector. The artifact is described and shown in Pedersen et. al (2003).

A subtle but clearly noticeable flashing artifact was seen in some of the STA images during movement. It was not visible in the individual images, only during movie playback. It had no visible influence on image quality.

4.3. Penetration

The differences in penetration depths between the two techniques are shown in Table 2 and the distribution is depicted in Fig. 6. As seen, there is only a slight but significant (p=0.008) difference in penetration depth; STA images on average had 0.48 cm more penetration. The first examiner, though, did not perceive any significant difference in penetration depth. The utilized signals and intensities were deliberately chosen to match penetration ability in conventional and STA imaging within the given safety limits. This shows that STA imaging is fully capable of producing images to at least the same depth as conventional ultrasound imaging.

4.4. Image Quality

The distributions and results of the image quality scoring are shown in Fig. 7 and Table 3 respectively. All three examiners scored a significant better image quality in STA images yielding a highly significant image quality improvement based on the pooled answers. The mean VAS score from all three examiners is not calculated, since it really makes no sense to do that. Also, one should be carefull to interpret the absolute VAS averages of each examiner, since the values heavily depend on that persons interpretation of the scale.

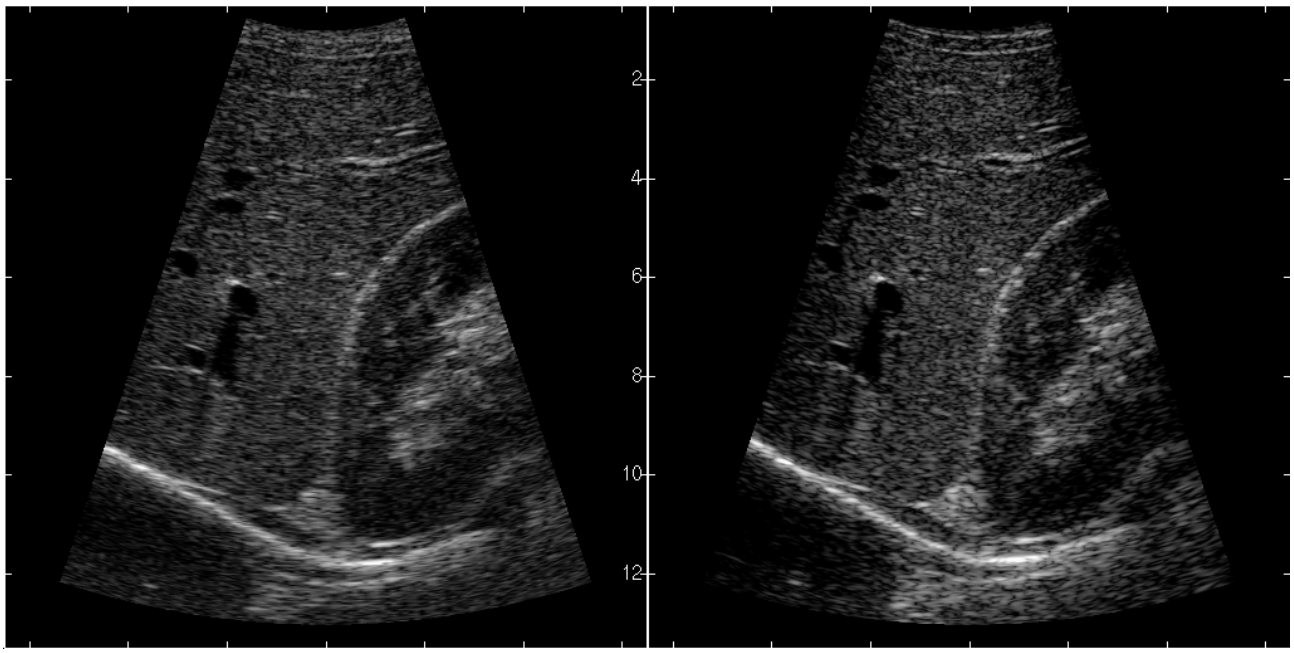

(a) Longitudinal section of right liver lobe showing cross sections of hepatic vein branches, longitudinal section of a portal a vein branch (upper left part), the kidney, and diaphragm at the bottom.

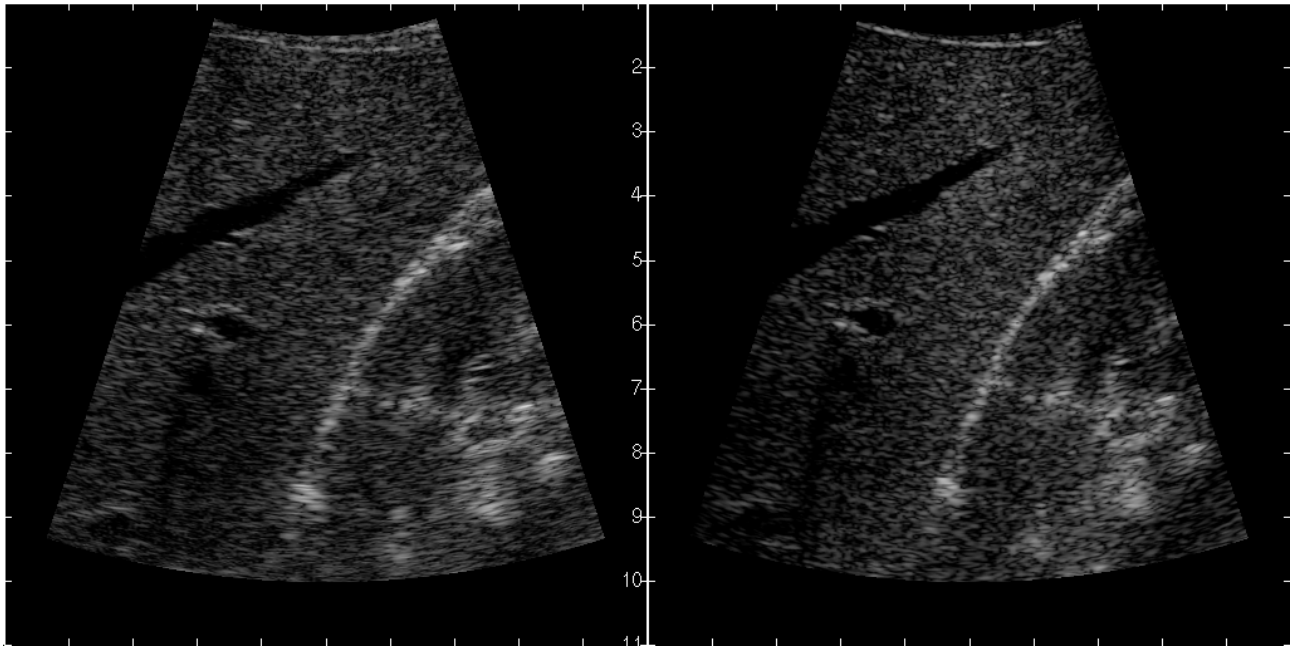

(b) Longitudinal section through right liver lobe including the right kidney. A hepatic vein branch is seen as a dark excavation in the liver.

Figure 8: Some examples of the produced in-vivo images. Left part is the conventional and right is the STA image.

Examiner	Conventional (cm)	STA (cm)	Difference (cm)	P value
S1	8.86	9.04	0.18	0.477
S2	8.21	8.79	0.57	0.076
S3	9.36	10.04	0.68	0.012
Pooled	8.81	9,29	0.48	0.008

Table 2: Results of answers to "At what depth [cm] does the image quality decrease significantly?"

Sonographer	Difference (VAS)	P value
S1	10.75	0.0011
S2	10.6	0.014
S3	3.64	0.0025
Pooled		< 0.001

Table 3. Mean VAS differences between conventional and STA images for each examiner. Positive values mean STA is better.

5. DISCUSSION

The results clearly show that synthetic transmit aperture imaging can be used in medical ultrasound. We believe this is the first published study that make a clinical comparison of conventional and synthetic aperture ultrasound imaging. The worry that tissue motion would make coherent summation of samples, and thereby image formation, impossible can be discarded for these abdominal images. Motion does introduce minor flash artifacts, though, which we expect to be able to remove by motion compensation in future works.[11] The synthetic aperture technique heavily depend on coded (chirp) excitation to obtain sufficient signal-to-noise ratio and therefore exhibits the same minor artifacts in our current implementation as described in earlier work.[9]

The clinical evaluation performed by the medical doctors shows a minute (0.48 cm) but significant (P=0.008) increase in penetration depth using synthetic aperture with coded excitation. Since the two techniques are totally different with regards to excitation method, aperture use, and pulse design, this value is not that interesting. Based on the statistical results, hypothesis one is rejected, and we conclude that STA imaging can obtain satisfying penetration within the current intensity limits. In the present case penetration is actually improved.

Image quality evaluation showed highly significant improvement in STA images compared to conventional images, which was also expected by the authors due to the apparent improved resolution throughout the STA images. Therefore, also hypothesis number two was rejected. One should be careful about interpreting the absolute VAS values, since the inter-observer variation in VAS scale interpretation is always large.

6. CONCLUSION

Synthetic aperture ultrasound imaging has been demonstrated and evaluated in-vivo. The clinical evaluation showed improved image quality in side-by-side comparison to conventional ultrasound imaging. This finding is very important to future real-time three-dimensional imaging methods based on synthetic aperture techniques.[12,13] Especially two- and three-dimensional vectorial flow estimation methods,[14] which heavily depend on the high acquisition rate delivered by STA imaging.

ACKNOWLEDGMENTS

Thanks to M.D. Dr.Med. Torben Larsen, M.D. Nis Nørgaard, and M.D. Bjørn Skjoldbye for evaluating the ultrasound images, and to the volunteers for participating.

This work is sponsored by grant 9700883 and 9700563 from the Danish Science Foundation, by Engineer Frode V. Nyegaard and wife's Foundation, by Ph.D. grant 11-3160-55173 from the Technical University of Denmark, and by B-K Medical A/S, Herlev, Denmark.

REFERENCES

1. M. Karaman, P. C. Li, and M. O'Donnell, "Synthetic aperture imaging for small scale systems," *IEEE Trans. Ultrason., Ferroelec., Freq. Contr.* **42**, pp. 429–442, 1995.
2. K. L. Gammelmark and J. A. Jensen, "Experimental study of convex coded synthetic transmit aperture imaging," in *Proc. IEEE Ultrason. Symp.*, pp. 1573–1576, 2002.
3. K. L. Gammelmark and J. A. Jensen, "Multielement synthetic transmit aperture imaging using temporal encoding," *IEEE Trans. Med. Imag.* **22**(4), pp. 552–563, 2003.
4. M. O'Donnell and L. J. Thomas, "Efficient synthetic aperture imaging from a circular aperture with possible application to catheter-based imaging," *IEEE Trans. Ultrason., Ferroelec., Freq. Contr.* **39**, pp. 366–380, 1992.
5. T. X. Misaridis and J. A. Jensen, "An effective coded excitation scheme based on a predistorted FM signal and an optimized digital filter," in *Proc. IEEE Ultrason. Symp.*, **2**, pp. 1589–1593, 1999.
6. J. A. Jensen, O. Holm, L. J. Jensen, H. Bendsen, H. M. Pedersen, K. Salomonsen, J. Hansen, and S. Nikolov, "Experimental ultrasound system for real-time synthetic imaging," in *Proc. IEEE Ultrason. Symp.*, **2**, pp. 1595–1599, 1999.
7. FDA, "Information for manufacturers seeking marketing clearance of diagnostic ultrasound systems and transducers," tech. rep., Center for Devices and Radiological Health, United States Food and Drug Administration, 1997.
8. AIUM, "Acoustic output measurement standard for diagnostic ultrasound equipment," tech. rep., American Institute of Ultrasound in Medicine & National Electrical Manufacturers Association, May 1998.
9. M. H. Pedersen, T. X. Misaridis, and J. A. Jensen, "Clinical evaluation of chirp-coded excitation in medical ultrasound," *Ultrasound Med. Biol.* **29**(6), pp. 895–905, 2003.
10. D. G. Altman, *Practical Statistics for Medical Research*, vol. 14, Chapman and Hall / CRC, London, 1997.
11. K. L. Gammelmark and J. A. Jensen, "Duplex synthetic aperture imaging with tissue motion compensation," in *Proc. IEEE Ultrason. Symp.*, pp. 1569–1573, 2003.
12. S. I. Nikolov, B. Tomov, F. Gran, R. Dufait, and J. A. Jensen, "Further development of synthetic aperture real-time 3d scanning with a rotating phased array," in *Proc. IEEE Ultrason. Symp.*, pp. 1899–1902, 2003.
13. C. R. Hazard and G. R. Lockwood, "Theoretical assessment of a synthetic aperture beamformer for real-time 3-D imaging," *IEEE Trans. Ultrason., Ferroelec., Freq. Contr.* **46**, pp. 972–980, 1999.
14. J. A. Jensen and S. I. Nikolov, "A method for real-time three-dimensional vector velocity imaging," in *Proc. IEEE Ultrason. Symp.*, pp. 1582–1585, 2003.

APPENDIX

C

Co-authored Articles

C.1 Ultrasound Research Scanner for Real-time Synthetic Aperture Image Acquisition

This article has been submitted for review to *IEEE Transactions on Ultrasonics, Ferroelectrics, and Frequency Control* in 2003.

Ultrasound Research Scanner for Real-time Synthetic Aperture Data Acquisition

Jørgen Arendt Jensen (1), Ole Holm (2), Lars Joost Jensen (2), Henrik Bendsen (2), Svetoslav Ivanov Nikolov (1), Borislav Gueorguiev Tomov (1), Peter Munk (1), Martin Hansen (2), Kent Salomonsen (2), Johnny Hansen (2), Kim Gormsen (2), Henrik Møller Pedersen (1,2) and Kim L. Gammelmark (1)

(1) Center for Fast Ultrasound Imaging, Ørsted•DTU, Build. 348, Technical University of Denmark, DK-2800 Kgs. Lyngby, Denmark
(2) IO Technologies A/S, Carl Jacobsens Vej 16, DK-2500 Valby, Denmark

September 9, 2004

Abstract

Conventional ultrasound systems acquire ultrasound data sequentially one image line at a time. The architecture of these systems is therefore also sequential in nature and processes most of the data in a sequential pipeline. This often makes it difficult to implement radically different imaging strategies on the platforms and makes the scanners less accessible for research purposes. For a system designed for imaging research flexibility is the prime concern. The possibility of sending out arbitrary signals and the storage of data from all transducer elements for 5 to 10 seconds allows clinical evaluation of synthetic aperture and 3D imaging. This paper describes a real-time system specifically designed for research purposes.

The system can acquire multi-channel data in real-time from multi-element ultrasound transducers, and can perform some real-time processing on the acquired data. The system is capable of performing real-time beamforming for conventional imaging methods using linear, phased, and convex arrays. Image acquisition modes can be intermixed, and this makes it possible to perform initial trials in a clinical environment with new imaging modalities for synthetic aperture imaging, 2D and 3D B-mode and velocity imaging using advanced coded emissions.

The system can be used with 128 element transducers and can excite 128 transducer elements and receive and sample data from 64 channels simultaneously at 40 MHz with 12 bits precision. Two-to-one multiplexing in receive can be used to cover 128 receive channels. Data can be beamformed in real time using the system's 80 signal processing units, or it can be stored directly in RAM. The system has 16 Gbytes RAM and can, thus, store more than 3.4 seconds of multi-channel data. It is fully software programmable and its signal processing units can also be reconfigured under software control. The control of the system is done over a 100 Mbit/s Ethernet using C and Matlab. Programs for doing *e.g.* B-mode imaging can directly be written in Matlab and executed on the system over the net from any workstation running Matlab. The overall system concept is presented along with its implementation and examples of B-mode and *in-vivo* synthetic aperture flow imaging.

1 Introduction

Modern ultrasound scanners employ digital signal processing to generate high quality images, which are dynamically focused in receive. Processing has to be made on data streams in the Gbytes per second range, and this necessitates the use of dedicated chips to perform processing in real time to maintain the cost, space, and power consumption moderate. Fundamental changes to the signal processing are, thus, difficult or impossible to make.

The current scanners perform image acquisition sequentially one line at a time, and the frame rate is, thus, limited by the speed of sound. When imaging flow, several emissions have to be made in the same direction, and this limits the frame rate, especially for large depths and large color flow sectors. For a 100 line image at 15 cm depth, the frame rate can be below 6 Hz, which is unacceptable for cardiac imaging.

New imaging techniques based on synthetic aperture (SA) imaging have therefore been suggested and investigated [1, 2, 3]. The methods can potentially increase both resolution and frame rate, since the images are reconstructed from RF data from the individual transducer elements. Hereby a perfectly focused image in both transmit and receive can be made. Research in real time 3D imaging is also underway [4, 5]. The purpose is to make systems that in real time can display a pyramidal volume of the heart, where different slices hereafter can be visualized.

It has been intensely discussed, whether SA imaging could give better images, and how they will be affected by tissue motion and limited signal-to-noise ratio. It has also been stated, that flow imaging cannot be performed with SA methods. A fundamental problem in SA imaging is the poor signal-to-noise ratio in the images, since a single element is used for emission. This gives a much lower emitted energy compared to using the full aperture in conventional imaging and therefore limits the depth of penetration. A potential solution to this is the use of coded excitation, and several groups are working on employing coded signals to enhance the signal-to-noise ratio [6, 7, 8]. Coded imaging can also be used to further increase the frame rate [9, 10, 11]. It has also recently been shown that SA imaging can be used for velocity estimation [12, 13]. This shows that SA systems can be made with all of the functionality of conventional systems. There are, thus, good reasons for constructing an experimental system capable of measuring SA data in-vivo to evaluate the proposed methods. It is the purpose of this paper to describe such a system and give some examples from its use, demonstrating that many of the problems in SA imaging mentioned above can be solved.

All of the above techniques require digital signal processing on signals from individual transducer elements. The most advanced techniques also uses different codes, that changes as a function of element and emission number, so that a fully flexible emissions system is needed. For research purposes both demands can be difficult to fulfill with commercial scanners, since they are often highly integrated, and it is difficult to access individual signals. Programming commercial scanners for new imaging techniques is often also either cumbersome or impossible. It is, thus, beneficial to develop a dedicated research system, that can acquire, store, process, and display ultrasound images from multi-element transducers for any kind of imaging strategy.

This paper describes such a research scanner, its design, implementation and use *in-vivo*. The primary purpose of the scanner is to acquire complete RF data sets, where the signals on the individual elements are stored and can be used for later processing in development of algorithms and imaging schemes. A large memory covering several heart cycles is, thus, needed. It must be possible to implement any kind of imaging and a fully flexible transmission system is needed. Not all mentioned methods can be implemented in real time, since the resources needed for real-time processing only can be determined after the algorithm has been developed. A key requirement is therefore to store all data and then transport them to general computer clusters for processing. To allow scanning on human volunteers, it is, however, necessary to have real-time processing capabilities for orientation of the scanning, and the various traditional scanning methods should be implemented. The processing should be so flexible that some of the new methods can be implemented or experimented with for real time implementation. Finaly, the scanner should be easy to program allowing one to implement entirely new scanning methods with minimal efforts. Such a system can assist in the development of scanning techniques and algorithms and facilitate pre-clinical trials. It also makes it possible to investigate the role of tissue motion in SA imaging and can be used for quantifying the emitted intensities for the advanced imaging methods.

The demands on the system are further elaborated in the next Section. A description of the individual units of the system is given in Section 3, and the actual implementation is also shown. The programming model for the system, and how phased array imaging can be done in few lines of code, is shown in Section 4. Examples of clinical use of the system on human volunteers is described in Section 5, and a summary of experiences with the

system and its further development is given in Section 6.

2 System specification

The purpose of the system is to make the acquisition of multi-channel data in real-time from clinical multi-element ultrasound transducers possible, and to enable real-time or near real-time processing of the acquired data. The system must be capable of performing the beam formation for all currently available imaging methods, and this makes it possible to carry out initial trials with new imaging modalities for synthetic aperture imaging, 3D imaging, and 2D and 3D velocity estimation. It must be capable of working in a clinical environment to evaluate the performance of various algorithms on human volunteers.

The system is specifically intended for research purposes, and is not intended for commercial use. The size of the system is, thus, not very important, and it is not necessary to make it easily transportable. Also it is only used by experts and the user interface to the medical doctor is of minor importance. Most efforts have been put on the flexibility of the system and its ease of configuration for new uses.

The function of the system is defined by the different imaging methods for which it can be used. Each of the imaging types is described below, and the consequences for the system then given.

Linear array imaging: A linear array image is generated by a multi-element transducer with 128 to 256 elements [14]. The beam is moved by selecting *e.g.* 64 adjacent elements and emitting a focused beam from these. The focusing in receive is also done by a number of elements, and dynamic focusing is used. Apodization in both transmit and receive are often applied. The number of active elements is usually 32 to 64. The transducer frequency is from 2 MHz to 10 MHz. Imaging is done down to a depth of 30 cm.

The demands on the system are, thus, for 64 channels simultaneous sampling at 40 MHz. The focusing delay for element i is given by

$$t_d(i) = \frac{|\vec{r}_i - \vec{r}_p| - |\vec{r}_c - \vec{r}_p|}{c}, \tag{1}$$

where c is speed of sound, $\vec{r}_p$ is the imaging point, $\vec{r}_c$ denotes the center element of the active aperture, and $\vec{r}_i$ is the location of the element. Assuming the point to be very close to the transducer gives the maximum delay

$$t_{d\_max} = \frac{|\vec{r}_i| - |\vec{r}_c|}{c}. \tag{2}$$

A linear array often have $\lambda = c/f_0$ pitch and the maximum delay is then

$$t_{d\_max} = \frac{N_e/2 \cdot c/f_0}{c} = \frac{N_e}{2f_0}, \tag{3}$$

where f_0 is center frequency and N_e is the number of active elements. For 64 elements and $f_0 = 2$ MHz t_{d_max} equals 16 μs.

The maximum time to sample one line to a depth of d is given by

$$t_s = \frac{2d}{c}. \tag{4}$$

This give $t_s = 430$ μs corresponding to 17,200 samples at 40 MHz for a depth of 30 cm.

Phased array imaging: The beam is electronically swept over the imaging area by using a 64 to 256 element array [15]. The beamforming delays are used both for steering and focusing. The pitch is reduced to $\lambda/2$ to

avoid grating lobes and a very conservative estimate of maximum delay is to assume the imaging point to be at the edge of the array. The maximum delay then is

$$t_{d\_max} = \frac{N_e \lambda/2}{c} = \frac{N_e}{2 f_0}, \tag{5}$$

which is equal to the demand for linear array imaging.

The transducer frequency is from 2 MHz to 10 MHz. Investigations are done to a depth of 20 cm.

The demands on the system is, thus, for 128 channels sampling at 40 MHz. The demands on focusing delays, sampling time, and storage are the same as for linear array imaging.

Flow estimation, spectrum: Beamforming is done in one direction with either a linear or phased array [16]. The flow signal from blood has 40 dB less power than that from stationary tissue. The dynamic range of the flow signal is 30 dB. The effective number of bits must be 12 or more, when the signals from all channels have been combined. The pulse emitted can have from 4 to 16 periods of the center frequency of the transducer or a coded signal can be employed.

Flow imaging: Imaging is done by pulsing repeatedly in one direction and then change the direction to generate an image [17]. An image can therefore be assembled from up to 1,000 pulse emissions.

Three-dimensional imaging: A matrix element transducer is used with *e.g.* 40×40 elements [18, 4]. Only some of the elements are used for transmit and receive. The area of the elements is small and pulsing should be done with 100 to 300 volts. Coded signals should be used. Coded pulses with up to 64 cycle periods must be possible with a high amplitude accuracy. This corresponds to emission over a period of 32 μs with a sampling frequency of 40 MHz and an accuracy of 12 bits.

The maximum delay conservatively corresponds to the transmission time over the aperture. Assuming $\lambda/2$ pitch gives

$$t_{d\_max} = \frac{\sqrt{2} N_e \lambda/2}{c} = \frac{N_e}{\sqrt{2} f_0}, \tag{6}$$

which for 64×64 elements and $f_0 = 2$ MHz gives 23 μs. Parallel lines are generated by using parallel beamformers and reusing data from one pulse emission. The system must be capable of reading the data sampled from one element a number of times, and use different phasing schemes for each cycle through the data. This gives a very high demand on the processing, that might not be obtainable by the system.

Synthetic aperture imaging: A standard linear or phased array multi-element transducer is used. Pulsing is done on a few elements and the received response is acquired for all elements [19, 20]. The image is then reconstructed from only a small number of pulse emissions by using the data from all elements.

This type of imaging needs large amounts of storage and the ability to reuse the data for the different imaging directions. The system must be capable of storing 3 seconds of data for all channels. For a 12 bits resolution at 40 MHz, 64 channels, and 3 seconds of data, this amounts to a total storage demand of more than 14 Gbytes.

The processing of the data cannot be done in the system, due to the very large demand on processing. This is solved by storing the data in real time and the transferring them to a multi-processor system for storage and image reconstruction.

Synthetic aperture flow imaging: The data is acquired in the same way as for synthetic aperture imaging, but the focusing is done continuously for all points in the image [21]. Hereby the data for flow estimation is present for all image locations for all time. It is, thus, very important that the image measurement is continuous over the whole data acquisition time.

Fast coded synthetic aperture imaging: Here the image is acquired by sending different codes on the individual elements for different emissions [9, 10, 11]. The image is then created by processing the received signals using different filters to separate out the individual signals.

The system must, thus, be capable of sending an arbitrary code that is different for the different channels, and that can change from emission to emission.

In general the demands for all of these imaging modes can be condensed to a few generic demands. The transmissions system should be capable of sending an arbitrary signal on each element. The signals can be different from element to element and from emission to emission. The transmission system must be capable of focusing the transmission differently for emission to emission. The sampling frequency should be 40 MHz and the resolution is determined by the dynamic range of the system, which should be above 60 dB. A 12 bits digital-to-analog is, thus, sufficient. Coded waveforms should be emitted for up to 32 μs and different codes should be emitted for different emissions and elements. For 100 image lines this gives 80 Ksamples of memory for each transducer element.

The receiving system should be capable of sampling full RF data from all channels. The sampling frequency should be 40 MHz and the resolution at least 12 bits. Sampling should be possible over a couple of heart beats. For 3 seconds of real time data at 40 MHz with 2 bytes per samples gives a demand of 229 Mbytes, so that a RAM of 256 Mbytes per channel is necessary. To process the data it must be possible to dynamically focus the data in real time. A focusing chip must be used for each channel, and this chip must have memory with parameters for the focusing, and the system must be capable of summing the data from the individual channels. Ideally the processing should be easily reconfigurable, and it must be possible to store the raw RF data, the focused data, or the focused and summed data. The beamformed and summed data should also be transported out of the system in real time for further processing and display on a screen.

3 System realization

The RASMUS (Remotely Accessible Software configurable Multi-channel Ultrasound Sampling) system consists of four distinct modules: Transmitters, analog amplifiers (Rx/Tx amplifiers), receivers, and a sync/master unit. The main blocks are depicted in Fig. 1. The connection to the transducer is through a 128 wire coaxial cable through the Rx/Tx amplifiers. The transmitter sends the signals through the transmit amplifiers, and the receiver unit samples the amplified and buffered signals from the Rx/Tx amplifiers. The sync/master unit holds a crystal oscillator and controls the central timing of the scanning process. The overall operation of the system is controlled through a number of single board PCs in the individual units interconnected through a standard 100 Mbit/s Ethernet. The waveforms and focusing delay data are transmitted from the controlling PC to the transmitters and receiver boards. The data from the sampling is processed by FPGAs (Field Programmable Gate Arrays), that can be configured for specific signal processing tasks over the net. One Focus FPGA is used for each element and a Sum FPGA is placed for each eight elements. The processed and summed signal can then be routed from Sum FPGA to Sum FPGA through a cascade bus. The resulting signal is read by one or more signal processors (ADSP), that can be connected through serial link channels capable of transmitting 40 Mbytes per second. The beamformed signal is send via the link channels to the PC for further processing and display.

The following paragraphs detail the overall design of the individual boards.

3.1 Transmitter

The overall diagram of the transmitter is shown in Fig. 2 and its layout is shown in Fig. 3. Each transmitter board has 16 channels each having a 128 Ksamples pulse RAM connected to a 40 MHz, 12 bits DAC. The pulse RAM is controlled by an FPGA, where the individual waveforms are selected as a memory start address and a transmit delay. The delay RAM holds the start address of the waveform in the pulse RAM and the corresponding

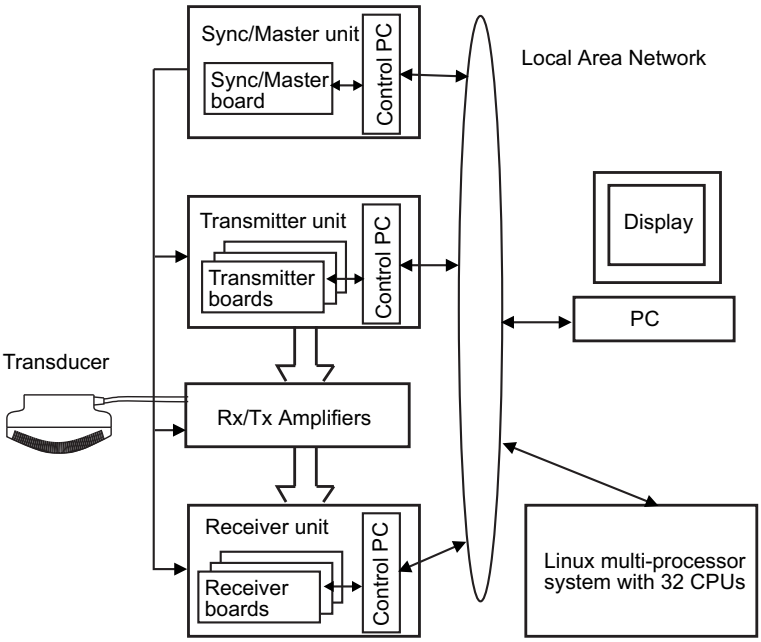

Figure 1: Overall diagram of system.

delay for each line. The delay RAM is implemented as 32 k $\times$ 32 bit SRAM. At the start of each line the pulse emission is delayed according to the delay value for each channel. Both the waveform and the delay can change for each emission, which ensures full flexibility in the transmissions. The length of the waveforms can be set, and waveform durations up to 100 μs can be emitted.

The whole board is controlled through a compact PCI interface from which all the memory can be accessed and the FPGAs can be programmed. The system houses 8 boards for a total of 128 independent emission channels.

3.2 Receiver

The Receiver board diagram is shown in Fig. 4. It samples and processes 8 analog signals selected from 16 inputs through a 2-to-1 multiplexer. Each of the input signals is sampled at 40 MHz and 12 bits into one of the two buffer SRAMs. While one of the buffer SRAMs is used for sampling and the other one is used for transferring data to the Focus FPGA associated with each channel. The data is then processed in the Focus FPGA using parameters from the 128 Mbytes Focusing RAM, and the result is passed on to the Sum FPGA. The processing can either be a dynamic receive focusing or the data can be passed unaltered for later storage. The Sum FPGA can either store the data in the 2 Gbytes storage RAM or it can sum all 8 channels with the result from a cascade bus and pass it on to the next receiver board through this cascade bus. The individual RF data can be both stored in the RAM and processed by the FPGAs at the same time. The last receiver board in the system then transmits the focused signal to the ADSP SHARC for transmission to the display PC [23]. The storage RAM can contain more than 3 seconds of real time data for each channel, that later can be accessed from the PCs controlling the system.

The actual board layout is shown in Fig. 5. All boards in the system have a size of 53 cm by 36.5 cm, and the receiver is manufactured using a 12 layer printed circuit board.

The receiver boards are accessible from a general purpose Linux based single board PC, which controls the different boards. All memory can be accessed from this interface, and it is possible to upload code to the FPGAs through the flash memory. A FIFO memory can be programmed to replace the SRAM for sampling and the FIFOs can be used for debugging the system. A mailbox interface to the SHARC ADSP is also accessible from the PCI

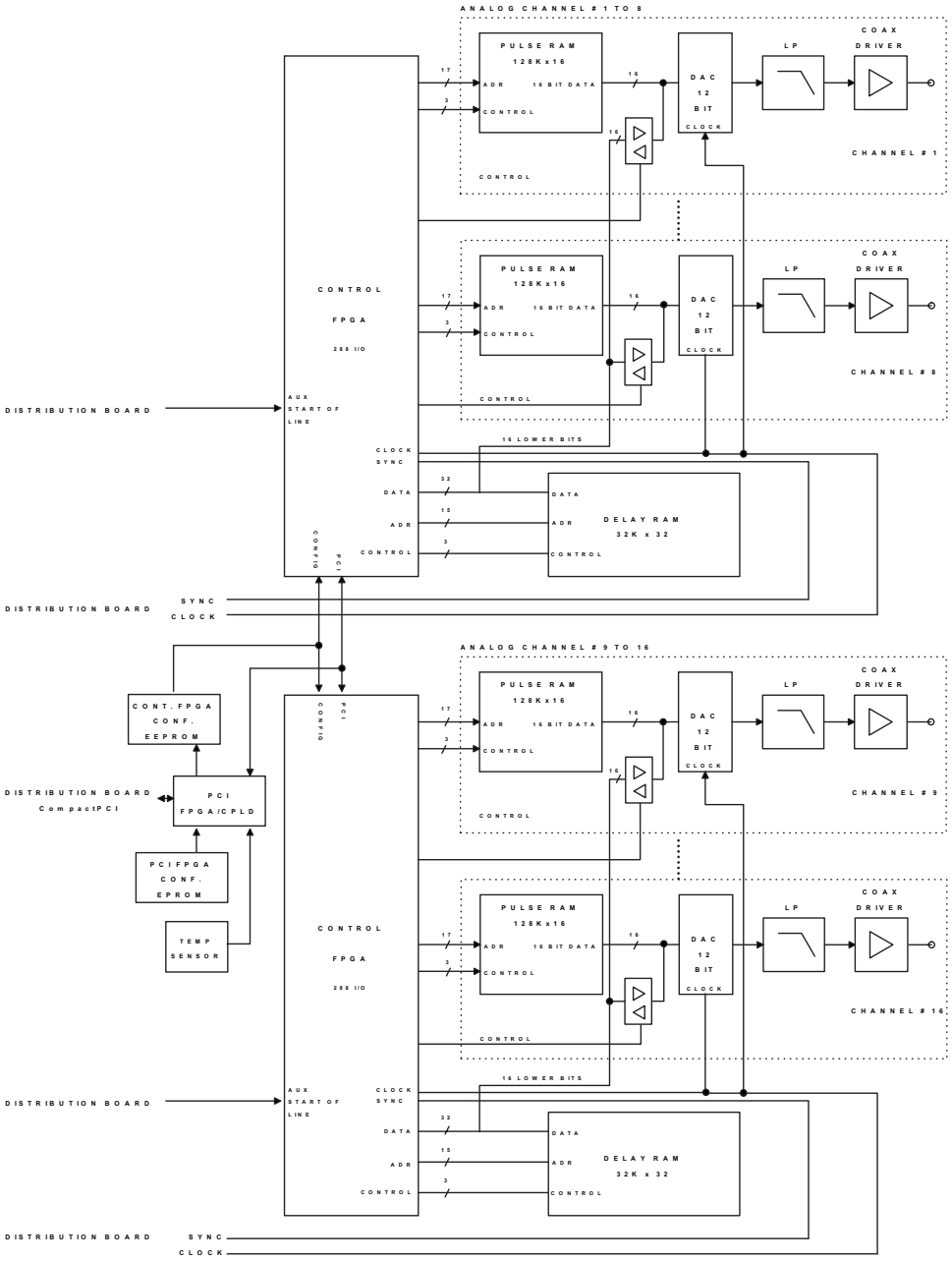

Figure 2: Main diagram of the transmitter board.

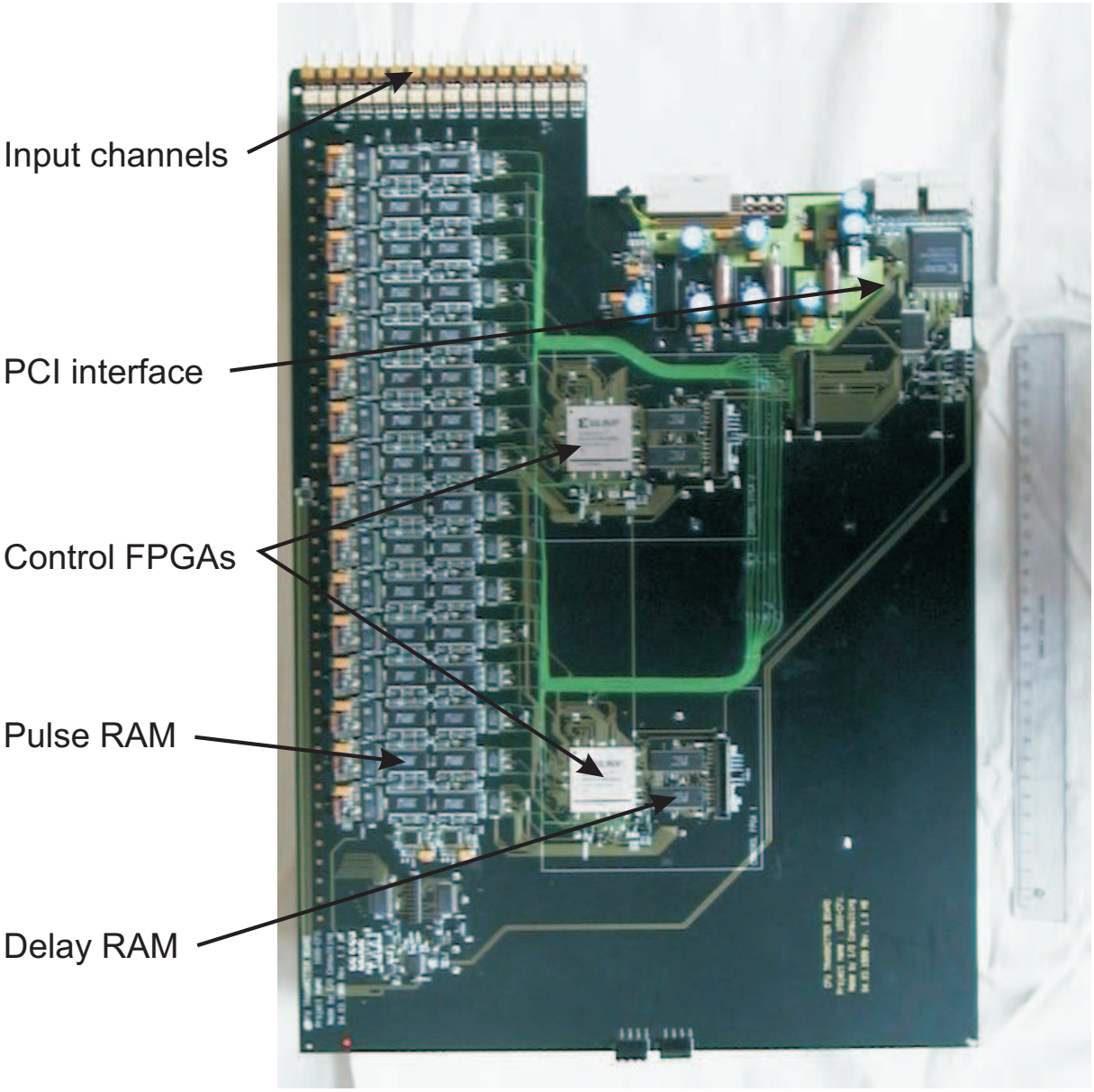

Figure 3: The transmitter board layout. The board size is 53 cm by 36.5 cm. The size is indicated by the 30 cm ruler on the right.

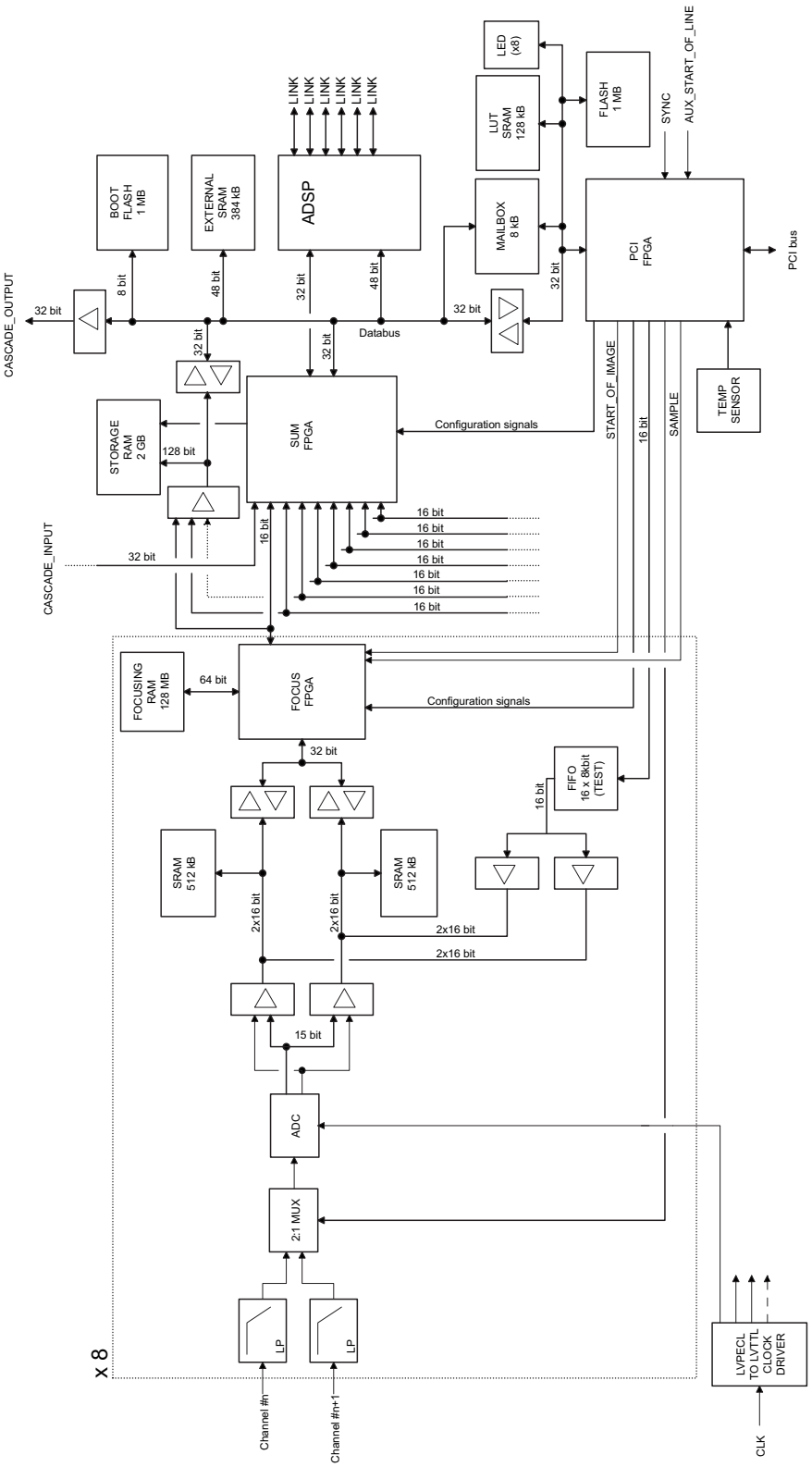

Figure 4: Main diagram of receiver board (from [22]).

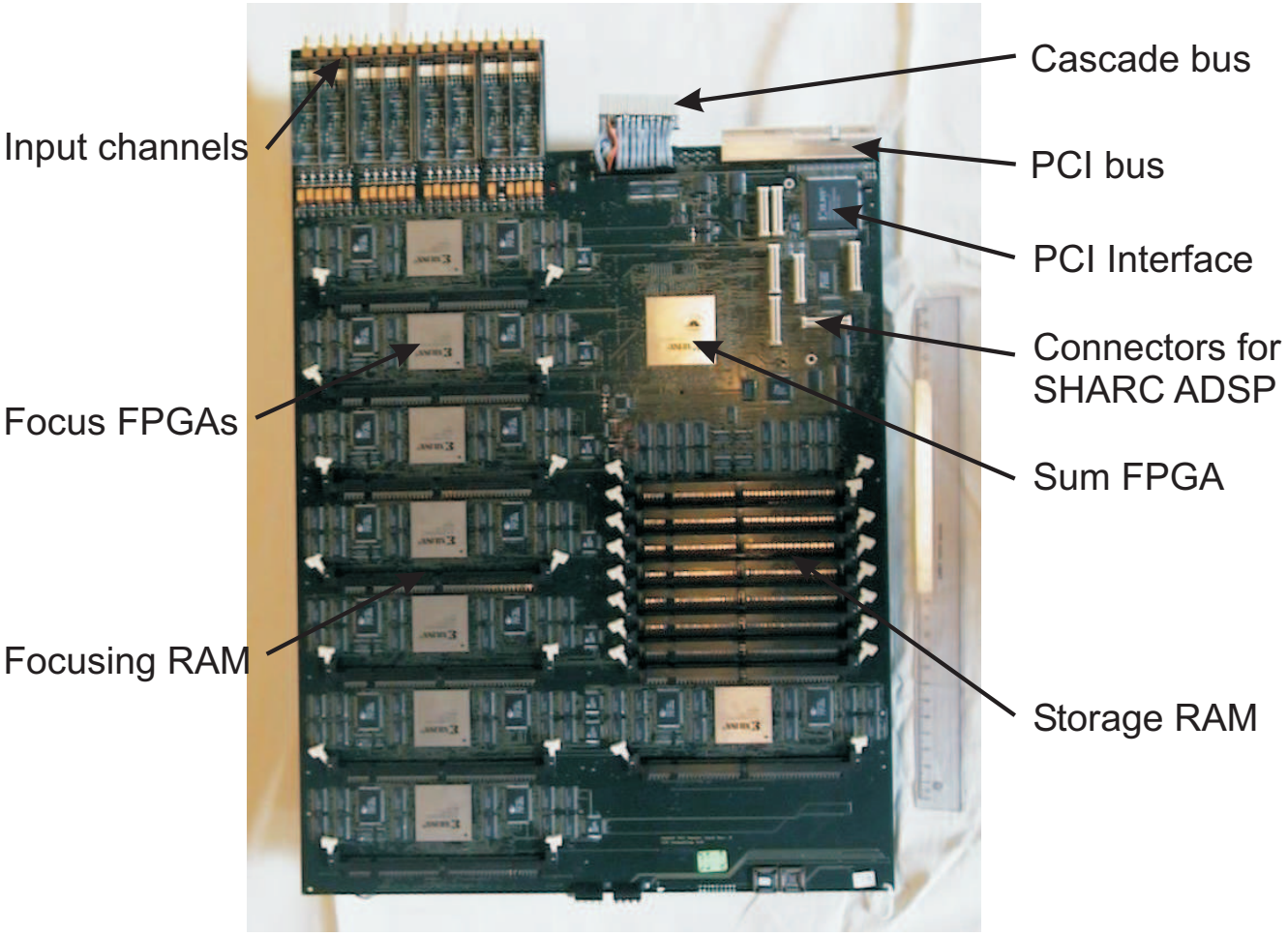

Figure 5: The receiver board layout without RAM modules to reveal the processing electronics. The board size is 53 cm by 36.5 cm.

interface. This is used for sending messages to the ADSP.

3.2.1 Focus FPGA

The Focus FPGA controls the initial storing and processing of the sampled data. The Focus FPGA fetches the sampled data from the SRAM and the corresponding focusing parameters from the Focusing RAM and processes the data before transferring the result to the Sum FPGA.

Two independent memory burst SRAM banks are used to bank switch between the sampled data and processed data. While the sampled data is being written to one of the two banks, the other bank can be read by the Focus FPGA. Each SRAM is implemented as 256 ksamples, which is equivalent to a line length of 3.3 ms sampled at 40 MHz, since samples are stored twice for making focusing faster.

The basic focusing algorithm currently implemented uses a combination of coarse and fine delays. The coarse delay is in steps of the 25 ns sampling interval, and it is implemented as a general table look up address generator. For each sample a 16 bit address index is read from the Focusing RAM. In this way focusing in any order can be implemented. The fine delay is implemented as a linear interpolation between two samples using two signed 16 bit apodization coefficients, which are read from the focusing RAM for each sample. To make one output sample per clock cycle, it is, thus, necessary to read two input samples, which is why the input samples are stored twice in the SRAM. Using this scheme any delay can be implemented, and the data can also be decimated during the focsuing process.

The Focus FPGA is implemented using a 300 Kgates XILINX device from the Virtex family: XCV300 in a 352 pin BGA package speed grade -4. The simple B-mode beamformer described above uses less than 10% of the logical resources of the chip for real-time B-mode beam formation. This leaves the possibility for investigating hardware implementations of more advanced beamformers including pulse compression, synthetic aperture, and parallel beamforming.

3.2.2 Sum FPGA

The Sum FPGA is used to perform digital signal processing on the 8 channels. The most basic operation is to sum the 8 focused channels. Further, it is used as a gateway between the eight independent sampling channels and the ADSP. The Sum FPGA controls the 2 Gbyte storage SDRAM.

When the focusing is done in the Focus FPGA, the 8 channels are added to the accumulated sum that is passed to the next Receiver board using a high speed cascade bus connecting the Sum FPGA's directly with each other. The last Sum FPGA in the chain uses the ADSP link ports to transfer the final result to an external PC, that displays the final image.

The Sum FPGA is implemented using a 1 Mgates XILINX device from the Virtex family: XCV1000 in a 560 pin BGA package speed grade -4. The simple design described above uses less than 5% of the logical resources of the chip for conventional real-time imaging.

3.3 Sync/master unit

The Sync/master unit controls the timing of the system. A highly stable oven controlled crystal oscillator generates the 40 MHz clock frequency. The clock jitter is below 5 ps. The clock is distributed using coax cables and emitter coupled logic (ECL) in order to minimize jitter. The timing source also transmits a synchronization signal. The receiver and transmitter uses the SYNC signal to start and stop the sampling cycles. An image consists of a number of lines, each with a transmission of a pulse and reception of the echoes. The transmitter and receiver generates an internal LINE signal from the SYNC signal to control the sampling process for the received signal.

The Sync/master board also generates the time gain compensation (TGC) signal used for the Rx/Tx boards. The sampling clock for the TGC waveform is 1 MHz. The values for the TGC and generation of the synchronization signals are loaded through the board's PCI interface.

3.4 Current processing capabilities

The current system only uses 10% of the available capacity in the FPGAs. With the programs it is possible to perform real-time beam formation for linear, phased, and convex arrays. The beam formation for all conventional ultrasound systems can, thus, be implemented. The post processing for image display and flow estimation is today done in PCs, but could be implemented in the SUM FPGA.

It is possible to focus data at a rate of 40 MHz. This gives 8,000 beamformed samples for a 200 μs acquisition corresponding to a depth of 15 cm. Sparse output samples could also be generated [24] and normally 512 complex samples per line is sufficient for B-mode display, so that a 1-to-8 parallel beamformer can easily be implemented. The remaining resources can then be used for filtration, code compression, or other processing.

Currently it is not possible to make real time processing of SA images. Here a full image must be formed after each pulse emission corresponding to more than 100 parallel beamformers. Compression of coded signal should also be done. The main bottlenecks are currently the data transfer rates, since the FPGAs still have room for more processing. The data acquisition can, however, always be done in real time, which is the most important feature for research purposes. Since different image sequences can be intermixed, a conventional B-mode image can be acquired and processed in real-time for orientation purposes. The SA image can then be acquired in between B-mode images and full orientation of the scanning can therefore be obtained.

3.5 Physical realization

Two 19 inch racks house the 8 transmitter and the 8 receiver boards, respectively, as shown in Fig. 6. The sync/master board is located in the rack cabinet for the receiver boards. Each of these racks also houses a slot PC running Linux, which controls the setup and operation of the boards. A separate enclosure is used for the analog front-end, which is shielded from the digital electronics. Here linear laboratory power supplies (Tellner TOE 8841 and 8852) are also used to supply the front-end to keep the noise low.

Although the system is quite large and weighs several hundred kilograms, it is still transportable and it can be moved around in the lab by two persons. The system is now fully functional and has been used for acquiring data for several new imaging methods as described in Section 5.

4 Programming of the system

From the software point of view, the system consists of several computers, that are directly connected to a number of transmitter and receiver boards and a single sync/master board. The computers are linked by a LAN, and use Linux as operating system and TCP/IP as the underlying communication protocol.

The software was designed to meet the following requirements:

- Flexibility and ease of use. It is of prime importance that new imaging methods can be quickly implemented with a minimal amount of programming even for new users.
- Data encapsulation. All data for the imaging algorithm are stored in the boards of the scanner.
- Distributed computations. The computers work independently of each another, and each calculates only those imaging parameters for boards, which are connected to that particular computer.
- Portability. The software is written in ANSI C and is platform independent.

Figure 6: The RASMUS scanner seen from the front with the receivers on the top, transmitters in the middle and the power supplies in the bottom. The analog front-end and transducer connection along with a control PC is placed in the other rack cabinet.

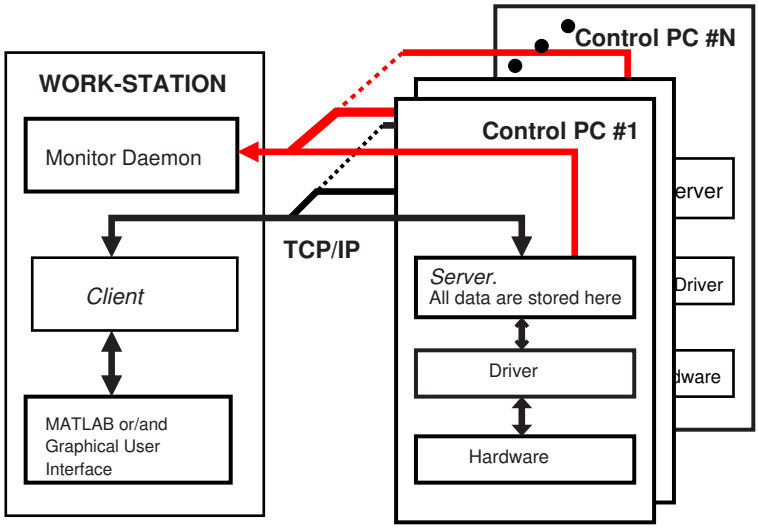

Figure 7: Client-server model of software.

The client/server communication model was adopted for the software. The computers controlling the boards run a *server* program. The server waits for requests coming from the LAN and processes them. The requests can be sent by any *client* program running on a computer connected to the LAN using the TCP/IP communication protocol.

Figure 7 shows the client-server model of the software. At start-up the server detects which boards are in the PCI enclosures. The computers can handle any combination of transmitter and receiver boards plugged into the same PCI back-plane. The server is in idle mode until an event occurs. In the case of a hardware malfunction, the server sends an emergency message to a program, called *monitor daemon*. Another event is a request by the *client*. The request can be for transferring parameters to the boards, for performing some calculations, or for retrieving data from the boards to the computer with the user.

The interface to the client program is implemented as a Matlab tool box. The function calls are implemented to be as close to the functions in the simulation program Field II [25] as possible. Algorithms created using Field II can thereby easily be tested on the scanner with only minor changes in the Matlab program. An example for setting the system to perform phased array B-mode imaging is shown below:

```
% Auto-detect and initialize the system
sys_init('auto');
% Set the pulse repetition frequency
sys_set_fprf(fprf);
% Set the sampling range gate in receive
sys_set_sampling_interval(start_depth, end_depth);
% Set the number of scan-lines per frame
sys_set_no_lines(no_lines);
% Define the transducer. Necessary for the delay calculations
tr_linear_array(no_elements, width, height, kerf);
% Do for all lines in the image:
for line_no = 1:no_lines
  % Set the pulse and the apodization for the current line
  xmt_excitation(waveform(line_no));
  xmt_apodization(line_no,xmt_apo(line_no,:));
  rcv_apodization(line_no,times, rcv_apo(line_no,:,:));
  % Set the focus, defined in 3D coordinates
```

```
  xmt_focus(line_no, focus(line_no));
  rcv_dynamic_focus(line_no, theta(line_no), fi(line_no));
end

% Set the time-gain compensation curve
tmg_tgc(tgc_vector);
% Start the continuous imaging process
tmg_start
```

In order to make the system perform linear array imaging only one line needs to be added, which changes the origin of the individual scan-lines.

5 Examples of use

The initial design of the system was started in October 1998 and the first images using the full system were acquired in the spring of 2001. The full real-time capabilities of the system were completed in 2002 and the RASMUS system is now capable of real-time focusing for conventional imaging and real-time data acquisition for all modes. This is illustrated in the following examples.

The first example shows a comparison between a traditional linear array image and a synthetic aperture image. A commercial 7 MHz probe is used and the system is programmed to alternate between linear array imaging and synthetic aperture imaging. Hereby both images are acquired at the same time on the same patient and view, and a direct comparison can be directly made. The linear array image uses 64 elements in transmit and 128 in receive, and the active aperture is moved across the physical aperture to perform the image. The synthetic aperture image is acquired using a number of spherical wave emissions. Normally one element is used in transmit, but to ensure sufficient transmitted energy, a number of elements are used in transmit. A set of 33 elements are used in transmission to form a spherical wave, and this emission aperture is moved over the physical aperture. This is done for 96 emissions. A 20 μs chirp signal is also used during emission, and two emissions are used for sampling the whole 128 element aperture using the 2-to-1 receive multiplexing. More details on this TMS (Temporally encoded multi-element SA imaging) method and the corresponding intensity levels can be found in [8].

The resulting images are shown in Fig. 8, with the linear array image to the left and the synthetic aperture image to the right. It can be seen that the SA image attains a 40 % increase in depth of penetration and that the resolution for the deeper lying wires are improved [8].

The second example demonstrates the system's ability to estimate flow *in-vivo*. The image is made using synthetic aperture techniques with a 7 MHz linear array. Here 11 elements are group for the emission. Eight emissions are used over the full 128 element aperture to form an image. A 20 μs chirp is used as excitation to ensure a good signal-to-noise ratio. The 64 elements closest to the center of the emission are sampled during reception and hereby signals from all 128 elements are sampled for the whole emission sequence. The sequence has been repeated 16 times for a total of 128 emissions with a pulse repetition frequency of 3 kHz. The velocity is then estimated by focusing along the direction of the flow and these signals are cross-correlated to estimate the movement and thereby the velocity. Details about the method can be found in [13]. The resulting image taken at the neck of a male volunteer of the carotid artery (bottom) and jugular vein (top) is shown in Fig. 9. It should be noted that the raw estimates are displayed, and the velocity is, thus, accurately estimated. The estimates only start at a depth of 13 mm due to the use of the chirp excitation. The white areas at the bottom of the artery are artifacts from the velocity estimation process. This is due to the selection of a wrong peak in the cross-correlation function [26], probably due to an insufficient signal-to-noise ratio.

In the last example data is sampled to a depth of 32 mm, although the pulse repetition frequency is 3 kHz, so that sampling is only done in 12.5 % of the time. The system is then capable of storing a sequence of image data

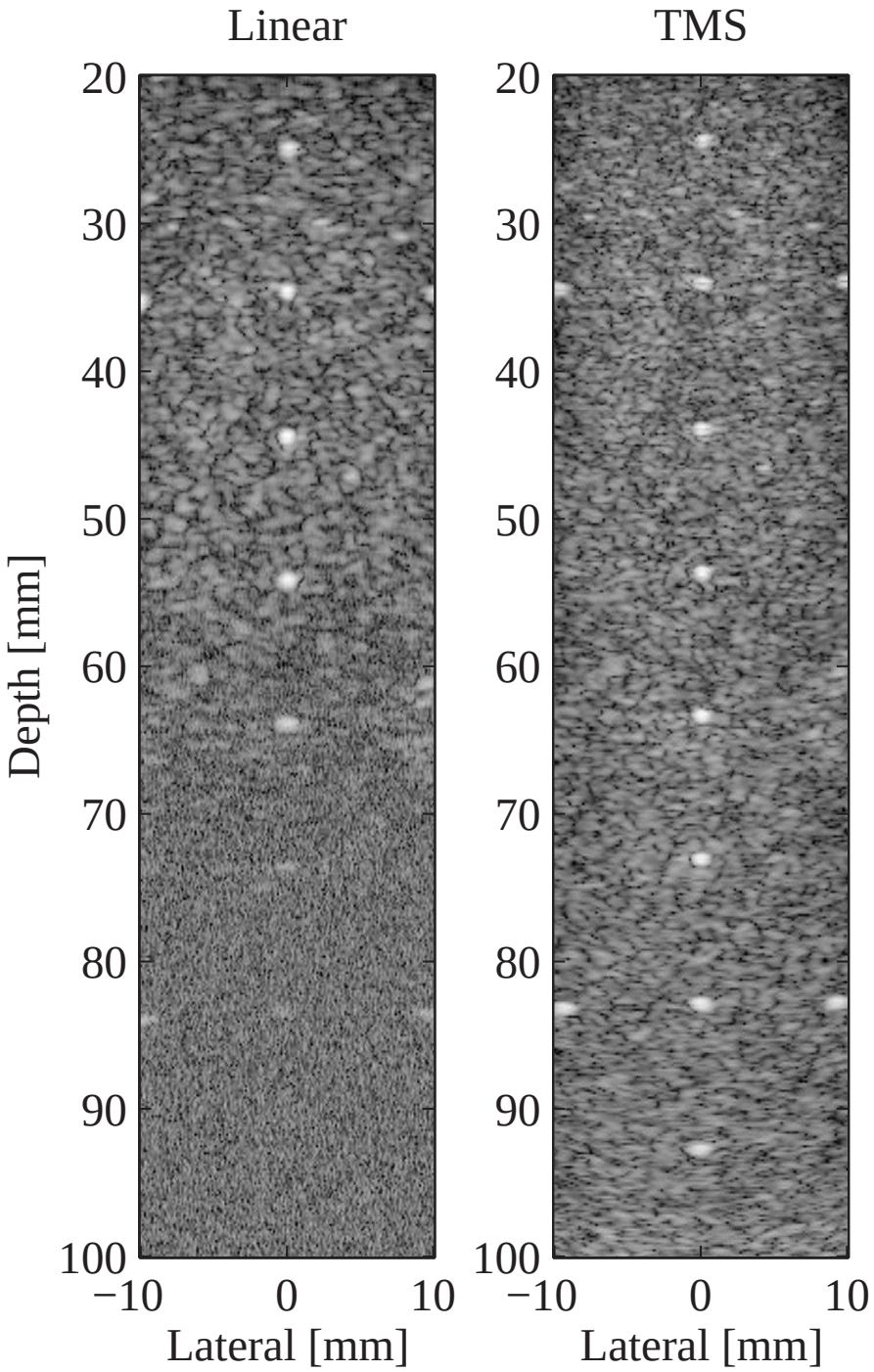

Figure 8: Linear array (left) and synthetic aperture scan (right) of nylon wires in a tissue mimicking phantom with an attenuation of 0.5 dB/[MHz cm] (from [8]).

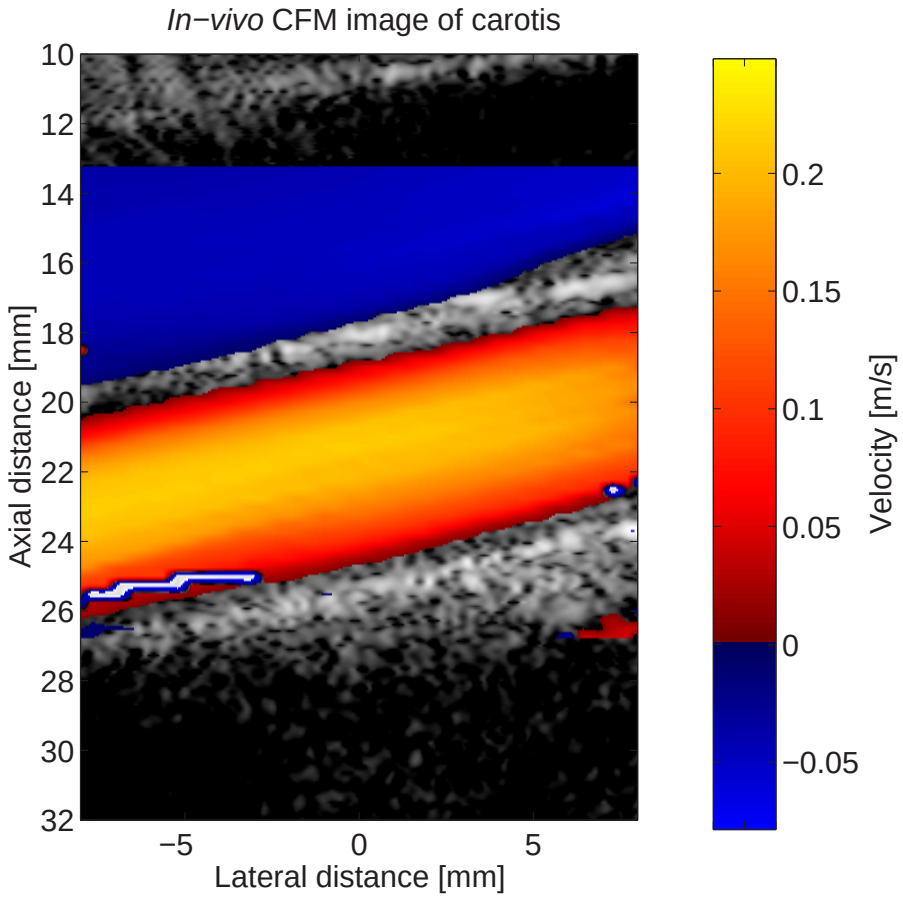

Figure 9: *In-vivo* color flow map image at a 77 degree flow angle for the jugular vein and carotid artery. The color scale indicates the velocity along the flow direction, where red hues indicate forward flow and blue reverse flow (from [13]).

for 26.9 seconds.

Several other image types have also been acquired like convex synthetic aperture image [27], 3D synthetic aperture data [28], and transverse flow data [29] and pre-clinical trials of convex array SA imaging [30]. The system has, thus, shown that it is a very flexible tool, that is able to sample data for nearly any imaginable application.

6 Summary and future extensions

The RASMUS system has been described in this paper. The system is currently fully operable and gives high quality *in-vivo* data, that can be used for devising and testing new imaging schemes like synthetic aperture imaging, directional flow techniques, and real-time three-dimensional imaging. The main method for operation has been real time data acquisition with storage of all the data in the system's RAM. The data are then transferred for later processing on a Linux cluster with 32 CPUs. The model of control under Matlab has shown to be very efficient, since the user can work at a very high level of control without being buried in the system's details. More than 15 people have currently been using the system without a very long introduction to its facilities. The software model has also greatly helped in debugging the system, since small scripts for testing can easily be written. The network feature has also eased the use. Most phantom experiments for debugging have been set-up in the laboratory, and then the script debugging and data acquisition is done from the office.

By far the most important feature is the flexible transmission system and the real time storage facility, that are nearly always used. The main annoyance in the use of the system has been the slow transfer of data out of the system's memory. This is currently done through the controlling PCs, and this is limited by the 100 MBit/s Ethernet and the PCI interface of the boards. The PCI interface is based on an FPGA, and it is currently slow and limited to a transfer rate of 2-8 Mbytes/s. A full experiment storing 16 Gbytes of data ideally takes nearly one hour to transfer to external disk at best, and often it takes longer. The slow transfer should be addressed in an updated version of the system, which could be based on a 1 Gbit/s Ethernet and an optimized PCI interface design.

The real-time capability has been the most difficult to get working. It relies on the global timing of the whole system and the coordination of all 72 FPGAs in the processing chain, and has been the last feature to work. Some of the examples mentioned in Section 5 has therefore been made by scanning with a normal B-K Medical 2102 scanner and then switch the probe to the RASMUS system for data acquisition, which is very cumbersome. The real-time processing can now make dynamic receive focusing for all transducer models. This makes real-time orientation possible, and the system can be programmed to acquire several different images in the same sequence for comparison. Also the potential of the FPGA processing solution needs to be determined. The current processing fills 10% of the FPGAs. Many more options exists and are currently being investigated.

The system has, however, already now been capable of acquiring high quality data for linear, phased and convex SA imaging and SA flow imaging, and the first pre-clinical trials comparing conventional and SA imaging have been conducted.

Acknowledgment

This work was supported by grant 9700883 and 9700563 from the Danish Science Foundation, by B-K Medical A/S, and by grant EF-782 from the Danish Academy of Technical Sciences. The anonymous reviewers are thanked for their many useful comments.

References

[1] J. T. Ylitalo and H. Ermert. Ultrasound synthetic aperture imaging: monostatic approach. *IEEE Trans. Ultrason., Ferroelec., Freq. Contr.*, 41:333–339, 1994.

[2] C. R. Hazard and G. R. Lockwood. Theoretical assessment of a synthetic aperture beamformer for real-time 3-D imaging. *IEEE Trans. Ultrason., Ferroelec., Freq. Contr.*, 46:972–980, 1999.

[3] S. I. Nikolov, K. Gammelmark, and J. A. Jensen. Recursive ultrasound imaging. In *Proc. IEEE Ultrason. Symp.*, volume 2, pages 1621–1625, 1999.

[4] S. W. Smith, H. G. Pavy, and O. T. von Ramm. High-speed ultrasound volumetric imaging system – Part I: Transducer design and beam steering. *IEEE Trans. Ultrason., Ferroelec., Freq. Contr.*, 38:100–108, 1991.

[5] G. R. Lockwood, J. R. Talman, and S. S. Brunke. Real-time 3-D ultrasound imaging using sparse synthetic aperture beamforming. *IEEE Trans. Ultrason., Ferroelec., Freq. Contr.*, 45:980–988, 1998.

[6] P. Li, E. Ebbini, and M. O'Donnell. A new filter design technique for coded excitation systems. *IEEE Trans. Ultrason., Ferroelec., Freq. Contr.*, 39:693–699, 1992.

[7] T. X. Misaridis, K. Gammelmark, C. H. Jørgensen, N. Lindberg, A. H. Thomsen, M. H. Pedersen, and J. A. Jensen. Potential of coded excitation in medical ultrasound imaging. *Ultrasonics*, 38:183–189, 2000.

[8] K. L. Gammelmark and J. A. Jensen. Multielement synthetic transmit aperture imaging using temporal encoding. *IEEE Trans. Med. Imag.*, 22(4):552–563, 2003.

[9] T. Misaridis. *Ultrasound imaging using coded signals*. PhD thesis, Ørsted•DTU, Technical University of Denmark, Lyngby, Denmark, 2001.

[10] T. Misaridis and J. A. Jensen. A new coding concept for fast ultrasound imaging using pulse trains. In *Proc. SPIE: Progress in biomedical optics and imaging*, volume 3, pages 68–78, 2002.

[11] F. Gran and J. A. Jensen. Multi element synthetic aperture transmission using a frequency division approach. In *Proc. IEEE Ultrason. Symp.*, pages 1942–1946, 2003.

[12] S. I. Nikolov and J. A. Jensen. Velocity estimation using synthetic aperture imaging. In *Proc. IEEE Ultrason. Symp.*, pages 1409–1412, 2001.

[13] J. A. Jensen and S. I. Nikolov. Transverse flow imaging using synthetic aperture directional beamforming. In *Proc. IEEE Ultrason. Symp.*, pages 1488–1492, 2002.

[14] Albert Macovski. Ultrasonic imaging using arrays. *IEEE Proc.*, 67:484–495, 1979.

[15] F. L. Thurstone and O. T. von Ramm. A new ultrasound imaging technique employing two-dimensional electronic beam steering. In P. S. Green, editor, *Acoustical Holography*, volume 5, pages 249–259, New York, 1974. Plenum Press.

[16] D. W. Baker. Pulsed ultrasonic Doppler blood-flow sensing. *IEEE Trans. Son. Ultrason.*, SU-17:170–185, 1970.

[17] C. Kasai, K. Namekawa, A. Koyano, and R. Omoto. Real-time two-dimensional blood flow imaging using an autocorrelation technique. *IEEE Trans. Son. Ultrason.*, 32:458–463, 1985.

[18] O. T. von Ramm, S. W. Smith, and Henry G. Pavy. High-speed ultrasound volumetric imaging system – Part II: Parallel processing and image display. *IEEE Trans. Ultrason., Ferroelec., Freq. Contr.*, 38:109–115, 1991.

[19] S. Bennett, D. K. Peterson, D. Corl, and G. S. Kino. A real-time synthetic aperture digital acoustic imaging system. In P. Alais and A. F. Metherell, editors, *Acoust. Imaging*, volume 10, pages 669–692, 1982.

[20] M. Karaman, P. C. Li, and M. O'Donnell. Synthetic aperture imaging for small scale systems. *IEEE Trans. Ultrason., Ferroelec., Freq. Contr.*, 42:429–442, 1995.

[21] S. I. Nikolov and J. A. Jensen. In-vivo synthetic aperture flow imaging in medical ultrasound. *IEEE Trans. Ultrason., Ferroelec., Freq. Contr.*, pages 848–856, 2003.

[22] J. A. Jensen, O. Holm, L. J. Jensen, H. Bendsen, H. M. Pedersen, K. Salomonsen, J. Hansen, and S. Nikolov. Experimental ultrasound system for real-time synthetic imaging. In *Proc. IEEE Ultrason. Symp.*, volume 2, pages 1595–1599, 1999.

[23] S. I. Nikolov, J. P. G. Gonzaléz, and J. A. Jensen. Real time 3D visualization of ultrasonic data using a standard pc. *Ultrasonics*, 41 (6):421–426, 2003.

[24] B. G. Tomov and J. A. Jensen. A new architecture for a single-chip multi-channel beamformer based on a standard FPGA. In *Proc. IEEE Ultrason. Symp.*, pages 1529 –1533, 2001.

[25] J. A. Jensen. Field: A program for simulating ultrasound systems. *Med. Biol. Eng. Comp.*, 10th Nordic-Baltic Conference on Biomedical Imaging, Vol. 4, Supplement 1, Part 1:351–353, 1996b.

[26] J. A. Jensen. Artifacts in velocity estimation using ultrasound and cross-correlation. *Med. Biol. Eng. Comp.*, 32/4 suppl.:s165–s170, 1994a.

[27] K. L. Gammelmark and J. A. Jensen. Experimental study of convex coded synthetic transmit aperture imaging. In *Proc. IEEE Ultrason. Symp.*, pages 1573–1576, 2002.

[28] S. I. Nikolov, R. Dufait, A. Schoisswohl, and J. A. Jensen. Three-dimensional real-time synthetic aperture imaging using a rotating phased array transducer. In *Proc. IEEE Ultrason. Symp.*, pages 1545–1548, 2002.

[29] J. A. Jensen and R. Bjerngaard. Directional velocity estimation using focusing along the flow direction: II: Experimental investigation. *IEEE Trans. Ultrason., Ferroelec., Freq. Contr.*, pages 873–880, 2003.

[30] M. H. Pedersen, K. L. Gammelmark, and J. A. Jensen. Preliminary in-vivo evaluation of convex array synthetic aperture imaging. In *Proc. SPIE - Progress in biomedical optics and imaging*, pages 33–43, 2004.

C.2 Synthetic Receive Beamforming and Image Acquisition Capabilities Using an 8x128 1.75D Array

This article was published in *IEEE Transactions on Ultrasonics, Ferroelectrics, and Frequency Control*, vol. 50, no. 1, pp. 40-57, 2003.

Synthetic Elevation Beamforming and Image Acquisition Capabilities Using an 8 × 128 1.75D Array

Anna T. Fernandez, *Student Member, IEEE*, Kim L. Gammelmark, *Student Member, IEEE*, Jeremy J. Dahl, Constance G. Keen, *Student Member, IEEE*, Roderick C. Gauss, and Gregg E. Trahey, *Member, IEEE*

***Abstract*—Ultrasound imaging can be improved with higher order arrays through elevation dynamic focusing in future, higher channel count systems. However, modifications to current system hardware could yield increased imaging depth-of-field with 1.75D arrays (arrays with individually addressable elements, several rows in elevation) through the use of synthetic elevation imaging. We describe synthetic elevation beamforming methods and its implementation with our 8 × 128, 1.75D array (Tetrad Co., Englewood, CO). This array has been successfully interfaced with a Siemens Elegra scanner for summed RF and single channel RF data acquisition. Individual rows of the 8 × 128 array can be controlled, allowing for different aperture configurations on transmit and receive beamforming. Advantages of using this array include finer elevation sampling, a larger array footprint for aberration measurements, and elevation focusing. We discuss system tradeoffs that occur in implementing synthetic receive and synthetic transmit/receive elevation focusing and show significant image quality improvements in simulation and phantom data results.**

I. Introduction

Over the past several decades, improvements in beamforming techniques have played an important role in increasing ultrasound image quality and the number of diagnostic applications for medical ultrasound. Almost all of these techniques have been developed and optimized for the lateral dimension of the array. Advances in transducer technology now allow for the elevation dimension to play a role in improving beamforming. Beamforming techniques used in the lateral dimension can be implemented in the elevation dimension with system hardware/software modifications. Significant image quality gains are made when incorporating elevation beamforming techniques. This paper presents methods for using a 1.75D array (array with individually addressable elements, several rows in elevation) to gain marked improvements in the imaging depth-of-field with potentially low-cost modifications by current scanner manufacturers and moderate losses in frame rate.

Several beamforming techniques have been developed for the lateral dimension, including apodization, expanding aperture, and synthetic aperture imaging. Apodization consists of using a weighting function (e.g., Hamming or Hanning windows) to taper the ends of the transmit or receive apertures to suppress the sidelobes of the radiated beam patterns [1]. Low sidelobes yield improved contrast measurement capabilities. Expanding aperture allows for increasing aperture size as imaging depth increases during receive imaging. This enables imaging to be kept at constant, low F-numbers (ratio of the focal distance to the aperture diameter) for a significant portion of the imaging depths [2]. The lateral resolution of an ultrasound imaging system is often defined as Resolution $= \frac{\lambda z}{D} = (F - \text{number}) \times \lambda$ where λ is the imaging wavelength, z is the focal distance, and D is the aperture size. As imaging depth z increases, maintaining a constant, low F-number (by varying D) ensures a constant resolution value. Transmit and receive apodization and receive expanding aperture are methods currently implemented in lateral dynamic focusing in commercial scanners. Dynamic focusing consists of continuously updating (with depth) the receive focal curves used in the delay-and-sum beamforming system hardware. In this paper, dynamic focusing refers to computations used to adjust incoming signals in real-time in the scanner. Any focusing calculations performed offline or in the system hardware with previously acquired signals are termed synthetic focusing computations.

Synthetic aperture imaging improves the performance of an imaging system by increasing the number of beamformed elements without having the actual number of channels needed [3] to access all of the elements at one time. This is done by using sequentially addressed subapertures. The echoes gathered from each subaperture are coherently summed to form an equivalent image from a larger array or a system with higher channel count. Lateral synthetic aperture imaging is currently implemented in most commercial systems to increase the aperture for improved resolution performance and a larger field-of-view. Apodization and expanding aperture can also be applied to each subaperture, as required, for improved imaging performance.

Manuscript received April 3, 2002; accepted July 26, 2002. This work was supported by NIH grant RO1-CA43334 and with in-kind and technical support from Siemens Medical Systems, Inc.

A. T. Fernandez, J. J. Dahl, C. G. Keen, and G. E. Trahey are with the Department of Biomedical Engineering, Duke University, Durham, NC 27708 (e-mail: anna.fernandez@duke.edu).

K. L. Gammelmark is with the Technical University of Denmark, Lyngby, Denmark.

R. C. Gauss is with Siemens Medical Systems, Ultrasound Group, Issaquah, WA.

Wildes *et al.* [4] described different array geometries and presented design specification considerations for higher order arrays. Table I details the proposed classifications. The array types vary in their ability to focus in the elevation dimension, the number of active elements (i.e., for a 2D array, a fraction of the elements are never used), the number of independent rows (i.e., 1.5D arrays have electronically tied channels from symmetric rows), and mechanical and electrical focusing capabilities. The electrical focusing is controlled by the scanner hardware; a lens at the face of the transducer serves for mechanical focusing. The higher order arrays also present manufacturing challenges, [i.e., 2D arrays are difficult to manufacture because of the large number of small elements (element widths $\sim \frac{\lambda}{2}$)].

Wildes *et al.* [4] demonstrated the importance of moving toward higher order arrays to improve lesion contrast resolution caused by smaller slice thicknesses in the scans and the capability of elevation focusing. Wildes *et al.* also showed the elevation beamforming capabilities of 1.25D and 1.5D arrays and design tradeoffs in simulation results using mechanical, fixed-focus, Fresnel, and Minimum Integrated Absolute time-delay Error (MIAE) designs. 1.75D transducers were also discussed in terms of requiring more channel counts and limited elevation steering capabilities because of geometrical constraints.

We describe the use of higher order 1.5D and 1.75D arrays in ultrasound imaging. Current commercial scanners are not equipped to take advantage of 1.75D multirow arrays. However, as system improvements occur, elevation beamforming issues will become more important and yield significant gains in image quality. Synthetic elevation beamforming methods are described for multirow arrays in Section II with simulation results presented in Section IV-A. Section III contains a description of our 8 × 128 1.75D array and acquisition capabilities. The system costs for future implementation of synthetic elevation beamforming are discussed in this section as well.

Experimental phantom results for synthetic beamforming with this array are presented in Section IV-B. The simulation and experimental results are further discussed in Section V. The effects of motion on synthetic beamforming performance are also described in this section. In addition to elevation beamforming, one of the main advantages of working with a 1.75D array is access to the individual channel echo signals. Previous work with a 1.75D 3 × 80 array was presented by Gauss [5] and involved breast aberration measurements. The individual echoes from the elements were used to calculate a 2D arrival-time-delay profile and correct the received signals. Initial results from this array indicated that better sampling in elevation would yield better aberration measurements. Section VI describes the use of our 1.75D 8 × 128 array in adaptive imaging in phase-aberration measurements.

II. Synthetic Elevation Beamforming

Two types of elevation beamforming principles are considered in this paper: synthetic receive aperture (SRA) beamforming and synthetic transmit aperture (STA) beamforming. These approaches can be applied separately or together and will be described in detail in this section. Simulation results using the FIELD II [6] ultrasound simulation program are presented in Section IV-A.

A geometrical analysis for the focal timing curves involves the x, y, and z (lateral, elevation, and axial, respectively) positions of the array elements and focal distance. Ideally, systems using higher order arrays could compute and apply time delays that incorporate the lateral and elevation position of the elements as described by the following equation for the time delay τ_{ideal} for an element at location $(x, y, 0)$ to focus at a location $(0, 0, z_f)$:

$$\tau_{\text{ideal}} = \frac{\sqrt{x^2 + y^2 + z_f^2} - R_f}{c} \tag{1}$$

where R_f is the distance (m) from the phase center of the array to the focal point, c is the sound speed (m/s), and τ is expressed in seconds.

For the synthetic elevation beamforming sections of this paper, the received signals are first beamformed laterally, resulting in one signal for each row in the aperture, and then beamformed in elevation using the different focusing schemes of interest. This is because focal delays associated with the elevation dimension can only be applied off-line (because of system constraints). If we assume that lateral and elevation beamforming are separable, the focusing time delay used when synthetic beamforming is described by τ_{synth}:

$$\begin{aligned} \tau_{\text{synth}} &= \tau_{\text{lateral}} + \tau_{\text{elevation}} \\ &= \frac{1}{c}\left[\sqrt{x^2 + z_f^2} - R_f\right] \\ &+ \frac{1}{c}\left[\sqrt{x_s^2 + y^2 + z_f^2} - R_f\right] \end{aligned} \tag{2}$$

where x_s is the selected, fixed lateral position used to calculate the elevation profile. This elevation profile is then applied at all lateral locations.

The error, $\varepsilon_{\text{synth}}$, associated with using τ_{synth} is

$$\varepsilon_{\text{synth}} = \tau_{\text{ideal}} - \tau_{\text{synth}} \tag{3}$$

For $x_s = 0\,m$, the value used in our processing, we obtain a root mean square (rms) error for $\varepsilon_{\text{synth}}$ equal to 7 ns across all elements in the array, with most of the error associated with the time delays corresponding to the corner elements of the array (34 ns maximum error on corner elements). Design issues in choosing x_s or choosing not to use the outer elements can be considered to reduce the rms errors associated in this implementation of synthetic elevation beamforming. A typical commercial system beamformer (Siemens Elegra) controls the timing delays at 144 MHz (6.9 ns) sampling frequency, so the rms error associated with this choice of elevation computation is on the order of a sample.

TABLE I
ULTRASOUND ARRAY TYPES BASED ON DESCRIPTIONS FOUND IN WILDES *et al.* [4].

Array types	1D linear	1.5D	1.75D	2D
Focusing capability	in azimuth	in azimuth	in elevation and azimuth	in elevation and azimuth
Array geometry	full	full	full	sparse
Independent rows	N/A	no*	yes	yes
No. of rows × No. of lateral elements	1 × N	(2 − 4) × N	(2 − 8+) × N	N × N
Electrical focusing in elevation	no	yes (symmetric)	yes	yes
Electrical steering in elevation	no	no	limited	yes
Mechanical focusing	yes	yes	yes	no

*1.5D arrays have independent symmetrically paired rows.

Generally, the laterally beamformed signal $s_n^l(k)$ for A-scan line l and row n is given by the conventional delay and sum expression:

$$s_n^l(k) = \sum_{c=1}^{C} a_c^l(k) r_{n,c}(k - \tau_c^l(k) f_s), \quad l = 1, 2, \ldots, L \tag{4}$$

where $a_c^l(k)$ is the dynamic apodization value for channel c and line l, $r_{n,c}(k)$ is the received signal from channel c on row n, $\tau_c^l(k)$ is the dynamic focusing time for channel c and line l, and f_s is the sampling frequency of the system. k is the sample number, $k = 1, 2, \ldots, K$, assuming K samples in each line, and L is the total number of A-lines in the image. If the product $\tau_c(k) f_s$ is not an integer, interpolation of the signal is needed to find the correct delay value.

In the following subsections, we initially consider the SRA beamforming capability of the 1.75D array and then look at STA beamforming, where transmit subapertures are used. The use of synthetic aperture imaging in both transmit and receive imaging is described as synthetic transmit and receive aperture imaging (STRA).

A. Synthetic Receive Imaging

The 1.75D multirow array can be used as a conventional 1D array with an increased elevation aperture and fixed elevation focus by simply summing the laterally beamformed row signals in (4):

$$S_{\text{conv}}^l(k) = \sum_{n=1}^{N} s_n^l(k) \tag{5}$$

where N is the number of rows in the array. We will define this as conventional imaging mode to denote how the array would be used in most current commercial scanners, with no unique elevation electronic delays applied for rows at different elevation positions. $S_{\text{conv}}^l(k)$ is the kth sample of A-line l. Hereby, a fixed elevation focus in both transmit and receive is obtained using the property of the lens. Strictly from a beamforming point of view, the purpose of using the 1.75D array is to obtain a uniform, narrow elevation beamwidth with low sidelobes to increase the detail and contrast resolution. Therefore, using a fixed elevation focus in both transmit and receive is not advantageous because the beam converges and diverges quickly before and after the focus, producing only a narrow beamwidth within a small region around the focus (see Section IV-A). It is therefore necessary to consider more advanced beamforming schemes to increase the depth of focus (DOF), also known as the depth-of-field. The depth-of-field is defined as the axial distance over which the beam maintains its approximate focused size [1].

The elevation performance of different types of 1.25D and 1.5D arrays has previously been described by Wildes *et al.* [4], demonstrating that slice-thickness can be significantly decreased when applying aperture growth and dynamic apodization in the elevation dimension.

Using the conventional delay and sum beamformer, SRA beamforming can be formulated in general terms as:

$$S_{\text{SRA}}^l(k) = \sum_{n=1}^{N} w_n(k) s_n^l(k - \tau_n(k) f_s) \tag{6}$$

where $w_n(k)$ is the synthetic apodization value for row n, $\tau_n(k)$ is the synthetic focusing time for row n, and $s_n^l(k)$ is the laterally beamformed line given by (4). Here, it is assumed that the same elevation beamforming scheme is applied to all lines in the image, which will often be the case. Also, $\tau_n(k)$ takes into account the lens delay by subtracting the lens-created delay from the geometrically calculated synthetic focusing time [i.e., $\tau_n(k) = \tau_{\text{n,synth}}(k) - \tau_{\text{n,lens}}(k)$].

Compared with 1.5D arrays, the 1.75D array has the advantage that each row is accessible. Thus, non-symmetric apodization functions and time delay profiles can be applied as described by (6), which makes the 1.75D array useful for compensating for 2D phase aberrations. Applying symmetric apodization functions and focusing profiles in (6) results in (conventional) 1.5D array beamforming.

Eq. (6) shows that several types of SRA beamforming schemes can be selected. Various combinations of fixed/synthetic focusing and aperture growth using different apodization functions and F-numbers are possible by adjusting the values of $w_n(k)$. It is well known that changing the receive focusing from fixed to dynamic yields significant improvements in the beam pattern. Introducing aperture growth with careful selection of the apodization function and F-number improves beamwidth uniformity

with a reduction in sidelobe levels [7]. However, this is obtained at the expense of a slightly wider beam, and the beam is still influenced by the fixed elevation transmit focus.

B. Synthetic Transmit Imaging

To obtain further improvements in the beam shape, STA imaging in the elevation dimension can be employed as in conventional (lateral) STA imaging, where one element is used at each transmission and all on receive [8]. The difference is that here a single row is used instead of a single element. This enables the possibility of applying synthetic focusing, apodization, and aperture growth on both transmit and receive in elevation. The influence of the fixed focus supplied by the lens is removed, and a constant beamwidth down to −40 dB with very low sidelobe levels can be obtained throughout the imaging region (see Section IV-A).

To understand STA beamforming, consider the transmit and receive beamforming steps as two separate operations. These can, however, be combined as will be described further. Let $s^l_{m,n}(k)$ be the laterally beamformed signal from transmit row m, receive row n, and image line l. Then, the STA receive beamformed data $S^l_m(k)$ for transmit row m and line l is given by:

$$S^l_m(k) = \sum_{n=1}^{N} w_n(k) s^l_{m,n}(k - \tau_n(k) f_s), \quad m = 1, 2, \ldots, M \tag{7}$$

where M is the number of transmit rows. This operation results in M signals for each line in the image, which have been beamformed on receive.

Transmit beamforming is performed in the same manner as in (7) with a simple change of variables. Thus, the STA beamformed signal $S^l_{\mathrm{STA}}(k)$ for line l is given by (8) (see next page), where $w_m(k)$ is the synthetic apodization value for transmit row m, $\tau_m(k)$ is the synthetic focusing time for row m, and (7) has been inserted to obtain the final expression. Eq. (8) states that STA beamforming can be implemented recursively and that both transmit and receive focusing can be performed simultaneously by combining the transmit and receive focusing times into one term using the time delay defined in (3). This will be referred to as STRA beamforming throughout the paper.

Inserting (4) into (8) yields (9) (see next page), where the synthetic apodization values, $W^l_{m,n,c}(k) = w_m(k) w_n(k) a^l_c(k)$, and the synthetic focusing times, $\tau^l_{m,n,c}(k) = \tau^l_c(k) + \tau_n(k) + \tau_m(k)$, have been combined. In practice, these values can be calculated beforehand, reducing the number of real-time calculations.

III. Experimental System Description

A. Tetrad 1.75D 8 × 128 Array

We describe results obtained with a 1.75D 8 × 128 array, built by Tetrad Corporation (Englewood, CO), which allows us to gather individual channel data from the 1024 channels available. The geometry and specifications of the array are shown in Fig. 1 and Table II. The lateral dimension was chosen to be similar to commercially available 1D arrays − 0.88 λ pitch. The elevation pitch is 1.5 mm or 6.5 λ. The element width was chosen to ensure good angular sensitivity through the amplitude modulation of the array response, decreasing the amplitude of the grating lobes [9]. A lens focused at 26 mm provides mechanical elevation focusing for real-time scanning, as our current ultrasound system is not capable of performing dynamic elevation focusing. The focus was also chosen for work in breast and small parts imaging. The footprint of the array is 12 × 26 mm, larger than commercial 1D arrays (e.g., a 5 × 26 mm-aperture). The array has high element uniformity, determined by the average nearest-neighbor correlation measurements. This uniformity indicates similar element impulse responses, a necessary condition for good phase aberration measurements. Further discussion on the array's aberration measurement capability is found in Section VI.

Fig. 2(a) shows a photograph of the array, and Fig. 2(b) shows the open case view of the transducer. The large size of the case is due to the multiplexer switch chips incorporated in the handle (further described in Section III-B). Air flow inside the transducer is also needed to disperse the

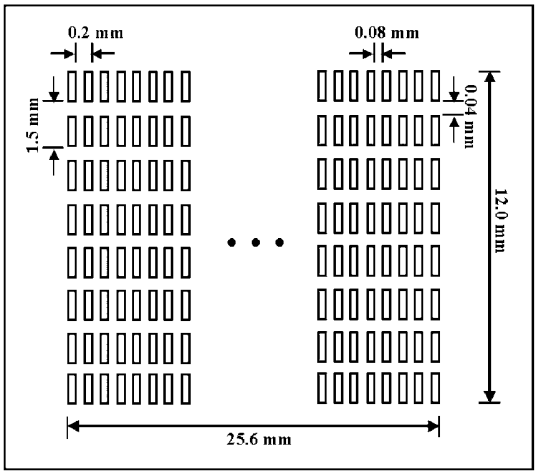

Fig. 1. 8 × 128 1.75D array geometry.

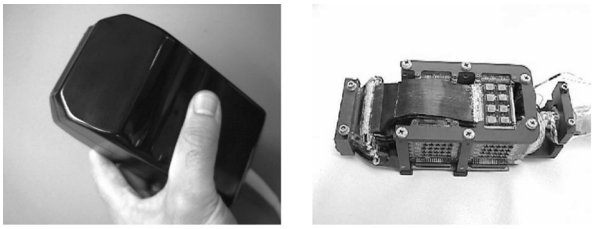

(a) (b)

Fig. 2. Tetrad 8 × 128 1.75D array. a) The array probe with a large case (because of the multiplexer circuitry incorporated into the handle), as seen in the open view in (b).

$$\begin{aligned} S^l_{\mathrm{STA}}(k) &= \sum_{m=1}^{M} w_m(k) S^l_m(k - \tau_m(k) f_s) = \sum_{m=1}^{M} w_m(k) \sum_{n=1}^{N} w_n(k) s^l_{m,n}(k - \tau_n(k) f_s - \tau_m(k) f_s) \\ &= \sum_{m=1}^{M} \sum_{n=1}^{N} w_m(k) w_n(k) s^l_{m,n}(k - \tau_n(k) f_s - \tau_m(k) f_s) \end{aligned} \tag{8}$$

$$\begin{aligned} S^l_{\mathrm{STRA}}(k) &= \sum_{m=1}^{M} \sum_{n=1}^{N} \sum_{c=1}^{C} w_m(k) w_n(k) a^l_c(k) r^l_{m,n,c}(k - \tau^l_c(k) f_s - \tau_n(k) f_s - \tau_m(k) f_s) \\ &= \sum_{m=1}^{M} \sum_{n=1}^{N} \sum_{c=1}^{C} W^l_{m,n,c}(k) r^l_{m,n,c}(k - \tau^l_{m,n,c}(k) f_s) \end{aligned} \tag{9}$$

TABLE II
8×128 1.75D ARRAY PARAMETERS.

Frequency	6.7 MHz
Transducer bandwidth	50%
Elevation lens focus	26.0 mm
Lateral element width	0.12 mm
Lateral pitch	0.20 mm
Elevation element height	1.46 mm
Elevation pitch	1.50 mm
Element nearest-neighbor correlation (i.e., element uniformity)	0.995

heat generated by the switches in the handle. Air cooling is provided by an aquarium pump through two holes at the base of the transducer handle.

The lateral and elevational performance of the array can be examined by using the Field II simulation program [6]. The array parameters, including the mechanical lens focused at 26 mm, were incorporated into the simulation to compute pulse-echo lateral and elevational beam plots at the 26-mm focus of the array, using all eight rows on transmit and receive. Fig. 3 shows the transmit and receive lateral beam plot for the 8×128 array. The beam plot is formed by plotting the integrated energy (rms value) of the non-zero pressure amplitudes along each A-line of the point-spread-function. The lateral resolution, defined by the -6 dB width of the beam plot, is computed to be 230 μm from the simulation results. This resolution is comparable with conventional 1D arrays. Fig. 3(b) is an extended view of 3(a), which shows the sidelobes and grating lobes.

The transmit and receive elevation beam plot is shown in Fig. 4(a). The elevation resolution is 485 μm, calculated from the -6 dB full-width at half-maximum (FWHM) off the simulated plot. The elevation resolution is significantly better for this 8×128 array than conventional 1D arrays. The grating lobes' locations can be calculated using $\sin^{-1}(\frac{\lambda}{\text{elevation pitch}})$, which results in locations at 9° (4.1 mm) in elevation from the center of the array. The grating lobes do not play a significant role when the imaging plane is axially in the middle of the array at the lens focus. Wildes *et al.* [4] stated that 1.75D arrays would have limited steering capabilities. This is verified for our array in the results shown in Fig. 4(b). Elevational beam plots were computed when the beam was electronically steered 0° to 15° in elevation off the axial plane. Most of the energy is distributed at the mechanical lens focus—at a steering angle of 0°, independent of the selected steering angle. In fact, the grating lobes for non-zero steering angles that are in the range of the lens get magnified, resulting in a grating lobe with higher energy than the main lobe located at the steering angle.

B. System Interfacing

Most commercial ultrasound scanners, including the Siemens Elegra scanner used in our research, have 128 receive channels. To collect more than 128 element RF signals, an external controller is incorporated into the acquisition setup. The array contains multiplexers in the handle for external control of the rows active on transmit and receive for each transmit firing. We built an external controller for elevation aperture configuration. The controller is synchronized with the Elegra system start-transmit signals. The Elegra software and hardware are used to control the lateral aperture used in imaging.

Fig. 5 shows the system setup. The elevation rows active on transmit and receive are controlled through signals sent by a custom-configured Altera University Program Design board (Altera Co., San Jose, CA) into the transducer handle's multiplexer switches. The time for switching between the transmit and receive configuration is 0.5 μs, a small fraction of the period over which no signal is received by the scanner (during this same period, the new row configurations are assigned via the handle circuitry). The multiplexer switches in the handle can electronically tie together any combination of rows in transmit and can independently tie rows on receive as well. This flexibility allows us to gather data in different configurations for

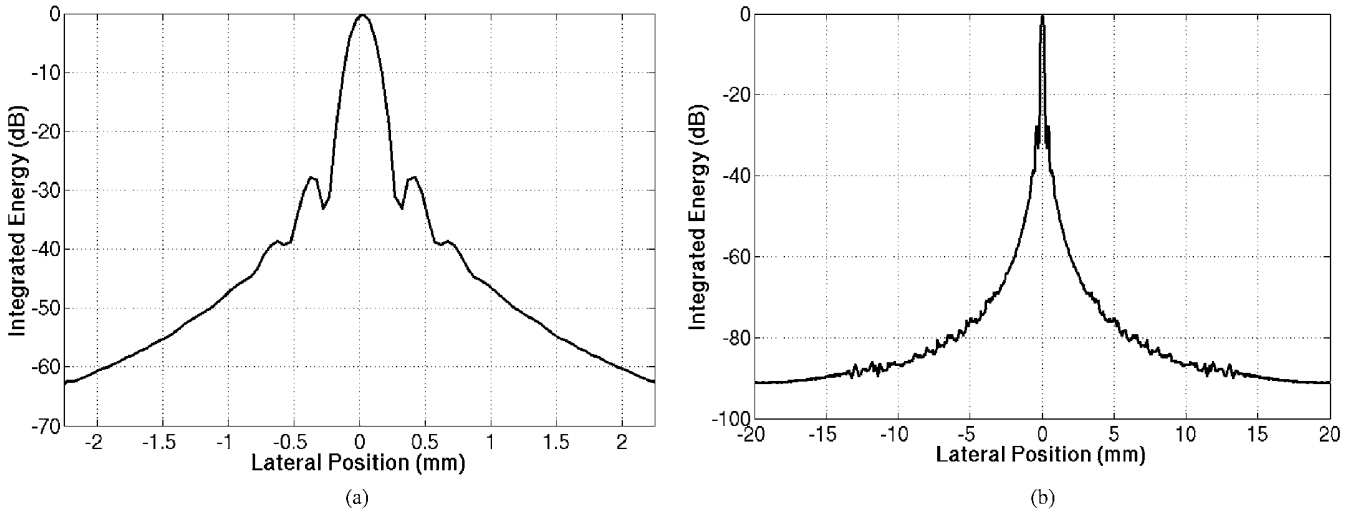

Fig. 3. Lateral beam plots for the 8 × 128 1.75D array. a) Lateral beam plot of the array for transmit and receive imaging, generated using Field II code. The calculated −6 dB resolution from the plot is 230 μm. b) An extended version of the plot.

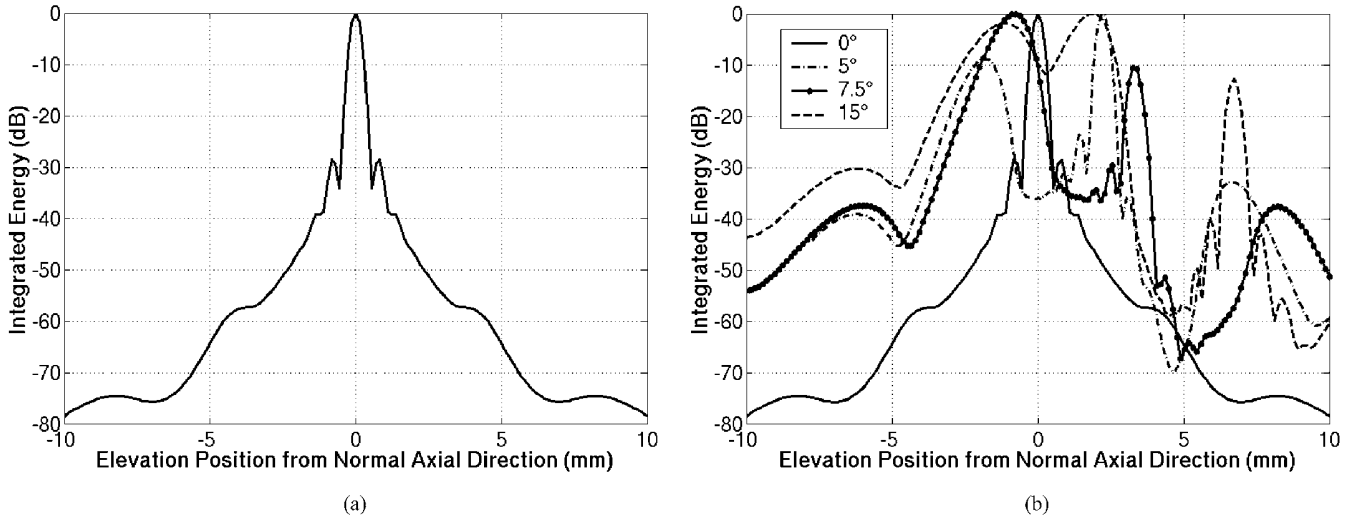

Fig. 4. Elevation beam plots for the 8 × 128 1.75D array. a) Elevation beam plot for transmit and receive imaging when the transducer is focused in the middle axial plane from the array (i.e., no steering). b) Elevation beam plots at several different steering angles. Note that the grating lobe levels (located at ±4.1 mm from the main lobe) are increased if they occur near the lens focus (0°), sometimes resulting in grating lobes with higher energies than the main lobe centered at the steering location.

offline processing to perform synthetic aperture elevation beamforming, discussed in Section II.

C. System Acquisition Capability

We can acquire data in one of two forms: as summed (A-line) RF data and as individual channel (not summed) RF data. The summed data are collected after it has passed the beamformer (delayed and summed) but before it has gone through scan conversion and image-processing. With the multiplexer controller box, data for each row in elevation can be collected. These data can be resampled to form synthetic receive elevation images.

System improvements that allow for implementing 1.75D arrays include more channels (ideally 1024 channels for this array) or a system to control the multiplexing of the channels in hardware and larger data storage capabilities to enable larger data sets for individual channel data acquisition. Real-time SRA and STRA imaging implementation can be achieved given a system with higher channel count, hardware that controls the elevation aperture, and front-end processing to delay and sum the elevation signals. In this paper, we present data that show the potential image improvements with this array. Frame rate and SNR are considered when evaluating future system design tradeoffs for use with the higher order arrays.

D. Frame Rate Costs and Signal-to-Noise Ratios

Synthetic aperture imaging allows the current 128 channel system to take advantage of the elevation performance of 1.75D arrays by addressing more receive or transmit and

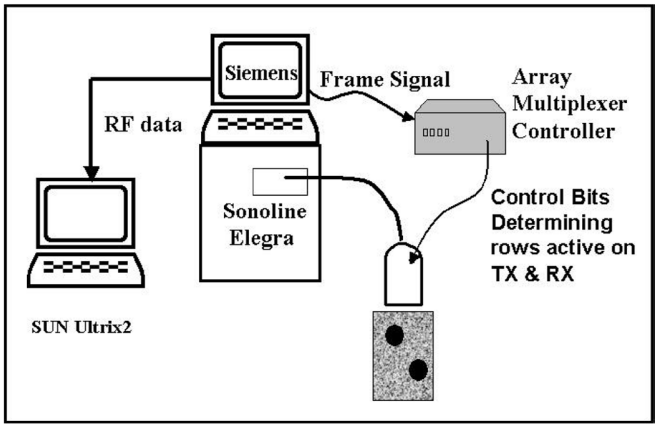

Fig. 5. Data acquisition setup.

TABLE III
GENERALIZED FRAME RATE REDUCTIONS WITH SYNTHETIC ELEVATION APERTURE IMAGING. P IS THE CONVENTIONAL FRAME RATE (FPS), N IS THE NUMBER OF ROWS IN THE RECEIVE APERTURE, M IS THE NUMBER OF ROWS IN THE TRANSMIT APERTURE.

Imaging mode	SRA factor	STRA factor	Frame rate
Conventional imaging	—	—	P
SRA (each row collected)	N	—	$\frac{P}{N}$
STRA (each row collected)	N	M	$\frac{P}{N \cdot M}$
SRA (using elevation symmetry)*	$\frac{N}{2}$	—	$\frac{P}{\frac{N}{2}}$
STRA (using elevation symmetry)*	$\frac{N}{2}$	$\frac{M}{2}$	$\frac{P}{\frac{N}{2} \cdot \frac{M}{2}}$

*1.5D array geometry.

receive elements. Raw RF data from individual rows are collected in real-time and then combined offline to form high resolution images. Such images can be generated by the system with minor hardware and software modifications. The main cost in implementing synthetic elevation beamforming is a reduction of the imaging frame rate.

The frame rate reflects the imaging speed—the time it takes to create an image. A data set used for synthetic elevation beamforming is collected over several transmit/receive events compared with conventional beamforming, where only one transmit/receive event is required. Table III presents a general description of the frame rate reductions that occur with synthetic elevation imaging for 1.75D arrays. P denotes the frame rate with conventional imaging. N and M are the number of unique rows used in receive and transmit, respectively. The number of transmit pulses needed is dependent on the implemented beamforming scheme.

For synthetic elevation aperture imaging, one simplifying assumption to reduce frame rate costs is to assume symmetric phase for rows about the center of the array. This is similar to using the 1.75D array as a 1.5D array (where symmetric rows are tied together). Thus, these frame rate reductions apply to 1.5D arrays used in synthetic elevation beamforming as well.

TABLE IV
FRAME RATES FOR DIFFERENT ELEVATION IMAGING SCENARIOS USING THE 8×128 1.75D ARRAY: N = 8 AND M = 8.

Imaging mode	Transmit pulses needed	Typical frame rates (fps)
Conventional B-mode	1	32
SRA (each row collected)	8	4
STRA (each row collected)	64	0.5
SRA (using elevation symmetry)*	4	8
STRA (using elevation symmetry)*	16	2

*1.5D array geometry.

Table IV gives the number of transmit pulses needed and resulting frame rates for the different imaging scenarios if our 8×128 1.75D array was used in current commercial systems. This is assuming that systems could control the acquisition of signals from different rows in the array and process the stored data from the individual row(s) together. The use of symmetric phase for this 8×128 1.75D array (i.e., 1.5D array geometry implementation) helps keep the frame rate high, as the same focusing delay can be applied to tied rows.

We examined the effects on image SNR caused by the summation of signals from different numbers of transmit/receive events at the focal area of the 8×128 1.75D transducer for the different imaging scenarios. Assume that electronic noise in the receiver amplifiers/cable attached to each element dominates and is uncorrelated for each element on each echo acquisition. Power SNR is defined using the formula

$$\text{SNR (in dB)} = 10 \log \frac{\sigma_{\text{sig}}^2}{\sigma_{\text{noise}}^2} \tag{10}$$

where σ_{sig}^2 is the variance of the zero-mean signal and σ_{noise}^2 is the variance of the noise. For conventional and SRA schemes, the expected SNR is the same because they use eight rows of received data and identical transmit apertures (eight rows fired together). For STRA imaging, 64 received rows are collected. Thus, the power SNR for STRA imaging is $\text{SNR}_{\text{STRA}} = \frac{1}{8} \text{SNR}_{\text{Conventional}}$. When SNR is reported in decibels, $\text{SNR}_{\text{STRA (in dB)}} = \text{SNR}_{\text{Conventional (in dB)}} - 9$ dB. Additional factors that impact SNR include the impedance characteristics of the multiplexers in their "on" and "off" modes and the target range.

SNR measurements were made on summed RF signals collected on a speckle-only generating phantom, built by Timothy J. Hall (University of Kansas). The phantom has 0.5 dB/MHz attenuation and an experimentally measured sound speed of 1543 ± 5 m/s. The rows were electronically tied together under the same setups used for conventional, SRA, and STRA imaging. The signals were taken from a 2-mm axial length window about the 26-mm focus. Noise was calculated from the subtraction of the two

signals examined. We computed an average SNR measurement (over several RF lines) for the imaging scenarios: $\mathrm{SNR}_{\mathrm{Conventional}} = 32.7$ dB, $\mathrm{SNR}_{\mathrm{SRA}} = 32.8$ dB, and $\mathrm{SNR}_{\mathrm{STRA}} = 28$ dB. We adjusted the brightness to display each of the three image types on the same grayscale for comparison purposes.

IV. Results

Results are presented for several different elevation beamforming SRA and STRA schemes in simulation in Section IV-A. Experimental phantom data are presented in Section IV-B using one STRA and one SRA beamforming configuration. Contrast measurements in the lesion phantoms are also presented.

A. Simulation Results

To investigate the different elevation beamforming schemes described in Section II, simulations using Field II [6] were performed. These simulations were used to evaluate the performance of the various elevation beamforming types in terms of the improvement in slice thickness and sidelobe levels and for comparison with matched phantom measurements (see Section IV-B). For this analysis, we are only concerned about the elevation beam profile.

The simulations were performed by defining a plane in the y-z (elevation-axial) dimension containing point scatterers spaced equidistant along both dimensions. The 1.75D array transmits a single row at a time along a fixed direction, and the signals received on all 1024 aperture elements are calculated for each point scatterer individually. For each row, the received signals are beamformed laterally using dynamic receive focusing and no aperture growth [i.e., $a_c^l(k) = 1$ for all l and c in (4) that defines the laterally beamformed signal $s_n^l(k)$], and then summed across the rows according to (4). The resulting eight signals, one for each row, are then stored for subsequent elevation beamforming. This is repeated for each individual transmit row. No attenuation effects are included in the simulations. This data set can be used for conventional, SRA, and STRA elevation beamforming. The 1.75D array is set up according to the specifications given in Table II, and the lateral transmit focus is set to the elevation focal point $(x, y, z) = (0, 0, 26\ mm)$. The point scatterer grid is placed at the lateral center of the aperture ($x = 0$) and has an axial length of 35 mm, starting at 5 mm with 1-mm spacing between the point scatterers. The separation between the point scatterers in the elevation dimension is 0.1 mm. Using this approach, a map of the elevation beam profile is obtained.

From Section II it is inferred that many different elevation beamforming schemes can be applied. However, to limit the discussion, we present results that describe the general trends observed. We considered seven beamforming schemes in these simulations:

- Conventional elevation beamforming with fixed transmit and receive focusing (conventional)
- SRA using synthetic receive focusing and fixed transmit focus with no expanding aperture ($\mathrm{SRA}_{\mathrm{Conv}}$)
- $\mathrm{SRA}_{\mathrm{Conv}}$ with expanding rectangular window and F-number = 2 with fixed transmit focus ($\mathrm{SRA}_{\mathrm{RecF2}}$)
- $\mathrm{SRA}_{\mathrm{Conv}}$ with expanding Hamming window and F-number = 2, with fixed transmit focus ($\mathrm{SRA}_{\mathrm{HamF2}}$)
- STRA using synthetic transmit and receive focusing with no expanding aperture ($\mathrm{STRA}_{\mathrm{Conv}}$)
- $\mathrm{STRA}_{\mathrm{Conv}}$ with expanding rectangular window and F-number = 2 on both transmit and receive ($\mathrm{STRA}_{\mathrm{RecF2}}$)
- $\mathrm{STRA}_{\mathrm{Conv}}$ with expanding Hamming window and F-number = 2 on both transmit and receive ($\mathrm{STRA}_{\mathrm{HamF2}}$).

To evaluate beamformer performance, we used the two parameters suggested by Wildes *et al.* [4] (i.e., the -6 dB and -20 dB beamwidths). The -6 dB beamwidth is used as a measure of the slice thickness or detail resolution, and the -20 dB beamwidth is used as a measure of the sidelobe levels or contrast resolution. Also, we mapped the beam pattern by calculating the peak intensity I_{sptp} of the beamformed signal from each point target. When calculating the -6 dB and -20 dB beamwidths, each depth was normalized to have a peak intensity of 0 dB to remove the variation in the sensitivity along the beam. Thus, the corresponding beam plots reflect the variation in the beamwidth throughout the imaged region.

The results are shown in Fig. 6 through Fig. 9 and Tables V and VI.

B. Experimental Phantom Results

Summed RF (already beamformed in the lateral dimension) data were collected with sequentially active rows on receive. The transmit aperture was always set to fire using all eight rows for SRA imaging. Only one row was active at a time when STRA data sets were collected. The transmit focus was set to 26 mm, and the lateral beamforming was controlled by the Elegra hardware and software settings. No lateral transmit apodization was used, but lateral, dynamic receive focusing was applied by the system to collect 36-MHz RF data.

Two phantoms were used: a tissue-mimicking phantom (Gammex RMI) with 2-mm diameter spherical anechoic lesions spaced 1 cm apart and a tissue-mimicking phantom with 4-mm diameter spherical anechoic lesions spaced 1 cm apart.

For all phantom results presented, we show three different images. All images were formed using lateral, dynamic receive beamforming (output from scanner). The imaging scenarios are a subset of those examined in simulations in Section IV-A.

- The conventional image used fixed receive focusing (from the array mechanical lens) in elevation. All individual RF echo signals were summed to form each A-line in the image. This image is what would be viewed

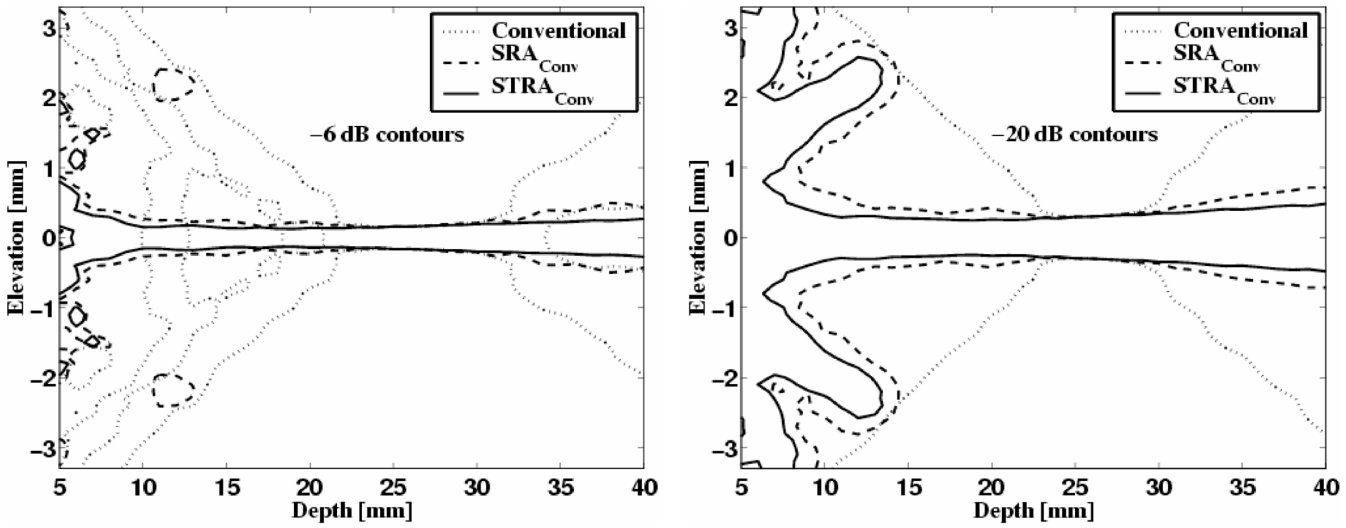

Fig. 6. Comparison of conventional, SRA_{Conv}, and $STRA_{\mathrm{Conv}}$ elevation beamforming. No apodization or expanding aperture growth was incorporated into these simulations. −6 dB (a) and −20 dB (b) contour plots for each imaging mode are shown.

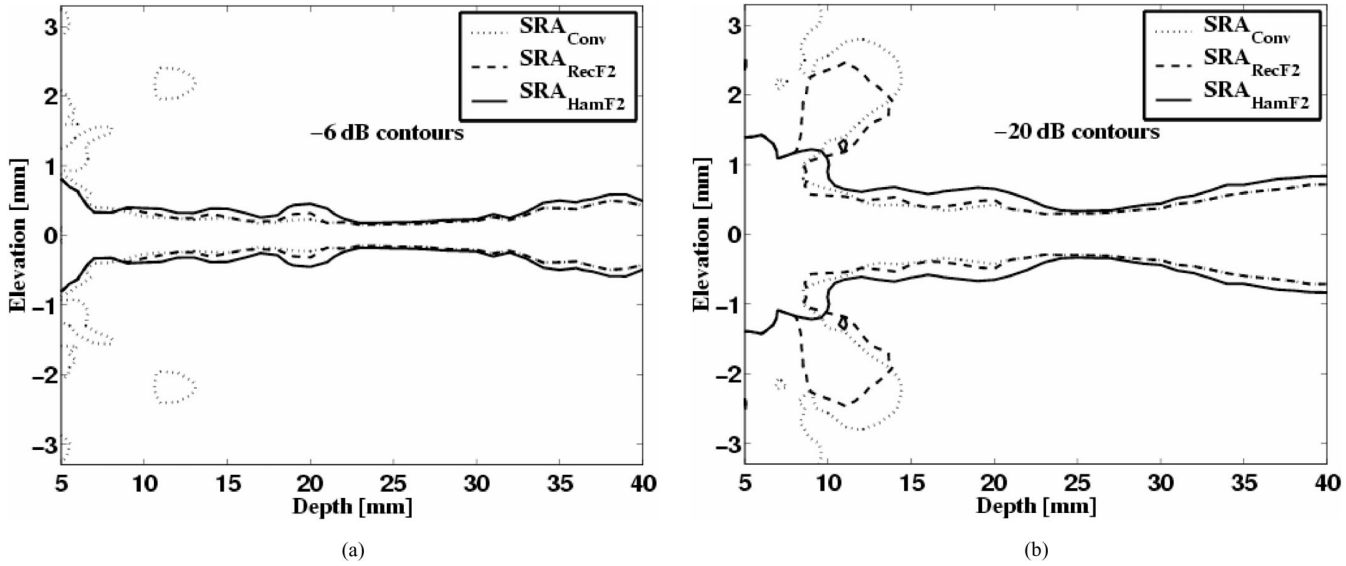

Fig. 7. Comparison of SRA elevation beamforming using different aperture growth functions and F-number = 2 expanding aperture growth. −6 dB (a) and −20 dB (b) contour plots are shown for SRA_{Conv} (no apodization or expanding aperture), SRA_{RecF2} (rectangular window apodization with F = 2 expanding aperture growth), and SRA_{HamF2} (Hamming window apodization with F = 2 expanding aperture growth).

TABLE V
−6 dB Beamwidth (in mm) as a Function of Depth—Simulation Results.

Type—depth	8 mm	14 mm	20 mm	26 mm	32 mm	38 mm
Conventional	5.81	4.08	1.44	0.32	1.02	3.16
SRA_{Conv}	3.12	0.48	0.46	0.32	0.45	0.99
SRA_{RecF2}	0.65	0.61	0.63	0.32	0.45	0.99
SRA_{HamF2}	0.65	0.77	0.90	0.38	0.49	1.17
$STRA_{\mathrm{Conv}}$	0.59	0.31	0.28	0.32	0.41	0.49
$STRA_{\mathrm{RecF2}}$	0.51	0.41	0.35	0.32	0.41	0.49
$STRA_{\mathrm{HamF2}}$	0.51	0.51	0.46	0.45	0.49	0.55

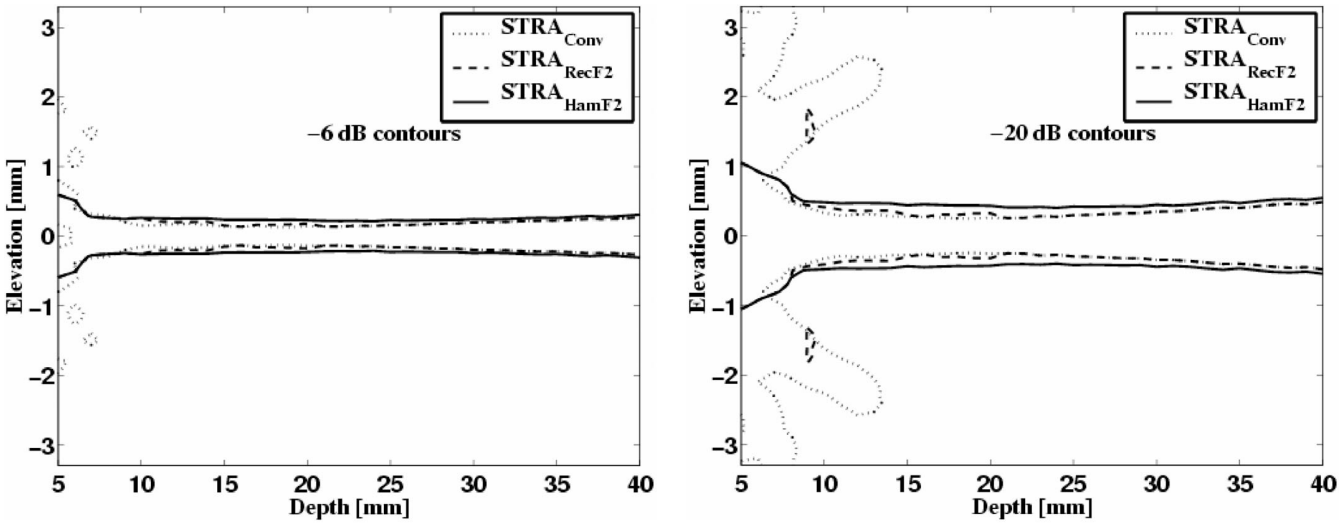

Fig. 8. Comparison of STRA elevation beamforming using different aperture growth functions and F-number = 2 expanding aperture growth. −6 dB (a) and −20 dB (b) contour plots are shown for $STRA_{\mathrm{Conv}}$ (no apodization or expanding aperture), $STRA_{\mathrm{RecF2}}$ (rectangular window apodization with F = 2 expanding aperture growth), and $STRA_{\mathrm{HamF2}}$ (Hamming window apodization with F = 2 expanding aperture growth).

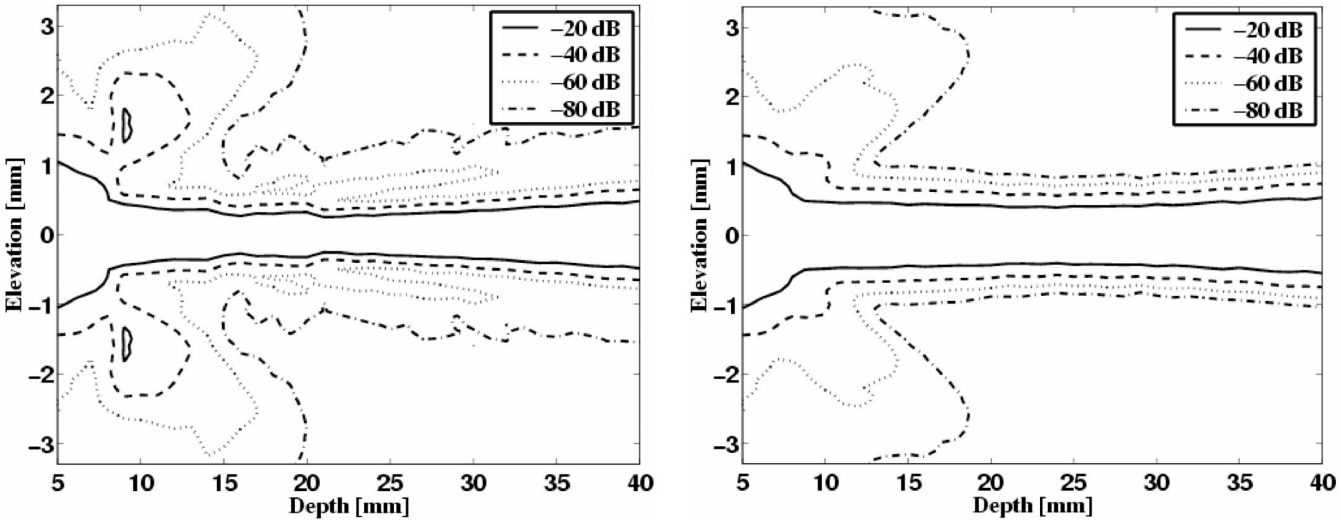

Fig. 9. Contour plots of a) $STRA_{\mathrm{RecF2}}$, STRA elevation beamforming using rectangular window weighting aperture growth with F-number = 2, and b) $STRA_{\mathrm{HamF2}}$, STRA elevation beamforming with Hamming window weighting aperture growth with F-number = 2. Contours range from −20 dB to −80 dB with a 20-dB spacing. Notice the very uniform beamwidth for $STRA_{\mathrm{HamF2}}$, shown in (b), even down to −80 dB.

TABLE VI
−20 DB BEAMWIDTH (IN MM) AS A FUNCTION OF DEPTH—SIMULATION RESULTS.

Type—depth	8 mm	14 mm	20 mm	26 mm	32 mm	38 mm
Conventional	—	4.96	2.22	0.59	2.12	4.54
SRA_{Conv}	—	5.08	0.86	0.60	0.92	1.35
SRA_{RecF2}	2.34	1.06	0.98	0.60	0.92	1.35
SRA_{HamF2}	2.34	1.36	1.31	0.68	1.11	1.62
$STRA_{\mathrm{Conv}}$	5.75	0.56	0.52	0.60	0.73	0.92
$STRA_{\mathrm{RecF2}}$	1.22	0.72	0.65	0.60	0.73	0.92
$STRA_{\mathrm{HamF2}}$	1.22	0.93	0.86	0.84	0.89	1.06

on the scanner if all eight rows were electronically tied in the handle.

- The synthetic receive image, $\mathrm{SRA_{HamF2}}$, employed elevation synthetic receive focusing with expanding aperture keeping an F-number of 2, with Hamming apodization in elevation.
- The synthetic transmit and receive image, $\mathrm{STRA_{HamF2}}$ used synthetic elevation beamforming in both transmit and receive. The synthetic beamforming implemented a Hamming window apodization and expanding aperture with F-number = 2.

The summed RF data were post-processed using the Hilbert transform to form the detected image. A depth-dependent gain was also applied within each image to create a more uniform brightness image. For all of the images presented, there is a noticeably brighter region of speckle in the focal area of 24 to 28 mm because the array exhibits close to ideal focusing at the mechanical lens focus of 26 mm.

Fig. 10 shows 4-mm diameter lesion phantom images for different elevation beamforming techniques. There are qualitative improvements in the visualization of the bottom and top rows of lesions with synthetic elevation beamforming, reflecting an extension of the depth-of-field.

Quantitative measures of contrast were made using

$$\text{Contrast} = 1 - \frac{\text{Signal}_{\text{in cyst}}}{\text{Signal}_{\text{speckle}}}. \tag{11}$$

User-defined, circular masks were used to outline each lesion in the image. The average diameter of the masks was 3.3 mm. The same masks were used on all of the 4-mm diameter lesion phantom images. Speckle signal located at the same depth and covering equal area as the lesion mask was used for each lesion contrast computation. The mean speckle brightness was measured for the signals inside the lesion and the signal outside the lesion. Table VII shows the contrast measurement results for the cysts defined in Fig. 10(d).

Elevation synthetic beamforming was also performed on the 2-mm diameter lesion phantom. Fig. 11 shows the images and the contrast measurements reported in Table VIII. The average diameter of the user-defined masks implemented for the contrast measurements was 1.5 mm. There is a marked increase in lesion detectability with synthetic aperture imaging. The top and bottom cysts are best visualized in the synthetic transmit image, although synthetic receive also shows more lesions than in the original, conventional, image.

TABLE VII
CONTRAST MEASUREMENTS FOR 4-MM CYST PHANTOM.

Lesion depth (mm)	Cyst label	Conventional contrast (%)	SRA contrast (%)	STRA contrast
11	A	28.0	72.7	87.5
	B	−14.5	67.9	85.9
16	C	53.2	70.4	86.0
21	D	93.2	91.2	91.7
	E	88.9	91.2	91.0
26	F	94.5	95.7	95.2
31	G	86.2	92.9	93.0
	H	80.2	91.6	92.4
36	I	54.5	82.3	85.3
41	J	46.3	63.5	76.3
	K	23.8	64.0	76.3
Mean		57.7	80.3	87.3
Std. Dev.		35.1	12.7	6.4

TABLE VIII
CONTRAST MEASUREMENTS FOR 2-MM CYST PHANTOM.

Lesion depth (mm)	Cyst label	Conventional contrast (%)	SRA contrast (%)	STRA contrast (%)
11	A	39.3	62.2	82.5
	B	8.3	51.4	80.6
	C	28.9	40.8	80.5
16	D	−12.3	76.1	85.1
	E	−56.0	71.6	85.3
21	F	66.7	82.8	89.8
	G	68.7	83.8	87.6
	H	86.9	87.5	82.4
26	I	87.8	93.1	93.8
	J	87.4	93.4	94.9
31	K	73.1	83.5	88.2
	L	42.2	70.5	84.6
	M	61.5	81.5	89.2
36	N	22.8	61.7	67.5
	O	34.3	56.4	68.5
Mean		42.6	73.1	84.0
Std. Dev.		40.7	15.7	7.8

V. Discussion

The simulation results shown in Fig. 6 through Fig. 9 and Tables V and VI demonstrate the dramatic improvements in depth-of-field using synthetic elevation aperture imaging. Fig. 10 and Fig. 11 show experimental data that follows the performance in simulations of the different imaging schemes.

From a clinical breast imaging perspective, high detail resolution is needed to identify lesion boundaries and microcalcifications. High contrast resolution improves the discrimination of cysts from solid lesions. Fig. 6(a) shows −6 dB contour plots, indicative of the elevation detail resolution performance, and Fig. 6(b) shows elevation contrast resolution performance in the −20 dB plots for conventional (dotted), $\mathrm{SRA_{Conv}}$ (dashed), and $\mathrm{STRA_{Conv}}$ (solid) beamforming. The −6 dB contour plots show that conventional beamforming (fixed elevation focus in both transmit and receive) results in a narrow beamwidth that is fairly constant only over a 10-mm range about the focus, but quickly diverges away from the focus. When synthetic receive focusing ($\mathrm{SRA_{Conv}}$) is applied, the depth-of-field is extended from the conventional case. Further improvement is obtained with synthetic focusing in both transmit and receive ($\mathrm{STRA_{Conv}}$). The resulting beam is approxi-

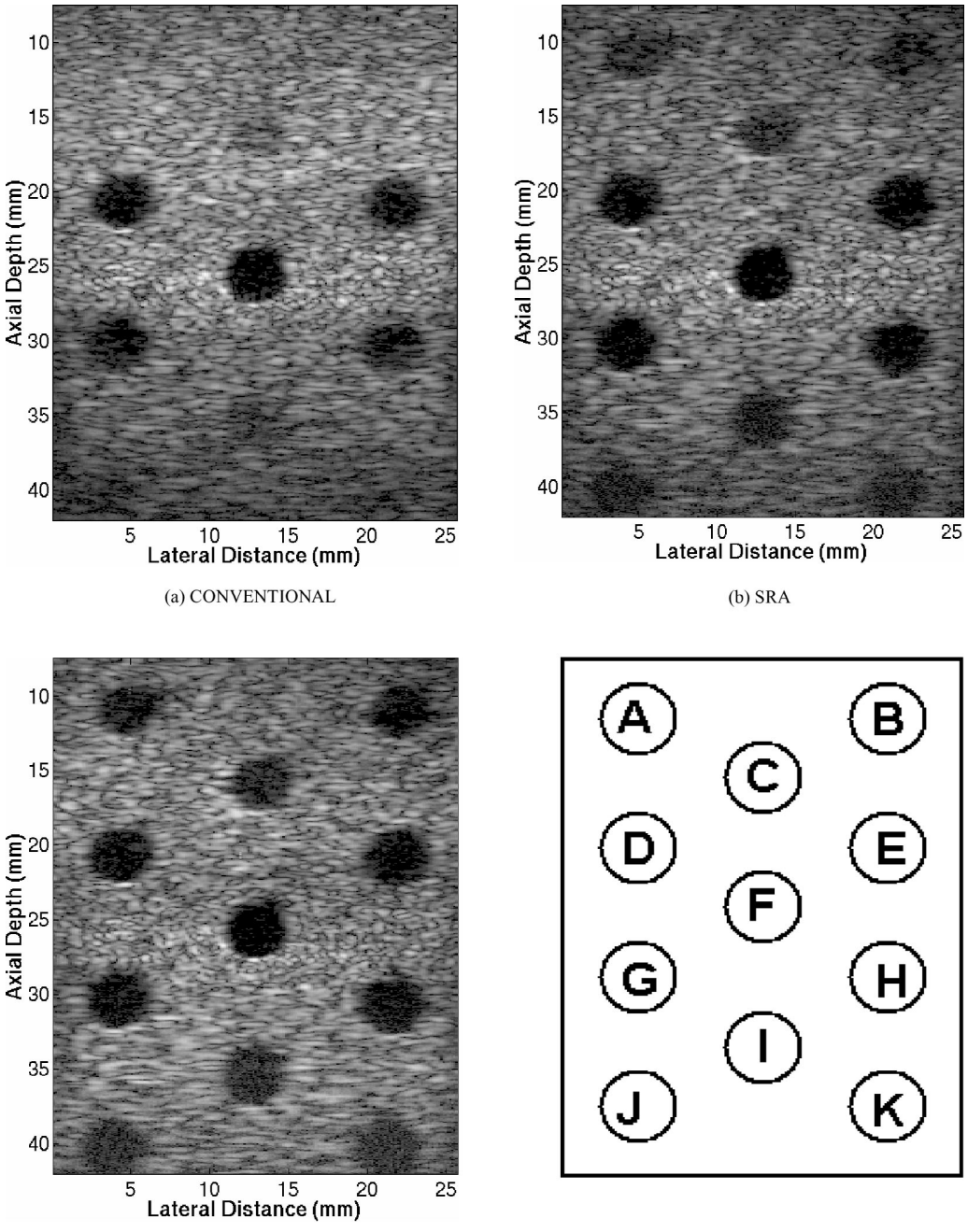

(a) CONVENTIONAL

(b) SRA

(c) STRA

(d) TEMPLATE

Fig. 10. 4-mm cyst lesion images and lesion identification scheme. a) Conventional 4-mm diameter lesion phantom with normal lateral beamforming and with elevation fixed receive focusing from the mechanical lens alone. b) SRA image that applies elevation synthetic receive focusing, $\mathrm{SRA}_{\mathrm{HamF2}}$. This image shows increased detectability of the top and bottom row of lesions compared with the conventional image. More lesions are identified in the STRA image (c), which employs elevation synthetic receive focusing on transmit and receive, $\mathrm{STRA}_{\mathrm{HamF2}}$. The synthetic receive focusing uses elevation expanding aperture (F-number = 2) and Hamming window apodization in transmit and receive. d) A schematic labeling of the cysts used in reporting contrast measurements in Table VII.

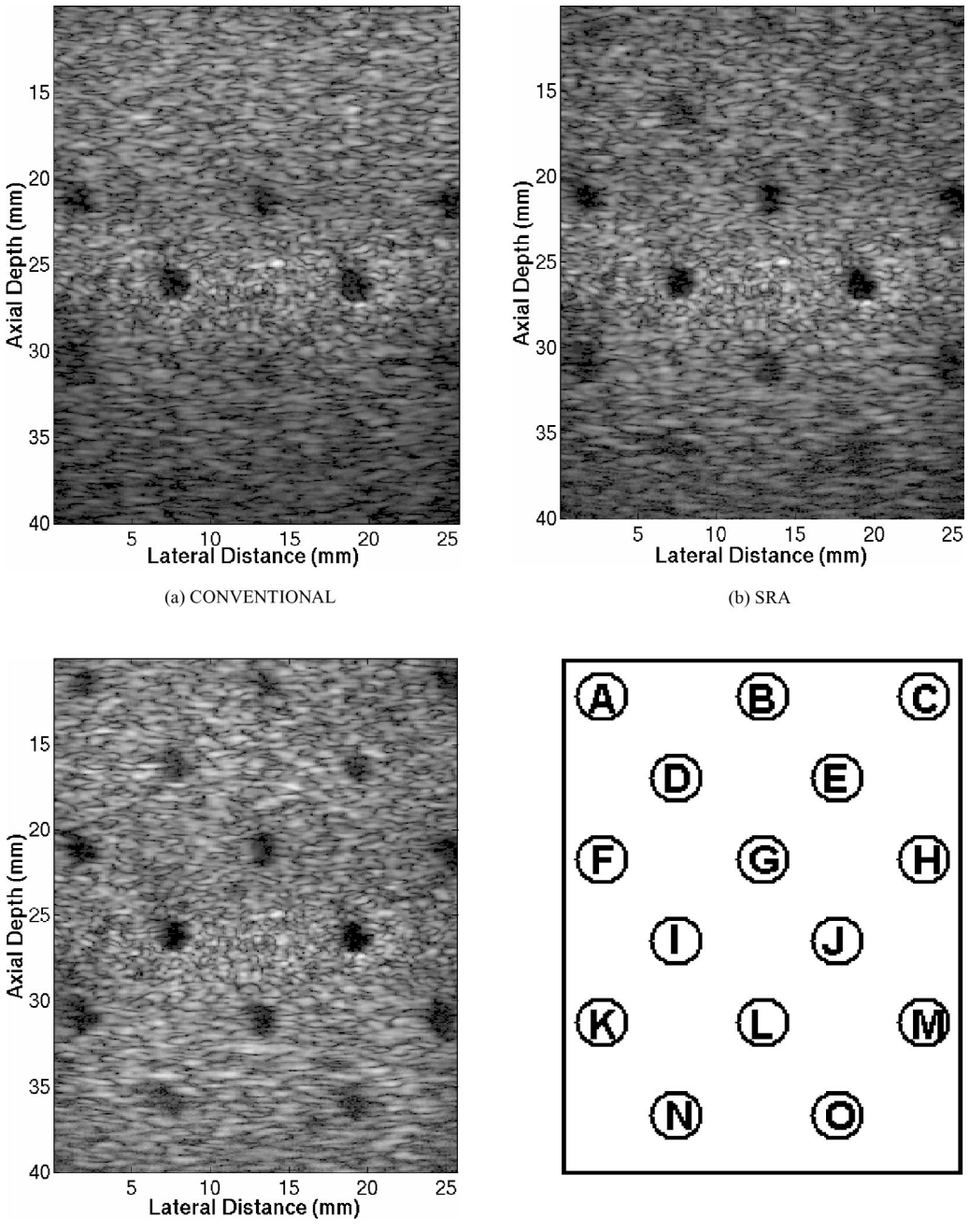

(a) CONVENTIONAL

(b) SRA

(c) STRA

(d) TEMPLATE

Fig. 11. 2-mm cyst lesion images and lesion identification scheme. a) 2-mm diameter cyst phantom conventional image with normal lateral beamforming and with elevation fixed receive focusing from the mechanical lens alone. b) SRA image employing elevation synthetic receive focusing, $\mathrm{SRA}_{\mathrm{HamF2}}$. This image shows increased detectability of the top and bottom row of lesions compared with the conventional image. c) STRA image showing the 2-mm cyst phantom with elevation synthetic focusing on transmit and receive, $\mathrm{STRA}_{\mathrm{HamF2}}$. The synthetic receive focusing uses elevation expanding aperture (F-number = 2) and Hamming window apodization in transmit and receive. d) A schematic labeling of the cysts used in reporting contrast measurements in Table VIII.

mately constant throughout the imaging region, and the small lobes located at 12 mm in the $\mathrm{SRA_{Conv}}$ beam have also been removed. The −20 dB contour plots in Fig. 6(b) show significant improvements in contrast resolution when $\mathrm{SRA_{Conv}}$ and $\mathrm{STRA_{Conv}}$ are used. However, close to the transducer, there are still large grating lobes outside the mainlobe. These regions of constructive interference arise in the near field because of the path length differences between the different rows and their directivity pattern. Aperture growth can be implemented to reduce or remove these grating lobes and increase the contrast resolution.

Fig. 7 compares SRA beamforming using different aperture growth functions [$\mathrm{SRA_{Conv}}$ (dotted), $\mathrm{SRA_{RecF2}}$ (dashed), and $\mathrm{SRA_{HamF2}}$ (solid)] at −6 dB (a) and −20 dB (b) contour levels. The small regions of constructive interference close to the transducer that appear in the $\mathrm{SRA_{Conv}}$ contours [Fig. 7(a)] are removed when either the rectangular window or the Hamming window is implemented. However, the beamwidth slightly increases before and after the focus. This effect is mainly observed when applying the Hamming window because of the reduction in the effective aperture size when this window type is applied. The −20 dB contour plots are shown in Fig. 7(b). Although the Hamming window causes an increase in the slice thickness, it clearly improves the near-field performance of the array. Improvements in the contrast resolution are also obtained using the rectangular window, but these are not as pronounced as for $\mathrm{SRA_{HamF2}}$.

The purpose of implementing synthetic beamforming with the 1.75D array is to obtain a constant and narrow beamwidth (i.e., good resolution) throughout the imaging region. $\mathrm{SRA_{HamF2}}$ shows an increase in the depth-of-field when compared with the conventional beamforming scheme in Fig. 6. However, as seen in Fig. 6, STRA beamforming can improve the results even further.

Fig. 8 shows the −6 dB (a) and −20 dB (b) contour plots of different aperture growth functions in STRA beamforming: $\mathrm{STRA_{Conv}}$, $\mathrm{STRA_{RecF2}}$, and $\mathrm{STRA_{HamF2}}$. The near-field performance improved both in terms of slice thickness and contrast resolution with the use of aperture growth. Also, very uniform beamwidths were obtained throughout the imaged region. This is especially noticeable in the −20 dB contour plot when the Hamming window was applied. Based on these results, $\mathrm{STRA_{RecF2}}$ and $\mathrm{STRA_{HamF2}}$ have similar performance. But, at lower beamwidth levels, shown in Fig. 9, we notice that $\mathrm{STRA_{HamF2}}$ has a better performance.

The results have been summarized in Tables V and VI, where the −6 dB and −20 dB beamwidths have been calculated for six equally spaced depths within the imaged region. Here, we also see that the variation in the beamwidth is smaller for $\mathrm{STRA_{HamF2}}$ at both −6 dB and −20 dB as compared with $\mathrm{STRA_{RecF2}}$.

The phantom experiment results demonstrate the improvements in increasing the depth-of-field. Tables VII and VIII report contrast measurements for the different lesions grouped by their depth. The results in Table VII show contrast increase with the use of synthetic beamforming in elevation. Most of the contrast improvements occur in the lesions located in the first 20 mm and after 30 mm, because of the larger depth-of-field for SRA and STRA imaging. Lesions D through H are located within the depth-of-field for a fixed elevation transmit and receive focus (i.e., focus with mechanical lens only), and, thus, there is no significant improvement in contrast with the use of synthetic beamforming.

The negative contrast measurement values, specifically for lesion B in Table VII, can be explained by speckle statistics. In the conventional image, the lesions from 10 to 18 mm are not visualized. The array resolution is poor in this region, and the speckle brightness in these regions are statistically indistinguishable from the surrounding areas. Thus, it is possible to have areas with varying brightness located throughout this depth, and the mask used for the cyst brightness measurements contains brighter speckle than the speckle mask, leading to a negative contrast value.

Using these measurements, we can quantify the improvements associated with synthetic beamforming. Table VII shows the contrast for the 4-mm diameter lesions. There are small improvements in contrast for the lesions in the fixed elevation transmit/receive (conventional) depth-of-field. The most significant improvements occur for the lesions outside this area (lesions A–C, I–K), where the average contrast improvement is 38.3% for SRA imaging and 51.0% for STRA imaging. Table VII also shows the mean and standard deviation of the contrast measurements for the three beamforming methods. The mean lesion contrast is highest for STRA imaging, but also important to note is the smaller standard deviation associated with STRA imaging than with SRA imaging and conventional imaging, indicating a more uniform contrast performance along depth when synthetic beamforming is employed.

The 2-mm lesion phantom contrast measurements in Table VIII show similar results. For the lesions located outside the conventional depth-of-field, the average improvement is 41.36% for SRA imaging and 57.0% for STRA imaging. The high mean contrast and low standard deviation measurements reported in the table for SRA imaging show that this imaging method results in more consistent contrast measurements over all depths compared with conventional imaging. STRA imaging shows further improvements with its reported low standard deviation measurement.

These contrast measurements are subject to error. If the image plane does not pass through the cyst's center (largest diameter cross-section), improved imaging could potentially degrade the contrast because different rows could receive signals off an incorrect slice plane. Speckle statistics could randomly place brighter/dimmer speckle areas in the measurement regions that influence the contrast measurements. Variations in the mask sizes used for contrast measurements can also produce different results. Still, the overall trends of contrast improvement with synthetic receive imaging and larger improvements with synthetic transmit imaging are shown.

The data collected for synthetic aperture imaging on the phantoms contain no significant motion. Thus, elevation synthetic transmit beamforming was not susceptible to the motion artifacts that will occur in real-time patient imaging. The frame-rate costs, as described in Section III-D, may be significant when combined with the elevation motion (see Section V-A with the use of transmit synthetic beamforming). The use of synthetic receive beamforming increases the array depth-of-field at a minimum frame rate cost.

TABLE IX
DIFFERENT TISSUE MOTIONS AND EFFECTS ON ELEVATION PSF MAIN LOBE WIDTH, E, FOR SRA IMAGING.

Tissue type	v velocity	E (μm)	ΔE (μm)	% change
Breast (supine position)	2.88 mm/s	500	$\pm$ 1.0	0.2 %
Breast (sidelying position)	0.81 mm/s	500	$\pm$ 0.28	0.06 %

A. Motion Effects

Synthetic beamforming techniques are sensitive to patient/transducer motion, as data for a single image line requires a longer acquisition time compared with conventional beamforming. Operator scanning techniques and/or patient (cardiac, breathing) motion can result in a relative displacement between the transducer and tissue. This displacement can occur in the lateral, elevation, or axial dimension.

When performing synthetic receive imaging in elevation, tissue motion among subaperture (one subaperture defined as one row of the array) signal acquisitions can contribute to image degradation. This motion could cause misalignment of the received signals in the post-processing combination of the subapertures. Nock [10] and Trahey [13] have described the effect of motion in lateral synthetic receive aperture imaging on image degradation along the lateral and axial dimensions. A similar analysis applies for the case of elevation synthetic receive aperture imaging. Resolution of a rectangular aperture of length D and wavelength λ at a focal distance z can be defined as $\frac{\lambda z}{D}$ [11].

For the array parameters described in Table II, the theoretical elevation resolution is calculated to be 500 μm when all eight rows are used. The lateral resolution is calculated to be 230 μm.

The effect of motion in the elevation dimension on the main lobe of the PSF, as described by Trahey [3], is a broadening of the main lobe (i.e., worse resolution) by ΔE:

$$\Delta E = \frac{v\,(s-1)}{P}. \tag{12}$$

Eq. (12) describes the amount of main lobe broadening as a function of P, the pulse repetition frequency (pulse repetitions per second); v, the relative transducer/tissue motion (mm/s); and the number of synthetic receive subapertures, s. This equation is equivalent for the change in lateral resolution, ΔL, caused by tissue motion.

Tissue motion varies among tissue types, depending on the patient position and proximity to the heart. We use our array for clinical imaging of breast tissue, one of the tissue types least susceptible to motion. El-Fallah *et al.* [12] presented results that show the average tissue motion expected in breast imaging with the patient in supine position to be 2.88 mm/s and sidelying position, 0.81 mm/s. Assuming a pulse repetition frequency of 20 kHz and the use of eight subapertures in elevation (for our 8×128 array), $\Delta E = 1.0$ and 0.28 μm for supine and sidelying tissue velocities, respectively (results shown in Table IX. These values reflect relatively small error contributions to image resolution.

Axial motion can cause significant degradation in the quality of the synthetic elevation beamformed images. Small differences in the arrival time for two RF signals can cause destructive interference. The maximum timing error [3] t caused by a tissue/transducer velocity v is

$$t = \frac{2\,v\,(s-1)}{P\,c} \tag{13}$$

where v is the tissue motion velocity (mm/s), s is the number of subapertures, P is the pulse repetition frequency, c is the acoustic velocity (mm/μs), and the timing error, t, is expressed in μs.

Table X shows the computed maximum timing errors associated for the synthetic elevation aperture imaging schemes at the different breast tissue velocities. For breast imaging, there are small timing errors associated with synthetic beamforming, especially when symmetry is used for acquiring the data. For a 36-MHz system, each data sample is 28 ns, so, for the velocities examined, the axial motion for the subapertures yields a shift on the order of a fraction of an axial sample. The sidelying position contributes the least amount of timing error in SRA imaging. If techniques were used to measure the misalignments (i.e., a correlation-based technique), then, theoretically, the subaperture images could be readjusted in time appropriately before being summed to form the final image. The efficacy of the techniques would rely on the correlation between the rows, which could be further decreased with tissue inhomogeneities (i.e., phase aberrations).

Nevertheless, the results presented in this paper indicate that these processing improvements could dramatically improve image quality. Axial motion is the type of motion that could contribute most to image degradation when synthetic elevation beamforming is performed, but the axial motion is on the order of one image sample (at most) for breast imaging. In addition, there is a high potential for even better performance with dynamic elevation imaging in future, higher-channel count scanners.

TABLE X
TIMING ERRORS, t, ASSOCIATED WITH AXIAL MOTION IN SYNTHETIC ELEVATION BEAMFORMING.

Imaging mode	Breast supine position ($v = 2.88$ mm/s)	Breast sidelying position ($v = 0.81$ mm/s)
SRA		
No symmetry used, $s = 8$	1.3 ns	0.37 ns
With symmetry, $s = 4$	0.55 ns	0.16 ns
STRA		
No symmetry used, $s = 64$	11.8 ns	3.3 ns
With symmetry, $s = 16$	2.8 ns	0.8 ns

VI. FURTHER ARRAY CAPABILITIES USING INDIVIDUAL ECHO SIGNALS

The array geometry and element uniformity play an important role in adaptive imaging. Adaptive imaging can be defined as a method to improve the imaging of a system by dynamically responding to the specific tissue being imaged. There are local and interpatient variations in tissue type that can distort the sound waves as they propagate through the tissue [13]. An adaptive imaging system would take an initial image, characterize the arrival time deviations in the returned sound waves from what is expected, then retransmit with adjusted waveforms. The received signals from this retransmit are adjusted in time again with the deviations used on transmit and will yield a properly focused beam. Individual RF echo signals from each element are necessary to be able to compute the arrival time delays for each A-line. There are several aspects of the array geometry, element size, and aberration measurement algorithm that are outside the scope of this paper. Walker [14], Gauss [5], [15], and Fernandez [16] are initial starting references covering these issues. However, to completely describe the advantages of 1.75D arrays, it is necessary to describe this arrays' use for phase aberration experiments.

If we assume a near-field aberration model [17], where all of the aberration occurs at the face of the transducer, then measuring the aberration involves an aberrator sampling issue for the array. Each element becomes a sampling point for the aberration measurement. From previous *in vivo* and *ex vivo* studies [5], [15], [18], [19], [20], and [21], the range of abdominal and breast aberration measurements is 2 to 8 mm FWHM (autocorrelation length of the aberration profile and 20 to 175 ns rms amplitude). The −6 dB FWHM autocorrelation length metric reflects the spatial frequency content of the aberrator. The aberration can vary in both dimensions of the tissue surface (along the lateral and elevation dimensions of the transducer). Therefore, sufficient element pitch (element-to-element spacing) is needed in both the lateral and elevation dimensions of the array for good aberration measurement. Using these previous measurements to determine the range of aberrators in breast tissue and the Nyquist sampling criterion, element-to-element spacing should be at most 1 mm in both the lateral and elevation dimensions to sufficiently sample the aberrators. This 1.75D 8 × 128 array forms a sampling grid of eight rows in elevation and 128 elements laterally to cover an array footprint of 12 × 26 mm. The lateral sampling of the aberrator is sufficient (lateral pitch = 0.2 mm), and the elevation pitch (1.5 mm) is sufficient, for most abdominal and breast aberrations clinically encountered. The main improvement from using a 1.75D array over conventional 1D arrays is the information received about the aberrator in elevation as well as having shorter element heights in elevation with the 1.75D array.

Breast scanning on volunteers was performed using individual RF echo signal acquisition for a 6 × 128 subaperture of this array. A least mean squares algorithm [15], [16] was used to calculate the arrival time delays associated with the near-field phase aberration model used. Fig. 12 shows the aberration profile measured from an example of clinical breast data. Tissue aberration varies along the lateral and elevation dimension of the transducer face, and the arrival time delay profile shows the two-dimensional variations. Because of the unique capability of the 1.75D array that enables arrival time estimates to be made in elevation, we can demonstrate the elevation variation of the phase aberration profile. This aberration profile is measured to be 4.56 mm FWHM (autocorrelation length) and 36.4 ns rms amplitude value. We should be able to perform better aberration measurements with this array than using conventional 1D arrays.

In addition to adaptive imaging, the capability of collecting individual channel data is also useful for motion tracking within the scans and between scans used in 3D volume rendering.

VII. CONCLUSIONS

We describe the capabilities of a 1.75D, 8 × 128 array demonstrating significant imaging improvements made solely from incorporating synthetic aperture imaging in elevation. The costs of synthetic receive imaging is in a reduction of frame rate and susceptibility to transducer/patient motion. This paper has shown increased visibility and contrast improvements of 2- and 4-mm lesions in ultrasound phantoms. Although motion artifacts will come into play with the frame rate costs to perform synthetic elevation imaging, they should not outweigh the gains from

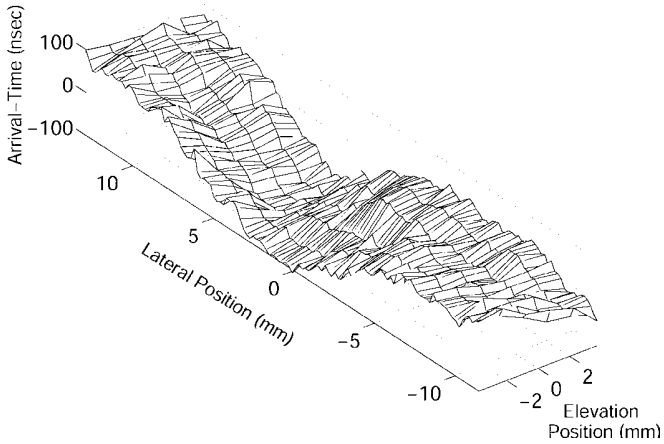

Fig. 12. Clinical measurement of a 2D aberration profile. This example was from breast data collected using the 8×128 1.75D array. The aberrator spatial variations are shown along both the lateral and elevation dimension.

taking advantage of the ability to synthetically adjust the time delays in elevation for 1.75D arrays.

It is currently feasible, with few system modifications in hardware/software, to perform synthetic elevation aperture imaging. The improved depth-of-field for 1.75D array and improved lesion resolution away from the lateral focusing and mechanical lens elevation focusing are significant advantages to implementing this system.

Because of the nature of a 1.75D array, acquisition of each individual channel is also possible. Lateral synthetic aperture imaging, phase aberration correction, and other imaging capabilities requiring individual signal data can be used with 1.75D arrays.

References

[1] D. A. Christensen, *Ultrasonic Bioinstrumentation*. New York: John Wiley & Sons, 1988.

[2] K. E. Thomenius, "Evolution of Ultrasound Beamformers," in *Proc. IEEE Ultrason. Symp.*, vol. 1, pp. 1615–1622, 1996.

[3] G. E. Trahey and L. F. Nock, "Synthetic receive aperture imaging with phase correction for motion and for tissue inhomogeneities—Part II: Effects of and correction for motion," *IEEE Trans. Ultrason., Ferroelect., Freq. Contr.*, vol. 39, no. 4, pp. 496–501, 1992.

[4] D. G. Wildes, R. Y. Chiao, C. M. W. Daft, K. W. Rigby, L. S. Smith, and K. E. Thomenius, "Elevation performance of 1.25D and 1.5D transducer arrays," *IEEE Trans. Ultrason., Ferroelect., Freq. Contr.*, vol. 44, no. 5, pp. 1027–1037, 1997.

[5] R. C. Gauss, G. E. Trahey, and M. S. Soo, "Wavefront estimation in the human breast," in *Proc. SPIE.*, vol. 4325, pp. 172–181, 2001.

[6] J. A. Jensen, "Field: A program for simulating ultrasound systems," *Med. Biol. Eng. Comp.*, vol. 4, no. 1, pp. 351–353, 1996.

[7] R. Y. Chiao, K. W. Rigby, and D. G. Wildes, "Optimization of 1.5D arrays," in *Proc. IEEE Ultrason. Symp.*, pp. 1835–1838, 1998.

[8] S. Nikolov, K. Gammelmark, and J. A. Jensen, "Recursive ultrasound imaging," in *Proc. IEEE Ultrason. Symp.*, pp. 1621–1625, 1999.

[9] O. T. von Ramm and S. W. Smith, "Beam steering with linear arrays," *IEEE Trans. Biomed. Eng.*, vol. 30, no. 8, pp. 438–452, 1983.

[10] L. F. Nock and G. E. Trahey, "Synthetic receive aperture imaging with phase correction for motion and for tissue inhomogeneities, part I: Basic principles," *IEEE Trans. Ultrason., Ferroelect., Freq. Contr.*, vol. 39, no. 4, pp. 489–495, 1992.

[11] M. Born and E. Wolf, *Principles of Optics*. Oxford: Pergamon Press, 1980.

[12] A. I. El-Fallah, M. B. Plantec, and K. W. Ferrara, "Ultrasonic measurement of breast tissue motion and the implications for velocity estimation," *Ultrasound Med. Biol.*, vol. 23, no. 7, pp. 1047–1057, 1997.

[13] G. E. Trahey, P. D. Freiburger, G. Ng, and D. C. Sullivan, "The impact of acoustic velocity variations on target detectability in ultrasonic images of the breast," *Invest. Radiol.*, vol. 26, no. 29, pp. 782–791, 1991.

[14] W. F. Walker and G. E. Trahey, "A fundamental limit on the performance of correlation based phase correction and flow estimation techniques," *IEEE Trans. Ultrason., Ferroelect., Freq. Contr.*, vol. 41, no. 5, pp. 644–654, 1994.

[15] R. C. Gauss, G. E. Trahey, and M. S. Soo, "Adaptive imaging in the breast," in *Proc. IEEE Ultrason. Symp.*, vol. 2, pp. 1563–1569, 1999.

[16] A. T. Fernandez, J. J. Dahl, D. M. Dumont, and G. E. Trahey, "Aberration measurement and correction with a high resolution 1.75D array," in *Proc. IEEE Ultrason. Symp.*, vol. 2, pp. 1659–1663, 2001.

[17] G. C. Ng, S. S. Worrell, P. D. Freiburger, and G. E. Trahey, "A comparative evaluation of several algorithms for phase aberration correction," *IEEE Trans. Ultrason., Ferroelect., Freq. Contr.*, vol. 41, no. 5, pp. 631–643, 1994.

[18] R. C. Gauss and G. E. Trahey, "Adaptive imaging in the thyroid using fundamental and harmonic echo data," in *Proc. IEEE Ultrason. Symp.*, vol. 2, pp. 1515–1519, 1999.

[19] P. D. Freiburger, D. C. Sullivan, B. H. LeBlanc, S. W. Smith, and G. E. Trahey, "Two-dimensional ultrasonic beam distortion in the breast: in vivo measurements and effects," *Ultrason. Imag.*, vol. 14, no. 4, pp. 398–414, 1992.

[20] Y. Sumino and R. C. Waag, "Measurements of ultrasonic pulse arrival time differences produced by abdominal wall specimens.," *J. Acoust. Soc. Amer.*, vol. 90, no. 6, pp. 2924–2930, 1991.

[21] L. M. Hinkelman, T. L. Szabo, and R. C. Waag, "Measurement of ultrasonic pulse distortion produced by human chest wall," *J. Acoust. Soc. Amer.*, vol. 101, no. 4, pp. 2365–2373, 1997.

Anna T. Fernandez (S'95) was born in Falls Church, VA on April 30, 1975. She received the B.S. degree in electrical engineering from the University of Maryland in College Park, MD in 1997. She received the M.S. in biomedical engineering in 2000 from Duke University, Durham, NC. She earned her doctoral degree in biomedical engineering at Duke University in December, 2002. Her dissertation topic is "Two-dimensional phase aberration measurement and correction using a 1.75D 8x128 ultrasonic array." She was awarded an NSF Graduate Fellowship in 1998.

Kim L. Gammelmark (S'02) was born in Fakse, Denmark on May 1, 1975. He received his M.S. degree in Electrical Engineering from the Technical University of Denmark, Kgs. Lyngby, Denmark, in August 2001.

He is currently a Ph.D. student in Biomedical Engineering at the Ørsted department at the Technical University of Denmark. His major research interest are the application of synthetic aperture techniques in medical ultrasound imaging, and synthetic aperture radar techniques.

Jeremy J. Dahl was born in Ontonagon, Michigan, on January 10, 1976. He received his B.S. in electrical engineering from the University of Cincinnati, Cincinnati, Ohio, in 1999. He is presently a graduate student working toward his doctoral degree at Duke University. He is currently researching real-time, adaptive, ultrasonic imaging with multi-dimensional arrays.

Constance G. Keen (S'97) received the BSEE degree from the Georgia Institute of Technology, Atlanta, Georgia, in 1984, and the MSEE degree from Washington University, St. Louis, Missouri, in 1989. She worked in missile guidance for McDonnell Douglas Astronautics, St. Louis, from 1984–1990. She worked on radar simulators for Scientific Research Corporation, Atlanta, Georgia, from 1992–1997. She is currently pursuing a doctorate degree with the Department of Biomedical Engineering, Duke University, under Dr. G. E. Trahey. Her current research focuses on the comparison of normal and tissue harmonic imaging with a multirow ultrasound array.

Roderick C. Gauss was born in Elmhurst, IL in 1968. He received the B.S. and M.S. degrees in Systems Engineering from Case Western Reserve University, Cleveland, OH in 1990 and 1992, respectively. He worked for two years developing industrial machine controls. He is currently pursuing a doctorate degree in biomedical engineering at Duke University, Durham, NC. He is currently employed with the ultrasound engineering group at Siemens Medical Systems, Issaquah, WA.

Gregg E. Trahey (S'83–M'85) received the B.G.S. and M.S. degrees from the University of Michigan, Ann Arbor, MI in 1975 and 1979, respectively. He received the Ph.D. degree in Biomedical Engineering in 1985 from Duke University. He served in the Peace Corps from 1975 to 1978 and was a project engineer a the Emergency Care Research Institute in Plymouth Meeting, PA, from 1980–1982. He is a Professor with the Department of Biomedical Engineering, Duke University. He is conducting research in adaptive phase correction, radiation force imaging methods, and 2-D flow imaging in medical ultrasound.

C.3 Equipment and methods for synthetic aperture anatomic and flow imaging

This paper was presented (invited) at the *IEEE International Ultrasonics Symposium* in Münich, Germany, October 2002, and published in the corresponding proceedings on pages 1518-1527.

Equipment and methods for synthetic aperture anatomic and flow imaging

Jørgen Arendt Jensen, Svetoslav I. Nikolov, Thanassis Misaridis and Kim L. Gammelmark

Center for Fast Ultrasound Imaging, Ørsted•DTU, Bldg. 348,
Technical University of Denmark, DK-2800 Kgs. Lyngby, Denmark

Abstract - Conventional ultrasound imaging is done by sequentially probing in each image direction. The frame rate is, thus, limited by the speed of sound and the number of lines necessary to form an image. This is especially limiting in flow imaging, since multiple lines are used for flow estimation. Another problem is that each receiving transducer element must be connected to a receiver, which makes the expansion of the number of receive channels expensive.

Synthetic aperture (SA) imaging is a radical change from the sequential image formation. Here ultrasound is emitted in all directions and the image is formed in all directions simultaneously over a number of acquisitions. SA images can therefore be perfectly focused in both transmit and receive for all depths, thus significantly improving image quality. A further advantage is that very fast imaging can be done, since only a few emissions are needed for forming an image, and a novel approach of recursive ultrasound imaging can be used to give several thousand images a second. A commercial SA imaging system has, however, not yet been introduced due to a number of problems. The fundamental problems are primarily that the signal-to-noise ratio and penetration depth are low and velocity imaging is thought not to be possible.

This paper will address all the issues above and show that they can all be solved using various techniques. The SNR is increased significantly beyond that for normal systems by using coded imaging and grouping of elements to form larger defocused emitting apertures. It is also possible to have many more receive channels, since different elements can be sampled during different emissions. The paper also shows that velocity imaging can be performed by making a special grouping of the received signals without motion compensation by using recursive imaging. With this technique continuous imaging at all points in the image is possible, which can significantly improve velocity estimates, since the estimates can be formed from a large number of emissions (100-200). The research scanner RASMUS, capable of acquiring clinical SA images, has been constructed and will be described. A number of phantom and in-vivo images will be presented showing *in-vivo* SA B-mode and flow imaging.

I Introduction

Modern digital ultrasound scanners acquire all images sequentially, where one direction in the image is measured at a time. The consequence of this is that the frame rate is limited by the image size and the speed of sound. The frame rate can be expressed as:

$$f_r = \frac{c}{2DN_l}, \tag{1}$$

where c is the speed of sound, D is the depth and N_l is the number of lines in one image. For normal anatomic imaging, this is in general not a problem. For flow imaging problems are encountered, since 8 or 16 emissions are necessary for each direction, and the frame rate is correspondingly reduced. Imaging the heart down to 15 cm and creating 100 image lines gives an unsatisfactory frame rate of 6.4 or 3.2 Hz (16 emissions/direction). This has been attempted solved by using explososcan [1], where a slightly broader beam is emitted with *e.g.* four lines being simultaneously created in receive to yield a four times increase in frame rate. The drawback is the slightly wider beam, where the effects of the single transmit focus is evident.

Another problem in conventional imaging is the single transmit focus, where the image is only narrowly focused at a single depth. This is often compensated for by making compound imaging, where one image line is made from several emissions with different transmit foci. The drawback here is the degradation in frame rate.

The frame rate problem also influences color flow mapping, since the number of emissions for one direction has to be kept to a minimum. The standard deviation of the estimates are therefore high. Another problem is that only the flow along the ultrasound beam is found, and a transverse flow will no be shown. The correct and accurate velocity is, thus, not shown in the current systems.

All of the problems are amplified when going to real-time three-dimensional scanning. To maintain a good frame rate, 16 beams must be reconstructed for each emission. This can give 15 volumes per second in the Duke 3D system [2], but is

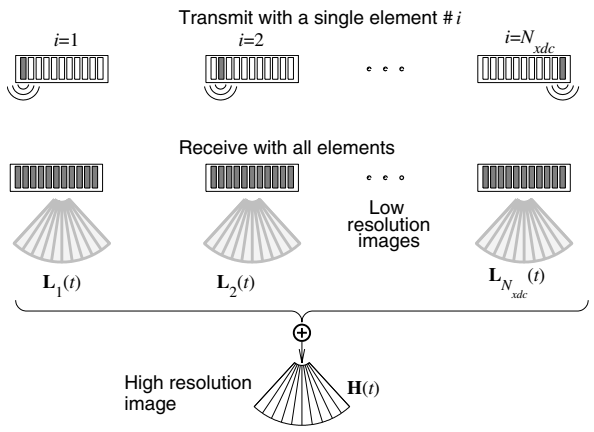

Figure 1: Principle of synthetic aperture imaging.

not sufficient to yield 3D flow data in real time. The system also have to use a sparse 2D array and have many channels in order to yield a good image quality.

The current systems, thus, have many limitations, which all can be related to the sequential data acquisition, that is limited by the speed of sound in tissue.

A natural step is to devise methods where parallelism is employed, and where the image can be made from only a few emissions. Many authors have investigated synthetic aperture imaging as a possible solution [3, 4, 5, 6, 7, 8]. There are, however, also problems here. The penetration depth is limited, since the emitted field is spread out in all directions. Flow imaging is also thought not to be possible, since the image is constructed from a number of emissions. Signals from moving scatterers will therefore not be in phase, and velocity estimation is therefore believed to be impossible.

This paper will give a brief introduction to synthetic aperture imaging, and it will be shown that the problems with limited penetration depth and flow estimation can be solved. Equipment constructed for measuring such images will be described and examples of *in-vivo* anatomic and flow synthetic aperture images are presented.

II Synthetic Aperture Imaging

The principle of synthetic aperture (SA) imaging is shown in Fig. 1. A defocused wave is emitted from a single element and the signal is received on all elements of the transducer. The geometric distance from the emission to the imaging point and back can then be calculated, and a low resolution image can be formed for all points in the image. The process is then repeated for other emitting elements and a series of low resolution images are formed. All of these are focused for the given transmission and receiving elements, and summing them gives a high resolution image, that is focused for all transmissions and receptions corresponding to a dynamically focused image in both transmit and receive.

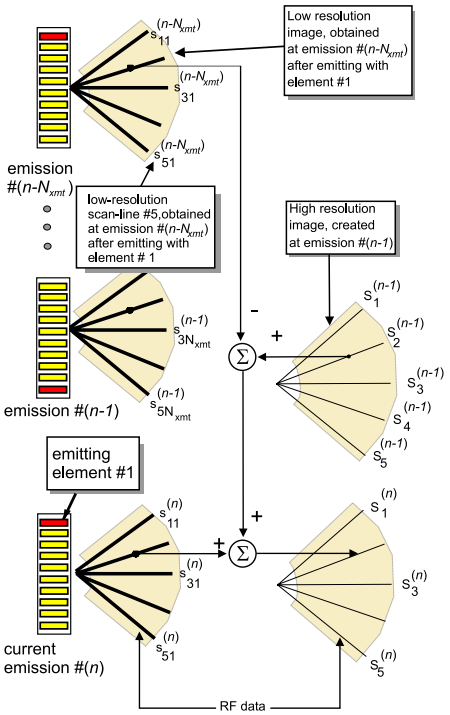

Figure 2: Recursive ultrasound imaging. In transmit only one element is excited. Multiple receive beams are formed simultaneously for each transmit pulse. Each element is excited again after N_{xmt} emissions where $N_{xmt} = N_{xdc} = 10$ in this example (from [9]).

This type of synthetic aperture imaging, thus, gives the best possible resolution for delay-sum beamforming at all places in the image. The number of receiving elements can also change per emission, and many more elements than in traditional imaging can be employed with less electronics. Also the frame rate can be increased, since a full image can be constructed for only a few emissions.

SA imaging can also be used for recursive ultrasound imaging [9], where an image is created after each pulse emission. This is possible since a high resolution image can be made at all times after a complete set of low resolution images have been acquired. It is, thus, possible to take the last N_{xmt} emissions to form an image, where N_{xmt} is the number of emissions for one high resolution image. It is sufficient to replace the oldest low resolution image with the last as shown in Fig. 2, if the data acquisition is performed continuously. A new image can then be made after each pulse emission, and the frame rate can be maintained at the pulse repetition frequency.

The drawbacks of SA imaging are that the image is formed over several emissions, so it is prone to tissue motion artifacts, and it cannot be used for flow imaging. Also only one

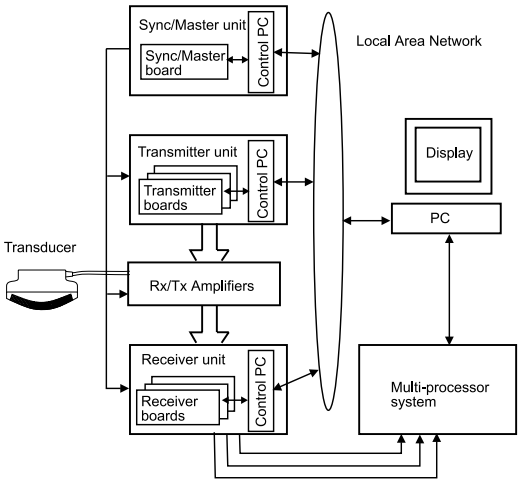

Figure 3: Overall diagram of system (from [10]).

element is used for a defocused transmission, and very little energy is therefore send into the tissue resulting in a low penetration depth. Sections IV and V will show that the penetration problem can be solved, and that SA imaging can attain a better penetration depth than traditional imaging. The clinical images in Section V also shows that motion is a minor problem for a typical clinical scanning. Section VII will show that it can be used for flow imaging with better results than traditional color flow map imaging. The final problem is how to construct a SA imaging system and this is addressed in the next Section.

III Equipment for synthetic aperture imaging

One of the main problems for investigating SA imaging has been that there does not exist systems for acquiring and processing the necessary data in real-time. We therefore set out in 1997 to build a fully flexible system, that could be used for all types of imaging. The system should have enough memory to sample RF data for each individual transducer element over a couple of seconds, and the transmitters should be capable of sending any kind of signal for any element and emission number. A full description of the system can be found in [10].

The RASMUS (Remotely Accessible Software configurable Multi-channel Ultrasound Sampling) system consists of four distinct modules: The transmitters, the analog amplifiers (Rx/Tx amplifiers), receivers, and the sync/master unit. The main blocks are depicted in Fig. 3.

Two 19 inch racks houses the 8 transmitters and the 8 receivers, respectively, as shown in Fig. 4. Each of these racks also houses a slot PC running Linux, which controls the setup and operation of the boards. A separate enclosure is used for

Figure 4: The RASMUS scanner seen from the front with the receivers on the top, transmitters in the middle and the power supplies in the bottom.

the analog front-end, which is shielded from the digital electronics. Here linear laboratory power supplies are also used to supply the front-end to keep the noise low.

Transmitter

Each transmitter board has 16 channels, which consists of a 128 ksamples RAM connected to a 40 MHz, 12 bits DAC. The RAM is controlled by an FPGA (Field Programmable Gate Array), where the individual waveforms are selected as a memory start address and a transmit delay. Both the waveform and the delay can change for each emission, which ensures full flexibility in the transmissions. The length of the waveforms can be set, and waveform durations up to 100 μs can be emitted.

The system houses 8 boards for a total of 128 independent emission channels.

Receiver

The Receiver board is illustrated in Fig. 5. It samples and processes 8 analog signals selected from 16 inputs through a 2-to-1 multiplexer. Each of the input signals are sampled at 40 MHz and 12 bits into one of the two SRAMs. The one SRAM is used for sampling and the second is used for transferring data to the Focus FPGA associated with each channel. The data is then processed in the Focus FPGA using param-

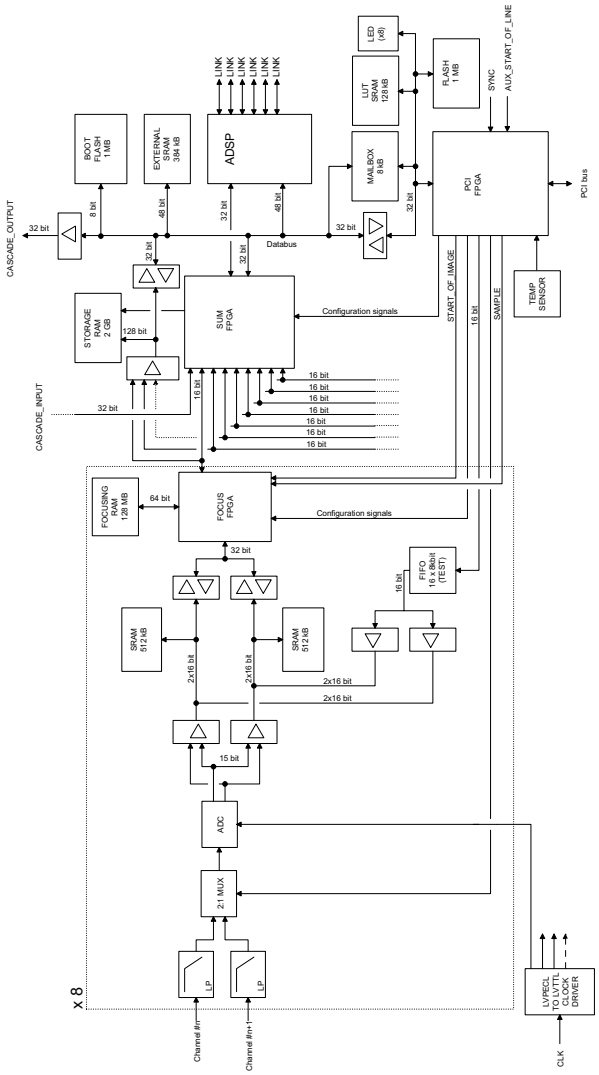

Figure 5: Main diagram of Receiver board (from [10]).

eters from the 128 MBytes Focusing RAM, and the result is passed on to the Sum FPGA. The processing can either be a dynamic receive focusing or the data can be passed unaltered for later storage. The Sum FPGA can either store the data in the 2Gbytes storage RAM or it can sum all 8 channels with the result from the cascade bus and pass it on to the next receiver board through the cascade bus. The last receiver board in the system then transmits the focused signal to the ADSP SHARC for transmission to the display PC.

The storage RAM can contain more than 3 seconds of real time data for each channel, that later can be accessed from the PCs controlling the system.

The actual board layout is shown in Fig. 6. All boards in the system has a size of 53 cm by 36.5 cm, and the receiver is manufactured using 12 layers.

Figure 6: The receiver board layout without RAM modules to reveal the processing electronics. The board size is 53 cm by 36.5 cm.

Software control

From the software point of view, the system consists of several computers that are directly connected to a number of transmitter and receiver boards. The computers are linked by a 100 Mbit LAN, and uses Linux as operating system and TCP/IP as the underlying communication protocol. A server program is running on each of the slot PCs and client programs can connect to the servers and setup the system.

The interface to the client program is implemented as a MATLAB toolbox and can be run by any PC connected to the net. The function calls are implemented to be as close to the functions in the simulation program Field II [11] as possible. Algorithms created using Field II can hereby easily be tested on the scanner with only minor changes in the Matlab program.

An example for setting the system to perform phased array B-mode imaging is shown below:

% Auto-detect and initialize the system
sys_init('*auto*'**);**
% Set the pulse repetition frequency
sys_set_fprf(*fprf***);**
% Set the sampling range gate in receive
sys_set_sampling_interval(*start_depth*, *end_depth***);**
% Set the number of scan-lines per frame
sys_set_no_lines(*no_lines***);**
% Define the transducer. Necessary for the delay calculations
tr_linear_array(*no_elements*, *width*, *height*, *kerf***);**
% Do for all lines in the image:
for *line_no* = 1:*no_lines*

```
  % Set the pulse and the apodization for the current line
  xmt_excitation(waveform(line_no));
  xmt_apodization(line_no,xmt_apo(line_no,:));
  rcv_apodization(line_no,times, rcv_apo(line_no,:,:));
  % Set the focus, defined in 3D coordinates
  xmt_focus(line_no,focus(line_no));
  rcv_dynamic_focus(line_no, theta(line_no), fi(line_no));
end

% Set the time-gain compensation curve
tmg_tgc(tgc_vector);
% Start the continuous imaging process
tmg_start
```

In order to make the system perform linear array imaging only one line needs to be added, which changes the origin of the individual scan-lines.

IV Solving the penetration problem

One of the main problems with SA is that only a single element is used for the emission. The spherical wave emitted will spread out in all directions, and the emitted intensity is therefore low, severely limiting the depth of penetration.

One approach to increase the energy is to use a number of elements to synthesize the emitted spherical wave thereby increasing the emitted energy. As showed experimentally by Karaman and coworkers [12], the amplitude of the wavefront created by the defocused subaperture consisting of N_t elements is proportional to $\sqrt{N_t}$. Using 11 elements, thus, gives an increase of 10.4 dB.

A second method is to use a coded excitation to increase the transmitted energy. Using a frequency modulated chirp and a matched filter for compression can increase the signal-to-noise ratio by a factor $T_c B/(T_p B_p)$, where T_c is the duration of the chirp and B is the bandwidth, and T_p and B_p are for the corresponding pulse excitation. An increase of 10 to 15 dB can be attained without a reduction in axial resolution and contrast [13, 14].

Combining the two approaches can give a significant increase in SNR, when it is also taken into account that the SA image is made from combining all the measurements [15]. The improvement in signal-to-noise ratio compared to an ordinary linear array image is [16]:

$$I_B = \frac{M N_t}{N_e^2} \frac{T_c}{T_p}, \tag{2}$$

where M is the number of SA emissions and N_e is the number of emitting elements for linear array scanning. For the typical case of a 7 MHz system with $M = 96$, $N_e = 64$, $N_t = 33$, $T_c = 20\mu$s, $T_p = 0.29\mu$s, and 128 receiving elements, the scheme gives an improvement factor I_B of 17 dB indicating that the SA system has a larger depth of penetration.

V Anatomic synthetic aperture images

An example of images measured by the RASMUS system using the method described in the previous Section is shown in Fig. 7, where a number of nylon wires embedded in a tissue mimicking phantom with an attenuation of 0.5 dB/[MHz cm] has been scanned. A 128 element linear 7 MHz array probe has been used with the system described in Section III. The left image shows the traditional linear array scan and the right image shows the SA image using 33 elements for each transmission together with a 20μs chirp. It can be seen that the wires are better defined and that the penetration depth has been increased by roughly 40 % from 70 mm to 100 mm.

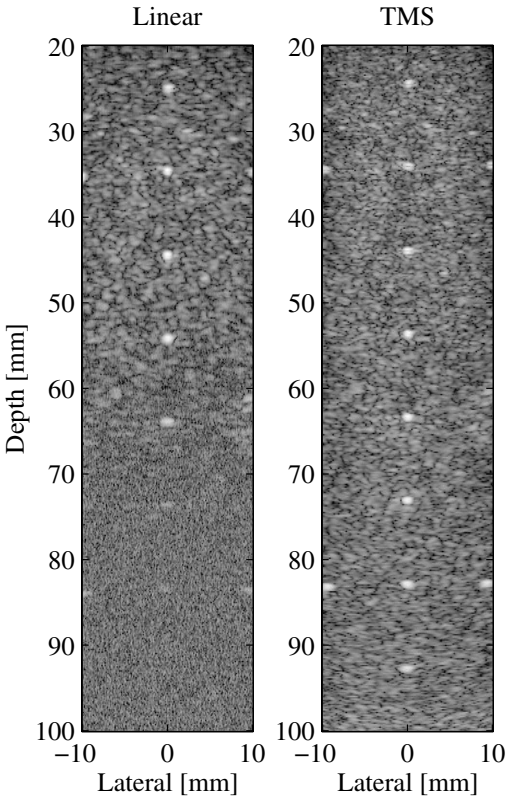

Figure 7: Linear array and synthetic aperture scan of nylon wires in a tissue mimicking phantom with an attenuation of 0.5 dB/[MHz cm] (from [16]).

Figure 8 shows *in-vivo* images of the abdomen of a healthy 27 year old male for conventional imaging (left) and synthetic imaging (right) using a convex array transducer. The transducer used for the measurement is a commercial 5.5 MHz convex array transducer with 192 elements and λ pitch.

For conventional imaging a 64 elements, Hamming weighted, transmit aperture is used with a fixed focus at 70 mm. A 2 cycle sinusoid at 5.5 MHz weighted with a Hanning window is used as the excitation pulse, and all 128 el-

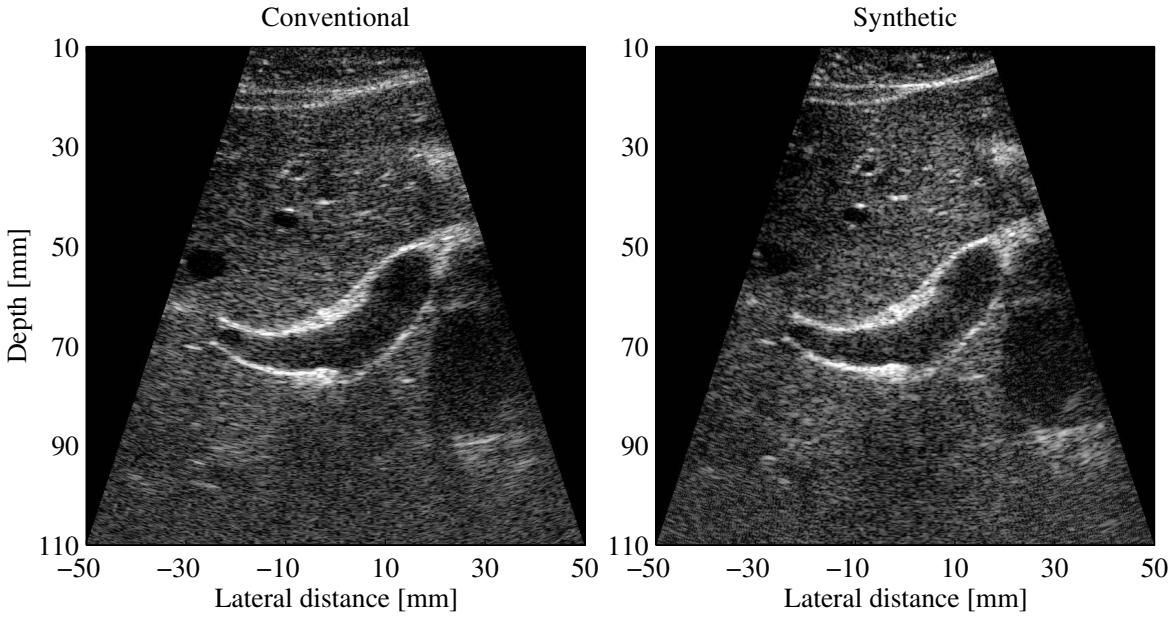

Figure 8: In-vivo images of the abdomen of a healthy 27 years old male using a convex array transducer. The left is the conventional convex array image and the right is the SA image.

ements are used on receive and for the subsequent beamformation. For synthetic imaging an 11 element subaperture is used to emulate the spherical wave transmission, and all 128 elements in the aperture are used on receive. The center of the transmit aperture is moved one element after each transmission, which results in a total of 118 emissions. A 20 μs linear FM signal with a center frequency of 5.5 MHz and 90% bandwidth is used as excitation signal. The FM signal has been weighted with a Tukey window to reduce the temporal sidelobes [13].

The conventional data are beamformed using dynamic receive focusing with delay updates for each sample. When beamforming both sets of data the element sensitivity is taken into account. The acceptance angle [6] is set to $\pm$50 degrees for each element, and, thus, an element is not applied in the beamformer until the point to be beamformed lies inside its acceptance angle.

Figure 8 shows a region of the abdomen, where there is motion from the heart and the pulsation of the vessels. It can been seen that the SA image is still of high quality despite the motion, and motion artifacts, thus, plays a minor role in SA imaging for this case.

VI Real-time three-dimensional imaging

SA imaging can also be used for creating three-dimensional images in real time. One approach is to use a two-dimensional array and then multiplex between the elements to measure from a large number of elements to have a good image quality [17]. Another approach is to use a rotating phased array transducer for sampling all spatial locations in a rotational movement. Such an approach is shown in Fig. 9. Here the array is continuously rotated and the synthetic aperture data are acquired from different positions. The position of the different receiving elements will be different for the different emissions, but this can be handled in the beamformation process by keeping track of the transducer position.

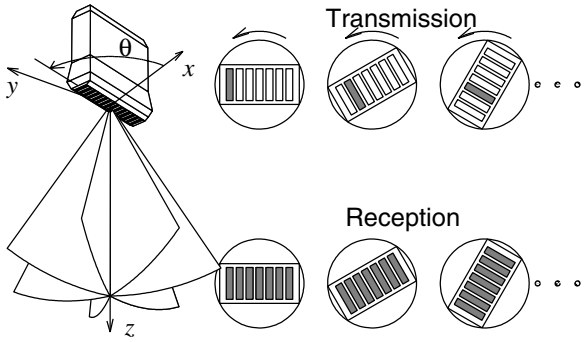

Figure 9: Three-dimensional scanning geometry.

For the given position a number of low resolution images will partly overlap as shown in Fig. 10. These can be used in the beamformation process to form the high resolution images. The overlap will be high at the center and less at the

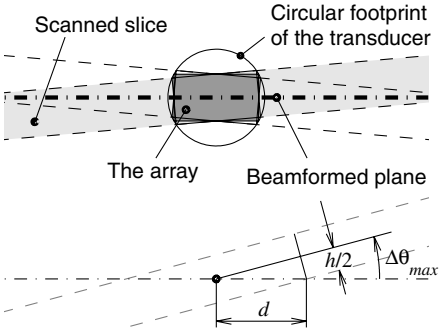

Figure 10: Slice reconstruction.

edges, so that less low resolution images can be used at the edge of the images.

Such a system has been implemented on the RASMUS system together with a rotating phased array transducer from Vermon [18]. The 3 MHz phased array transducer has 64 elements and can rotate back and forth more than 10 times per second to generate 10 volumes a second. Using an f_{prf} of 5 kHz gives 500 emissions per volume. A sufficient overlap between planes is ensured by making 64 emissions using 11 defocused elements. To ensure the same focusing over the image, the element firing order is [1 9 17 ... 57, 2 10 ... 58,, , 8 16 ... 64], so that the outer parts of the image are beamformed with received data from the full aperture.

The benefit of using this rotating aperture approach is that the point spread function is formed from all directions, and the effect of the elevation focus can be diminished to give point spread function focused in all three dimensions.

An example of such an image is shown in Fig. 11, which was scanned from a cyst phantom. Different scan planes from the acquired volume are shown.

VII Synthetic Aperture Flow Imaging

It is generally believed that SA imaging cannot be used for flow estimation based on the fact that the images are acquired over several emissions, and that they therefore cannot image moving objects. This statement is true, if the correctly summed image of the object is needed, but this is not the case. A flow imaging system uses the correlation between two measurements to derive either a phase or time shift to determine the velocity [20]. There is no demand that the image needs to be a correct depiction of the structure, which it actually is not, since the wavelength is much larger than *e.g.* the red blood cells. What is needed are measurements taken in exactly the same way to give signals where the only change is the motion [19]. A system that can do this is shown in Fig. 12. Here only two emissions are made for each SA. The image made by combining the emissions $[(n-3),(n-2)]$ is obtained in exactly the same way as for emissions $[(n-1),(n)]$. Corre-

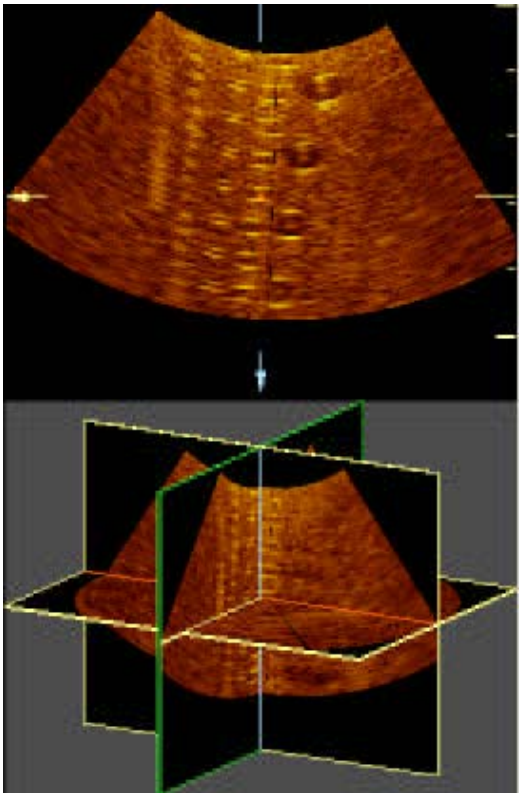

Figure 11: Three-dimensional image acquired by the rotating phased array transducer from a cyst phantom.

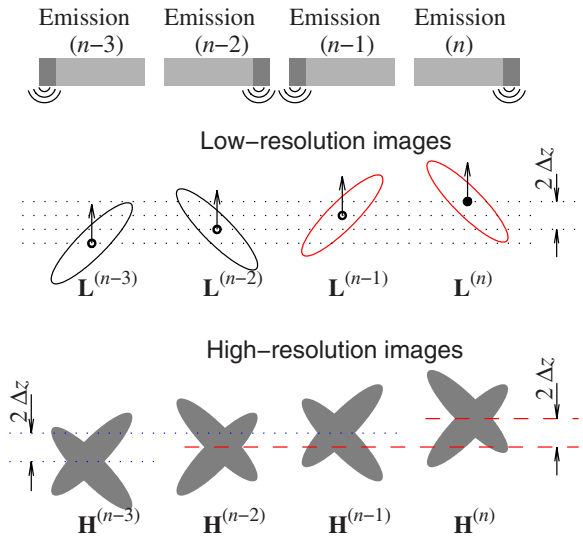

Figure 12: Creating several successive high-resolution images (from [19]).

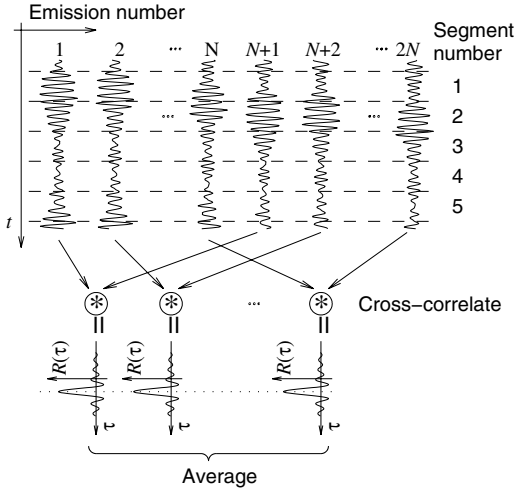

Figure 13: Creation of the cross-correlation function and its averaging over several emissions (from [19]).

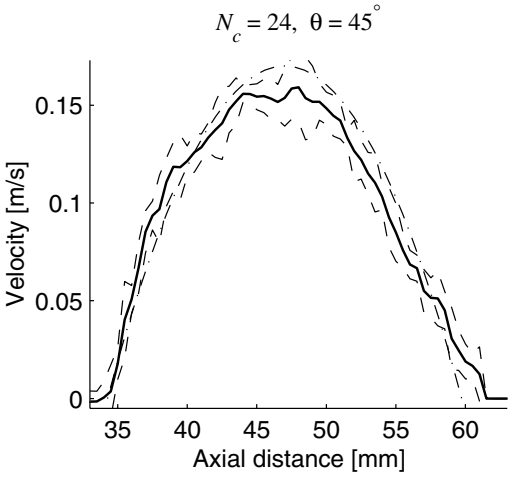

Figure 14: Velocity profile measured on a flow phantom (from [19]).

lating these images and finding the shift in position can, thus, give the velocity. It should also be noted that the image pairs $[(n-2),(n-1)]$ and $[(n),(n-1)]$ also can be correlated and will give the same correlation function. A new correlation function can, thus, be made after each emission [19] and all these functions can be averaged to give a good estimate as shown in Fig. 13. The approach can be extended to any number of emissions, but it must be ensured that the correlation functions are roughly alike, so the number of emissions is limited by the acceleration of the flow.

Since the approach measures data in all direction of the image simultaneously, all data at all image points are available at all times. Much more advanced echo canceling schemes can therefore be employed using the continuous data, and the initialization problems in current filters are avoided. The estimates can also be averaged over many more emissions to increase the accuracy.

Results from using the approach are shown in Fig. 14. Flow in a circulating flow rig has been measured using the RASMUS system. A 7 MHz linear array probe with 64 elements was used. Eleven elements were used in transmit with 4 separate transmissions of a 20μs chirp. All 64 elements in receive were sampled. Using only 24 emissions gave the velocity profiles shown, were the solid line is the mean of the profiles and the dashed lines are $\pm$ 3 standard deviations. The dashed-dotted line is that predicted by a mass flow meter.

The approach can also be used *in-vivo*. The image shown in Fig. 15 was acquired using only 24 emissions from the carotid artery of a 28 years old male. The pulse repetition frequency is 7 kHz, so more than 290 independent images can be presented per second.

A further advantage of SA imaging is that beamformation can be done in any direction. It is, thus, possible to beamform the received data along the flow lines to track the flow and thereby find the correct velocity magnitude as suggested in [21, 22]. An example of this approach for a flow angle of 60 degrees is shown in Fig. 16 for flow rig data. The RASMUS system has been used for the data acquisition together with the 7 MHz linear array. Eight emissions spread out over 128 elements has been made using 11 transmitting elements and a 20μs chirp. Data from 128 elements have been sampled by using the system's multiplexers, and 128 emissions has been used for making the estimates. Data from 20 profiles is shown at the top and the mean $\pm$3 standard deviations is shown on the bottom. The relative standard deviation compared to the peak velocity is 0.36 % (0.65 mm/s). Using the same setup for the purely transverse flow a std. of 1.2 % (2.1 mm/s) is obtained. A full color flow image can also be made from the data, and this is shown for the transverse flow in Fig. 17. The color scale indicates the velocity along the flow direction, where red hues indicate forward flow and blue reverse flow. The intensity of the color indicates the velocity magnitude.

Finally, an *in-vivo* image of the carotid artery of a 29 years old male is shown in Fig. 18 using the same set-up as for the flow rig experiment. Flow in both the carotid artery and the jugular vein is seen. The velocity along the flow direction is shown giving the velocity magnitude in the vessel.

VIII Conclusion

It has been demonstrated that synthetic aperture imaging can be used for both anatomic and flow imaging. The method can increase both depth of penetration, focusing, and contrast by employing a group of elements in transmit along with a coded transmission. It was also demonstrated that SA imaging can be used for directional flow imaging, where data is continu-

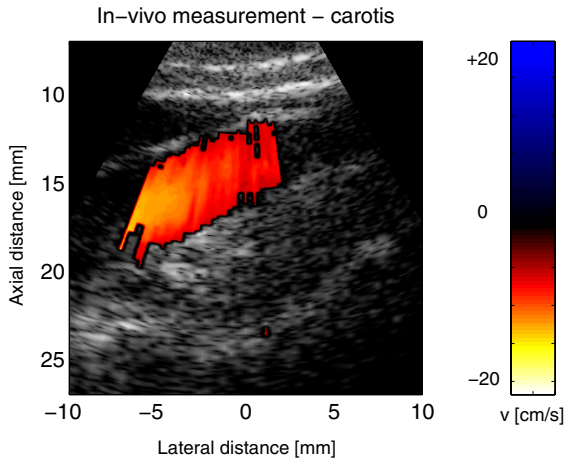

Figure 15: In-vivo synthetic aperture flow image of the carotid artery.

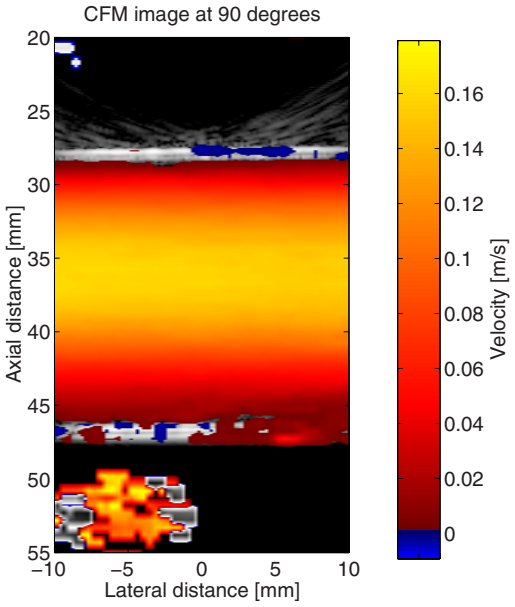

Figure 17: Color flow map SA image of flow in a flow rig at a 90 degree flow angle obtained by using directional beamforming along the flow lines. The color scale indicates the velocity along the flow direction, where red hues indicate forward flow and blue reverse flow.

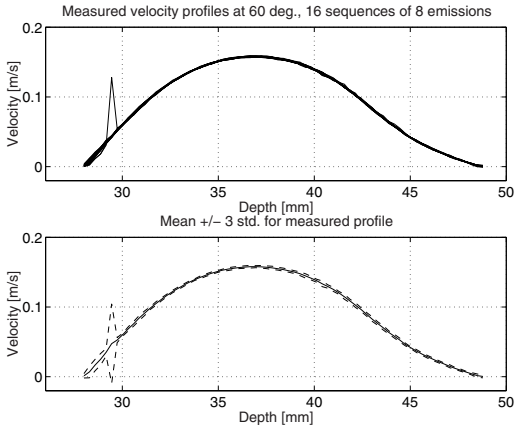

Figure 16: Estimated profiles from the flow rig at a 60 degree flow angle. The top graph shows the 20 independent profiles estimated and the bottom graph shows the mean profile (solid line) $\pm$ 3 standard deviations (dashed lines).

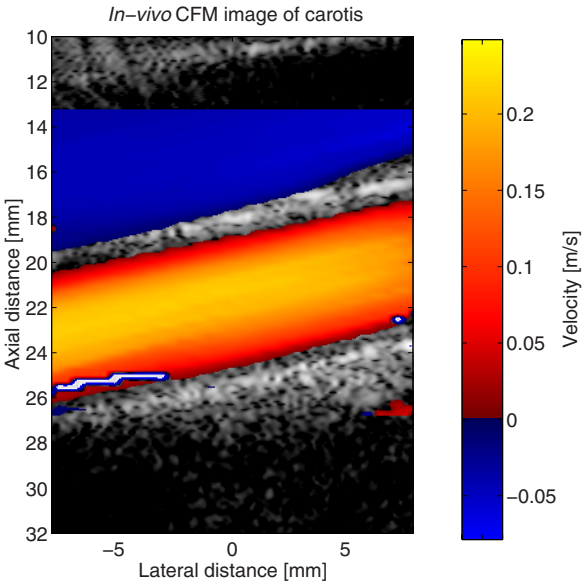

Figure 18: *In-vivo* color flow map image at a 77 degree flow angle for the jugular vein and carotid artery. The color scale indicates the velocity along the flow direction, where red hues indicate forward flow and blue reverse flow.

ously available in all directions of the image. The estimates can hereby be improved, and it is possible to determine a flow transverse to the traditional ultrasound beam. The approaches can also be used to acquire data from many more elements than traditional scanners by using multiplexers and the image quality can hereby be even further increased. This can also be used for making fast and high-quality three-dimensional images.

ACKNOWLEDGEMENT

This work was supported by grant 9700883, 9700563 and 26-01-0178 from the Danish Science Foundation, by the Academy of Technical Sciences, by Frode Nygaards Foundation, and by B-K Medical A/S, Herlev, Denmark. I/O Consulting A/S, Valby Denmark made the electronic design and manufacturing of the RASMUS system.

IX REFERENCES

[1] D. P. Shattuck, M. D. Weinshenker, S. W. Smith, and O. T. von Ramm. Explososcan: A parallel processing technique for high speed ultrasound imaging with linear phased arrays. *J. Acoust. Soc. Am.*, 75:1273–1282, 1984.

[2] O. T. von Ramm, S. W. Smith, and Henry G. Pavy. High-speed ultrasound volumetric imaging system – Part II: Parallel processing and image display. *IEEE Trans. Ultrason., Ferroelec., Freq. Contr.*, 38:109–115, 1991.

[3] S. Bennett, D. K. Peterson, D. Corl, and G. S. Kino. A real-time synthetic aperture digital acoustic imaging system. In P. Alais and A. F. Metherell, editors, *Acoust. Imaging*, volume 10, pages 669–692, 1982.

[4] K. Mayer, R. Marklein, K. J. Langenberg, and T. Kreutter. Three-dimensional imaging system based on Fourier transform synthetic aperture focusing technique. *Ultrasonics*, 28:241–255, 1990.

[5] L. J. Busse. Three-dimensional imaging using a frequency-domain synthetic aperture focusing technique. *IEEE Trans. Ultrason., Ferroelec., Freq. Contr.*, 39:174–179, 1992.

[6] M. O'Donnell and L. J. Thomas. Efficient synthetic aperture imaging from a circular aperture with possible application to catheter-based imaging. *IEEE Trans. Ultrason., Ferroelec., Freq. Contr.*, 39:366–380, 1992.

[7] J. T. Ylitalo and H. Ermert. Ultrasound synthetic aperture imaging: monostatic approach. *IEEE Trans. Ultrason., Ferroelec., Freq. Contr.*, 41:333–339, 1994.

[8] S. I. Nikolov. *Synthetic aperture tissue and flow ultrasound imaging*. PhD thesis, Ørsted•DTU, Technical University of Denmark, 2800, Lyngby, Denmark, 2001.

[9] S. I. Nikolov, K. Gammelmark, and J. A. Jensen. Recursive ultrasound imaging. In *Proc. IEEE Ultrason. Symp.*, volume 2, pages 1621–1625, 1999.

[10] J. A. Jensen, O. Holm, L. J. Jensen, H. Bendsen, H. M. Pedersen, K. Salomonsen, J. Hansen, and S. Nikolov. Experimental ultrasound system for real-time synthetic imaging. In *Proc. IEEE Ultrason. Symp.*, volume 2, pages 1595–1599, 1999.

[11] J. A. Jensen. Field: A program for simulating ultrasound systems. *Med. Biol. Eng. Comp.*, 10th Nordic-Baltic Conference on Biomedical Imaging, Vol. 4, Supplement 1, Part 1:351–353, 1996b.

[12] M. Karaman, P. C. Li, and M. O'Donnell. Synthetic aperture imaging for small scale systems. *IEEE Trans. Ultrason., Ferroelec., Freq. Contr.*, 42:429–442, 1995.

[13] T. X. Misaridis and J. A. Jensen. An effective coded excitation scheme based on a predistorted FM signal and an optimized digital filter. In *Proc. IEEE Ultrason. Symp.*, volume 2, pages 1589–1593, 1999.

[14] T. Misaridis. *Ultrasound imaging using coded signals*. PhD thesis, Ørsted•DTU, Technical University of Denmark, Lyngby, Denmark, 2001.

[15] K. Gammelmark. Multi-element synthetic transmit aperture imaging using temporal encoding. Master's thesis, Ørsted•DTU, Technical University of Denmark, Lyngby, Denmark, 2001.

[16] K. L. Gammelmark and J. A. Jensen. Multi-element synthetic transmit aperture imaging using temporal encoding. In *Proc. SPIE: Progress in biomedical optics and imaging*, volume 3, pages 25–36, 2002.

[17] G. R. Lockwood, J. R. Talman, and S. S. Brunke. Real-time 3-D ultrasound imaging using sparse synthetic aperture beamforming. *IEEE Trans. Ultrason., Ferroelec., Freq. Contr.*, 45:980–988, 1998.

[18] A. Nguyen-Dinh, P. Mauchamp, N. Felix, R. Dufait, P. Auclair, and A. Flesch. Integrated mechanism based multiplane/3D ultrasonic imaging probes. In *Proc. IEEE Ultrason. Symp.*, volume 2, pages 1147–1150, 2001.

[19] S. I. Nikolov and J. A. Jensen. Velocity estimation using synthetic aperture imaging. In *Proc. IEEE Ultrason. Symp.*, pages 1409–1412, 2001.

[20] J. A. Jensen. *Estimation of Blood Velocities Using Ultrasound: A Signal Processing Approach*. Cambridge University Press, New York, 1996.

[21] J. A. Jensen and I. R. Lacasa. Estimation of blood velocity vectors using transverse ultrasound beam focusing and cross-correlation. In *Proc. IEEE Ultrason. Symp.*, pages 1493–1497, 1999.

[22] J. A. Jensen. Efficient focusing scheme for transverse velocity estimation using cross-correlation. In *Proc. of SPIE: Progress in biomedical optics and imaging*, volume 4325, pages 242–256, 2001.